



# TIMODAZ

## Thermal Impact on the Damaged Zone Around a Radioactive Waste Disposal in Clay Host Rocks

(Contract Number : FI6W-CT-2007-036449)

### Deliverable D13 – Annex 1 Hollow cylinder test in Boom Clay

Editor(s): **Robert Charlier**

Authors : **Robert Charlier, René Chambon, Frédéric Collin, Arnaud Dizier, Bertrand François, Benoit Garitte, Antonio Gens, Chen Guangjing, Lyesse Laloui, Ferdinando Marinelli, Yannick Sieffert**

Laboratories: **CIMNE, ESV EURIDICE GIE, EPFL, ULg, UJF**

Reporting period: **01/10/2009 - 31/03/2010**

Date of issue of this report: **30/08/2010**

Start date of project: **01/10/2006**

Duration : **48** Months

Project co-funded by the European Commission under the Euratom Research and Training Programme on Nuclear Energy within the Sixth Framework Programme (2002-2006)

#### Dissemination Level

<b>PU</b>	Public	
<b>RE</b>	restricted to a group specified by the partners of the TIMODAZ project	PU
<b>CO</b>	confidential, only for partners of the TIMODAZ project	

TIMODAZ

IMR –N°: **D13 – Annex 1**

Dissemination level: **PU**

Date of issue of this report: **30/08/10**

1/142



## DISTRIBUTION LIST

Name	Number of copies	Comments
Mr. Christophe Davies (European Commission)	One electronic copy on CIRCA One paper copy	
All consortium members	One electronic copy available on the restricted area of the TIMODAZ web portal	

TIMODAZ

IMR –N°: **D13 – Annex 1**

Dissemination level: **PU**

Date of issue of this report: **30/08/10**

2/142



<b>1</b>	<b><i>Introduction</i></b> .....	<b>5</b>
<b>2</b>	<b><i>Executive summary</i></b> .....	<b>5</b>
<b>2.1</b>	<b>Introduction</b> .....	<b>5</b>
<b>2.2</b>	<b>The benchmark exercise</b> .....	<b>6</b>
<b>2.3</b>	<b>Additional computations</b> .....	<b>14</b>
<b>2.4</b>	<b>Conclusions</b> .....	<b>25</b>
<b>3</b>	<b><i>Introduction, short description of associated experiments, by the lab realising the experiment</i></b> .....	<b>27</b>
<b>4</b>	<b><i>Exercise, idealization proposed</i></b> .....	<b>27</b>
<b>4.1</b>	<b>Geometry</b> .....	<b>27</b>
<b>4.2</b>	<b>Initial conditions</b> .....	<b>27</b>
<b>4.3</b>	<b>Boundary conditions</b> .....	<b>28</b>
<b>4.4</b>	<b>Constitutive models and parameters</b> .....	<b>30</b>
4.4.1	Mechanical model .....	30
4.4.2	Hydraulic and thermal constitutive models .....	32
4.4.3	Balance equations.....	33
4.4.4	Strain rate .....	34
<b>4.5</b>	<b>Parameters</b> .....	<b>35</b>
<b>4.6</b>	<b>Description of the calculation</b> .....	<b>36</b>
<b>5</b>	<b><i>General form of the numerical results</i></b> .....	<b>37</b>
<b>5.1</b>	<b>Results of modelling: hydro-mechanical aspects</b> .....	<b>37</b>
5.1.1	Elastic perfectly plastic model (case A) .....	37
5.1.2	Friction angle hardening elastoplastic model (case B) .....	44
5.1.3	Combined angle friction hardening and cohesion softening model (case C) .....	47
5.1.4	Combined angle friction hardening and cohesion softening model with permeability as a function of porosity (case D).....	50
5.1.5	Comparison between the four cases .....	53
<b>5.2</b>	<b>Results of modelling: thermo-hydro-mechanical aspects</b> .....	<b>58</b>
5.2.1	Elastic perfectly plastic model (case A) .....	59
5.2.2	Friction angle hardening elastoplastic model (case B).....	66
5.2.3	Combined angle friction hardening and cohesion softening model (case C) .....	69
5.2.4	Combined angle friction hardening and cohesion softening model with permeability as a function of porosity (case D).....	72
5.2.5	Comparison between the four cases .....	76
<b>6</b>	<b><i>Comparison of all results</i></b> .....	<b>77</b>
<b>6.1</b>	<b>Comparisons for the hydro-mechanical part</b> .....	<b>78</b>
<b>6.2</b>	<b>Comparisons for the thermo-hydro-mechanical part</b> .....	<b>79</b>
<b>7</b>	<b><i>Additional computations (EPFL)</i></b> .....	<b>82</b>
<b>7.1</b>	<b>Constitutive models and parameters</b> .....	<b>82</b>
<b>7.2</b>	<b>Simulation results</b> .....	<b>83</b>



7.2.1	Calibration tests.....	83
7.2.2	Benchmark exercise .....	85
<b>7.3</b>	<b>Conclusions.....</b>	<b>92</b>
<b>8</b>	<b><i>Additional computations (CIMNE) .....</i></b>	<b>92</b>
<b>8.1</b>	<b>Modelling domain, boundary conditions and parameters .....</b>	<b>92</b>
<b>8.2</b>	<b>Simulation results (base case) .....</b>	<b>94</b>
<b>8.3</b>	<b>Simulation results (variants).....</b>	<b>96</b>
<b>8.4</b>	<b>Discussion of the mechanisms .....</b>	<b>99</b>
<b>9</b>	<b><i>Additional computations (EURIDICE) .....</i></b>	<b>100</b>
<b>9.1</b>	<b>2D plane strain model.....</b>	<b>100</b>
9.1.1	Modelling results.....	101
<b>9.2</b>	<b>2D axisymmetric model .....</b>	<b>103</b>
9.2.1	Modelling results.....	104
<b>10</b>	<b><i>Additional computations (UJF) .....</i></b>	<b>106</b>
<b>11</b>	<b><i>Additional computations (ULg) .....</i></b>	<b>112</b>
<b>11.1</b>	<b>Mohr Coulomb criterion .....</b>	<b>113</b>
11.1.1	Mohr-Coulomb criterion- mechanical model .....	113
11.1.2	Results of the modelling: hydro-mechanical aspect .....	114
11.1.3	Results of the modelling: thermo-hydro-mechanical aspect.....	117
11.1.4	Comparison Mohr-Coulomb Drucker-Prager.....	120
<b>11.2</b>	<b>2D plane strain case .....</b>	<b>123</b>
11.2.1	Introduction .....	123
11.2.2	Geometry and boundary conditions.....	123
<b>11.3</b>	<b>2D axisymmetric case .....</b>	<b>139</b>



# 1 Introduction

The aim of the Workpackage 3.3 is to study, through laboratory tests, the fracturing and sealing processes that develop in the Excavation Damaged Zone (EDZ) around galleries in clayey formations and the impact of a thermal phase on their evolution. Related to this Workpackage 3.3, the WP 5 tries to develop constitutive models which are able to reproduce thermo-hydro-mechanical (THM) effects in the EDZ. The results of the experimental work done in the WP 3.3 will be used for benchmark exercises in task 1 of the WP 5.2.

In the framework of this benchmark exercise, different phases of simulations will be proposed. The first goal of this benchmark was to propose a relatively simple modelling case in order to validate the numerical tools used by the different teams. To that end, a one-dimensional axisymmetric case was considered. Then, in a second step, to catch the main experimental observations, the 1D problem has been extended toward various 2D cases. The first part of this report presents the modelling results for the 1D axisymmetric problem as defined in the benchmark statement. After the description of the geometry and the boundary conditions, the results are presented in two steps: (i) a coupled thermo-hydro-mechanical calculation with constant temperature; (ii) extended to non-isothermal conditions. In the second part of the report, the results of the additional computations considering 2D conditions are presented, discussed and compared with experimental results, for some of them.

## 2 Executive summary

### 2.1 Introduction

In the context of the TIMODAZ project, hollow cylinder tests have been designed and performed on Boom Clay in the framework of the workpackage WP3.3. The experiment has been developed to study the fracturing and others irreversible processes that develop in the Excavation Damaged Zone (EDZ) around galleries in clayey formations and the impact of a thermal phase on their evolution. It consists in hollow cylinder samples of Boom Clay which are submitted to mechanical and thermal loadings fairly similar to the evolution that will be encountered around disposal galleries for heat emitting radioactive waste. In parallel to the experimental aspects, numerical simulations were performed in order, first, to predict the expected thermo-hydro-mechanical behaviour of Boom Clay in the experiment and, then, to interpret the obtained results in terms of constitutive behavioural features.

In the definition of the time schedule of WP 5.2, it has been decided to perform the numerical simulations in parallel with the design and the carrying out of the experiment. So doing, a benchmark exercise has been proposed to the team involved in the numerical modelling of the hollow cylinder on Boom Clay. This exercise has been defined in agreement with the planned experimental procedure, in terms of thermo-hydro-mechanical conditions. However, in the course of the design of the experiment, the conditions have been slightly modified, which explain the small difference between the conditions applied during the tests and for the numerical simulations.



In a second step, in addition to the benchmark exercise, a series of additional computations have been carried out in order to study some more specific features of behaviour that have been underlined during the experiment. Those simulations consist, for most of them, in an analysis and a constitutive interpretation of experimental results in order to validate and calibrate the used numerical models and materials parameters. For this step of the work, the liberty was given to use the constitutive models, the geometry of the mesh and the boundary conditions that each team considers as the most appropriate regarding to the features of behaviour that they expected to observe. Also, for this part, the boundary conditions have been taken in agreement with the experimental conditions.

This executive summary presents the main concepts and results that have been obtained in the framework of the numerical modelling of the hollow cylinder experiment on Boom Clay. It is divided in two parts: the benchmark exercise and the additional computations.

## **2.2 The benchmark exercise**

### ***Problem definition***

The problem is treated as a one dimensional process (radial-axisymmetric) that is an idealization of the hollow cylinder sample of a porous isotropic medium. At the inner end of the mesh, the boundary conditions is governed by the evolution of radial stress, pore water pressure and temperature imposed while the THM conditions at the outer end is kept constant, corresponding to the in-situ conditions of Boom Clay at the depth of the repository.

The geometry, the initial and the boundary conditions of the sample are illustrated in Figure 1(a). The internal radius  $R_i$  is equal to 7 mm and the external radius  $R_e$  to 43 mm. The clay is supposed to be homogeneous and isotropic. It is considered to be fully saturated. The considered initial conditions (isotropic total stress field of 4.5 MPa and pore water pressure of 2.2 MPa) are close to the one encountered in Boom Clay at the depth of the repository. This modelling includes two steps: the first one represents the process of excavation under isothermal condition and during the second step a thermal loading is applied at the inner cavity of the cylinder (Figure 1(b)).



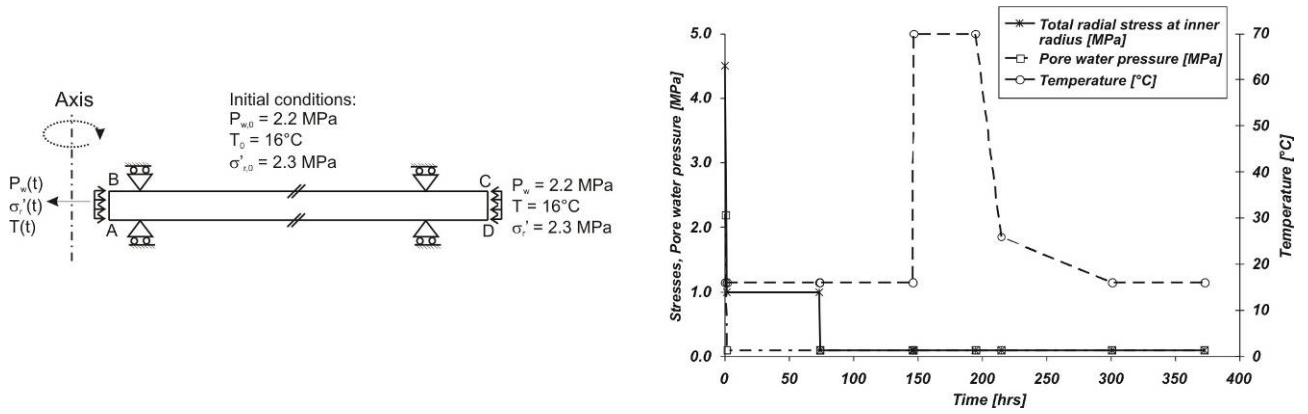


Figure 1: Geometry, initial and boundary conditions (a). THM loading paths (b)

### Governing equations and parameters

The mechanical model used for the plastic clay is a non-associated elastoplastic constitutive law. The yield surface is defined by a Drucker-Prager criterion characterized by a circle in the deviatoric plane. The Drucker-Prager yield limit is given by the following equation:

$$f \equiv II_{\hat{\sigma}} + m \left( I_{\sigma} - \frac{3c}{\tan \phi_c} \right) = 0 \quad (2.1)$$

with  $\phi_c$  the friction angle in compression and  $c$  the cohesion,  $I_{\sigma} = \sigma_{ii}$  the first stress invariant,

$$II_{\hat{\sigma}} = \sqrt{\frac{1}{2} \hat{\sigma}_{ij} \hat{\sigma}_{ij}}$$

the second deviatoric stress invariant with  $\hat{\sigma}_{ij} = \sigma_{ij} - \frac{I_{\sigma}}{3} \delta_{ij}$  and

$$m = \frac{2 \sin \phi_c}{\sqrt{3}(3 - \sin \phi_c)}.$$

In this modelling, two processes of isotropic hardening (friction angle) and softening (cohesion) are possible. Thus, different cases will be considered as a function of the hardening/softening. The thermo-mechanical model is based on thermo-elasticity. So, the thermal strain is defined as  $\dot{\epsilon}_{ij}^{e,th} = \beta_s \dot{T} \delta_{ij}$  where  $\beta_s$  is the solid thermal expansion coefficient and  $\delta_{ij}$  is the Kronecker symbol.

The field equations consider the medium as a deformable two-phase material (i.e., a water saturated medium) in which mass transfers occur. The general Darcy flow law is used and defines the Darcy fluid velocity  $\underline{q}_w$  as a linear function of permeability and the gradient of fluid pressure  $p_w$  :

$$\underline{q}_w = -\frac{k_{int}}{\mu_w} (\nabla p_w) \quad (2.2)$$

TIMODAZ

where  $k_{int}$  is the intrinsic permeability and is considered as a scalar in isotropic situation.  $\mu_w$  is the fluid dynamic viscosity which is supposed to be linearly dependent of temperature following:

$$\mu_w(T) = \mu_{w0} - \alpha_w \mu_{w0} (T - T_0) \quad (2.3)$$

where  $\alpha_w$  is the liquid dynamic viscosity thermal coefficient.

In order to investigate the modification of the permeability in the damage zone, a modification of the permeability with the porosity is taken into account. In this model, two cases can be studied:

- The permeability  $k_{int}$  is constant:  $k_{int} = k_{int}^{sat}$
- The permeability  $k_{int}$  is a function of porosity:  $k_{int} = k_{int}^{sat} \cdot k_{r,n}$ ,

with:

$$\begin{aligned} k_{r,n} &= 1 && \text{if } n - n_0 < 0 \\ k_{r,n} &= 1 + 2.10^9 (n - n_0)^3 && \text{if } 0 < n - n_0 < 10^{-2} \\ k_{r,n} &= 1 + 2.10^3 && \text{if } n - n_0 > 10^{-2} \end{aligned}$$

The heat flow is governed by the following equation:

$$q_T = -\Gamma \cdot \nabla T + c_{p,w} \cdot \rho_w \cdot \underline{q}_w \cdot (T - T_0) \quad (2.4)$$

where  $\Gamma$  is the thermal conductivity of the saturated material,  $c_{p,w}$  the heat capacity of water and  $\rho_w$  the density of water.

The material parameters are summarized in Table 1 and Table 2. Let's note that four different versions of the Drucker-Prager model have been considered. Case A is the elastic perfectly plastic model. Case B considers a friction angle hardening elastoplastic model. Case C corresponds to a combination of a friction angle hardening elastoplastic model with cohesion softening. Finally case D is the same elastoplastic model as case C but the permeability is considered as a function of the porosity.

Geomechanical characteristics		Case A	Case B	Cases C and D
Young elastic modulus [MPa]	$E_0$	300	300	300
Poisson ratio [-]	$\nu$	0.125	0.125	0.125
Specific mass [kg/m <sup>3</sup> ]	$\rho$	2682	2682	2682
Initial cohesion [kPa]	$c_0$	300	300	300
Final cohesion [kPa]	$c_f$	300	300	100
Softening parameter [-]	$\beta_c$	-	-	0.01
Initial friction angle [°]	$\phi_{c0}$	18	5	5
Final friction angle [°]	$\phi_{cf}$	18	18	18
Hardening parameter [-]	$\beta_\phi$	-	0.01	0.01
Dilatation angle [°]	$\psi$	0	0	0

Table 1: Geomechanical characteristics

TIMODAZ



<b>Hydraulic characteristics</b>		
Initial porosity	$n_0$	0.39
Initial intrinsic permeability [m <sup>2</sup> ]	$k_{int}^{sat}$	$4 \cdot 10^{-19}$
Water specific mass [kg/m <sup>3</sup> ]	$\rho_w$	1000
Fluid dynamic viscosity [Pa.s]	$\mu_w$	$10^{-3}$
Liquid compressibility coefficient [MPa <sup>-1</sup> ]	$1/\chi_w$	$5 \cdot 10^{-4}$
<b>Thermal characteristics</b>		
Thermal conductivity [W/(mK)]	$\lambda$	1.35
Volumetric heat capacity [J m <sup>-3</sup> .K <sup>-1</sup> ]	$\rho C_p$	2.84E6
Linear solid thermal expansion coefficient [K <sup>-1</sup> ]	$\beta_s$	$10^{-5}$
Volumetric liquid thermal expansion coefficient [K <sup>-1</sup> ]	$\beta_w$	$3 \cdot 10^{-4}$
Liquid dynamic viscosity thermal coefficient [K <sup>-1</sup> ]	$\alpha_w$	0.01

**Table 2: Hydraulic and thermal characteristics**

## Results

The first objective of this benchmark exercise was to validate the numerical tools used by the different modelling teams by comparing simulation results of each team (i.e., EPFL, EURIDICE, ULg, UJF and UPC). EPFL, UJF and ULg have used the finite element code LAGAMINE while UPC and EURIDICE used code BRIGHT.

For the hydro-mechanical parts, the four different versions of the Drucker-Prager model, as defined in Table 1, have been considered by each teams. On the contrary, for the non-isothermal part, Case A was imposed for each team and the liberty was given to consider an additional case per team. So, the comparison between the results of each team was only possible for the perfectly plastic model (case A of Table 1).

In this benchmark, results of each team have been compared in term of the radial profiles of the three principal stresses, the pore water pressure, the radial displacements, the water flux and the temperature. It has been concluded that the results obtained by the different teams are very similar. The only very slight difference comes from the pore water pressure and temperature profiles obtained by UPC at the end of the heating phase. However, this discrepancy is really negligible.

The second objective of this benchmark exercise was to evaluate the response of each version of the constitutive model. First, it has been observed that the radial displacement grows with the successive introductions of hardening and softening processes. Also, the increase of water permeability with the porosity (Case D) decreases the final convergence of the hole because of the strengthening effect of the water drainage (Figure 2).

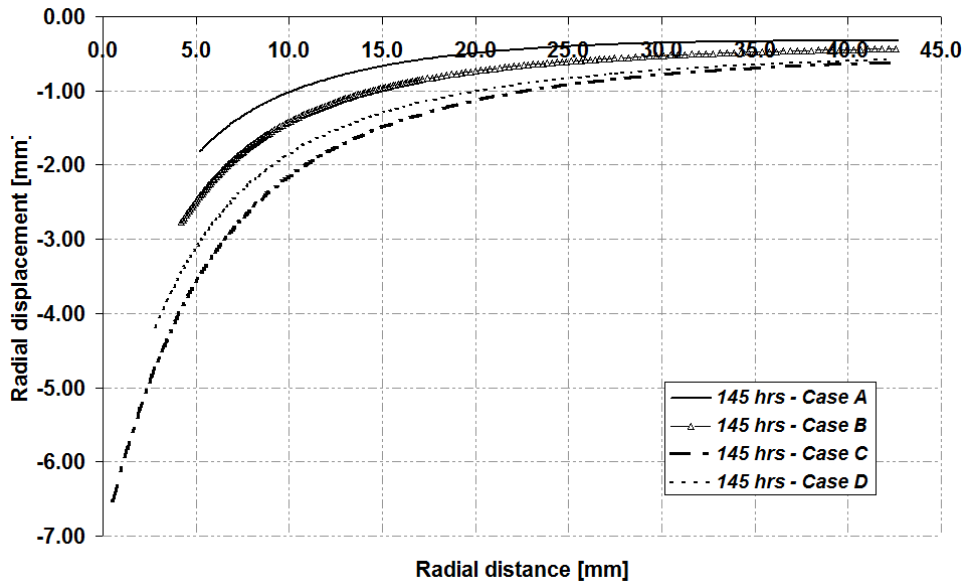


**Figure 2: Comparison of the radial displacement profile at the end of the second stabilization period (t = 145 hours) obtained with the four versions of the Drucker-Prager model**

In term of pore water pressure evolution, during the stabilization periods, the pore water pressure reaches equilibrium between the two imposed values at the inner and outer faces. So, at the end of the each stabilization phase, the pore water pressure profile obtained in cases A, B and C are very similar. The only difference is due to the change of the geometry of the cylinder, different with each model. Excepted that, the profile of the pore water pressure at equilibrium is independent of the mechanical and hydraulic parameters, assuming that the Boom Clay characteristics remain homogeneous (Figure 3). Nevertheless, if the damage process induces a modification of the water permeability (i.e., a lost of the sample homogeneity), the pore water pressure at equilibrium is modified, as it is observed in Case D. Also, let's note that the permeability enhancement due to the porosity increase induces a higher level of water flux passing across the hollow cylinder.

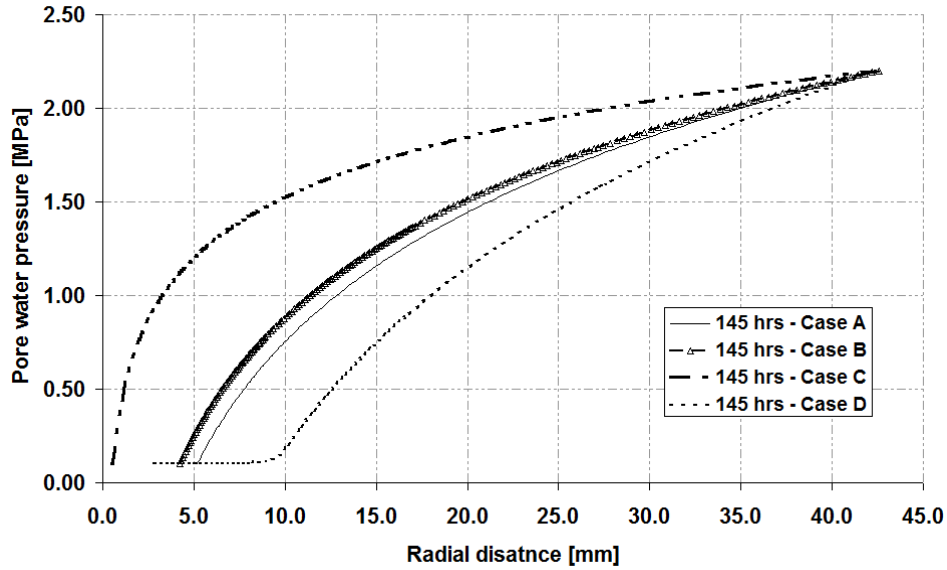


**Figure 3: Comparison of the pore water pressure profile at the end of the second stabilization period ( $t = 145$  hours) obtained with the four versions of the Drucker-Prager model**

In term of the principal stresses (radial, orthoradial and axial stresses), the predicted profile are affected by the plastic processes. Starting from an isotropic stress state, the decrease of the radial effective stress at the inner face produce a stress redistribution and an increase of the orthoradial stress with respect to the axial and radial stresses. As a consequence, the orthoradial stress is the major principal stress. Using the perfectly plastic model (Case A), the plastic zone is clearly identified because of the peak of the orthoradial stress that characterized the limit between the elastic zone (in the external region of the cylinder) and the plastic zone (in the vicinity of the hole). At the end of the second mechanical unloading, the plastic radius is about 35 mm (with respect to the 43 mm of the external radius). On the contrary, the use of hardening/softening model (Case B, C and D) does not allow us to evidence the sharp transition between the elastic and plastic regions. Indeed, due to the progressive mobilization of the plastic mechanisms, it is no longer possible to distinguish a clear elastic zone because the entire domain is plastic. Figure 4 displays the profile of the orthoradial effective stress at the end of the second stabilization period for each case.

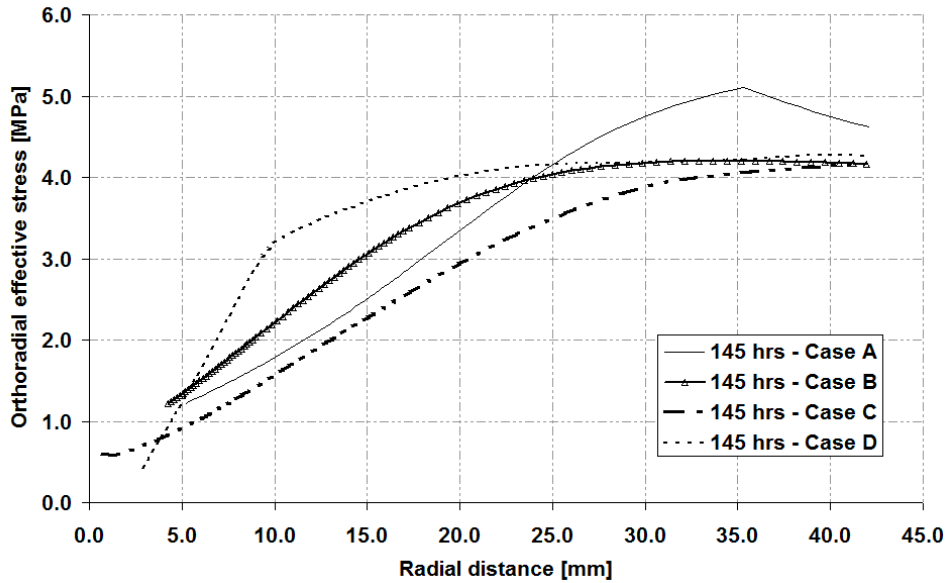
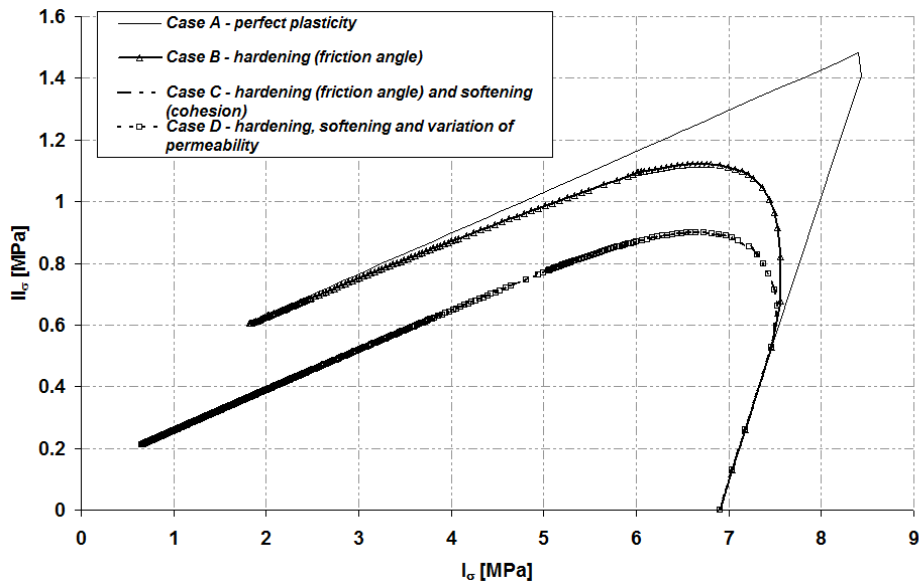


Figure 4: Comparison of the orthoradial effective stress profile at the end of the second stabilization period ( $t = 145$  hours) obtained with the four versions of the Drucker-Prager model

At the inner phase, the process occurs under drained condition and the stress path in the  $(I_{\sigma} - II_{\phi})$  plane is at  $45^{\circ}$  ( $dI_{\sigma} = dII_{\phi}$ ) as long as the stress point remains in the elastic domain, as shown in Figure 5. Then, at the inner face, when plasticity occurs, the increment of deviatoric stress is reduced. Then, the deviatoric stress passes through a peak value and finally decreases. This process occurs along with a strong reduction of the mean effective stress during the mechanical unloading. This reduction of the mean stress induces a porosity increase in the vicinity of the hole. Each version of the model predicts similar trends. The perfectly plastic model predicts the maximum value of deviatoric stress that the material can sustain and the minimum reduction of the mean effective stress. The successive introductions of the friction hardening and then the cohesion softening induce a reduction of the maximum deviatoric stress and an increase of the mean effective stress drop. So, the magnitude of plasticity increases successively between case A, B and C.



**Figure 5: Comparison of the followed stress path stress obtained with the four versions of the Drucker-Prager model**

During the thermal phase, the higher thermal expansion of water than that of the solid skeleton induces pore water pressure increase in the hollow cylinder (Figure 6,  $t = 146,47$  hrs). Then, during the thermal stabilization, the thermal increment of the pore water pressure dissipates and a new pore water pressure profile is reached. The pore water pressure at high temperature is slightly lower than the one at ambient temperature (Figure 6,  $t = 194$  hrs) because of the enhancement of water permeability with temperature that is more important in the vicinity of the hole (because temperature is higher). Finally, after cooling, the pore water pressure profile before heating is recovered (Figure 6,  $t = 372$  hrs). The prediction of the temperature profile and pore water pressure in the four cases are very similar. With the used constitutive models and the imposed boundary conditions, the hydro-mechanical processes that occur in the hollow cylinder during the thermal cycle appear to be reversible because the followed stress path takes place in the elastic domain.

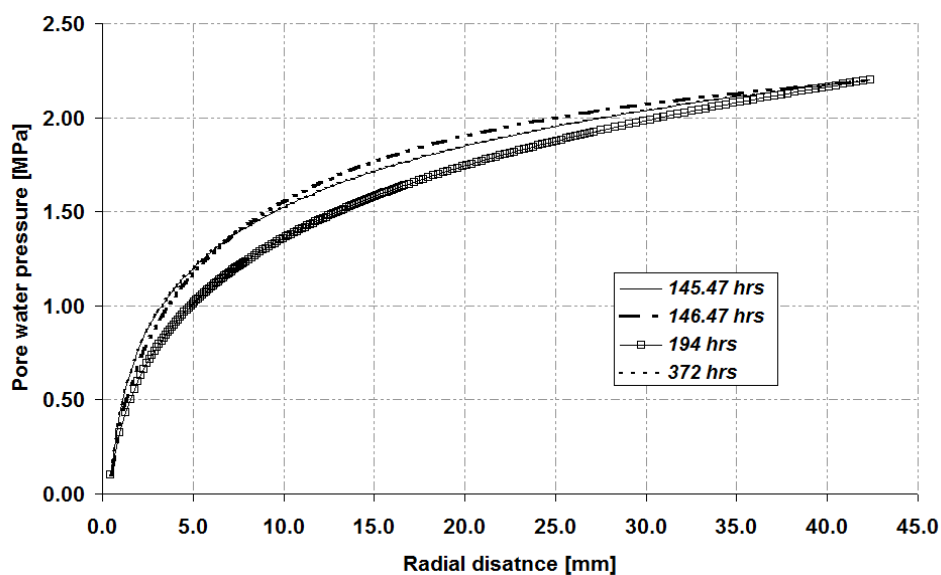


Figure 6: Evolution of pore water pressure with radial distance during the thermal phase in case C. Results obtained in cases A and B are very similar

## 2.3 Additional computations

In addition to the benchmark exercise, when the first experimental results have been obtained, it has been decided to perform additional computations in order to reproduce some of the experimental observations that were not considered in the benchmark statement. Each modelling team has considered their own model, set of parameters and geometry that they considered has the most appropriate or relevant to reproduce the experimental observations.

ULg addressed three distinct aspects. (i) Applying the same geometry and boundary conditions that the ones defined in the benchmark exercise, a Mohr-Coulomb criterion, in stead of the Drucker-Prager yield limit, has been considered. (ii) Then, in order to study a possible anisotropic response of the Boom-Clay, numerical simulations considering 2D plane strain problem have been performed. (iii) Finally, 2D axisymmetric conditions have been assumed in order to study the effects of axial boundary conditions on the behaviour of the mid-plane section.

The Soil Mechanics Laboratory of EPFL has performed the simulations of the hollow cylinder tests considering the parameters of Boom Clay with the ACMEG-T model, in addition to the Drucker-Prager model. This model considers non-linear elasticity, hardening and/or softening irreversible processes, multi-mechanism plasticity, a progressive mobilization of plasticity inside the external yield limit and the possible irreversible strain induced by thermal loading (thermo-plasticity).

EURIDICE performed two kinds of simulation using successively a 2D plane strain model and a 2D axisymmetric model. The first one aims at studying the role of elastic cross-anisotropy on the global elasto-plastic response of Boom Clay while the latter one has been done in order to

TIMODAZ

evaluate the relevance of the plane strain assumptions with respect to the real axial strain conditions.

UJF has simulated the effect of strain softening and strain localization on the global response of the hollow cylinder, assuming 2D plane strain conditions and cross-anisotropic elasticity coupled with a Drucker-Prager plastic model. To describe the post-peak behaviour, where the localized zones appear, a second gradient model is added to the mechanical part.

CIMNE has implemented and used a anisotropic linear elastic law with a perfect plastic Mohr Coulomb type yield surface and non associated plasticity allowing null volumetric plastic strain. A number of simulation has shown the effect of each ingredient, with comparison with the experimental results.

In the following sub-sections, the main conclusions of each modelling teams are successively presented.

### ***EPFL contributions***

The Soil Mechanics Laboratory of EPFL has performed the simulations of the hollow cylinder tests as defined in the benchmark statement with the ACMEG-T model and compares the obtained results with the prediction of the perfectly plastic Drucker-Prager model. The behaviour is assumed isotropic. The parameters of the ACMEG-T model were determined from calibration on laboratory tests. The Drucker-Prager model predicts a sharp transition between the elastic and plastic states, as seen on the orthoradial effective stress profile (Figure 7(c)). On the contrary, the results obtained with the ACMEG-T model exhibit a progressive mobilization of the plastic mechanisms, and it is no longer possible to distinguish a clear elastic zone because the entire domain is plastic (Figure 7(d)).

The numerical modelling reveals the drastic increase of the deviatoric stress in the inner part of the cylinder induced by the inner radial stress decrease. Dilatancy plastic strain is produced at the inner hole face, while the external part of the cylinder is subjected to slight plastic hardening characterized. This distinction is clear visible in the (p'-q) plane (Figure 8) where the point at the vicinity of the hole is subject to a strong decrease of mean effective stress while this mean stress increases at the outer face. The predicted convergence of the inner hole clearly depends on the model used. The Drucker-Prager model forecasts 2 mm of radial displacement while the ACMEG-T model predicts a quasi-closure of the inner hole (6.8 mm of convergence on the 7 mm of initial radius) (Figure 7(a) and Figure 7(b)). The convergence of the hole is split up into 1.6 mm of convergence during the first unloading and the rest during the second unloading. During the thermal phase, a small thermo-plastic hardening produces 2% of the volumetric plastic contraction strain in the first millimetres around the hole. However, this thermo-plastic process does not affect significantly the convergence of the hole because this hole is already almost closed before the heating phase.

TIMODAZ

IMR -N°: **D13 – Annex 1**

15/142

Dissemination level: **PU**

Date of issue of this report: **30/08/10**



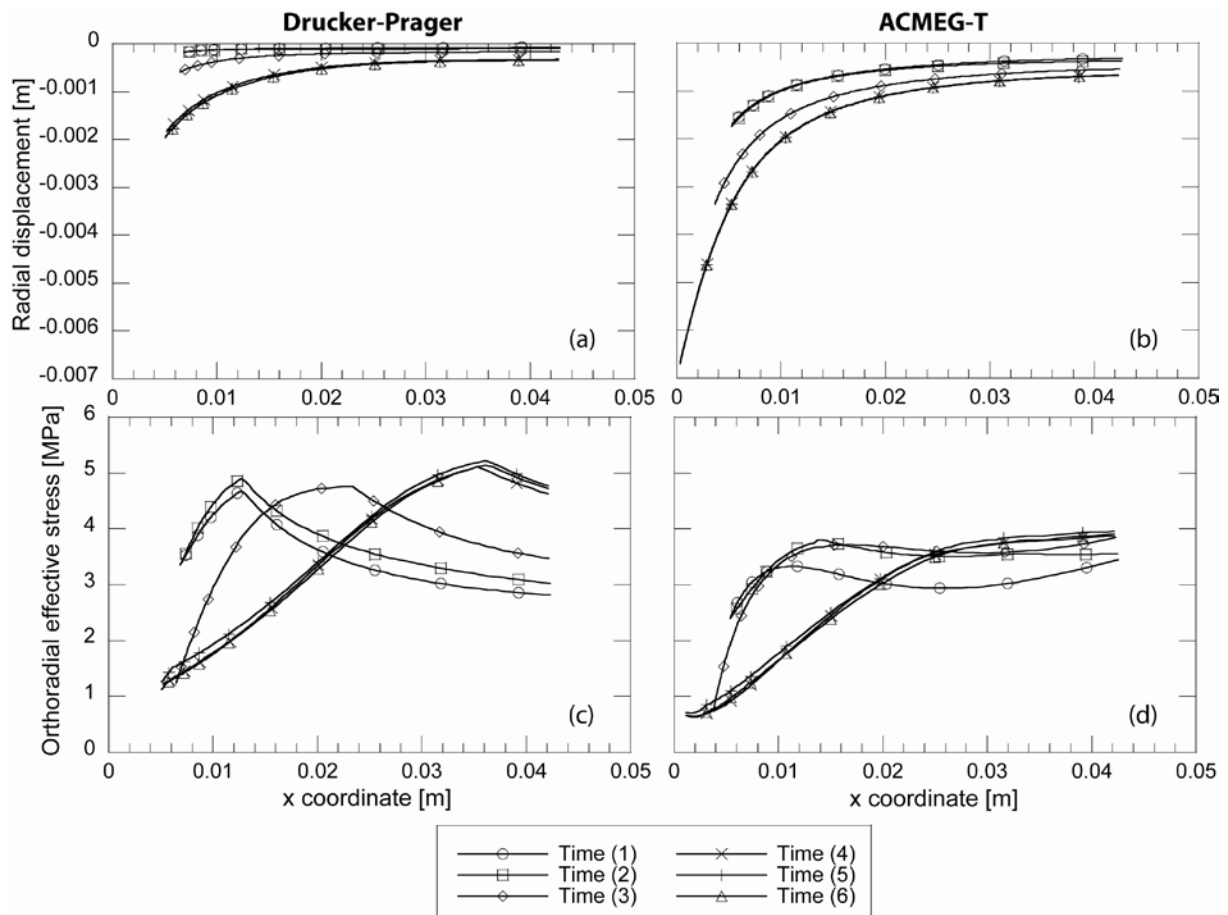


Figure 7: For different times, distribution in space of computed (a, b) radial displacement and orthoradial effective stress (c, d). Comparisons between predictions using the Drucker-Prager model (left) and ACMEG-T model (right). The selected times correspond to the end of the first mechanical unloading (1), the end of the first stabilization phase (2), the end of the second unloading phase (3), the end of the second stabilization phase (4), the middle of the thermal phase (5) and the final state (6)

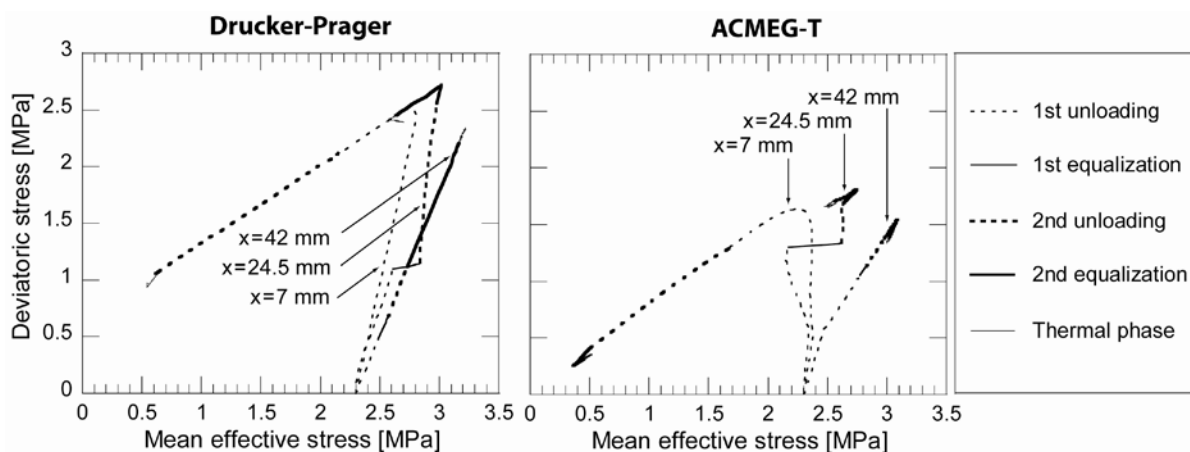


Figure 8: Stress paths in the (p'-q) plane at three different radial coordinates (7 mm, 24.5 mm and 42 mm). Comparisons between predictions using the Drucker-Prager model (left) and ACMEG-T model (right)

It is to note that the imposed mechanical unloading defined in the benchmark exercise was higher than the unloading that has been applied experimentally. It explains the higher convergence of the central hole obtained numerically.

### *CIMNE contributions*

As Boom clay presents a bedding plane structure due to its sedimentary origin, some anisotropic features may be considered. In the elastic domain, the stress-strain relationship is described by an anisotropic linear elastic constitutive law. The elastic domain is limited by a Mohr-Coulomb type yield surface. Plastic deformations are non-associated (null volumetric plastic strain) and perfect plasticity is considered.

With the basic case, a qualitative agreement between measurements and simulation is observed: both show a more important cavity wall displacement in the direction of the bedding plane, a displacement plateau (equivalent to 0 strain) in the farther field and a less displacement of the outer cylinder wall in the bedding plane direction.

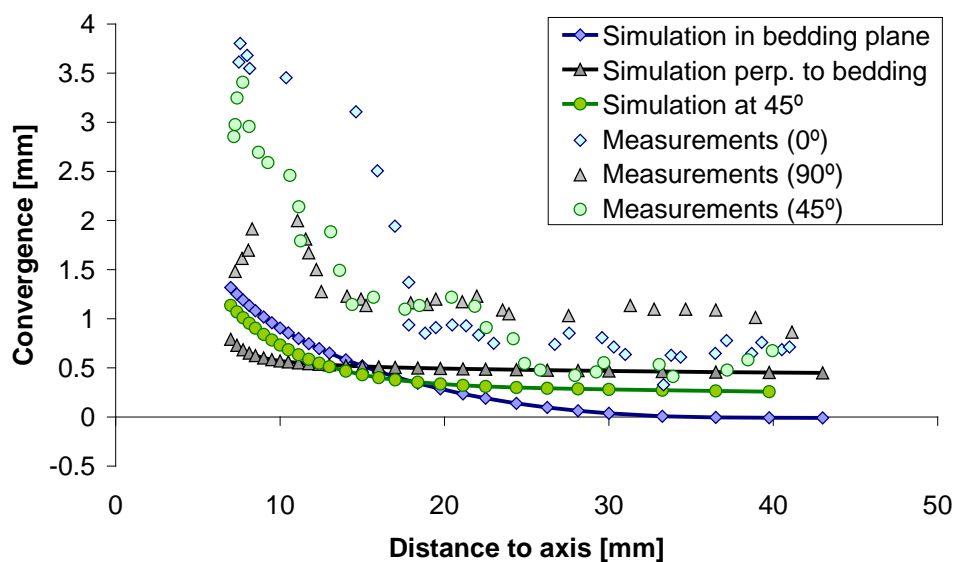


**Figure 9: Comparison of measured and simulated displacement profiles in the three directions**

Some changes were applied to the base case in order to increase the understanding of the system:

- Variant 1: only elastic case (no yield limit)
- Variant 2: associated flow rule (plastic volumetric strain is allowed)
- Variant 3: reduced friction angle, resulting in an increased intensity of the plastic mechanisms

The simulation results for variant 1 (elastic case) differs one order of magnitude from the measurements. This is an indication that most of the strain observed in the experiment is due to plastic mechanisms. Moreover, the simulated convergence (radial displacement of the inner wall) shows an inverse tendency as the displacements.

If volumetric plastic strains are allowed, the influence of the anisotropic part of the mechanical law (i.e. in the elastic region) is minimized and the sample behaviour seems to be most isotropic. Finally the friction angle was reduced to quite a low (and unrealistic) value of  $10^\circ$  in order to achieve a quantitative match of the measured displacement profiles ().

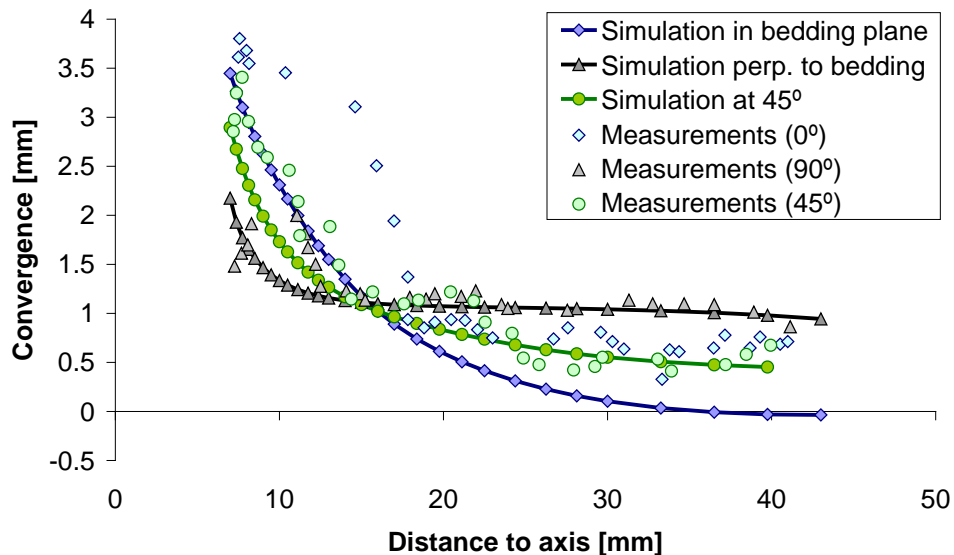


Figure 10: Comparison of measured and simulated displacement profiles in the three directions (reduced friction angle,  $10^\circ$ )

### *EURIDICE contributions*

EURIDICE simulated the hollow cylinder test, applying the experimental boundary conditions with two distinct models: 2D plane strain model and 2D axisymmetric model.

#### 2D plane strain model

Due to the symmetric nature and plane strain condition of the problem, a quarter of the cross section is selected for numerical modelling. The boundary conditions are in agreement with the experimental conditions. Three cases are simulated to investigate the effects of hydro-mechanical anisotropy on the radial displacement in the sample. In each case, the friction angle is limited to  $10^\circ$ .

Case 1 considers cross-anisotropic elasticity with the perfectly plastic Drucker-Prager. The modelling gives the consistent trend of the anisotropic radial displacements to that of measured displacements, and the magnitude of the displacements could be considered good.

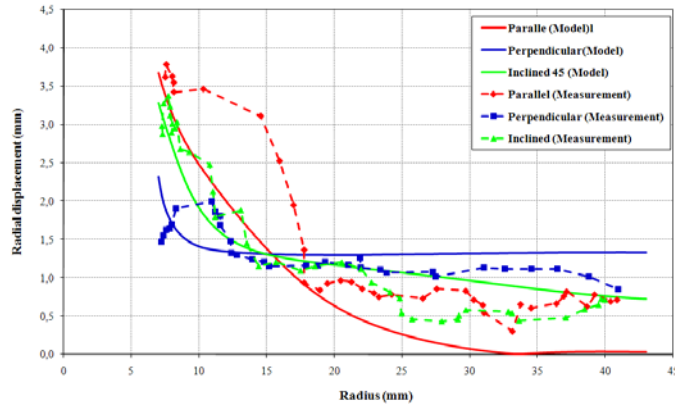


**Figure 11: Radial displacement profile after mechanical unloading and water pressure dissipation in the direction parallel, perpendicular and at 45° to the bedding plane**

Case 2 only investigates the hydraulic anisotropy with mechanical behaviour being isotropic. The modelled radial displacements give the reverse trend of the anisotropic radial displacements to that of Case 1, the displacement being larger in the direction perpendicular to bedding. It is not in agreement with experiment. Case 3 investigates both hydraulic anisotropy and mechanical anisotropy. The modelling also gives the reverse trend of the anisotropic radial displacements to that of Case 1.

As a conclusion, it seems that the mechanical anisotropy might contribute to the experimentally measured anisotropic convergence, while hydraulic anisotropy presents anisotropic convergence on the contrary.

### 2D axisymmetric model

2D axisymmetric model without considering the anisotropic hydro-mechanical behavior of the sample has been simulated. The bottom of the sample is assumed to be impermeable and vertically fixed. The top of the cap is subjected to the same history and magnitude of pressure as the radial pressure at the outer surface. To compare with the 2D axisymmetric model, 2D plane strain model has been simulated with isotropic hydro-mechanical conditions with a friction angle of 10° and a cohesion of 300 kPa. It reveals that the 2D axisymmetric model underestimates the measured axial displacement, but gives the similar trend of the displacement (Figure 12). So, based on the present modelling, it is indicated that hollow cylinder test is not exactly plane strain problem.

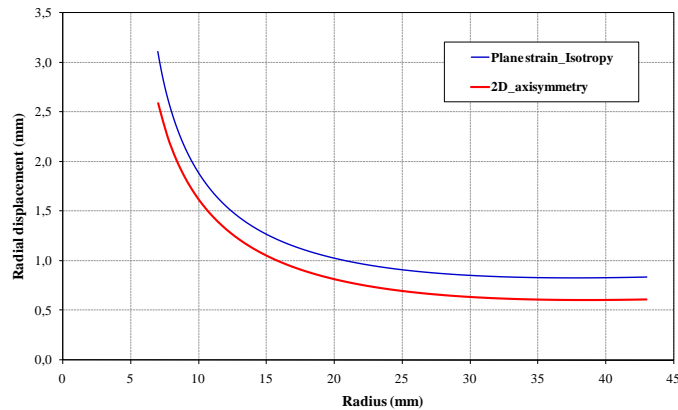


**Figure 12: Comparison between the radial displacement profiles obtained with the 2D axisymmetric and the 2D plane strain problems**

### *UJF contributions*

2D plane strain problem have been simulated considering a quarter of the entire section. A strain cohesion softening Drucker-Prager model coupled with cross-anisotropic elasticity has been used. To describe the post-peak behaviour, where the localized zones appear, a second gradient model is added to the mechanical part. Doing so, the computation is not affected by mesh-dependency and the objectivity of the solution is reached. The cohesion varies between 300 kPa at the peak until 100 kPa at the residual state. Friction angle is maintained constant at a value of  $18^\circ$ . The hydro-mechanical loading path is in agreement with the experimental test. Only, the 70 minutes of the unloading phase has been modelled.

The focus has been made on how the localization phenomenon appears around the inner part of the sample. At the beginning of the unloading, the plastic deformation appears around the element at  $45^\circ$  with respect to the bedding plane (Figure 13). Then, the strain localization begins in the direction of bedding plane, accumulating plastic strains. As a consequence the displacements are bigger in the direction of bedding. Indeed, the plastic strain clearly tends to move in the direction of the most rigid plane (the bedding plane). At the beginning of the plasticity process, the maximum displacement is in the direction perpendicular to bedding that is characterized by the lower Young modulus. Due to the localization of plastic deformation, the horizontal becomes the direction where the displacements are more important.

The results gives a good qualitatively distribution of the displacement fields. However, the order of magnitude of the displacement between numerical and experimental results is not comparable (from 0.2 to 0.3 mm in stead of 2 to 4 mm).

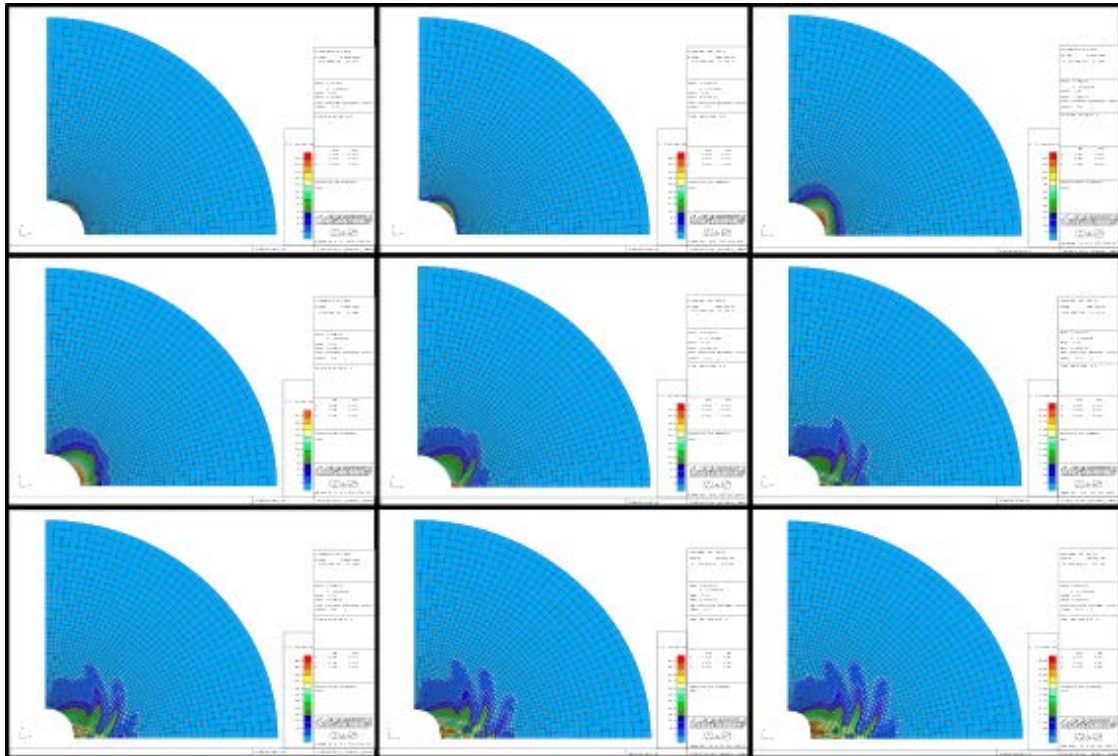


Figure 13: Equivalent plastic strains at different times: 2268 s - 2940 s - 3360 s - 3617 s - 3711 s - 3900 s - 4026 s - 4100 s - 4200 s

### *ULg contributions*

#### Mohr Coulomb criterion

Using the same problem definition as for the benchmark exercise (1D axisymmetric conditions), a Mohr-Coulomb plastic criterion has been used in stead of the Drucker-Prager yield limit. The results show an increase of radial displacement (from 2 mm with the Drucker-Prager model to 5.2 mm with the Mohr-Coulomb criterion) because the Mohr-Coulomb model allows a plastic behaviour at a lower stress than the Drucker-Prager criterion (for the same friction angle and cohesion) ((a)). As a consequence, the maximum deviatoric stress that the material may sustain is reduced which is clearly visible in the stress path in  $(I_{\sigma} - II_{\hat{\sigma}})$  plane ((b)).

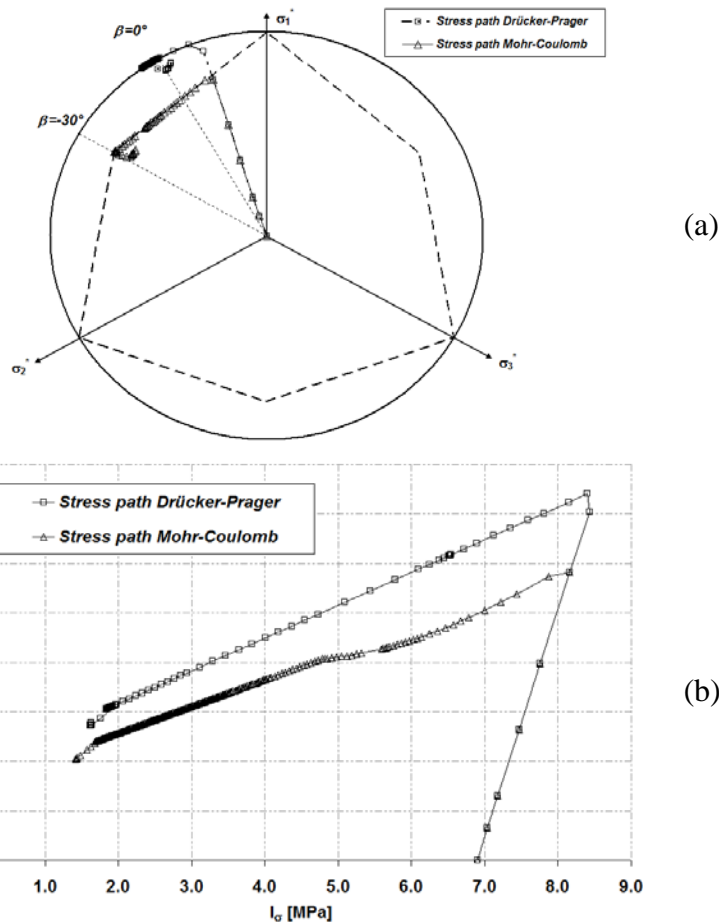


Figure 14: Representation of the stress path for the Drucker-Prager model and the Mohr-Coulomb model :  
 (a) in the principal stress plane and (b) in the  $(I_\sigma - II_\epsilon)$  plane

During the thermal heating-cooling cycle, no clear difference can be observed between both models predictions because in both case, the thermo-mechanical response is governed by the same thermo-elastic processes.

### 2D plane strain case

In order to catch the anisotropic response of the material and the possible strain localisation, 2D plane strain modelling has been performed. The objective of this simulation is to reproduce the behaviour of the material in the mid-plane section of the hollow cylinder, assuming plane strain conditions. Because of the symmetry of the problem, a quarter of the entire section is considered. To reproduce as well as possible the experimental results, the boundary conditions that have been applied experimentally have been considered. The total stress and the pore water pressure at the external boundary are kept constant at 4.5 MPa and 2.2 MPa, respectively. At the inner face, a decrease of total stress from 4.5 MPa to 1.0 MPa is considered, while the pore water pressure is reduced from 2.2 to 0.6 MPa. This mechanical unloading is applied in 70 minutes and then an 11h20min period is imposed to reach a hydro-mechanical steady-state. No thermal phase is considered.

In order to reproduce the anisotropic response of the materials, a Drucker-Prager hardening model (similarly to the benchmark exercise) has been coupled with cross-anisotropic elasticity as well as a dependency of the cohesion with respect to the angle between the major principal stress direction and the normal to bedding plane.

A parametric study has been performed in order to determine the most suitable set of parameters able to reproduce the intensity of radial displacement as a function of the radial direction with respect to the bedding orientation. Five cases have been considered: cross-anisotropic elasticity (no plasticity, case 1), cross-anisotropic elasticity and perfectly plastic Drucker-Prager model (case 2), cross-anisotropic elasticity and hardening/softening Drucker-Prager model (case 3), cross-anisotropic elasticity and perfectly plastic Drucker-Prager model with reduced friction angle of  $10^\circ$  (case 4), cross-anisotropic elasticity and hardening/softening Drucker-Prager model with anisotropic cohesion (case 5). The material parameters are summarized in .

Geomechanical characteristics		Case 1	Case 2	Case 3	Case 4	Case 5
Young elastic modulus [MPa]	$E_{//}$	500	500	500	500	500
Young elastic modulus [MPa]	$E_{\perp}$	250	250	250	250	250
Poisson ratio [-]	$\nu_{///}$	0.125	0.125	0.125	0.125	0.125
Poisson ratio [-]	$\nu_{//\perp}$	0.125	0.125	0.125	0.125	0.125
Initial cohesion [kPa]	$c_0$	-	300	300	300	270 ( $0^\circ$ )
						255 ( $45^\circ$ )
						525 ( $90^\circ$ )
Final cohesion [kPa]	$c_f$	-	300	100	300	90 ( $0^\circ$ )
						85 ( $45^\circ$ )
						175 ( $90^\circ$ )
Softening parameter [-]	$\beta_c$	-	-	0.01	-	0.01
Initial friction angle [ $^\circ$ ]	$\phi_{c0}$	-	18	5	10	5
Final friction angle [ $^\circ$ ]	$\phi_{cf}$	-	18	18	10	18
Hardening parameter [-]	$\beta_\phi$	-	-	0.01	-	0.01
Dilatation angle [ $^\circ$ ]	$\psi$	-	0	0	0	0

**Table 3: Geomechanical characteristics used in the 2D plane strain problem**

The purely elastic case (Case 1) emphasises the anisotropic behaviour of the material with the larger displacements being obtained in the more compressible direction (perpendicular to bedding). However, this case largely underestimates the obtained displacement (around 0.1 mm) with respect to experimental results (2 to 4 mm). In case B, the directional dependency of the radial displacement is obtained but the displacements remains much lower than the experimental results (0.3 mm in stead of 2 to 4 mm).

In case C, the cohesion softening allows us to model the post peak response of the Boom Clay. The magnitude of displacements obtained in the simulations is now more in agreement with the experimental displacements. However, the effect of the direction on the central hole displacements is not large enough with respect to the experimental observations ((a)). In case D, a perfectly plastic Drucker-Prager model is kept and the friction angle is reduced from  $18^\circ$  to  $10^\circ$ . In that case, the anisotropic radial displacements of the central hole are much better reproduced but the displacements of the outer region perpendicularly to bedding are negative which correspond to extension of that external zone. This aspect is not in agreement with

**TIMODAZ**



experiment ((b)). Finally, an anisotropic plastic criterion coupled with a hardening/softening Drucker-Prager model, assuming that the material cohesion depends on the angle between major principal stress and the normal to the bedding plane, allows us to get the best agreement with respect to the experimental measurements ((c)).

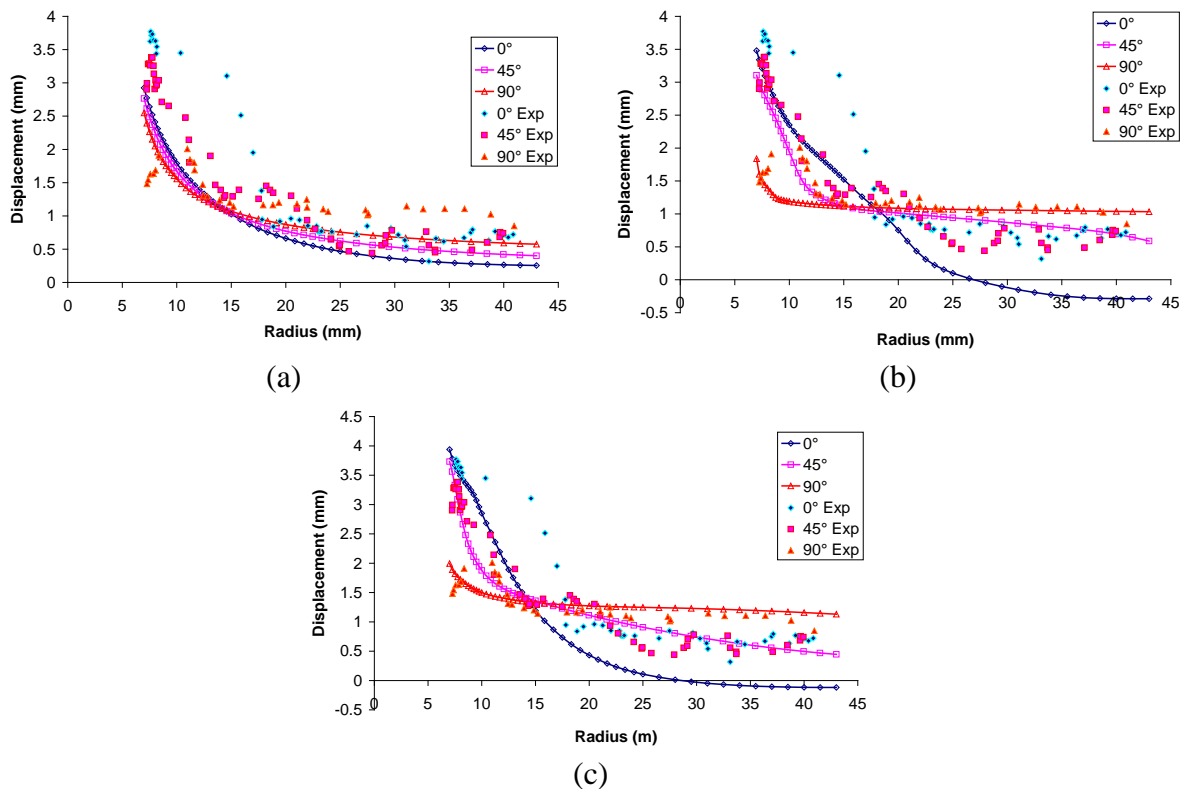


**Figure 15: Radial displacement profile after mechanical unloading and water pressure dissipation in the direction parallel, perpendicular and at 45° to the bedding plane. Comparison with experimental measurements for case 3 (a), case 4 (b) and case 5 (c)**

Also, the aspects of strain localization have been considered, using the local second gradient model in order to properly model the post-peak behaviour by introducing an internal length scale. The strain localization has been studied for the case 3. After the excavation, almost all the section is plastic but it is clear that some shear bands pattern appears. Between these bands, the behaviour is elastic and the contour of the increment deviatoric strain highlights the activity of the bands in terms of shear strains. At  $t = 5000$  s and  $t = 6000$  s, the process of shear banding shows that some bands occur and then become less active. The competition between these different bands is clearly observed. At  $t = 10000$  s, the localization pattern becomes more stable and the final structure of the most active shear bands is only composed of three bands.

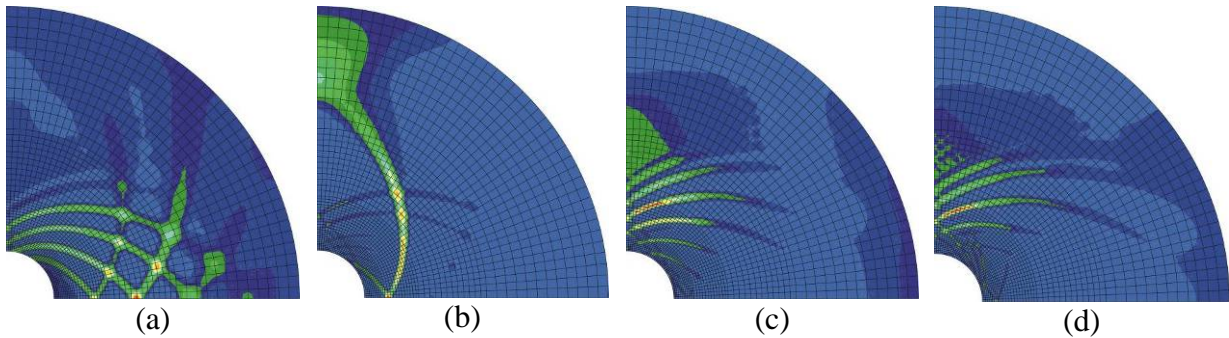


**Figure 16: Contour of normalized increment of deviatoric strain at  $t = 4200$  s (a),  $t = 5000$  s (b),  $t = 6000$  s (c),  $t = 10000$  s (d)**

### 2D axisymmetric case

The previous simulations assume plane strain state while the experimental conditions are stress-controlled in the axial direction and the radial displacements are constrained at the top and at the bottom of the hollow cylinder. In order to study the effects of axial boundary conditions on the behaviour of the mid-plane section, 2D axisymmetric modelling have been performed with two models: the perfectly plastic Drucker-Prager model and the hardening/softening Drucker-Prager model. The comparisons between the radial displacements obtained in the mid-plane section with the 2D plane strain and 2D axisymmetric conditions shows almost identical results (). It proves that the effect of axial boundary conditions on the behaviour of the mid-section may be considered as negligible.

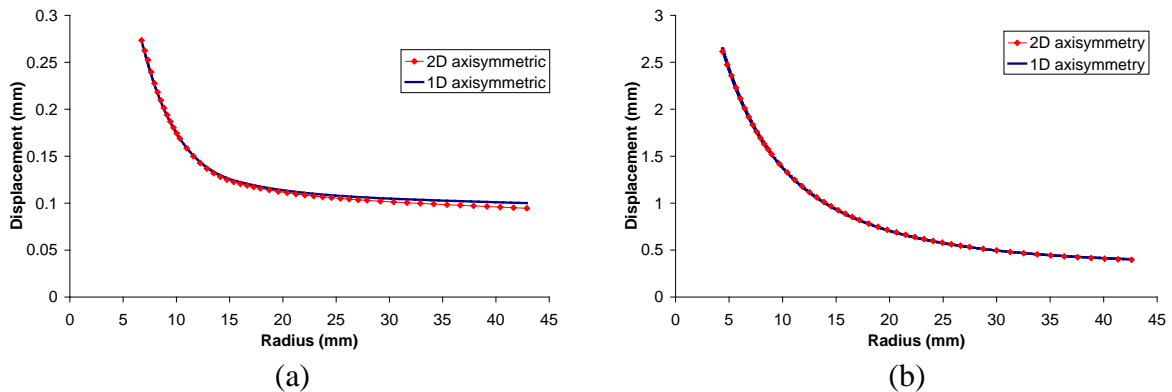


**Figure 17: Comparison of the radial displacement profile after mechanical unloading and water pressure dissipation with the 2D plane strain and the 2D axisymmetric conditions: (a) the perfectly plastic Drucker-Prager model, (b) the hardening/softening Drucker-Prager model**

## 2.4 Conclusions

The numerical modelling of the hollow cylinder experiment on Boom Clay has been carried out in two successive steps. First, a benchmark exercise has been defined before obtaining the experimental results. The results of this exercise were used to validate the numerical tools used by the different teams (ULg, EPFL, EURIDICE, CIMNE, UJF). Then, after obtaining the first

experimental results, a second series of numerical simulations have been performed to reproduce the experimental evidences.

During the benchmark exercise, agreement between the predicted results of the different teams has been obtained. Also, first interpretations of predicted results have been made in term of principal stress evolution, followed stress path, pore water pressure and displacement profiles. Those simulations consisted in blind predictions.

Then, in the second phase of simulations, the liberty was given to each team to focus on any specific features of behaviour related to the experimental evidences. The following aspects have been mainly addressed: (i) the anisotropic response of Boom Clay, (ii) the strain localisation process, (iii) the strain softening behaviour and (iv) the effect of the axial boundary conditions on the global response of the hollow cylinder.

To reproduce the magnitude of displacements measured in the hollow cylinder experiment, it has been noticed that the plastic strength must be drastically reduced with respect to the usual values of  $18^\circ$  for the friction angle and 300 kPa for the cohesion of Boom Clay. Three alternatives have been used: (i) a reduced friction angle of  $10^\circ$ , (ii) a strain cohesion softening from 300 kPa (at peak) to 100 kPa (at the residual state) or (iii) a Cam-Clay type model that allow softening in the wet part of the yield limit. The strain cohesion softening model induces strain localization that has been model with a second gradient model including an internal length scale.

We have no clear experimental evidences on the possible development of shear bands in the hollow cylinder, probably because the X-Ray Tomography scan has been performed after reaching a steady state. At that time, the sum of each localized phenomenon produces quite a diffuse pattern of the shear strain distribution that could avoid any clear observation of localized phenomenon at that moment of observation. However, the irregularity in the measured displacement profile could be an indication of possible localized phenomena.

An other important aspect on the mechanical behaviour of Boom Clay that as been observed during the hollow cylinder experiment is the cross-anisotropic response. From a constitutive point of view, it has been addressed with cross-anisotropic elasticity and also a possible dependence of the cohesion with respect to the direction of bedding.

As a conclusion, through numerical modelling of the hollow cylinder experiment, we have shown that the developed numerical models are able to reproduce the main processes that occur in Boom Clay during the hydro-mechanical hollow cylinder tests.



### 3 Introduction, short description of associated experiments, by the lab realising the experiment

### 4 Exercise, idealization proposed

#### 4.1 Geometry

The problem treated is a one-dimensional problem (radial-axisymmetric). It corresponds to an idealization of the hollow cylinder sample in a porous isotropic medium.

The geometry of the sample is illustrated in Figure 18. The internal radius  $R_i$  is equal to 7 mm and the external radius  $R_e$  to 43 mm. The number of elements is indicative and may be adapted by each partner.

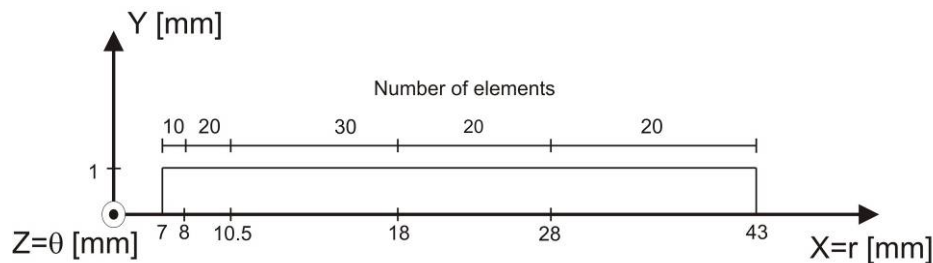


Figure 18 : Geometry

#### 4.2 Initial conditions

The clay sample is considered as homogeneous and isotropic. It is supposed to be fully saturated. Initial conditions to be considered are listed in Table 4. These initial conditions are close to the one encountered in Boom clay formation. Let's note that gravity is not considered in this modelling.

Initial state		Boom Clay
Total stresses [MPa]	$\sigma_{r0}$	4.5
	$\sigma_{z0}$	4.5
Pore pressure [MPa]	$p_{w0}$	2.2
Effective stresses [MPa]	$\sigma'_{r0}$	2.3
	$\sigma'_{z0}$	2.3
Temperature [°C]	$T_0$	16

Table 4 : Initial state stresses, pore water pressure and temperature

TIMODAZ

### 4.3 Boundary conditions

Mechanical boundary conditions are imposed such as:

- the axial displacements are fixed on the boundaries AD and BC
- the radial stress is fixed equal to  $\sigma_{r0}$  on the boundary CD

Hydraulic boundary conditions are imposed such as:

- the boundaries AD and BC are impervious
- $p_w$  is fixed to  $p_{w0}$  on the boundary CD

Thermal boundary conditions are imposed such as:

- the boundaries AD and BC are adiabatic
- T is fixed equal to  $T_0$  on the boundary CD

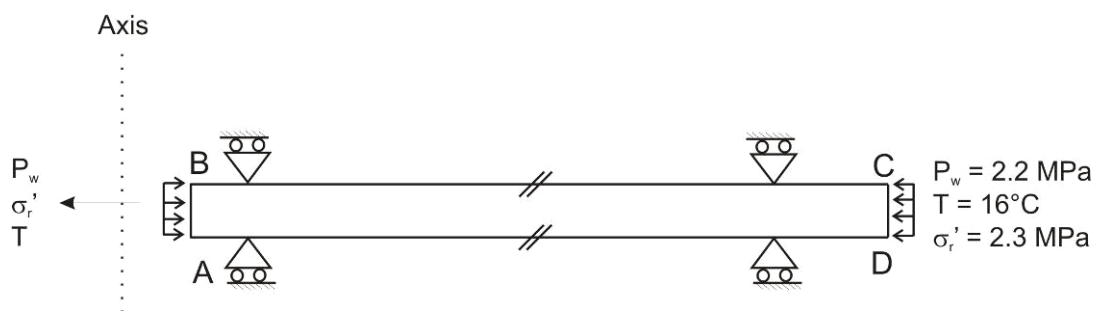


Figure 19 : Boundary conditions

To model the excavation, the total radial stress and the pore water pressure at the cylinder inner face (AB) decrease linearly respectively to 1 MPa and to 0.1 MPa. The reduction of stress and pore water pressure are realized in 70 minutes. After this, we allow a 72 hours period during which the pore pressure can stabilise in the rock material (see Figure 20).

In a second step, the total radial stress at the cylinder inner face (AB) decreases linearly to 0.1 MPa (the water pressure remains at 0.1 MPa at the inner face). The reduction of stress is realized in 18 minutes. As done previously, a period of 72 hrs is observed during which the pore water pressure can stabilise in the rock.

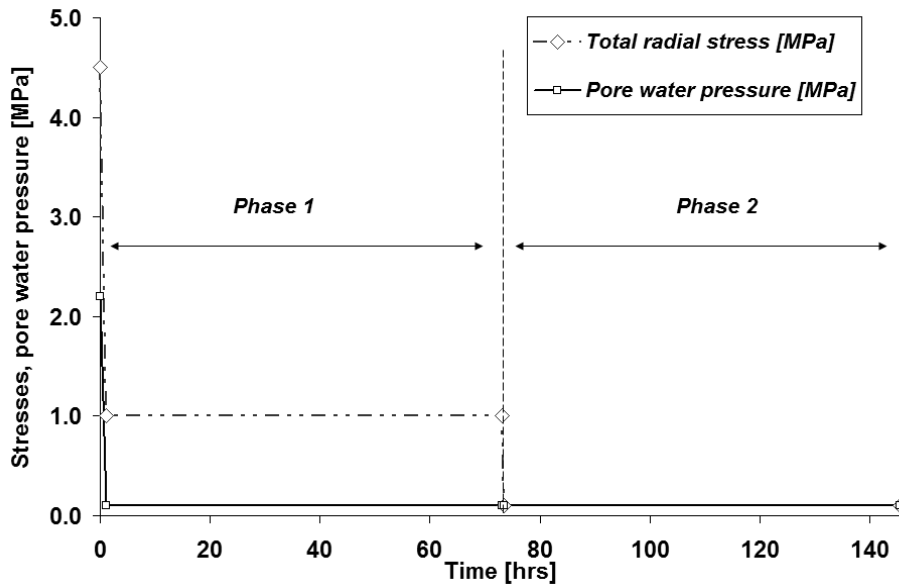


Figure 20 : Hydraulic and mechanical loadings at the inner radius

In a third step, the temperature at the inner radius increases from 16°C to 70°C in 1 hour. Following this period of rise in temperature, we let a period of 48 hrs of stabilisation. Then the cooling phase begins. First, the temperature decreases down to 26°C in 20 hrs. The second part of this cooling cycle brings the temperature at 16°C in 80 hrs. Finally, a period of stabilisation is imposed during 72 hrs (see Figure 21).

It is worthwhile to note that the time evolution and the magnitude of the boundary conditions do not correspond exactly to the conditions imposed during the experiment. Indeed, the benchmark exercise has been defined as a preliminary exercise before the final definition of the experimental procedure. Between the definition of the benchmark exercise and the carrying out of the experiment, the experimental boundary conditions have been modified. It explains why numerical simulations and experimental results do not correspond to the same conditions.

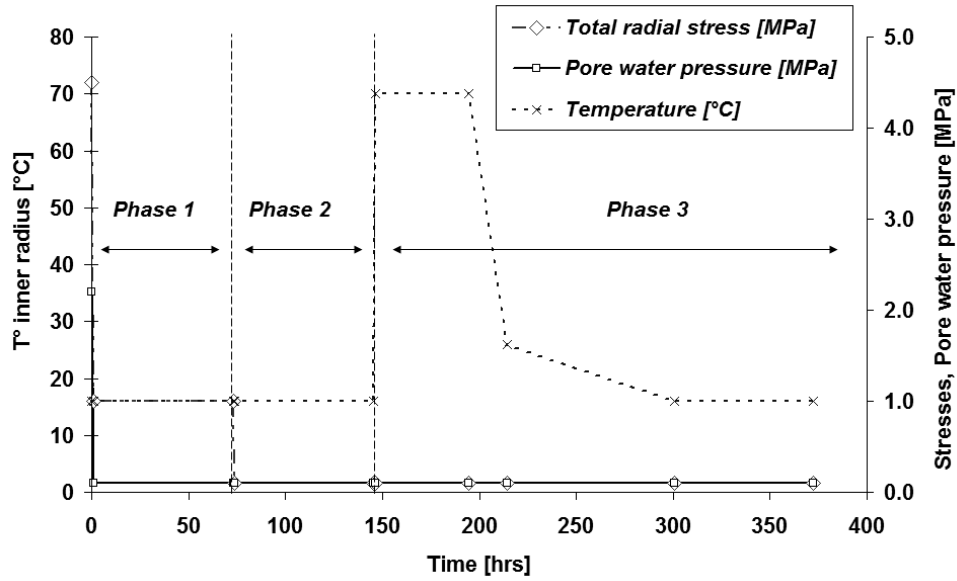


Figure 21: Thermo-hydro-mechanical loadings applied at the inner radius during the whole modelling

## 4.4 Constitutive models and parameters

### 4.4.1 Mechanical model

In a first step of the TIMODAZ project, this modelling consists in “blind predictions”. The experimental results are not known and an appropriated constitutive law can not be used. For this reason, a classical constitutive law with different hardening rules is chosen for these first calculations.

The mechanical model used for the plastic clay is a non-associated elastoplastic constitutive law. The yield surface is defined by a Drucker-Prager criterion. The trace of this plasticity surface in the deviatoric plan is a circle. The yield function  $f$  uses a linear relationship between the first stress tensor invariant and the second deviatoric stress tensor invariant. The mechanical parameters are defined in Table 5.

The Drucker-Prager yield limit is given by the following equation:

$$f \equiv II_{\hat{\sigma}} - m \left( I_{\sigma} + \frac{3c}{\tan \phi} \right) = 0 \quad (4.1)$$

with  $\phi_c$  the friction angle in compression and  $c$  the cohesion ;

$I_{\sigma} = \sigma_{ii}$  the first stress invariant ;

$II_{\hat{\sigma}} = \sqrt{\frac{1}{2} \hat{\sigma}_{ij} \hat{\sigma}_{ij}}$  the second deviatoric stress invariant with  $\hat{\sigma}_{ij} = \sigma_{ij} - \frac{I_{\sigma}}{3} \delta_{ij}$  ;

TIMODAZ

$$m = \frac{2 \sin \phi_c}{\sqrt{3}(3 - \sin \phi_c)}$$

In this model, two processes of isotropic hardening and softening are possible:

- Hardening of friction angle;
- Softening of cohesion.

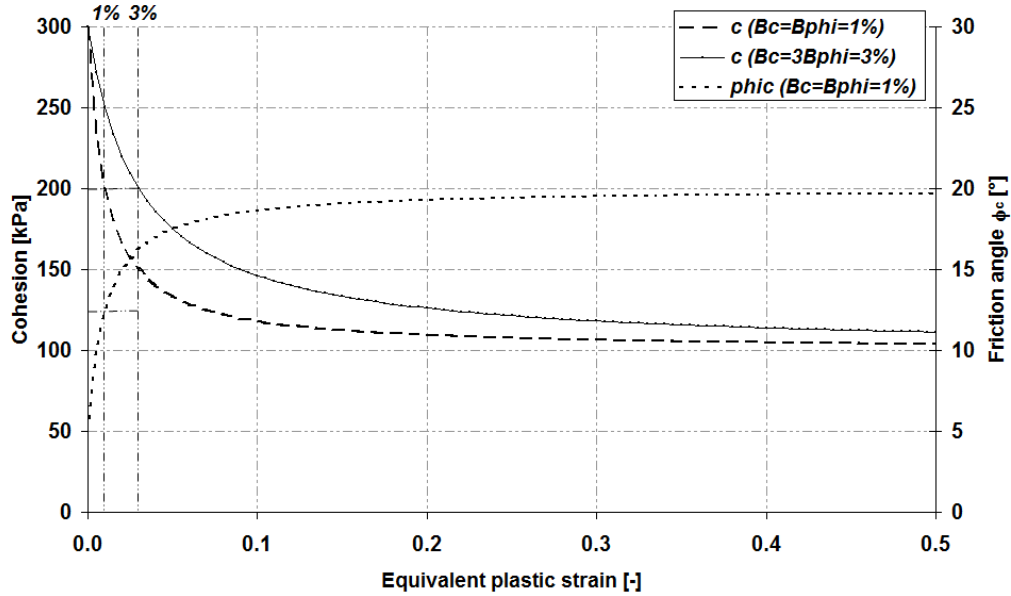


**Figure 22: Hardening/softening hyperbolic relation (example for  $c_0 = 300$  kPa,  $c_f = 100$  kPa,  $\phi_{c0} = 5^\circ$  and  $\phi_{cf} = 20^\circ$ )**

These two processes are independent, so they can be used simultaneously or separately. The plastic flow is assumed to induce hardening/softening of the yield surface, which is introduced via a hyperbolic variation of the internal variables ( $\phi_c'$  and  $c'$ ) as a function of the Von Mises equivalent plastic strain  $\varepsilon_{eq}^p$  (Figure 22):

$$\varphi_c = \varphi_{c0} + \frac{(\varphi_{cf} - \varphi_{c0})\varepsilon_{eq}^p}{\beta_{\varphi_c} + \varepsilon_{eq}^p} \quad (4.2)$$

$$c = c_0 + \frac{(c_f - c_0)\varepsilon_{eq}^p}{\beta_c + \varepsilon_{eq}^p} \quad (4.3)$$

where the Von Mises equivalent plastic strain is obtained by integration of the Von Mises equivalent plastic strain rate  $\dot{\varepsilon}_{eq}^p$  :

$$\varepsilon_{eq}^p = \int_0^t \dot{\varepsilon}_{eq}^p dt \quad \text{with} \quad \dot{\varepsilon}_{eq}^p = \sqrt{\frac{2}{3} \dot{\varepsilon}_{ij}^p \dot{\varepsilon}_{ij}^p} \quad (4.4)$$

Coefficients  $\beta_{\phi_c}$  and  $\beta_c$  represent respectively the values of the equivalent plastic strain for which the half of the hardening (or softening) of the frictional angle (or the cohesion) is achieved.

#### 4.4.2 Hydraulic and thermal constitutive models

##### *Darcy's law*

For this benchmark, the clay is considered as perfectly saturated. The general Darcy flow law is used and defines the Darcy fluid velocity  $\underline{q}_w$  as a linear function of permeability and the gradient of fluid pressure  $p_w$  :

$$\underline{q}_w = -\frac{k_{\text{int}}}{\mu_w}(\nabla p_w) \quad (4.5)$$

where  $k_{\text{int}}$  is a scalar in isotropic situation  $k_{\text{int}} = K_w \frac{\mu_w}{\rho_w \cdot g}$  ;

$k_{\text{int}}$  is the intrinsic permeability coefficient [m<sup>2</sup>] ;

$K_w$  is the isotropic permeability [m/s] ;

$\mu_w$  is the fluid dynamic viscosity [Pa/s].

##### *Intrinsic permeability $k_{\text{int}}$*

In this model, two cases can be studied:

- The permeability  $k_{\text{int}}$  is constant:  $k_{\text{int}} = k_{\text{int}}^{\text{sat}}$
- The permeability  $k_{\text{int}}$  is a function of porosity:  $k_{\text{int}} = k_{\text{int}}^{\text{sat}} \cdot k_{r,n}$  ,

with:

$$\begin{aligned} k_{r,n} &= 1 && \text{if } n - n_0 < 0 \\ k_{r,n} &= 1 + 2 \cdot 10^9 (n - n_0)^3 && \text{if } 0 < n - n_0 < 10^{-2} \\ k_{r,n} &= 1 + 2 \cdot 10^3 && \text{if } n - n_0 > 10^{-2} \end{aligned}$$

This formulation is illustrated in Figure 23.



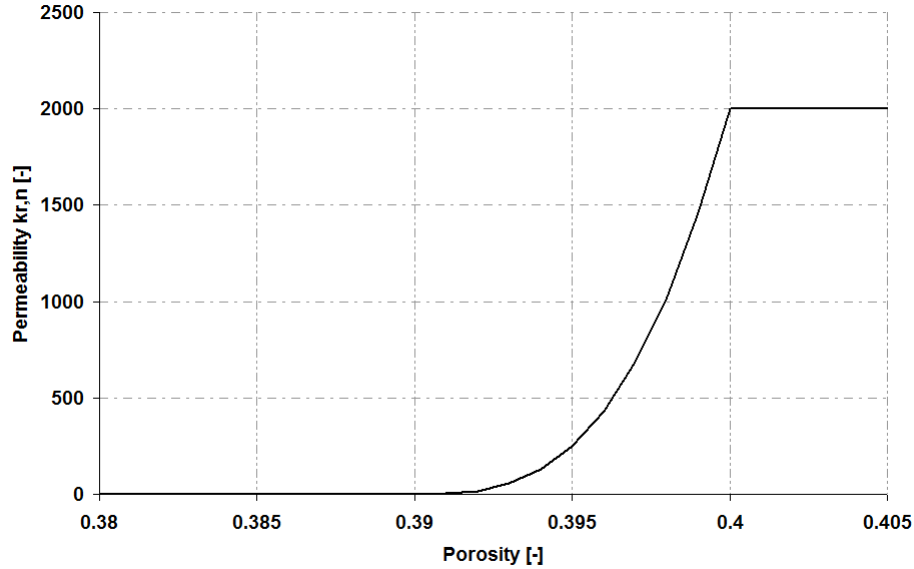


Figure 23 : Porosity/permeability relation (example for  $n_0 = 0.39$ )

**Fluid dynamic viscosity  $\mu_w$**

$\mu_w(T) = \mu_{w0} - \alpha_w \cdot \mu_{w0} \cdot (T - T_0)$  where  $\alpha_w$  is the liquid dynamic viscosity thermal coefficient

**Water specific mass  $\rho_w$**

$\rho_w(T, p_w) = \rho_{w0} \cdot \left[ 1 + \frac{p_w - p_{w0}}{\chi_w} - \beta_w \cdot (T - T_0) \right]$  where  $\beta_w$  is the liquid thermal expansion coefficient

**4.4.3 Balance equations**

**Momentum balance equation**

The momentum balance equation is written for quasi-static conditions:

$$\text{div}(\sigma_{ij}) = 0 \tag{4.6}$$

where  $\sigma_{ij}$  is the total stress tensor [Pa]

The total stress is expressed by:

$$\sigma_{ij} = \sigma'_{ij} + p_w \tag{4.7}$$

**Water mass balance equation**



We suppose that the water is only in its liquid phase. Then, the water mass balance equation can be written:

$$\dot{S}_w + \text{div}(\underline{f}_w) = Q_w \quad (4.8)$$

where  $\dot{S}_w$  is the water storage term [ $\text{kg}\cdot\text{m}^{-3}\cdot\text{s}^{-1}$ ],  $Q_w$  is a term of production / consumption of water [ $\text{kg}\cdot\text{m}^{-3}\cdot\text{s}^{-1}$ ] and  $\underline{f}_w$  is the water mass flux [ $\text{kg}\cdot\text{m}^{-2}\cdot\text{s}^{-1}$ ] defined by:

$$\underline{f}_w = \rho_w \cdot \underline{q}_w \quad (4.9)$$

where  $\underline{q}_w$  is the mean speed of the liquid phase compared to the solid phase [ $\text{m}\cdot\text{s}^{-1}$ ].

Finally, the water mass balance equation is written:

$$\frac{\partial}{\partial t}(\rho_w \cdot \phi) + \text{div}(\rho_w \cdot \underline{q}_w) - Q_w = 0 \quad (4.10)$$

### ***Heat balance equation***

We suppose that the water is only in its liquid phase. The heat balance equation can then be written:

$$\dot{S}_T + \text{div}(\underline{V}_T) - Q_T = 0 \quad (4.11)$$

Where  $S_T$  represents the stored heat quantity [ $\text{J}/\text{m}^3$ ],  $\underline{V}_T$  the heat flux [ $\text{W}/\text{m}^2$ ] and  $Q_T$  the volumetric heat source [ $\text{W}/\text{m}^3$ ].

### **Stored heat quantity per unit volume**

The system enthalpy is defined as the sum of the contribution of each component of the system:

$S_T = \sum H_i$  with, for a soil completely saturated:

$$H_w = n \cdot \rho_w \cdot c_{p,w} \cdot (T - T_0) \quad (4.12)$$

$$H_s = (1 - n) \cdot \rho_s \cdot c_{p,s} \cdot (T - T_0) \quad (4.13)$$

### **Heat transfer per unit volume**

$$V_T = \underbrace{-\lambda_s \cdot \nabla T}_{\text{conduction}} + \underbrace{c_{p,w} \cdot \rho_w \cdot \underline{q}_w \cdot (T - T_0)}_{\text{convection}} \quad (4.14)$$

## **4.4.4 Strain rate**

The total strain rate  $\dot{\varepsilon}_{ij}$  is the sum of the mechanical elastic strain rate  $\dot{\varepsilon}_{ij}^e$ , the mechanical plastic strain rate  $\dot{\varepsilon}_{ij}^p$  and the thermal elastic strain rate  $\dot{\varepsilon}_{ij}^{e,th}$ :

$$\dot{\varepsilon}_{ij} = \dot{\varepsilon}_{ij}^e + \dot{\varepsilon}_{ij}^p + \dot{\varepsilon}_{ij}^{e.th} \quad \text{with} \quad \dot{\varepsilon}_{ij}^{e.th} = \beta_s \cdot \dot{T} \cdot \delta_{ij} \quad (4.15)$$

$\beta_s$  is the linear solid thermal expansion coefficient [ $\text{K}^{-1}$ ] and  $\delta_{ij}$  is the Kronecker symbol

## 4.5 Parameters

We present here the thermo-hydro-mechanical characteristics of the plastic clay constituting the hollow cylinder (Table 2, 3 and 4). The properties are given for the initial temperature and pore pressure.

Geomechanical characteristics		Boom Clay
Young elastic modulus [MPa]	$E_0$	300
Poisson ratio [-]	$\nu$	0.125
Specific mass [ $\text{kg}/\text{m}^3$ ]	$\rho$	2682
Initial cohesion [kPa]	$c_0$	300
Final cohesion [kPa]	$c_f$	100
Softening parameter [-]	$\beta_c$	0.01
Initial friction angle [ $^\circ$ ]	$\phi_{c0}$	5
Final friction angle [ $^\circ$ ]	$\phi_{cf}$	18
Hardening parameter [-]	$\beta_\phi$	0.01
Dilatation angle [ $^\circ$ ]	$\psi$	0
Biot's coefficient [-]	$b$	1

Table 5 : Geomechanical characteristics

Hydraulic characteristics		Boom Clay
Initial porosity	$n_0$	0.39
Initial intrinsic permeability [ $\text{m}^2$ ]	$k_{\text{int}}^{\text{sat}}$	$4.10^{-19}$
Water specific mass [ $\text{kg}/\text{m}^3$ ]	$\rho_w$	1000
Fluid dynamic viscosity [Pa.s]	$\mu_w$	$10^{-3}$
Liquid compressibility coefficient [ $\text{MPa}^{-1}$ ]	$1/\chi_w$	$5.10^{-4}$

Table 6 : Hydraulic characteristics

Thermal characteristics		Boom Clay
Thermal conductivity [ $\text{W}/(\text{mK})$ ]	$\lambda$	1.35
Volumetric heat capacity [ $\text{J m}^{-3} \cdot \text{K}^{-1}$ ]	$\rho C_p$	2.84E6
Linear solid thermal expansion coefficient [ $\text{K}^{-1}$ ]	$\beta_s$	$10^{-5}$
Volumetric liquid thermal expansion coefficient [ $\text{K}^{-1}$ ]	$\beta_w$	$3.10^{-4}$
Liquid dynamic viscosity thermal coefficient [ $\text{K}^{-1}$ ]	$\alpha_w$	0.01

Table 7 : Thermal characteristics

TIMODAZ



## 4.6 Description of the calculation

Three isotropic mechanical models will be studied. In the first one, we use an elastic perfectly plastic model, in the second one a friction angle hardening elastoplastic model and the third one uses a combined friction angle hardening and cohesion softening model. The permeability is supposed to be constant for the three first cases. For the fourth case, the permeability is considered as a function of the porosity and the mechanical model is the same as the third case. Table 8 summarizes the different cases.

Case	HM coupling	Perfect plasticity	Friction angle hardening	Cohesion softening	Permeability evolution	Thermal loading
A						
B						
C						
D						
E						

Table 8: Summary of the different cases to be model

## 5 General form of the numerical results

### 5.1 Results of modelling: hydro-mechanical aspects

#### 5.1.1 Elastic perfectly plastic model (case A)

##### *Pore water pressure*

The modelling takes place in 2 phases: during the first one, the pore water pressure decreases linearly to 0.1MPa and the total radial stress to 1MPa. During the second one, the total radial stress decreases to 0.1MPa while the pore pressure is maintained at 0.1MPa. The first phase is realised in 70 minutes and, a period of 72 hours (hrs) occurs during which the equalization of the pore pressure can take place in the rock material. The second reduction is realised in 18 minutes and a period of 72 hours of stabilisation occurs.

Figure 24 illustrates profiles of the pore pressure with the radial distance. The first phase is represented with 3 curves: one at 35 minutes which represents the half of the first reduction, the second at 70 minutes at the end of the reduction and, at last, at 73.17 hrs which is the end of the first phase. We see during this first phase a drawdown of pore water pressure because of the reduction of the pore water pressure at the inner radius. During the stabilisation phase, a dissipation of the pore pressure occurs. The profile at 73.17 hrs corresponds to this dissipation and it has the same shape as the profile at 35 minutes.

The two last curves, respectively at 73.47 hrs and at 145 hrs, illustrate the second phase. At the end of the second phase (at 73.47 hrs), an inversion of pore water pressure gradient is observed. This inversion may be explained by some change in volume inducing a decrease in pore water pressure. So, to maintain the pore pressure at inner radius at 0.1MPa, the gradient must be reversed. At the end of the calculation (at 145.17 hrs), the pore water pressure is stabilized in the rock material and we have the same kind of profile as the end of the first phase.

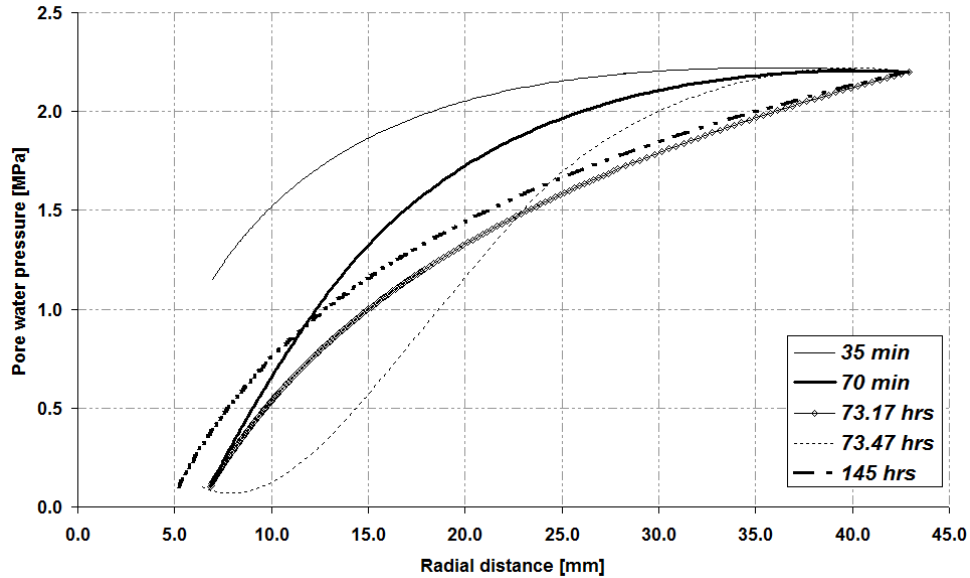


Figure 24 : Evolution of pore water pressure with radial distance at different times in case A

### *Radial effective stress*

Figure 25 shows radial profiles of radial effective stress during the total duration of calculation. At 35 minutes, half of the first phase of reduction, a decrease of the radial stress at the inner cavity is observed. The curve at 70 minutes shows the end of the first phase of reduction. And finally, the curve 73.17 hrs marks the end of the first phase. We remark an increase of radial stress at this time in comparison to the profile at 70 minutes. It can be explained by the dissipation of pore water pressure, as we can see in Figure 24, which increases radial effective stress following the Terzaghi's principle.

The second phase is marked by two curves, the first one at 73.47 hrs and the second one at 145 hrs. The profile at 73.47 hrs indicates the end of the second reduction phase. As a result, a reduction of the effective stress is observed at the inner cavity. The profile at 73.47 hrs exhibits higher effective stress than the profile at 145 hrs. As we have noticed in Figure 7, when the pore pressure is stabilized in rock material at 145 hrs, a higher profile of pore pressure is obtained. As a consequence, the radial effective stress must be reduced with respect to Terzaghi's principle.

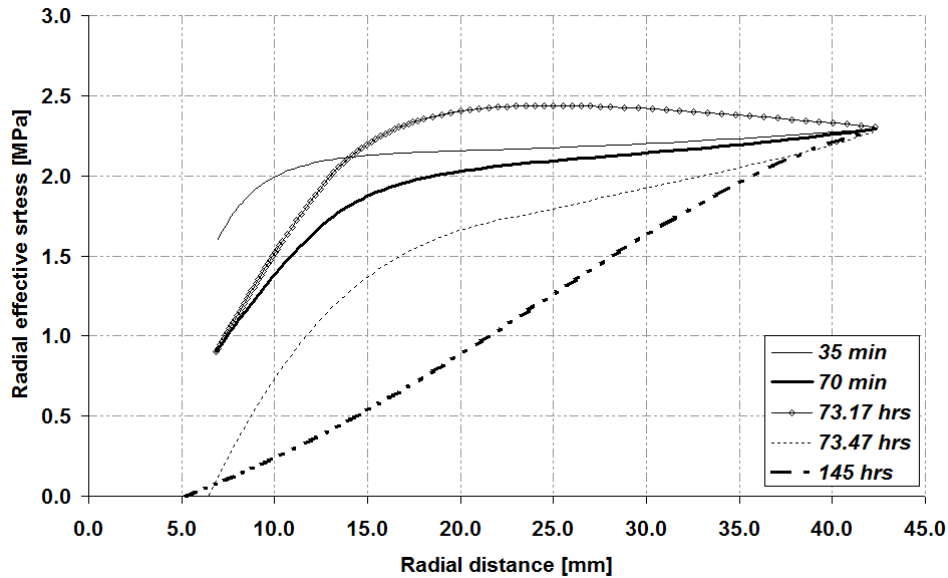


Figure 25: Radial profile of radial effective stress at different times in case A

### *Orthoradial effective stress*

Orthoradial effective stress profiles are illustrated in Figure 26. When the stress increases as a function of the radial distance, the stress state is plastic and when it's decreasing the stress state is elastic. At 35 minutes, the maximum of the stress is reached at the inner radius. Thus the stress state at this time is elastic. At 70 minutes, a peak is observed which indicates transition from plastic behaviour to elastic regime. Then, similar profiles are obtained at 70 min and at 73.17 hrs. As a result, there is no evolution of the plastic zone during the stabilisation period. At the end of the first phase, the plastic radius is approximately equal to 13 mm for the two last curves.

During the second phase of modelling, an evolution of the peak appears. This one indicates the growth of the plastic radius and so an increase of the plastic zone with the reduction of total stress.

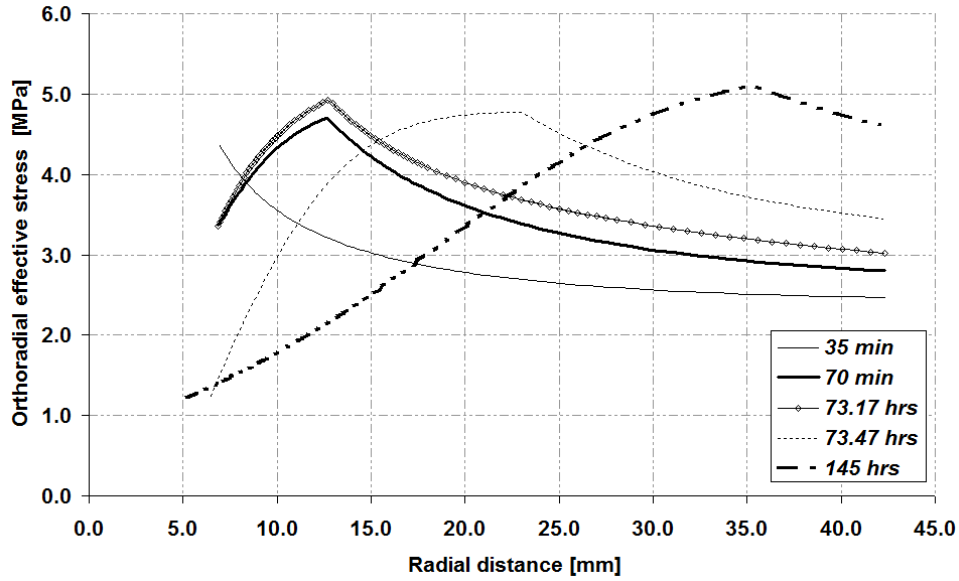


Figure 26: Radial profile of orthoradial effective stress at different times in case A

### *Axial effective stress*

Figure 27 illustrates the behaviour of the axial effective stress with the radial distance. The same kind of profiles as previously, in Figure 26, is observed. But for this stress, the transition between the two different behaviours is less tidy than for the previous stress.

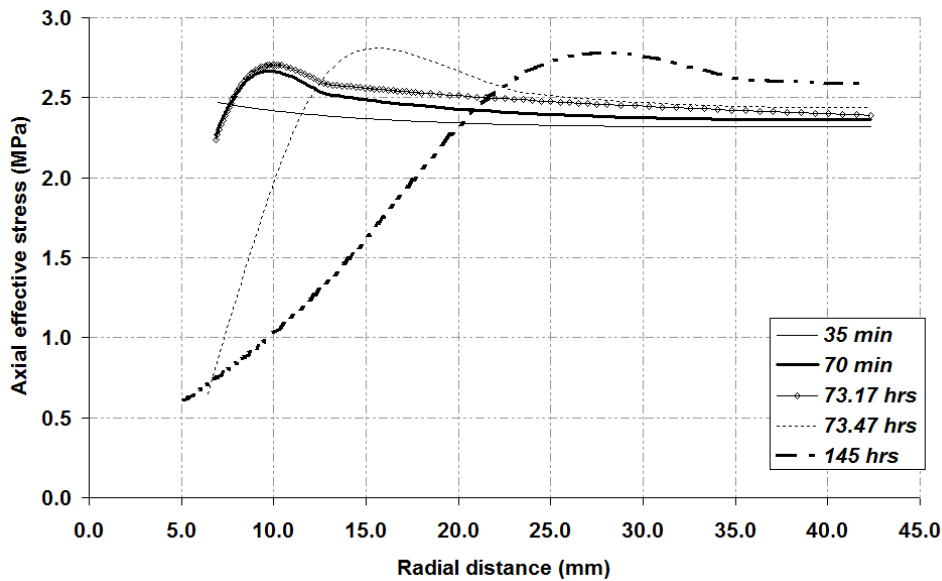


Figure 27: Radial profile of axial effective stress at different times in case A

### *Plastic indicator*

The plastic indicator is considered strictly inferior to 1 when the stress state is elastic and equal to 1 when the behaviour is plastic. Figure 28 shows the evolution of the plastic indicator during

TIMODAZ

the total duration of calculation. At 35 minutes, the plastic indicator is strictly inferior to 1. Thus, the stress state at this time is elastic. After this time, an evolution of the plastic zone appears, as we have seen in Figure 26.

During the second phase, the plastic radius increases and at the end of the modelling, at 145 hrs, the plastic radius is approximately equal to 35 mm.

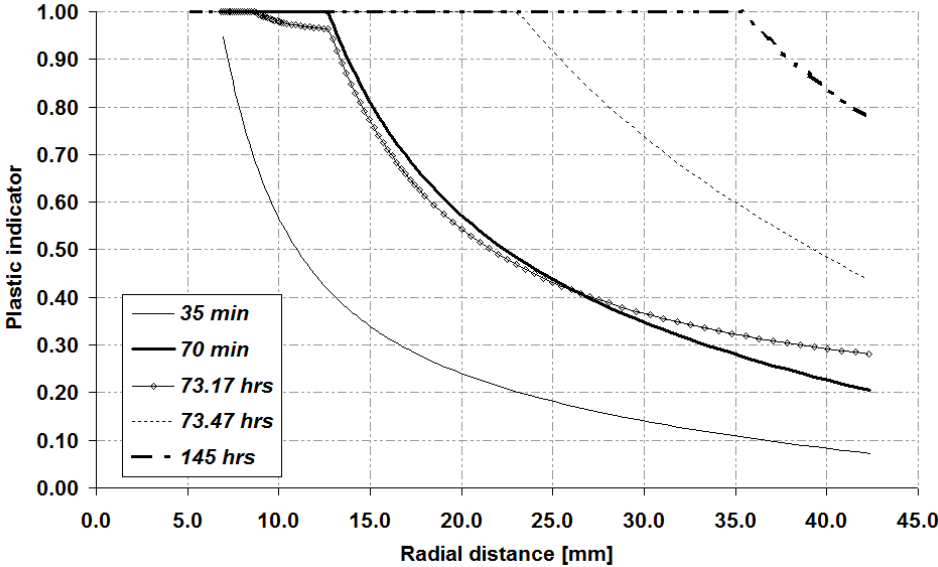


Figure 28: Radial profile of plastic indicator at different times in case A

**Water mass flux**

Figure 29 shows the evolution of the water mass flux with radial distance. During the first phase, we notice negative values for profiles at 35 minutes, 70 minutes and 73.17 hrs which indicate a water mass flux in direction of the inner cavity. We note an injection of water at 73.47 hrs. This injection is related to the inversion of pore water gradient as a consequence of dilatancy effect (see Figure 24). After stabilisation of pore water pressure in rock material, the values become again negative (profile at 145 hrs).



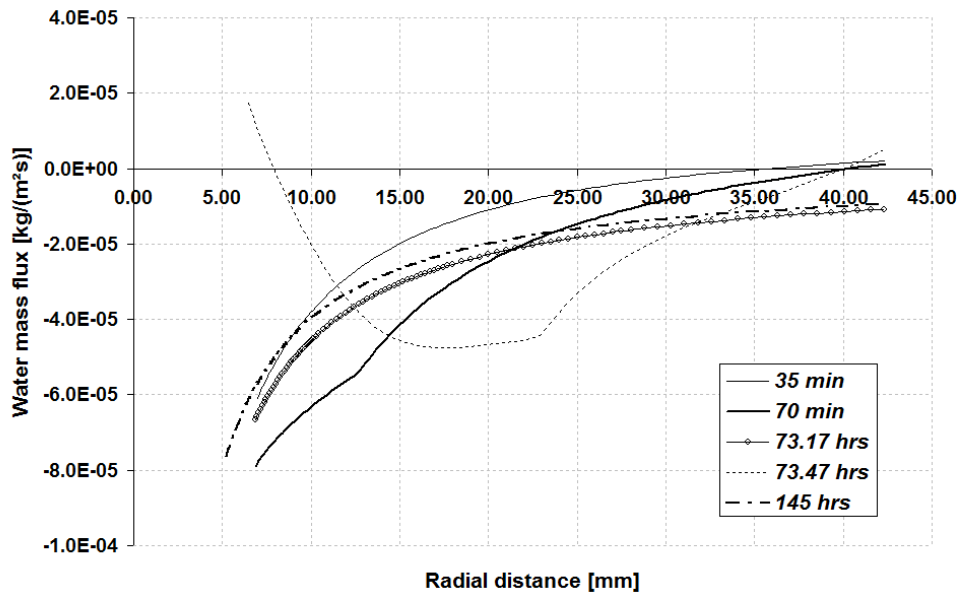


Figure 29: Radial profile of the water mass flux at different times in case A

### Water flux

Figure 30 illustrates the evolution of water flux as a function of the time at the inner and external radius. At the inner face, a transient state flow is noticed before a stationary state flow which runs until the end of the first phase. The second phase begins at 73.17 hrs with a decrease of the water flux due to the second reduction of total stress. We observe that the water flux becomes negative which indicates an injection of water. After this injection, water flow becomes stationary. The same behaviour for the flux at the external radius with an opposite sign is observed. When the hydraulic steady state is reached the two fluxes are equal but have opposite sign.

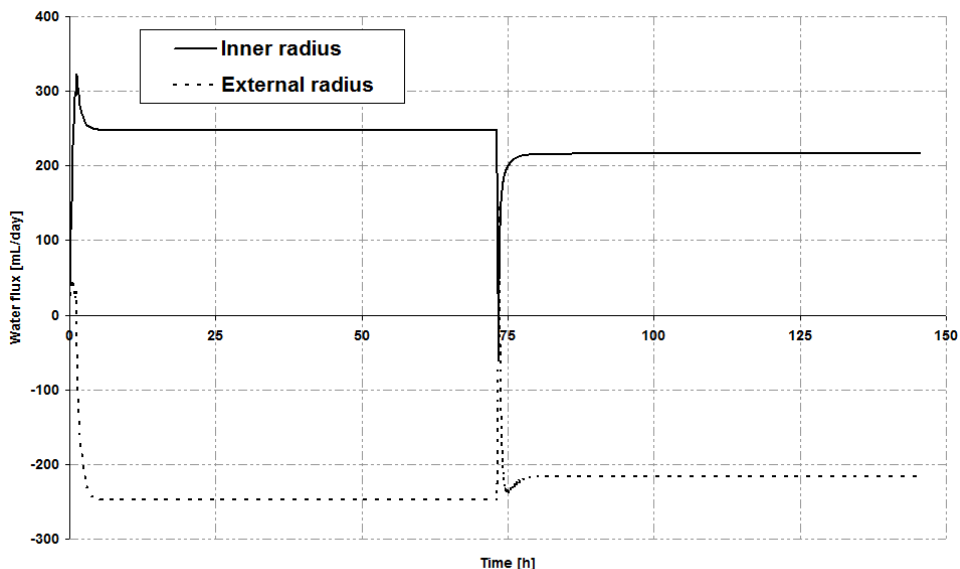


Figure 30: Water flux evolution at the internal and external radius during the total duration of the modelling in case A

TIMODAZ

### Radial displacement

Figure 31 shows the profile of radial displacement. When releasing the total stress, the inner cavity converges and the final convergence is equal to 1.83 mm. The displacements are relatively small at 35 minutes and increase with the excavation at 70 minutes. The same profiles are observed at 35 minutes and at 73.17 hrs. During the second phase of excavation, an increase of the displacements, at 73.47 hrs and 145 hrs, is observed due to the extension of the plastic zone generated by the reduction of the total stress at the inner radius.

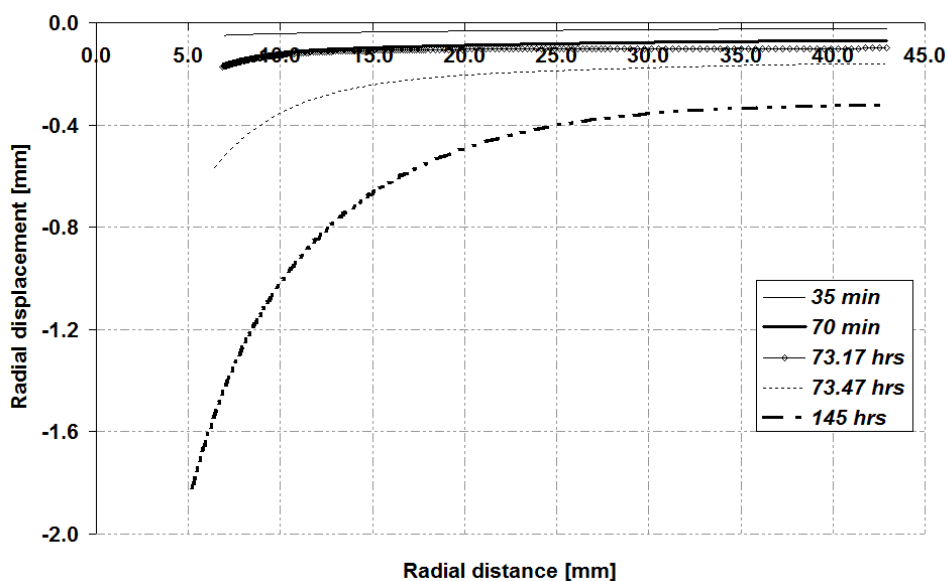


Figure 31: Radial displacement vs radial distance in case A

### Stress path at inner radius

Figure 32 shows the effective stress path at the inner radius in the  $(I_\sigma, II_\sigma)$  stresses plane. It describes in details the stress evolution during the total duration of calculation at the inner cavity. The Drucker-Prager yield limit is also plotted (dot-dashed line).

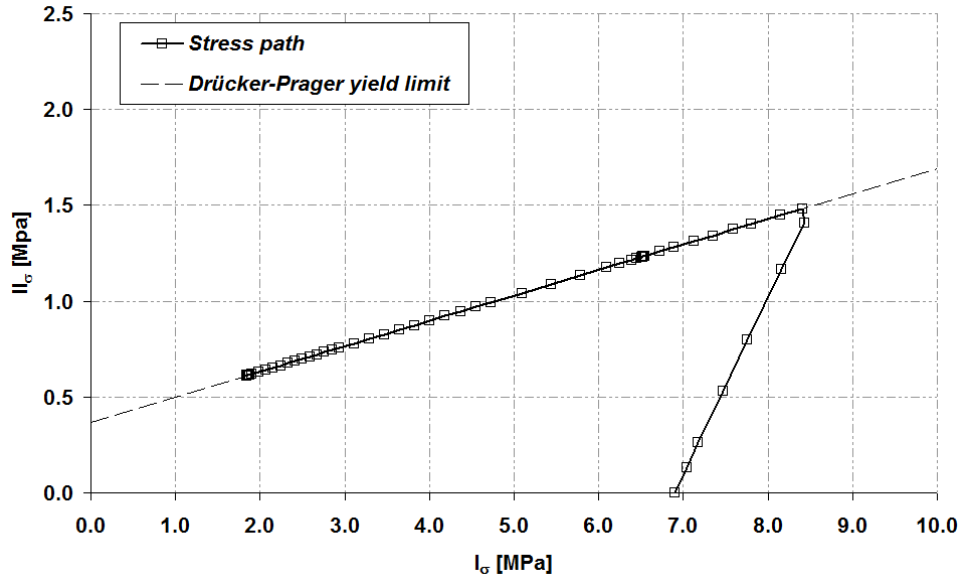


Figure 32: Effective stress path at inner radius in case A

When total stresses and pore pressure in the cylinder cavity start decreasing (“excavation”), the mean effective and deviatoric stress increases until the stress state reaches the yield limit. As there is no hardening, the stress path is then constrained to follow the yield limit till the end of the modelling.

### 5.1.2 Friction angle hardening elastoplastic model (case B)

This section presents the results of the case B which corresponds to an elastoplastic constitutive law with a friction angle hardening. The final value of the friction angle is the same as the previous case.

#### *Pore water pressure*

The evolution of the pore water pressure as a function of the radial distance is presented in Figure 33. These profiles are relatively the same as in case A (see Figure 24). During the first phase, at 35 minutes, 70 minutes and 73.17 hrs, a drawdown of the pore water pressure related to the decrease of the inner pressure. At 73.47 hrs, which corresponds to the end of the second reduction phase, the inversion of the pore water pressure noticed in case A has disappeared. At 145 hrs, the pore pressure is stabilised in rock material and the same kind of profile as at 73.17 hrs is obtained.

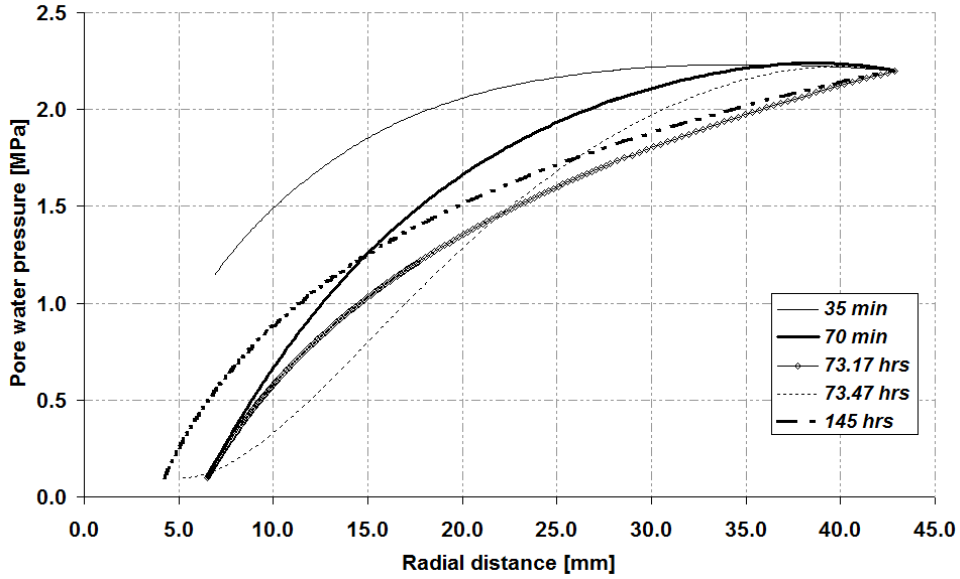


Figure 33 : Pore water pressure in function of radial distance in case B

### Stress path

In Figure 34, the effective stress path at the inner radius is plotted in the  $(I_\sigma, II_\sigma)$  stresses plane for case B. When total stress and pore pressure in the inner cavity start decreasing (“excavation”), the mean effective and deviatoric stress increases until the stress state reaches the yield limit. The mechanical model in case B corresponds to a friction angle hardening elastoplastic model. Thus, the plasticity appears for a lower stress state in comparison to case A

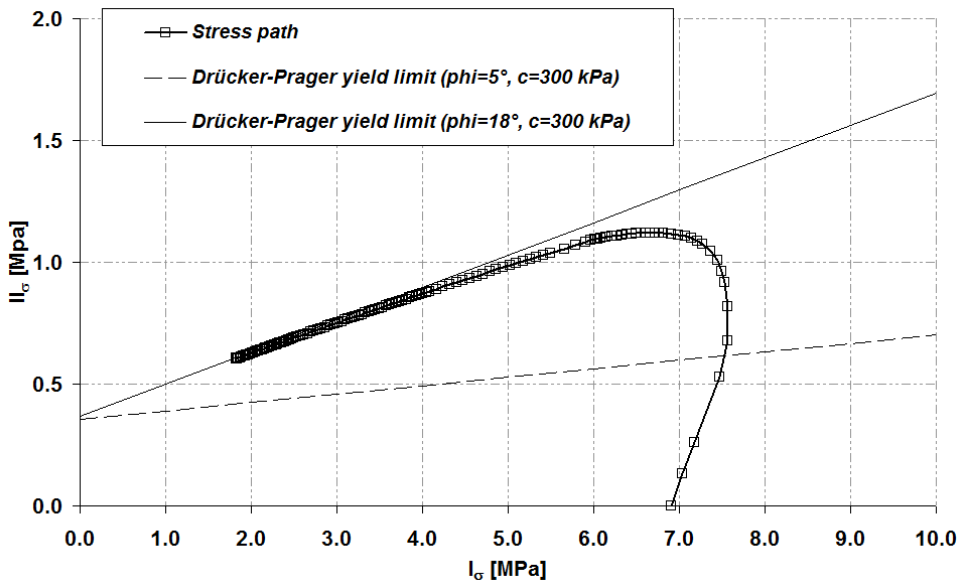


Figure 34: Stress path at the inner cavity in case B for a friction angle hardening model

### Radial displacement

The evolution of radial displacements as a function of the radial distance is presented in Figure 35. An increase of the radial displacement with time is observed due to the excavation. The final convergence, in case B, is equal to 2.78 mm. Thank to the mechanical model which allow more plasticity the final convergence is higher than previously in case A (see also Figure 31).

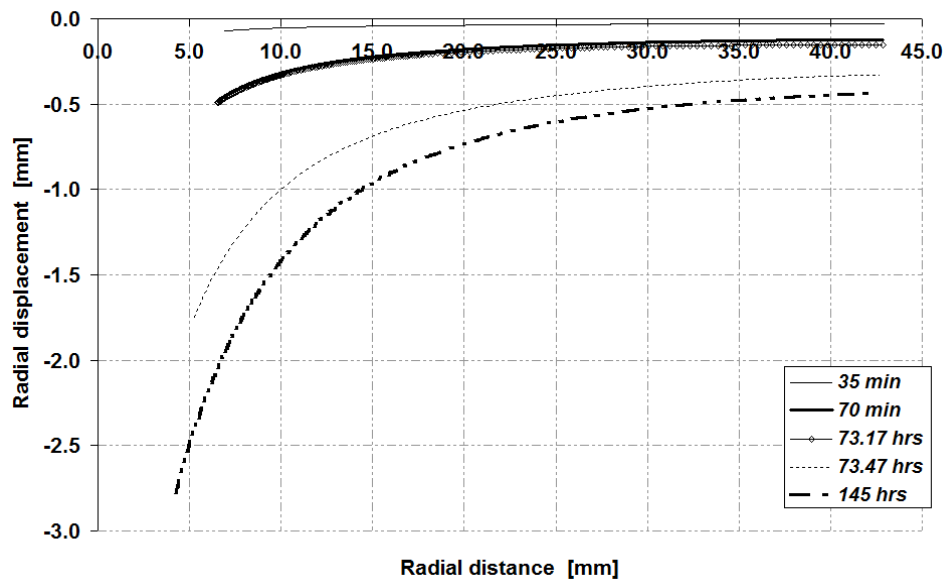


Figure 35: Radial displacement versus radial distance in case B.  
The final convergence is equal to 2.78 mm

### Plastic indicator

Figure 36 represents the evolution of the plastic indicator as a function of the radial distance for different times. At 35 minutes, plastic indicator is equal to 1 near the inner cavity and thus a plastic radius already exists. At 70 minutes the plastic radius increases. At 73.17 hrs, an elastic unloading is observed. This unloading is marked by a decrease of the plastic indicator around the middle of the model.

During the second phase, the plastic indicator is equal to 1 for the whole hollow cylinder and for the two time steps (73.47 hrs and 145 hrs). As a consequence, the stress state is plastic in the whole cylinder.

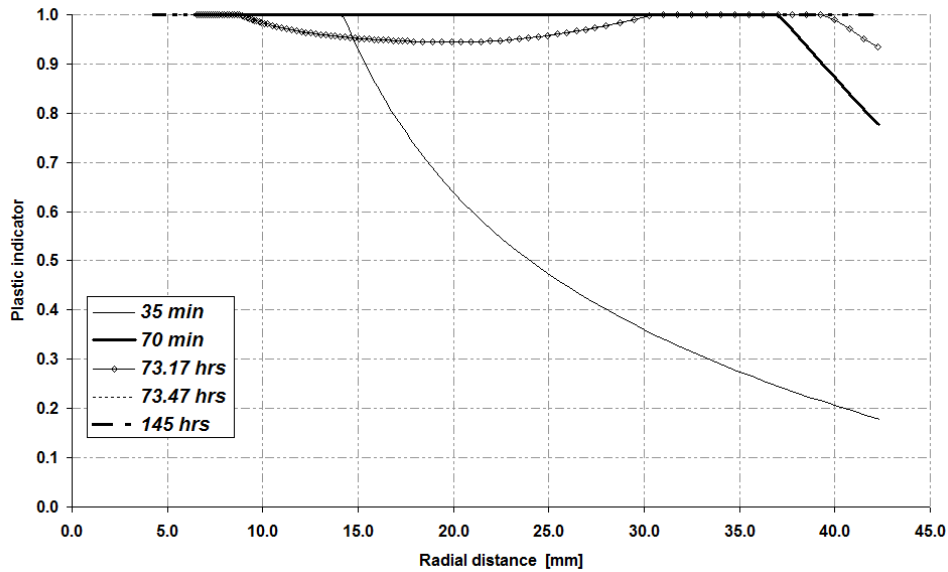


Figure 36: Evolution of plastic indicator with radial distance (case B)

### 5.1.3 Combined angle friction hardening and cohesion softening model (case C)

#### *Pore water pressure*

The profile of the pore water pressure as a function of the radial distance is presented in Figure 37. The first phase is relatively the same as case A and case B. In fact, a drawdown and a dissipation of pore water pressure occur as a function of the time.

During the second phase of the modelling, the profiles have same shape as in case B with an increase of the pore pressure at 145 hrs thank to the rise in displacement which almost closes the cavity of the cylinder.

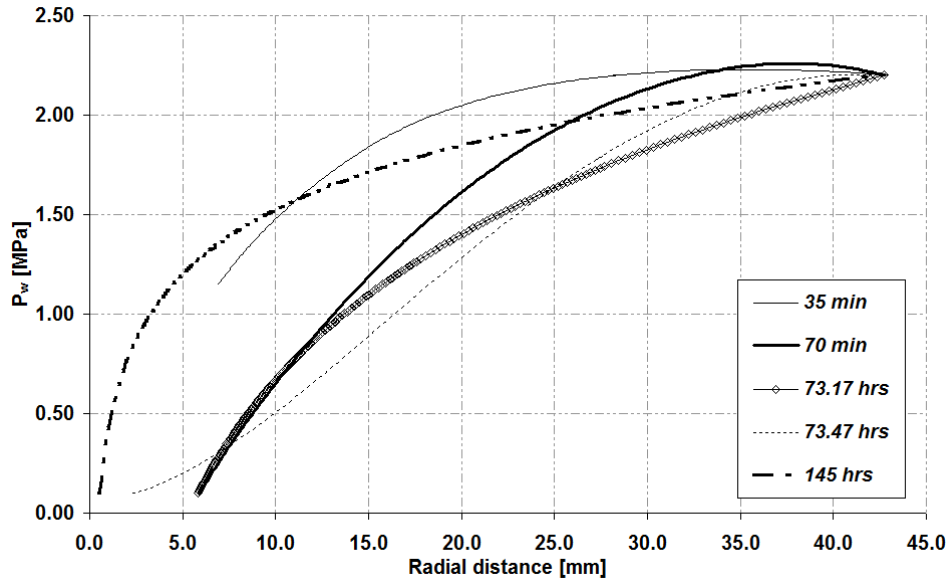


Figure 37: Evolution of pore water pressure with radial distance in case C

### Stress path

Figure 38 shows stress path at inner cavity in case C. When total stress and pore pressure in the inner cavity start decreasing (“excavation”), the mean effective and deviatoric stress increases until the stress state reaches the yield limit. The evolution of the Drucker-Prager criterion is due to a combined friction angle hardening and cohesion softening elastoplastic model. This mechanical model allows more plasticity than the previous. At the end of the calculation, the stress state is plastic.

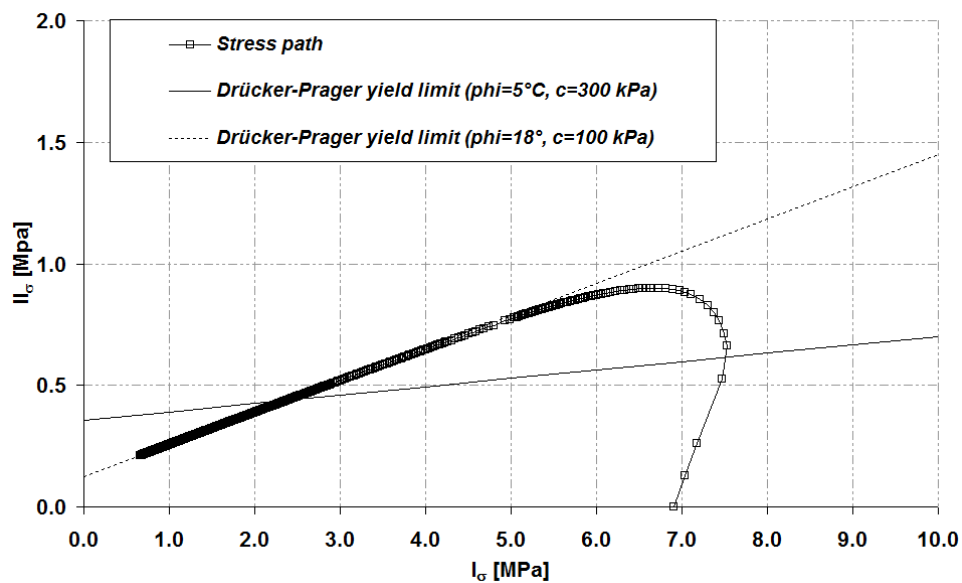


Figure 38: Stress path with a combined hardening friction angle and a softening cohesion model in case C

### Radial displacement

The profile of radial displacement for case C is illustrated in Figure 39. These profiles are relatively the same as previously but there is an increase of the final convergence which is equal to 6.53 mm. This increase is due to the mechanical model which allows more plasticity and thus more convergence.

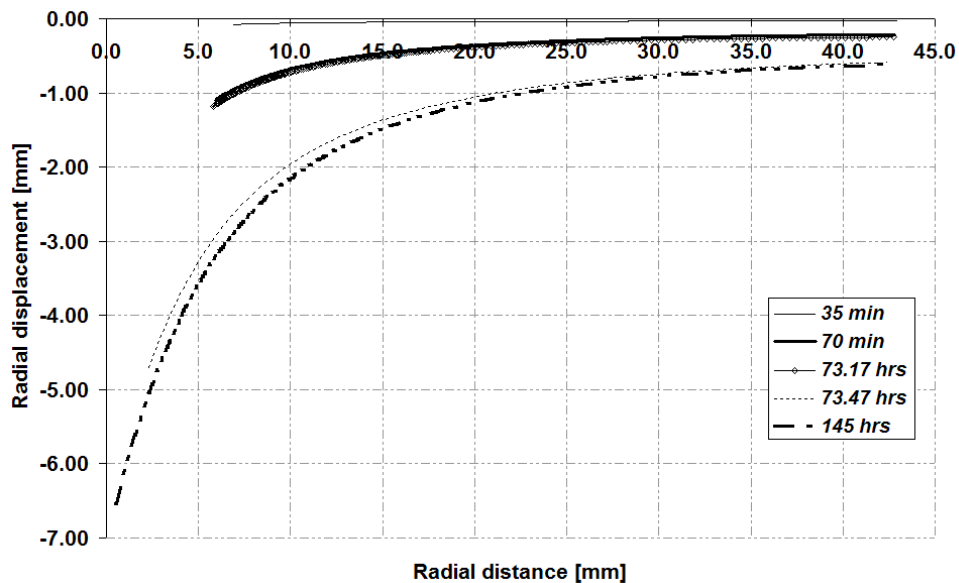


Figure 39: Radial displacement versus radial distance in case C. The final convergence is equal to 6.53 mm

### Plastic indicator

In Figure 40, the plastic indicator as a function of the radial distance is plotted. At 35 minutes, a plastic zone appears. After that, the plastic indicator is equal to 1 for each profile except for the time step 73.17 hrs which indicates an elastic unloading. At the end of the calculation, at 145 hrs, we notice an elastic unloading around the external radius and the plastic radius is more or less equal to 31.2mm.

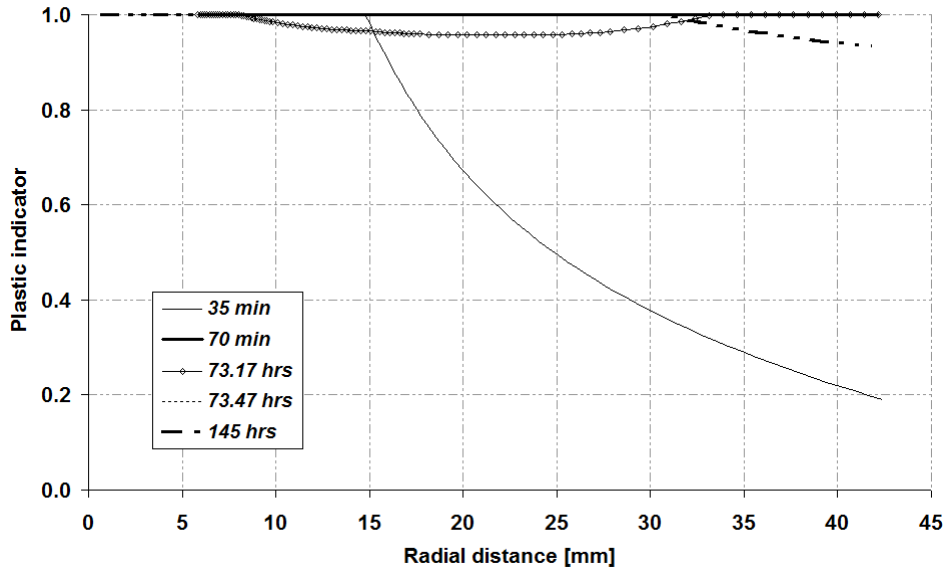


Figure 40: Evolution of plastic indicator with radial distance in case C

#### 5.1.4 Combined angle friction hardening and cohesion softening model with permeability as a function of porosity (case D)

##### *Intrinsic permeability*

Figure 41 shows variation of the intrinsic permeability as a function of porosity. The first phase exhibits small variation of permeability in comparison to the second phase where the permeability differs with two orders of magnitude. This variation develops particularly around the inner cavity and permeability does not change for a radial distance larger than 10 mm.

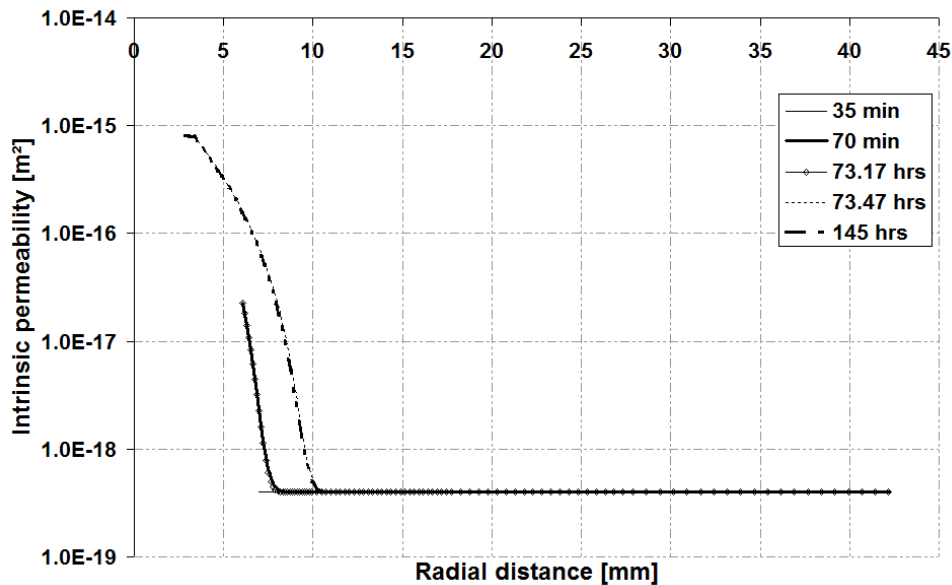


Figure 41: Evolution of intrinsic permeability with radial distance

TIMODAZ



### Pore water pressure

The evolution of the pore water pressure with radial distance is illustrated in Figure 42. At 35 minutes, we observe a drawdown of pore pressure as seen in other cases. After this time, an enhancement of permeability around the inner cavity (Figure 41) appears as a consequence of the evolution of permeability as a function of porosity. A constant level of pore pressure around the inner radius followed by a profile where pore pressure increases with radial is observed. This constant level is explained by the increase of permeability which induces additional drainage and a reduction of the pore water pressure.

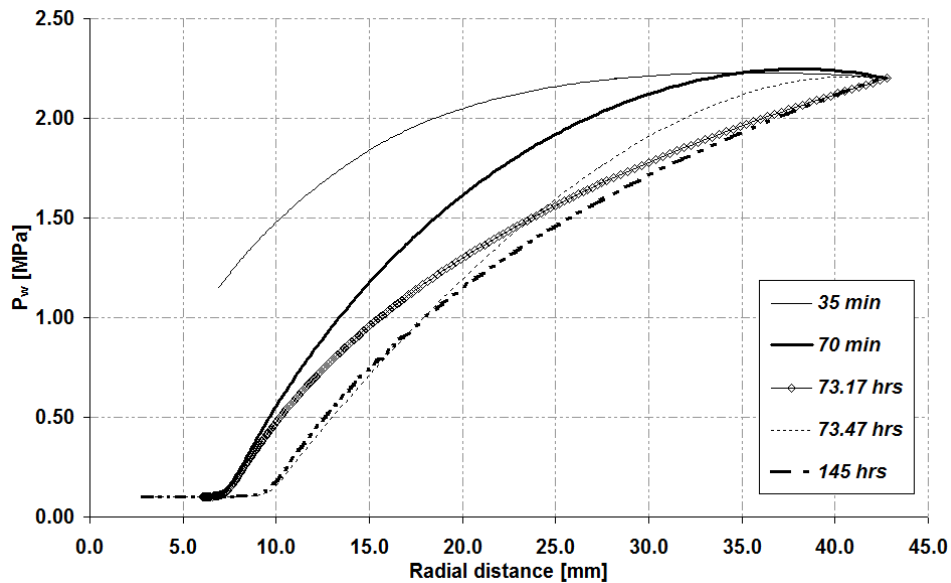


Figure 42 : Evolution of pore water pressure with radial distance in case D

### Stress path

Figure 43 shows the stress path at the inner cavity in case D. This case combines angle friction hardening and cohesion softening elastoplastic model with a variation of permeability as function of the porosity. When total stress and pore pressure in the inner cavity start decreasing (“excavation”), the mean effective and deviatoric stress increases until the stress state reaches the yield limit. This stress path is similar to the stress path obtained in case C.

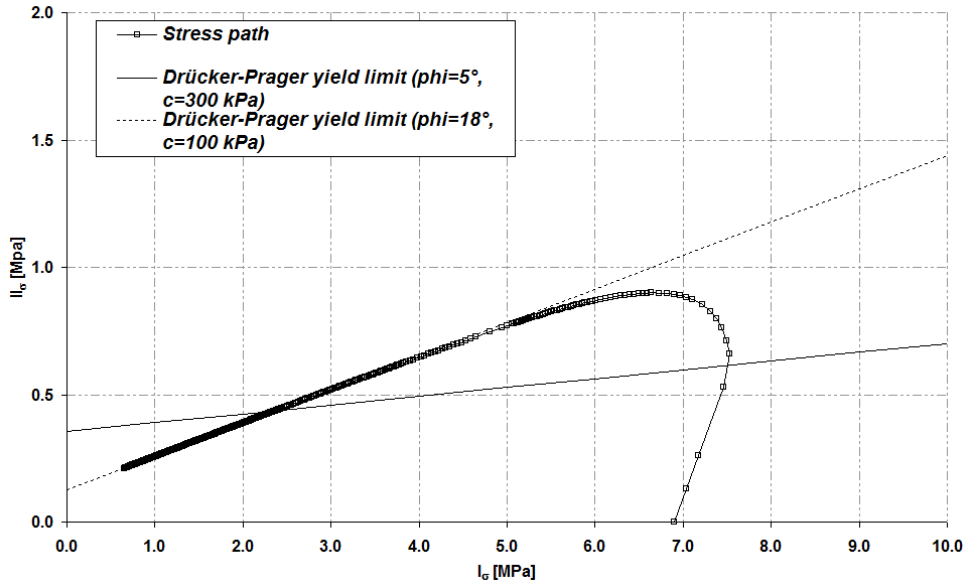


Figure 43: Stress path at inner radius with permeability in function of porosity and a combined friction angle hardening and cohesion softening model

### Radial displacement

Figure 44 illustrates the radial profiles of radial displacement at different time steps. During the first phase, we observe the same profile at 70 minutes and 73.17 hrs. During the second phase, the same conclusion with profile at 73.47 hrs and 145 hrs is done. The final convergence of the cavity is equal to 4.12 mm.

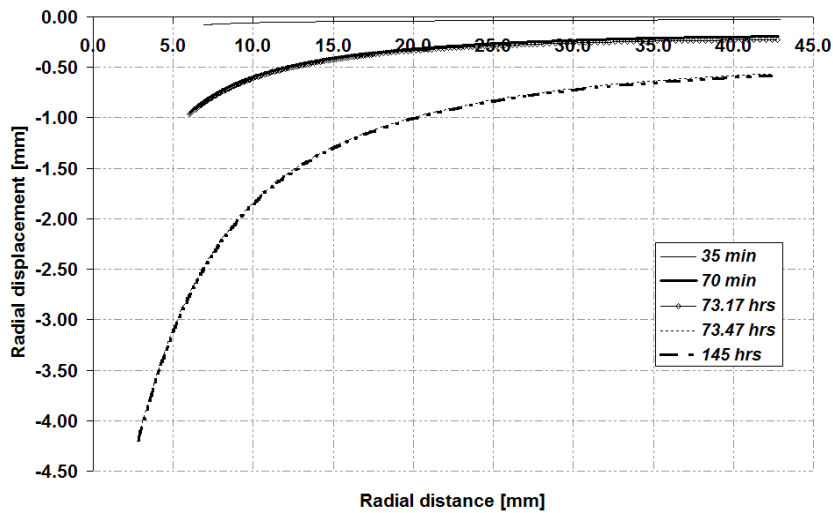


Figure 44: Radial displacement versus radial distance in case D. The final convergence is equal to 4.12 mm

### Plastic indicator

TIMODAZ



Figure 45 shows evolution of plastic radius (plastic indicator) as a function of the radial distance in case D. At 35 minutes, we have two behaviours, the first one is plastic and the second one is elastic with a plastic radius more or less equal to 15 mm. An elastic unloading of the stress state is observed at the end of each phase (at 73.17 hrs and 145 at hrs). This elastic unloading will be explained below in Figure 52.

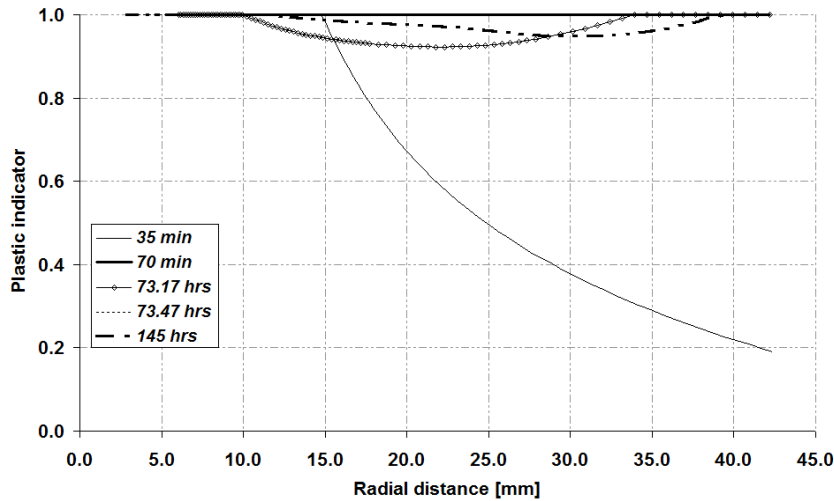


Figure 45: Plastic indicator with radial distance in case D

### 5.1.5 Comparison between the four cases

This section describes the difference obtained with the different mechanical models. Case A is the elastic perfectly plastic model. Case B considers a friction angle hardening elastoplastic model. Case C corresponds to a combination of a friction angle hardening elastoplastic model with cohesion softening. Finally case D is the same elastoplastic model as case C but the permeability is considered as a function of the porosity.

#### *Pore water pressure*

Figure 46 shows the distribution of the pore pressure in all cases at 145 hrs. The three first cases show relatively the same shape of profiles with higher pore pressure in case C due to the high convergence of the cavity. The profile in case D has a different shape and shows a plateau due to the increase of permeability in the medium around the hole.

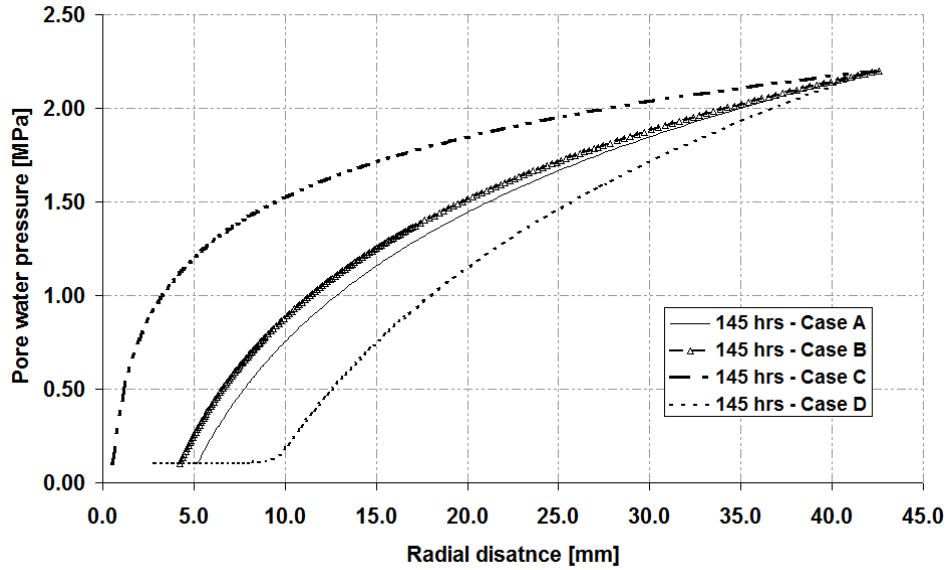


Figure 46: Comparison between the different cases at 145h. Evolution of the pore water pressure with radial distance

### *Radial effective stress*

Figure 47 illustrates the difference of radial effective stress profiles obtained for the four cases. For case A, case B and case C, the same kind of profile is observed. However case D exhibits higher value of the radial effective stress. It can be explained by a large decrease of pore water pressure in this case (see Figure 46). Consequently radial effective stress must increase to respect Terzaghi's principle.

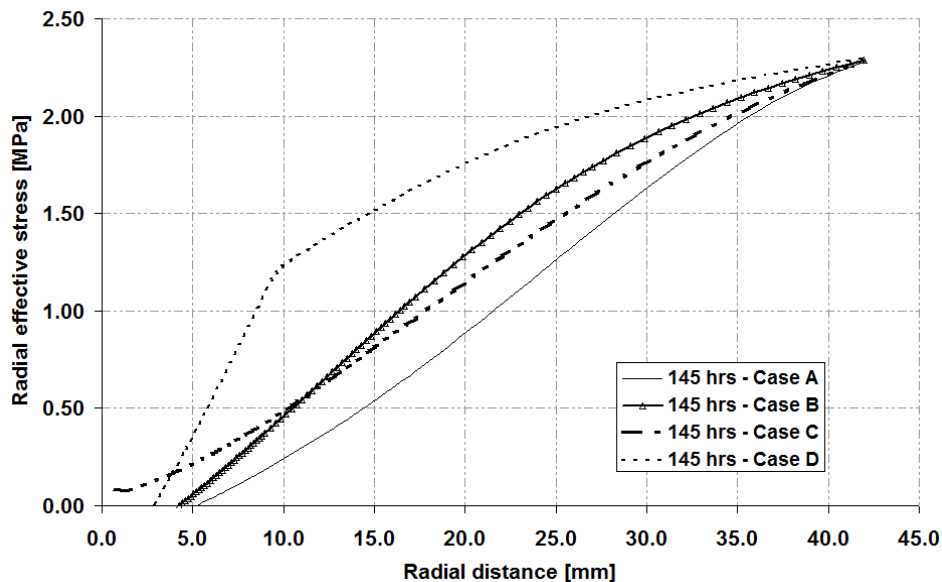


Figure 47: Radial effective stress in function of radial distance for the four cases

### *Orthoradial effective stress*

TIMODAZ

Figure 48 shows the different profiles of orthoradial effective stress in relation with each case. The peak which indicates the transition between plastic (increase of the stress) and elastic (decrease of the stress) behaviour is observed in case A. The orthoradial effective stress does not decrease as a function of the radial distance in the other cases because the plasticity is reached for the whole cylinder.

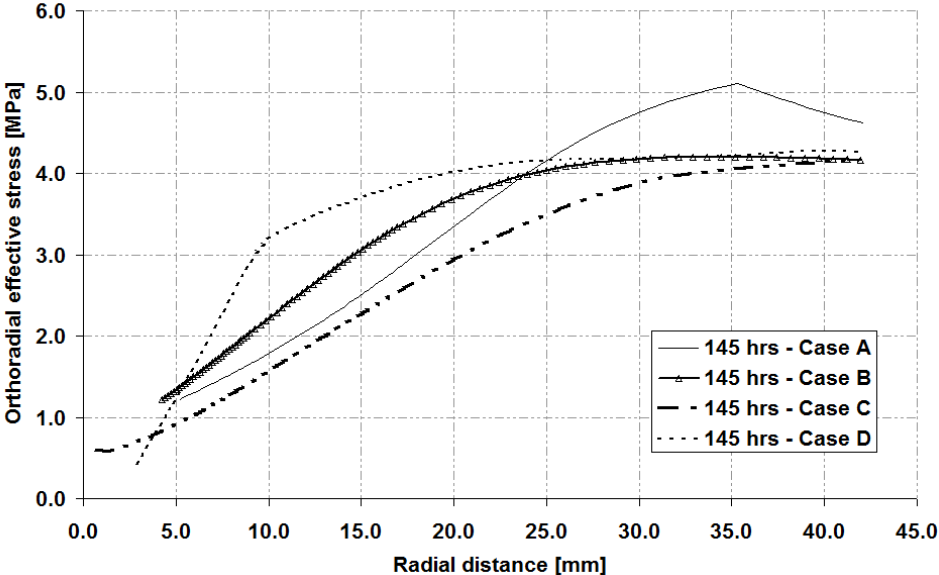


Figure 48: Comparison of orthoradial effective stress for the four cases

*Plastic indicator*

Figure 49 compares profiles of the plastic indicator in the four cases. Case A shows a plastic and elastic zone. Case B is totally plastic. Case D exhibits an elastic unloading and case C is relatively the same as case A but the plastic radius is more important in case A.



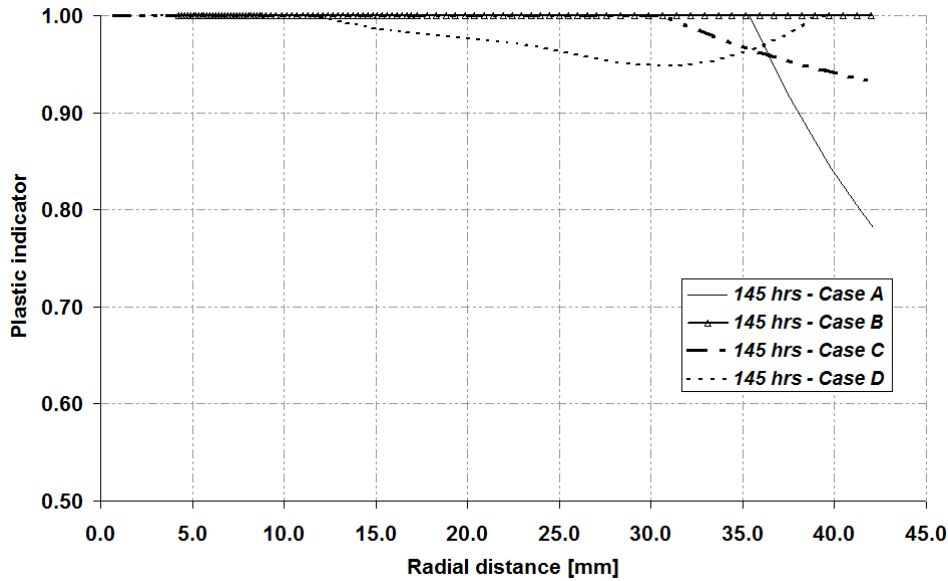


Figure 49: Plastic radius in function of radial distance at 145h for the four cases

### Radial displacement

We can show in Figure 50 the profiles of radial displacement for all cases at 145 hrs. We see that the displacement increases with the successive introductions of hardening and softening processes. In case D we have a final convergence inferior to case C. It can be explained by elastic unloading which happens in case D as we have seen in Figure 49.

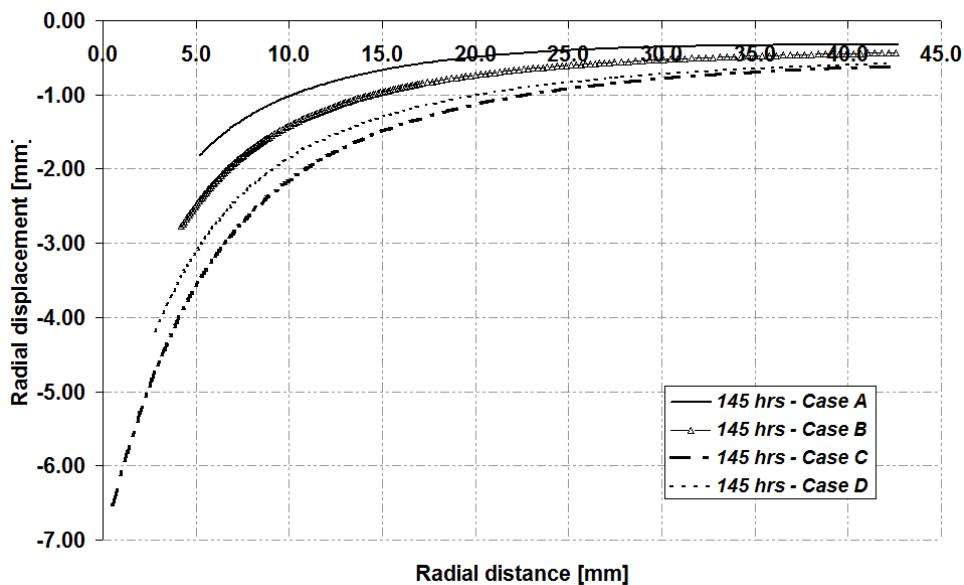


Figure 50: Radial displacement versus radial distance

### Stress path at the inner radius

TIMODAZ



The comparison between stress paths at the inner radius shows the difference between the four mechanical models used for this modelling. These stress paths may be seen in Figure 51.

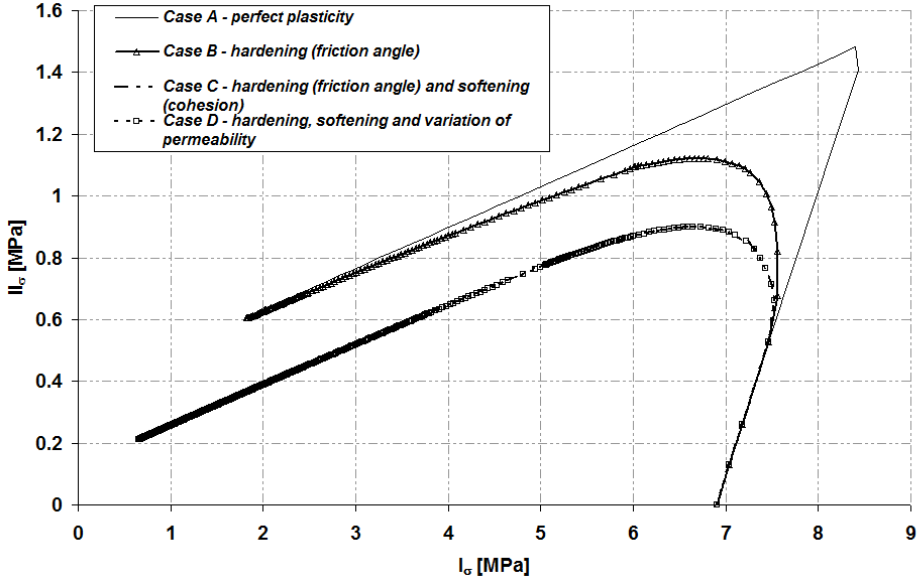


Figure 51: Comparison between stress paths at the inner radius for the four cases

Case A is an elastic perfectly plastic model thus there is no hardening or softening of the yield limit. Case B shows friction angle hardening which is marked by an evolution of the Drucker-Prager yield limit. Case C and D show the same stress path at the inner cavity and illustrate a combined friction angle hardening and cohesion softening model

*Stress path for a point located at 20mm from the inner cavity*

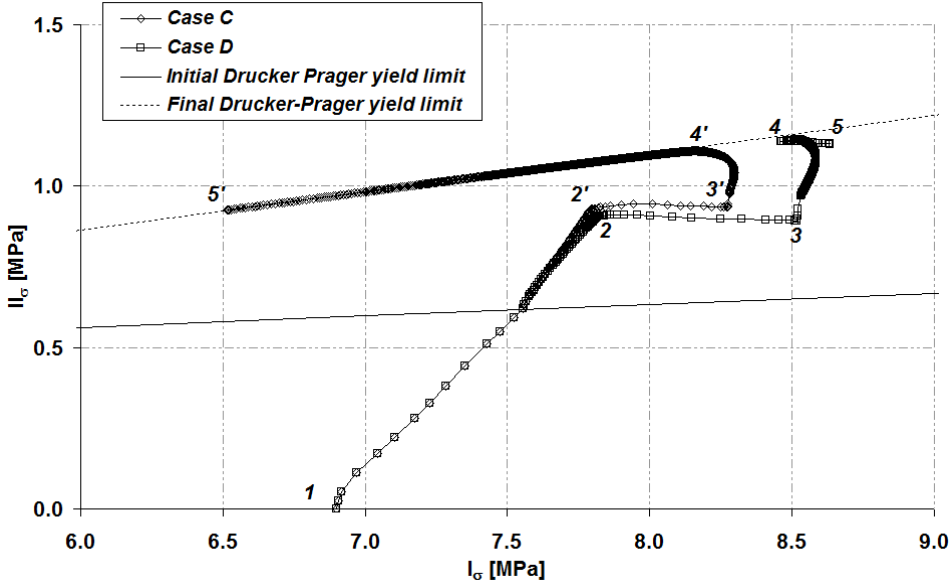


Figure 52: Comparison between stress paths for an element situated at 20mm from the inner radius for case C and case D

TIMODAZ



Figure 52 shows the evolution of stress path for a point which is located at 20 mm from the inner cavity for case C and D. The analysis of these stress paths allows seeing more clearly the different behaviour existing between these two cases. Path 1-2-3-4-5 illustrates stress path in case D and path 1-2'-3'-4'-5' presents stress path in the other case (case C). The point 1 and points 5 and 5' are respectively the beginning and the end of this modelling. The points 2 and 2' and the points 4 and 4' are respectively the end of the first and the second decrease of stresses. The points 3 and 3' represent the end of the first phase (at 73.17 hrs). In case D, an increase of the mean effective stress after point 4 is observed. This rise is due to the decrease of the pore pressure (see Figure 46) with respect to Terzaghi's principle. Thus, the stress state moves away the yield limit (path 4-5) and an elastic unloading appears in this case for this time step. In comparison to case C where the pore pressure increases and thus, the stress state stays plastic during the path 4'-5'.

**Water flux**

Figure 53 shows the different profiles of the water flux as a function of time at the inner radius. This comparison exhibits difference especially during the second phase. A higher level of water flux in case D, where the permeability is depending on porosity, is observed. Case C exhibits the smallest level of water flux. The results from case A and B are close. The difference between the three first cases and the case D is due to the variability of permeability with the porosity. In Figure 41, the permeability increases during the second phase. As a result, an increase of water flux during the second phase in case D is noticed.

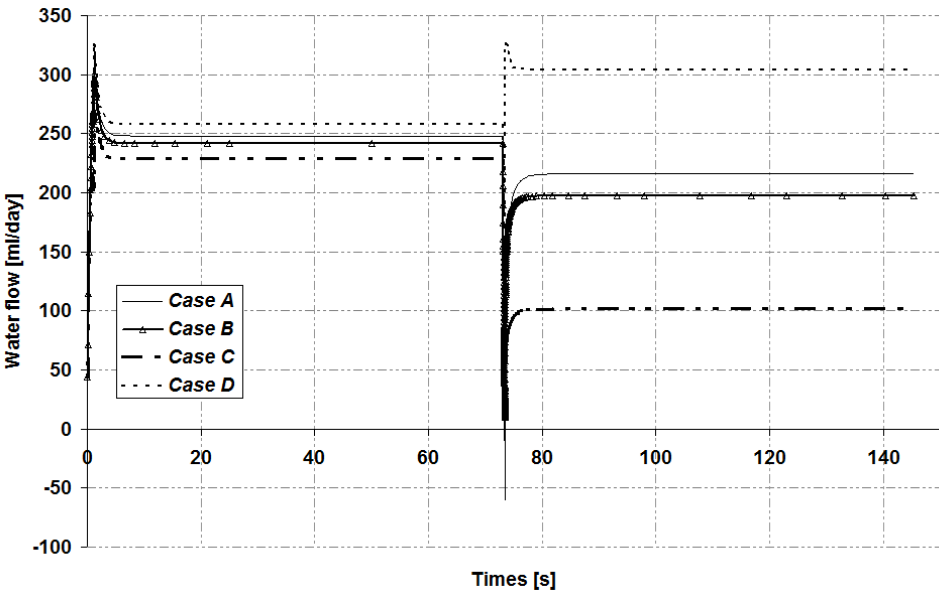


Figure 53: Comparison of water flux in function of times in the four models

**5.2 Results of modelling: thermo-hydro-mechanical aspects**



The first part of this report is dedicated to the hydro-mechanical response of a cylinder to an “excavation”. This section deals with the application of a thermal loading at the surface of the cavity. As the preceding section, the case A will be described in details while the other cases will be summarised.

### 5.2.1 Elastic perfectly plastic model (case A)

#### *Temperature evolution*

The evolution of the profiles of temperature is shown in Figure 54. After excavation (at 145.47 hrs), the temperature increases from 16°C to 70°C in 1 hour at the surface of the cavity. So, at 146.47 hrs, the temperature at the inner radius is equal to 70°C. Then the temperature is maintained constant at the inner radius until 194 hrs. As a consequence, a slight rise in temperature in the whole sample in comparison to the previous profile (at 146.47 hrs) is noticed. Following this stabilisation period, the temperature begins to decrease in three steps. First, temperature decreases down to 26°C in 20 hrs (from 194 hrs to 214 hrs). The second step consists in a reduction of the temperature to 16°C in 86 hrs (from 214 hrs to 300 hrs). Finally, the third step consists of a stabilisation period of 72 hrs which ends the calculation (372 hrs). At 300 hrs and 372 hrs the same profiles of temperature are observed and are equal to the initial value.

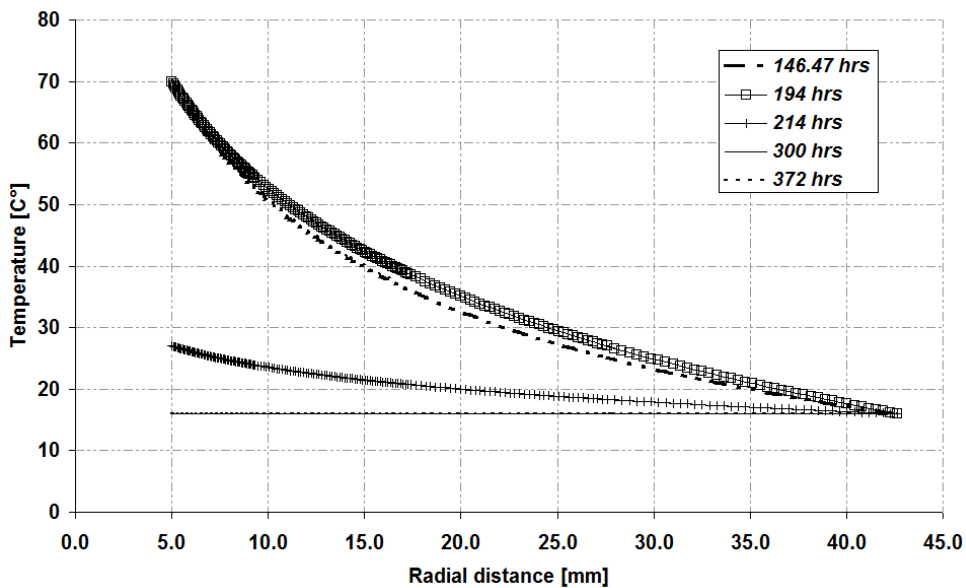


Figure 54: Evolution of the temperature in function of the radial distance for several times

#### *Pore water pressure*

In Figure 55, the evolution of the pore water pressure as a function of the radial distance is presented for the heating/cooling cycle. In the purpose of highlighting the thermo-hydro-mechanical behaviour, only 4 curves are plotted. At 145.47 hrs, the hydro-mechanical part of the experiment is ended. Then, a thermal loading is applied at the inner radius of the cylinder and the

TIMODAZ

temperature increases till to 70°C. So, this rise in temperature induces an increase of pore water pressure (146.47 hrs). This increase is due to the dilation of the water which is characterized by a thermal coefficient expansion greater than for the solid. During the stabilisation phase (from 146.47 hrs to 194 hrs), the pore water decreases due to the dissipation of the pore pressure caused by additional drainage generated by an increase of the permeability of water. During the cooling cycle, an increase of the pore water pressure is observed. Indeed, the diminution of the temperature increases the viscosity. As a consequence, the permeability decreases which induces an increase of the pore pressure. Finally, at the end of the calculation (at 372 hrs), the profile of the pore water pressure is quite similar to the profile at 145.47 hrs which is the beginning of the heating/cooling cycle.

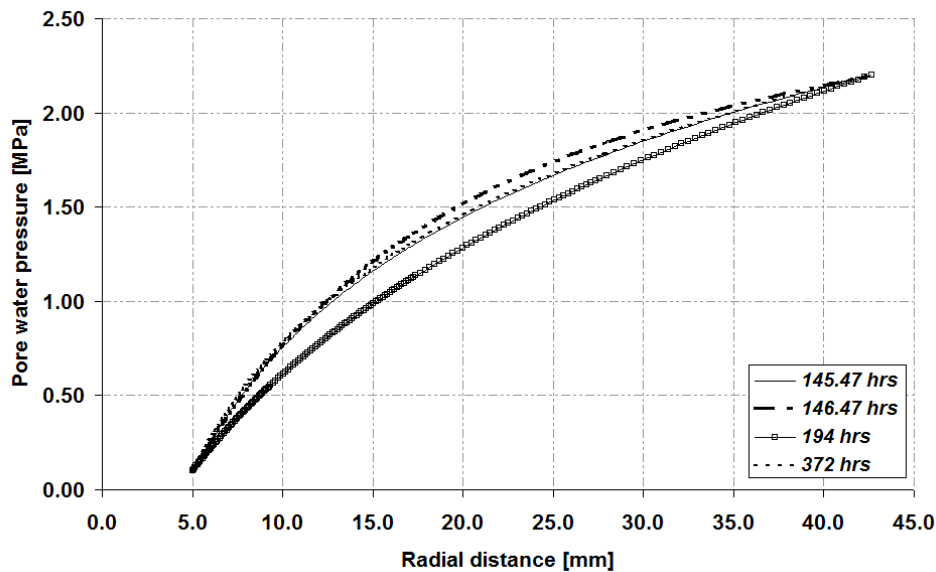


Figure 55 : Evolution of pore water pressure with radial distance in case A

### *Radial effective stress*

Figure 56 presents the evolution of the radial effective stress as a function of the radial distance for several times. The profile at 145.47 hrs, which indicates the end of the excavation phase, is the beginning of the heating/cooling cycle. At the end of the heating phase (at 146.47 hrs), due to the increase of the pore water pressure (see Figure 55) the radial effective stress decreases with respect to the Terzaghi's principle. The profile at 194 hrs representing the end of the stabilisation phase shows an increase of the radial effective stress in the clay sample. This increase is induced by the decrease of the pore water pressure observed in Figure 55. Following this period, cooling begins and the pore water pressure increases. For this reason, the radial effective stress decreases to finally recover the same profile as before thermal loading (372 hrs).

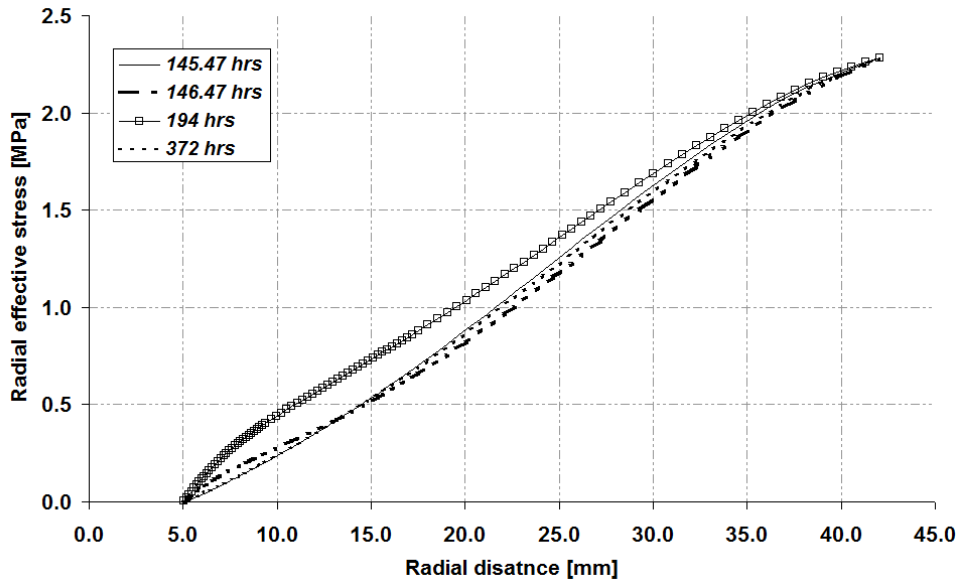


Figure 56: Radial profile of radial effective stress at different times during heating/cooling cycle in case A

### *Orthoradial effective stress*

The same conclusion as previously may be done for the analysis of the profiles of the orthoradial effective stress as a function of the radial distance. The evolution of this stress is plotted in Figure 57. The increase of pore water pressure induced by the thermal loading decreases the orthoradial effective stress (146.47 hrs). Then the drainage appears and the pore water pressure dissipation produces an increase of effective stresses (194 hrs). After this moment, the temperature decreases, the pore water pressure increases and thus, the stresses decrease following the Terzaghi's principle (372 hrs). During this thermal cycle, there is no evolution of the peak indicating the transition between plastic and elastic behaviour.

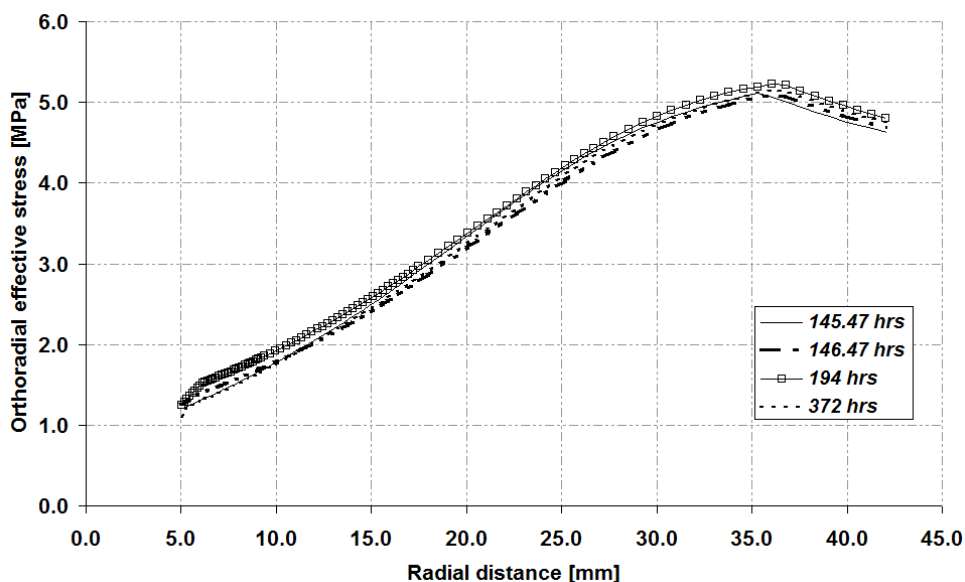


Figure 57: Radial profile of orthoradial effective stress at different periods in case A  
TIMODAZ

### *Axial effective stress*

Figure 58 shows the evolution of the radial profiles of axial effective stress versus the radial distance. The same conclusion than the analyses made previously for the other stresses can be done for the axial effective stress. During the heating phase, the axial effective stress decrease due to the pore water pressure increase (146.47 hrs). When stabilisation occurs, an increase of the stress is generated (194 hrs). During the cooling phase, axial effective stress decreases due to the rise in pore water pressure (372 hrs).

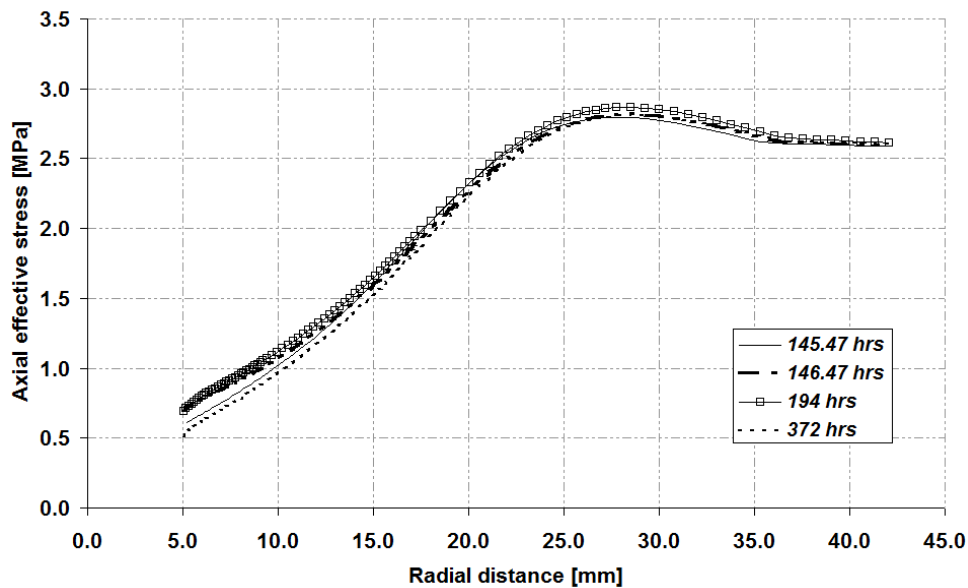


Figure 58: Radial profile of axial effective stress at different times in case A

### *Plastic indicator*

Figure 59 shows the radial profiles of the plastic indicator as a function of time. As compare to the profile obtained at 145.47 hrs (see also Figure 28). An elastic unloading in the sample is observed during heating/cooling phase. The diminution of pore pressure at 194 hrs resulting in drainage increases the effective stresses. As a consequence, plastic indicator at this time exhibits higher elastic unloading than the profiles at other times. During the stabilisation period, the pore pressure increases and, consequently, the stresses decrease. As a result, the plastic indicator increases (372 hrs). At this time, an elastic unloading is observed around the cavity.

TIMODAZ

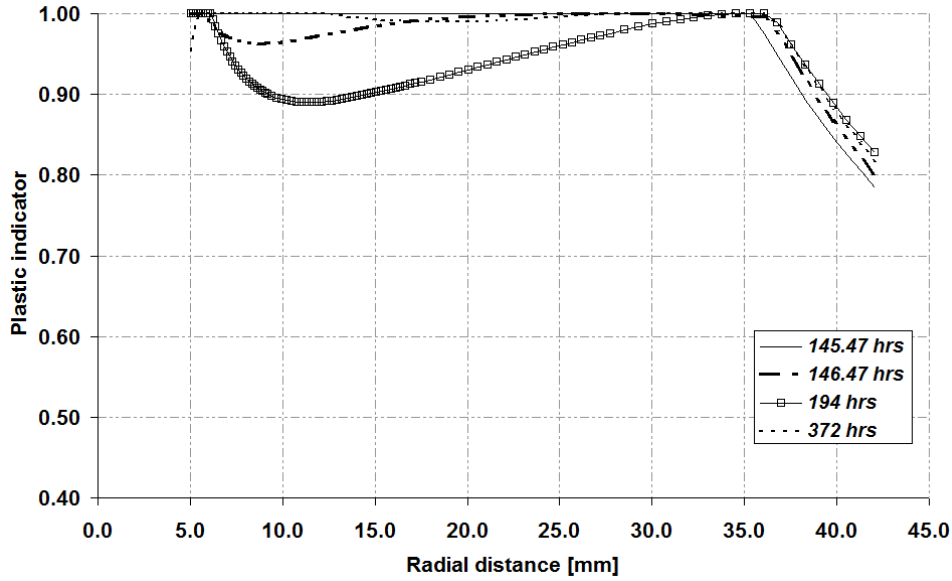


Figure 59: Radial profile of plastic indicator at different times in case A

### Water mass flux

In Figure 60, the evolution of the radial profiles of the water mass flux is plotted at different times. Remember that negative values of the water mass flux mean a flux in direction of the inner radius. First, a decrease of the water mass flux is generated at the end of the heating process (146.47 hrs) which means that an increase of the water mass flux towards the inner radius is induced by the thermal loading. This rise in water mass flux can be explained by the thermal increase of water permeability. During the stabilisation phase (194 hrs), the water mass flux increases. The stabilisation period is characterised by a decrease of the absolute value of the water mass flux to reach at last the same profile before the heating/cooling phase (372 hrs).

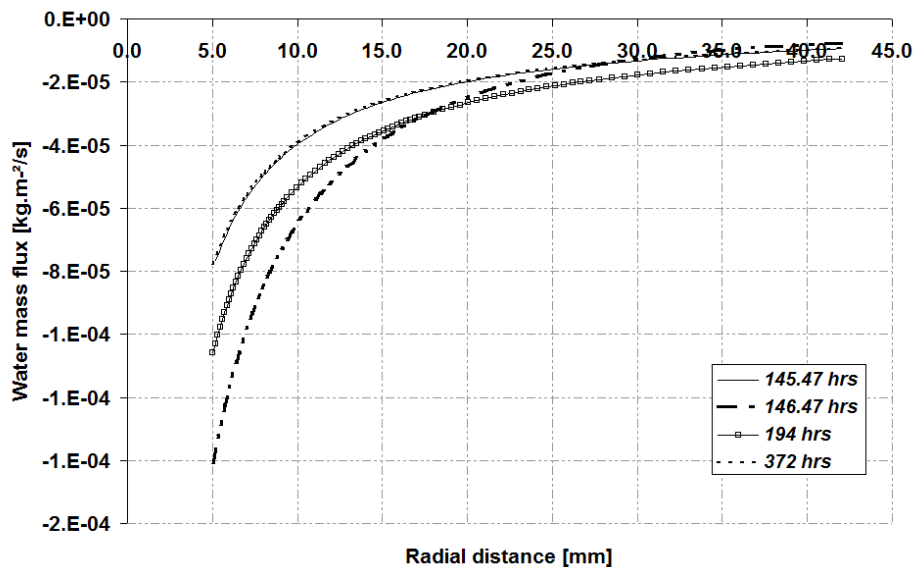


Figure 60: Radial profile of water mass flux at different times in case A

TIMODAZ

## Water flux

The water flux as a function of time is plotted in Figure 61 for the total duration of the modelling. The first part of the curve (till 145.47 hrs) has been explained in Figure 30. The rise in temperature induces an increase of the flux thank to a decreased viscosity. During the heating phase, a transient state is observed. This state is characterised with a peak at 146.47 hrs and a decrease of the flux to attain a constant level and, thus, a stationary state during the stabilisation period. Around 194 hrs, the water flow decreases with the slow decrease of the temperature to reach finally the value before the heating/cooling cycle. When the stationary state is attained, the inner and the external flux are equal.

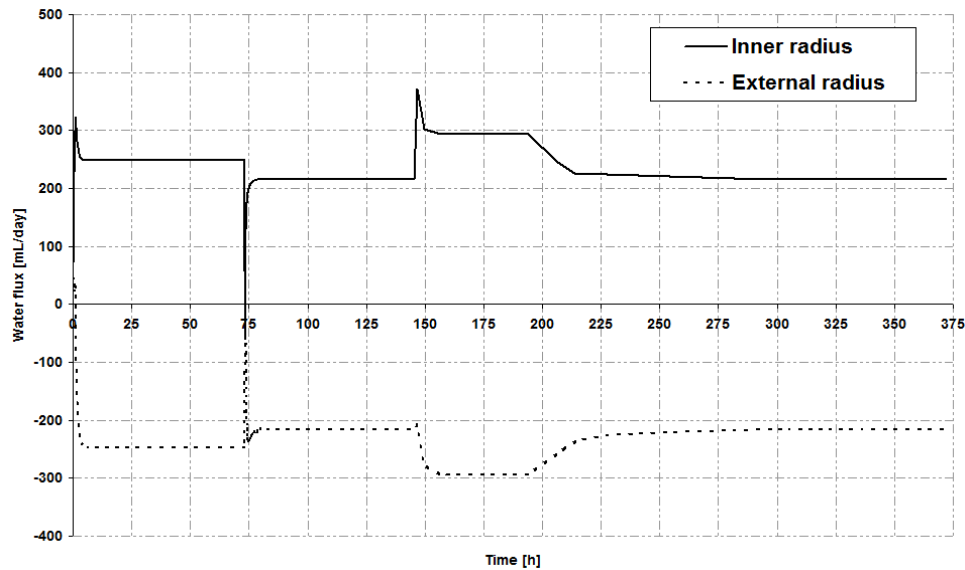


Figure 61: Water flux evolution at the internal and external radius during the total duration of the modelling in case A

## Radial displacement

Figure 62 presents the evolution of the radial profiles of the radial displacement as a function of time. A very slight increase of the convergence is observed with the temperature during the heating/cooling cycle. Then, the final value of the radial displacement is equal to 1.98 mm as compare to 1.83 mm obtained at the end of the first phase which was only due to hydro-mechanical effect (profile at 145.47 hrs).

TIMODAZ

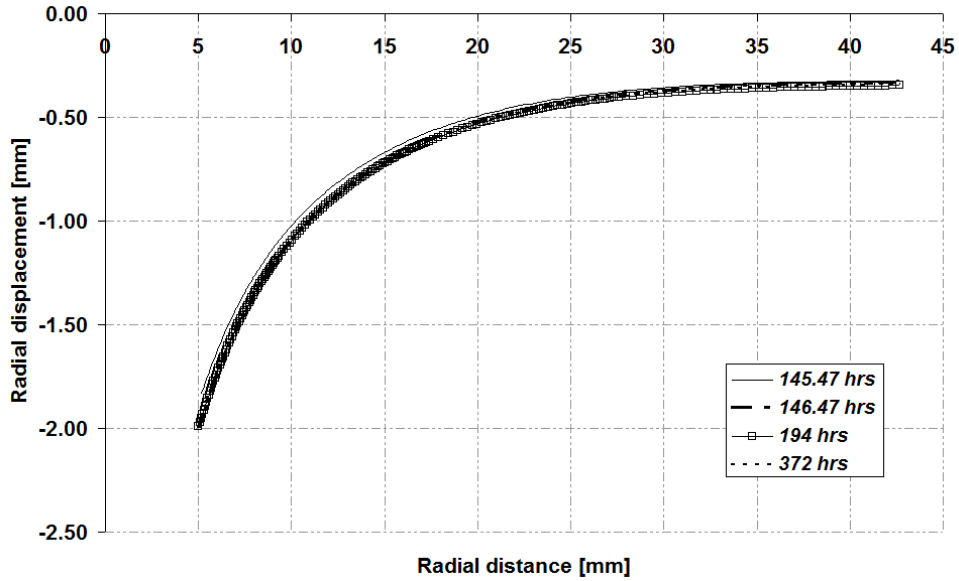


Figure 62: Radial displacement versus radial distance in case A

### Stress path at inner radius

The influence of the temperature on the stress path is shown in Figure 63. The variation of the deviatoric and the mean effective stress are very limited with this thermal cycle. This variation is much localised and the temperature induces an elastic unloading of the stress state.

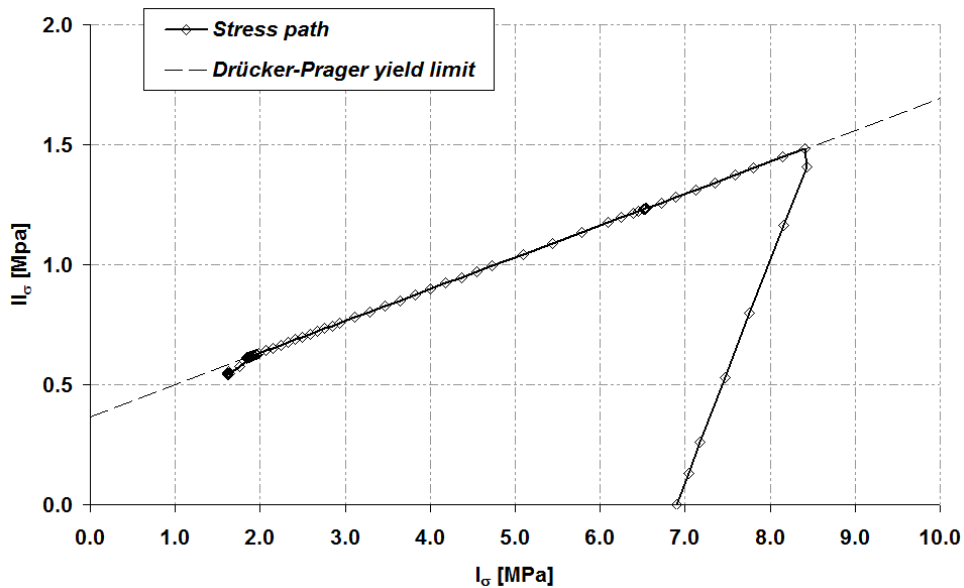


Figure 63: Effective stress path at inner radius in case A

In the purpose of underline the thermal effect on the stress path, a zoom of the Figure 63 is plotted in Figure 64. The rise in temperature induces an increase of the mean and deviatoric stress in respect with the Drucker-Prager criterion. Indeed, stress path stays on the yield limit during the heating phase. Only slight variation of the state stress is observed during the

TIMODAZ

stabilisation period (from 146.47 hrs to 194 hrs) and the state stress stays plastic. Following this stabilisation period, the temperature begins to decrease which induces elastic unloading at the surface of the cavity. This elastic unloading has a tendency to disappear with the stabilisation period and the stress path turns toward the yield limit.

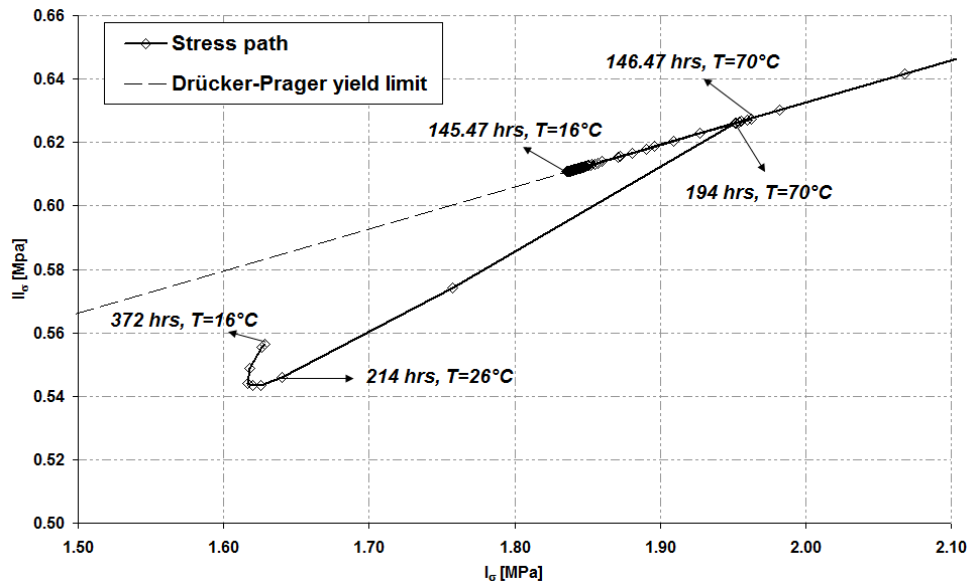


Figure 64: Zoom on the effective stress path in order to underline the thermal loading effect

## 5.2.2 Friction angle hardening elastoplastic model (case B)

In this section, the results obtained with an elastoplastic constitutive law with friction angle hardening will be briefly described. Indeed, the thermal loading has the same effect in all cases thus it is not necessary to describe in details all the results as it has been made in case A.

### *Pore water pressure*

In Figure 65, the distribution of the pore water pressure as a function of the radial distance is shown. So, 145.47 hrs indicates the end of the excavation phase and the beginning of the thermal cycle. At 146.47 hrs, the rise in temperature induces an increase of the pore water pressure. Then, the temperature is maintained constant and the pore water pressures are dissipated thank to drainage (194 hrs). Following this stabilisation phase, the cooling phase begins and the pore water pressure increases in the medium to reach the initial profile at last. This increase of pore water pressure is due to the diminution of the permeability with the decrease of the temperature. Consequently, the soil system has a lower capacity of drainage which induces a rise in pore pressure.

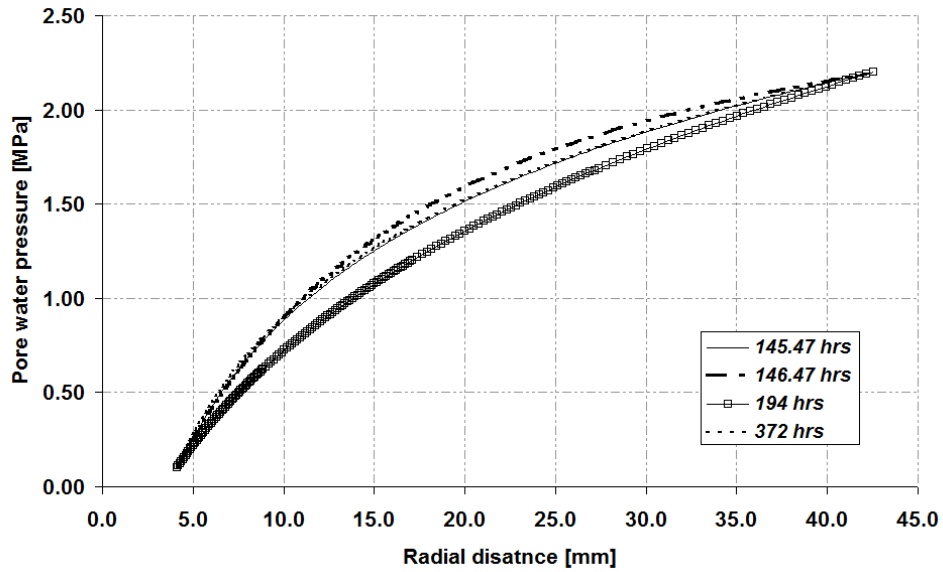


Figure 65 : Pore water pressure in function of radial distance in case B during heating/cooling cycle

### Stress path

The stress path in this case is shown in Figure 66. As the preceding case, the thermal effect is localised and it is not very important in comparison to the hydro-mechanical effect. An elastic unloading is observed during the heating/cooling cycle as mentioned before in case A.

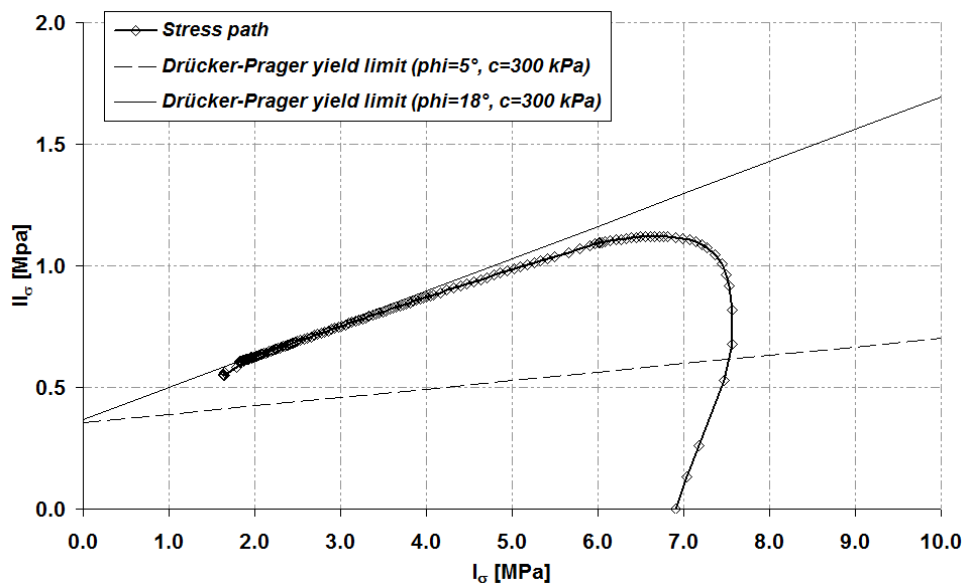


Figure 66: Stress path at the inner cavity in case B for a friction angle hardening model

### Radial displacement

In Figure 67, the evolution of the radial displacement as a function of the radial distance is presented for different times. As previously in case A, a slight increase of the convergence is induced during the thermal cycle that is reversible upon cooling. The final value of the radial distance is equal to 2.89mm.

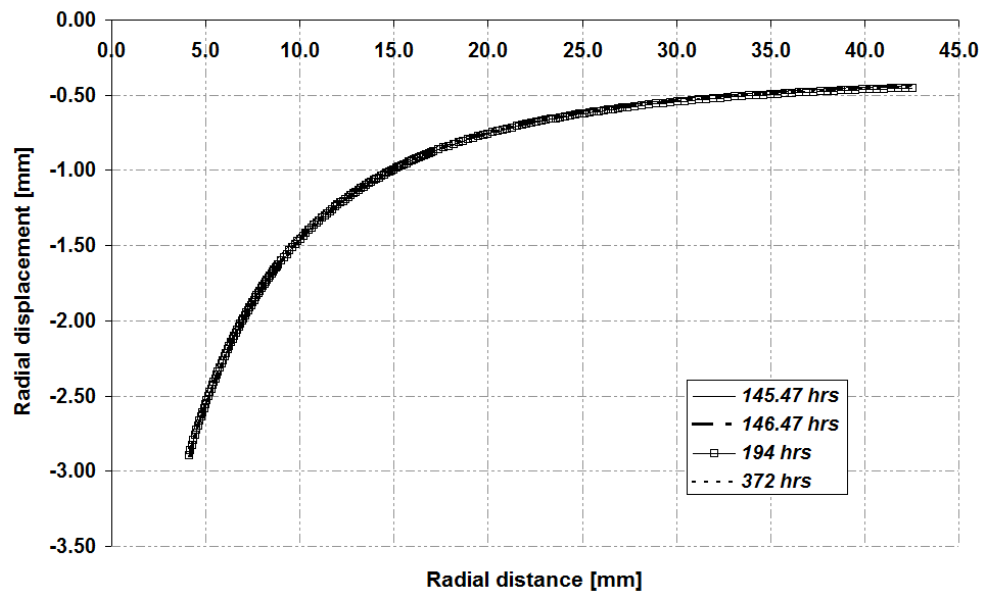


Figure 67: Radial displacement versus radial distance in case B

### Plastic indicator

Figure 68 presents the radial profile of the plastic indicator for various times. At 145.47 hrs, at the end of the excavation phase, plastic indicator is equal to 1 in the whole sample. An elastic unloading in the vicinity of the cavity is induced at the end of the heating phase (146.47 hrs). During the stabilisation phase, the pore water pressure decreases thus the mean effective stress increases and elastic unloading more important than at 146.47 hrs is observed. The cooling phase induces a rise in pore pressure and a decrease of the mean effective stress decreases. Thus the stress state tends to the yield limit and the plastic indicator tends to 1 at 372 hrs.

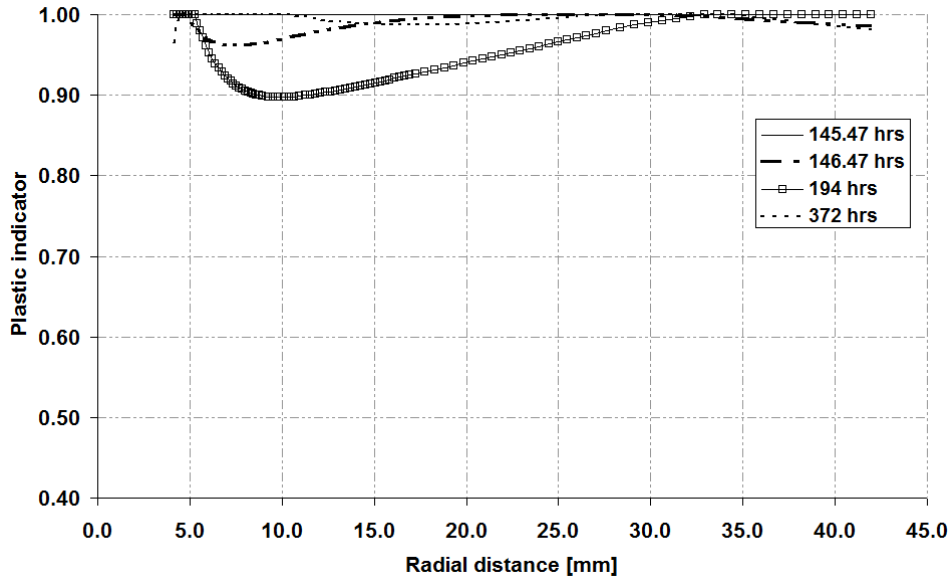


Figure 68: Evolution of plastic indicator with radial distance (case B)

### 5.2.3 Combined angle friction hardening and cohesion softening model (case C)

This part deals with a combined angle friction and cohesion softening elastoplastic model. Only a few results will be discussed as the preceding case.

#### *Pore water pressure*

The conclusions observed previously for the analysis of the pore water pressure can be done in Figure 69. This figure represents the evolution of the pore water pressure in function of the radial distance. At 146.47 hrs, the pore water pressure increases thank to the heating phase. At 194 hrs, the profile exhibits a decrease of the pore pressure caused by thermal consolidation. As a result of the cooling process, the pore water pressure increases (372 hrs).

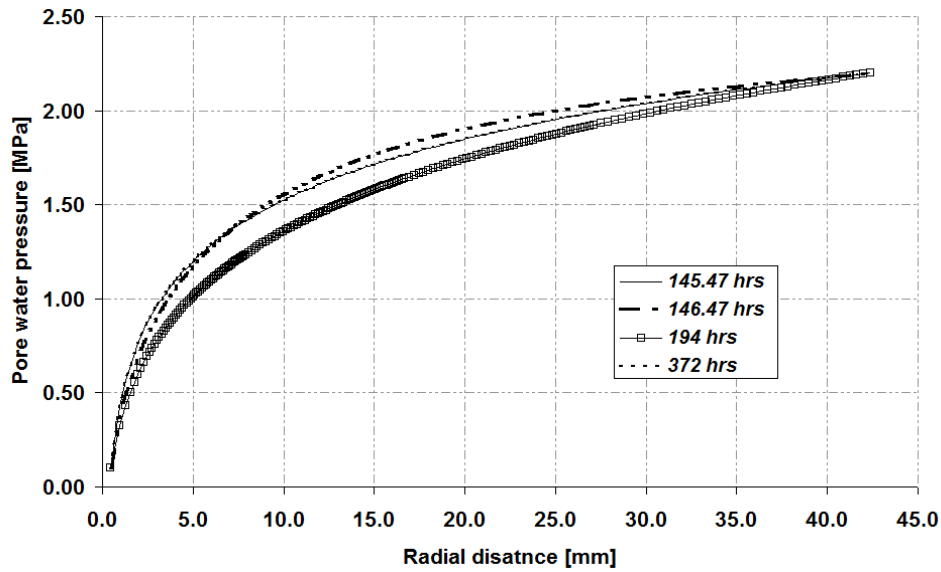


Figure 69: Evolution of pore water pressure with radial distance in case C

### Stress path

The stress path at the inner radius for this mechanical model is plotted in Figure 70. For this model, the temperature induces very slight variation of the stress state. At the end of the calculation, the stress path is on the yield limit.

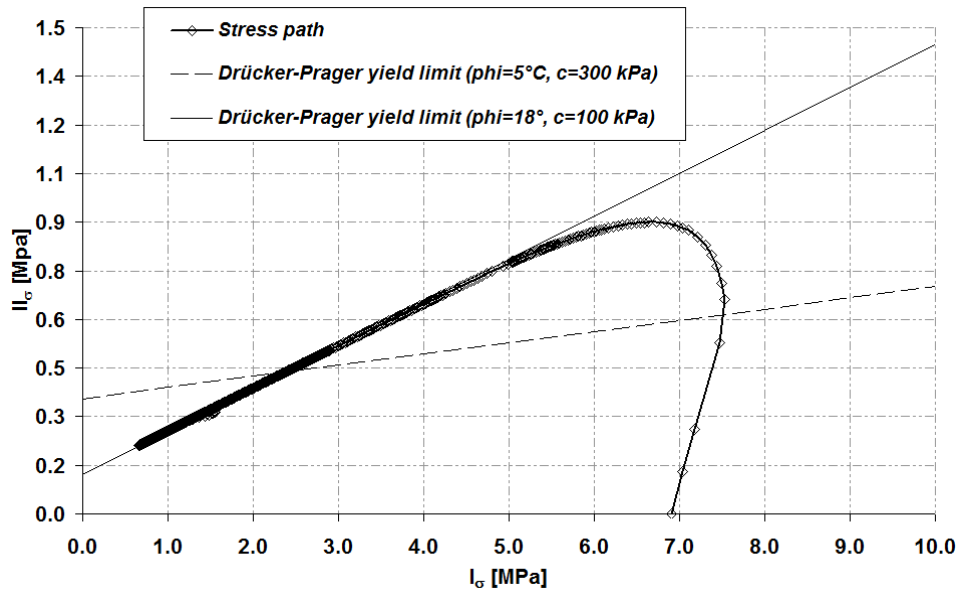


Figure 70: Stress path with a combined hardening friction angle and a softening cohesion model in case C

### Radial displacement

Figure 71 illustrates the evolution of the radial displacements as a function of the radial distance at different time steps. At the end of the excavation phase, the convergence is very high and is

TIMODAZ

equal to 6.54 mm. Consequently, there is no new additional significant displacement during the heating/cooling phase and profiles of the evolution of the radial displacement are same as at the end of the hydro-mechanical part.

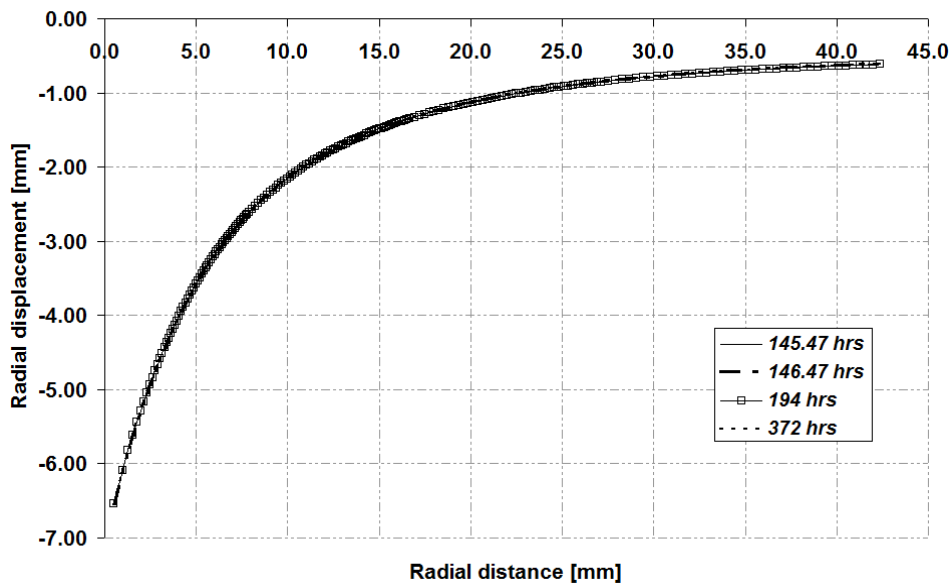


Figure 71: Radial displacement versus radial distance in case C

### Plastic indicator

The plastic indicator as a function of the radial distance is plotted in Figure 72. At 145 hrs, the stress state is plastic in the whole sample and the plastic indicator is equal to 1. At the end of the heating phase (146.47 hrs), an elastic unloading occurs around the inner radius. At 194 hrs which is the end of the stabilisation phase, a major part of the sample has a plastic indicator lower than 1. It can be explained by the decrease in pore water pressure which increases the stresses. During cooling process, the plastic indicator increases in the sample. At last, an elastic unloading is observed in the middle of the sample and stress state is plastic around the cavity.

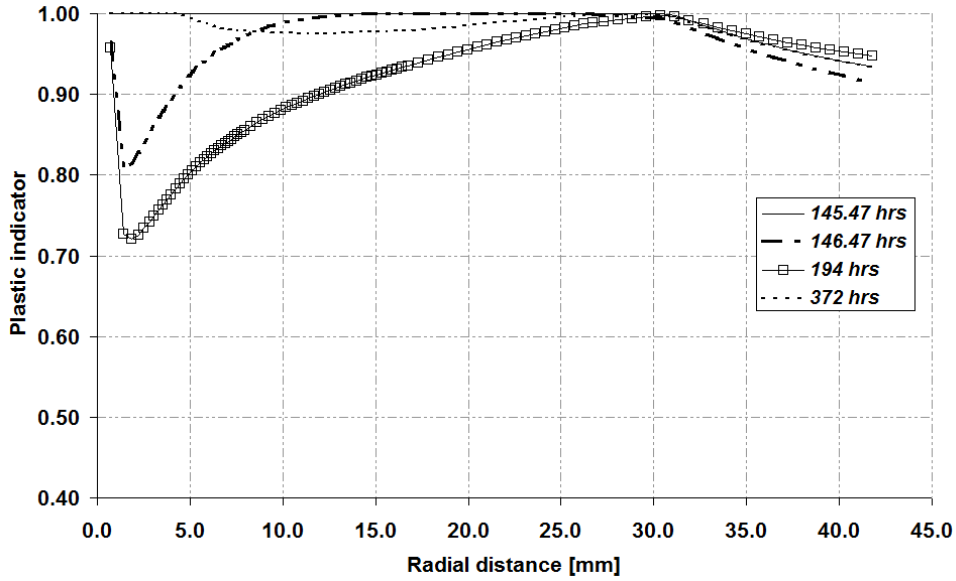


Figure 72: Evolution of plastic indicator with radial distance in case C

### 5.2.4 Combined angle friction hardening and cohesion softening model with permeability as a function of porosity (case D)

#### *Intrinsic permeability*

The intrinsic permeability versus the radial distance is plotted in Figure 73. In this case, the intrinsic permeability is considered as a function of the porosity. The temperature does not affect significantly the porosity and, as a result, the intrinsic permeability does not change during the heating/cooling cycle.

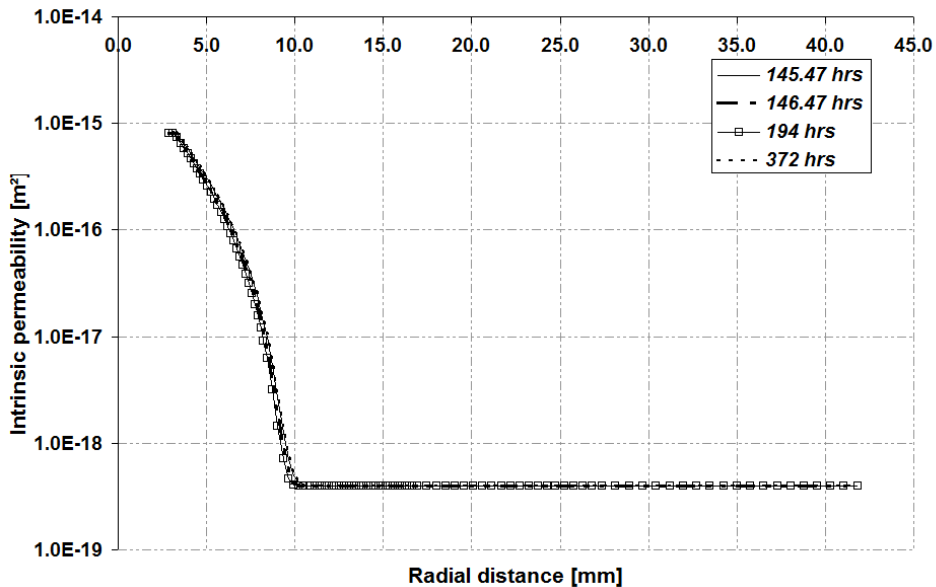


Figure 73: Evolution of intrinsic permeability with radial distance



### *Pore water pressure*

Figure 74 illustrates the evolution of the pore pressure versus the radial distance at different times. The same conclusion as the other cases can be done. Indeed, pore pressure increases with a rise in temperature (146.47 hrs). During the stabilisation phase, the pore pressure decreases as a consequence of the thermal consolidation (194 hrs). Finally, the pore water pressure increases during the cooling phase (372 hrs).

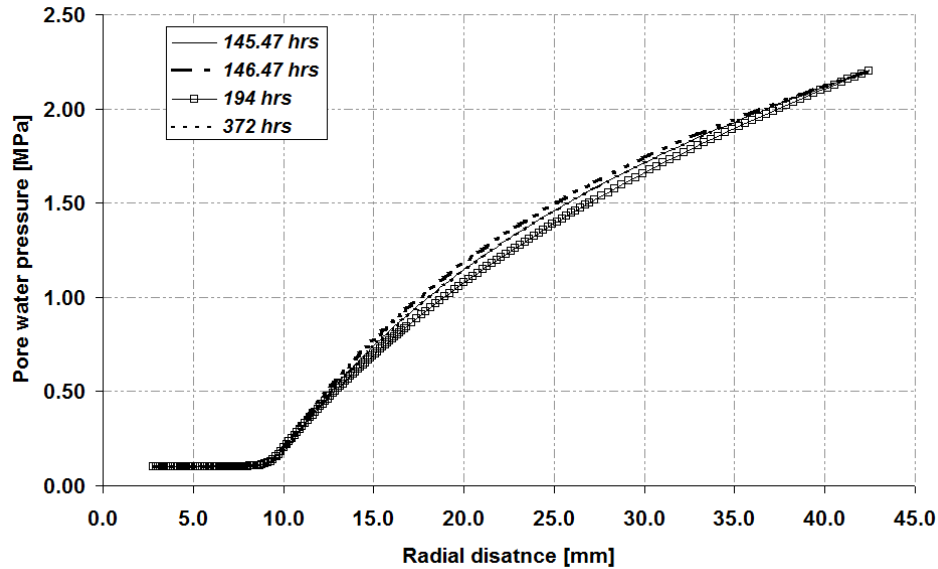


Figure 74 : Evolution of pore water pressure with radial distance in case D

### *Stress path*

The stress path at the inner radius for this case is plotted in Figure 75. The effect of the temperature is similar to the case C. At the end of the modelling, the stress state stays on the yield limit.

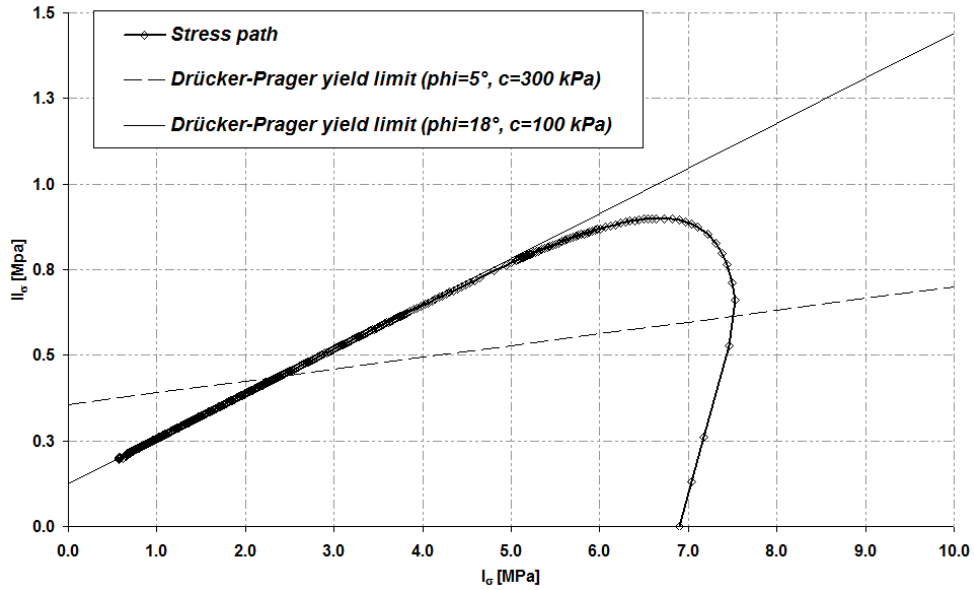


Figure 75: Stress path at inner radius with permeability in function of porosity and a combined friction angle hardening and cohesion softening model.

### *Radial displacement*

The radial displacement as function of the radial distance is illustrated in Figure 76. The effect of the temperature is negligible in this case. Indeed, there is no evolution of the convergence with the heating/cooling cycle.

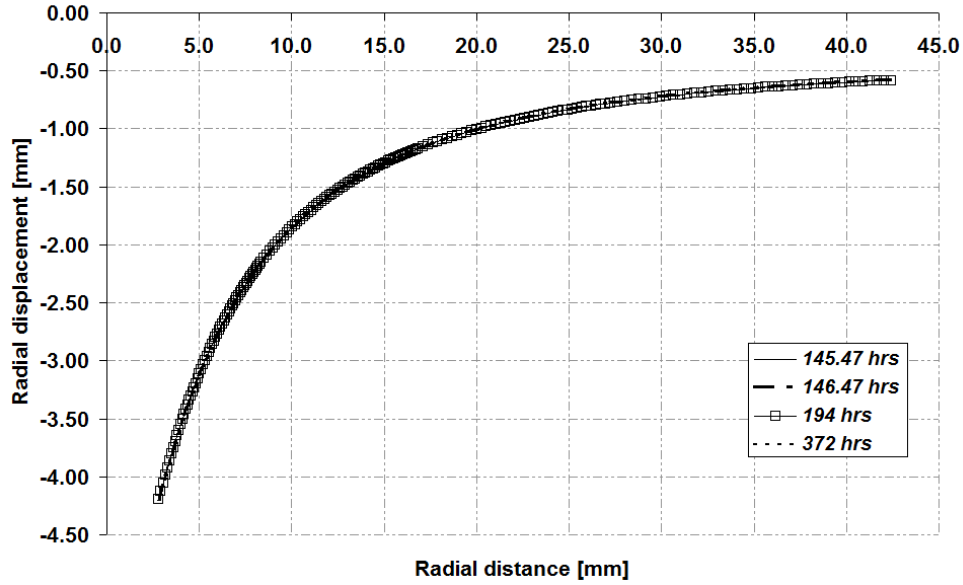


Figure 76: Radial displacement versus radial distance in case D

### Plastic indicator

In Figure 77, we can see the evolution of the plastic indicator during the heating/cooling cycle. At the end of the hydro-mechanical part (at 145.47 hrs), an elastic unloading occurs as compared to case C (see Figure 72). During the heating/cooling phase, only slight variation of the plastic indicator occurs and the global behaviour is the same during this cycle.

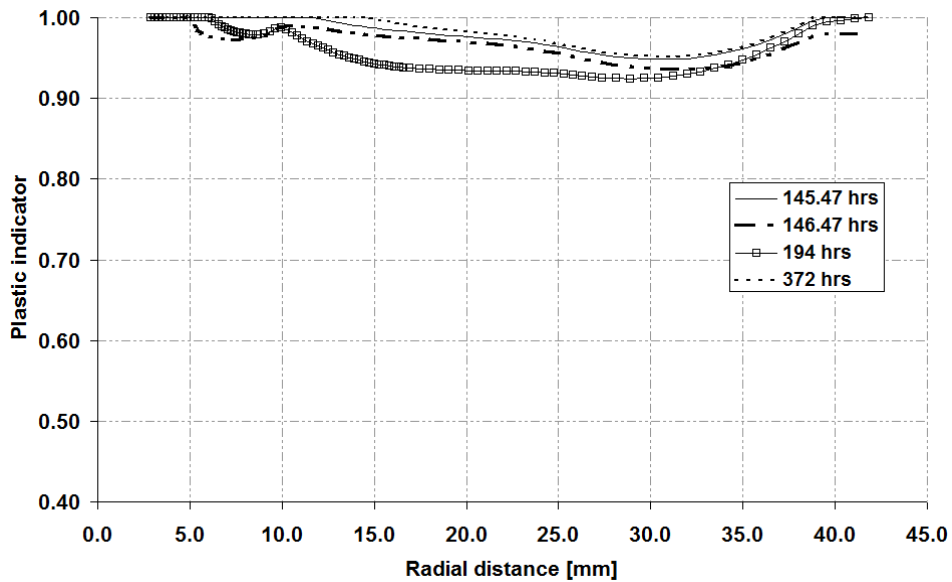


Figure 77: Plastic indicator with radial distance in case D

## 5.2.5 Comparison between the four cases

The effect of the temperature is not very different between the different cases. The effect of the temperature may be summarised like this:

- A pore water pressure increase is induced by heating.
- A dissipation of the pore pressure occurs due to drainage during the stabilisation phase.
- Finally, the pore pressure increases during the cooling phase.

The main difference observed for the four cases between the hydro-mechanical and the thermo-hydro-mechanical modelling can be found in the representation of the stress path and the representation of the plastic indicator.

### *Plastic indicator*

Figure 78 illustrates the plastic indicator for the four models at the end of the thermo-hydro-mechanical modelling. As compare to what happens at the end of the hydro-mechanical modelling (see Figure 49), we observe some elastic unloading around the cavity for case A and case B.

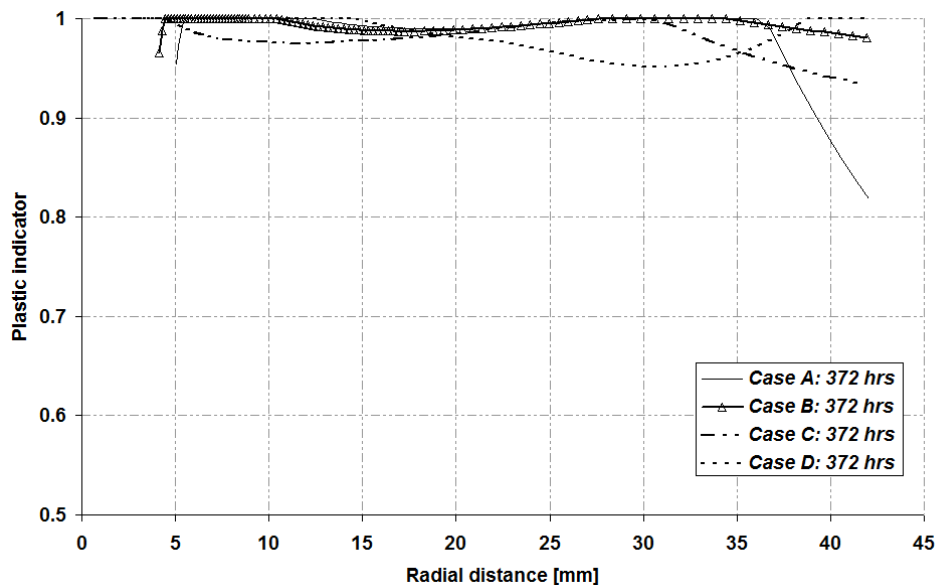


Figure 78: Plastic radius in function of radial distance at 372h for the four cases

### *Stress path at the inner radius*

Figure 79 shows stress path for the four cases treated in this modelling. In all cases, heating/cooling cycle does not affect significantly the stress path. In case A and in case B, stress state becomes elastic at the end of the modelling. For case C and case D stress state stay plastic.

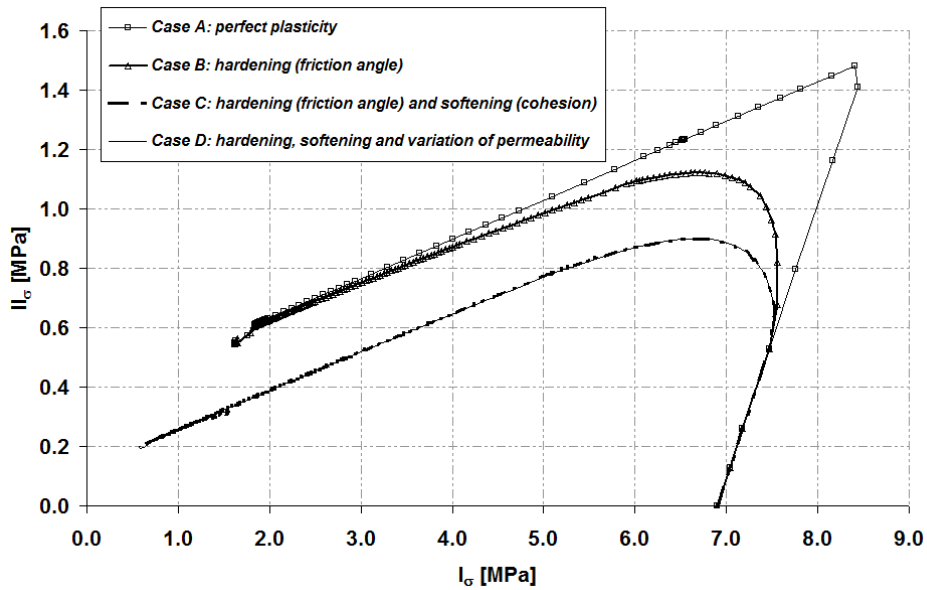


Figure 79: Comparison between stress paths at the inner radius for the four cases

## 6 Comparison of all results

This section deals with a comparison between the teams who have realised this benchmark that is to say: EPFL, EURIDICE, ULg, UJF and UPC. EPFL, UJF and ULg have used the finite element code LAGAMINE developed at ULg while UPC and EURIDICE used code BRIGHT. The comparisons will be presented following the hydro-mechanical part and then with the thermo-hydro-mechanical parts. Table 9 summarizes which modelling have been realised by each team in the hydro-mechanical part of this benchmark. For this part, each team has realised the same calculations. From a general point of view, we will see that the results of the different teams converge to the same solution.

Hydro-mechanical part	Case A	Case B	Case C	Case D
EURIDICE	X	X	X	X
EPFL	X	X	X	X
UJF	X	X	X	X
ULg	X	X	X	X
UPC	X	X	X	X

Table 9: Modelling realised by each team for the hydro-mechanical part of the benchmark

Concerning the thermo-hydro-mechanical part, each team has realised the case A and an other case which was free. Table 10 presents what the different teams have done. For the free case, EPFL realised a calculation with the ACMEG-T law. EURIDICE has made a case which was a

combination of the friction angle hardening with the variation of the permeability with the porosity (Case E).

Thermo-hydro-mechanical part	Case A	Case B	Case C	Case D	Case E	ACMEG-T
EPFL	X					X
EURIDICE	X				X	
UJF	X		X			
ULg	X	X	X	X	X	
UPC	X	X	X	X		

Table 10: Modelling realised by each team for the thermo-hydro-mechanical part of the benchmark

## 6.1 Comparisons for the hydro-mechanical part

In this paragraph, comparisons between all teams are presented. This comparison concerns the hydro-mechanical part of the calculation. As mentioned previously, the results are very similar, thus only a few figures will be presented in order to illustrate our discussion.

Figure 80 presents the radial evolution of the pore water pressure during the hydro-mechanical part for the different teams. These profiles are linked with the case A. We show that the results are very close. This observation is extended to all the considered cases.

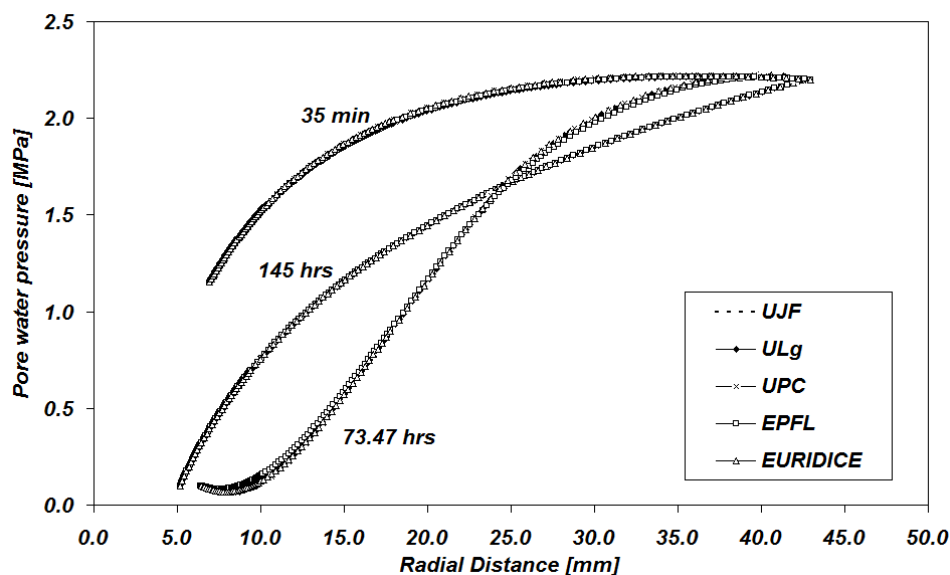


Figure 80: Comparisons of the radial evolution of the pore water pressure for all teams. Comparisons realised for the hydro-mechanical part

Another example of this similarity may be observed in Figure 81 which shows the stress path for a point located at the inner cavity. All the teams have the same results.

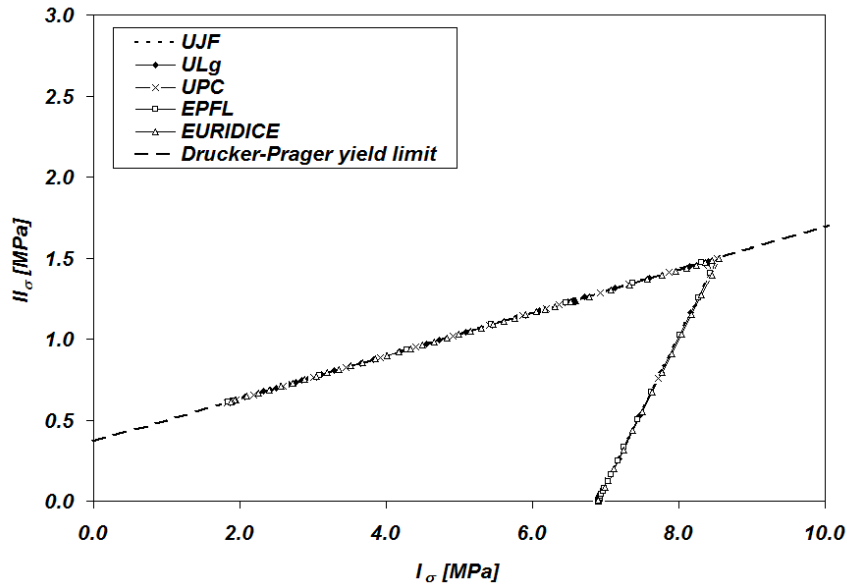


Figure 81: Comparisons of the stress paths for all teams for case A

## 6.2 Comparisons for the thermo-hydro-mechanical part

Concerning the thermo-hydro-mechanical part, some differences appear between the different teams. As the previous paragraph, the results are very similar between all teams except for UPC. Figure 82 show the radial profile of temperature for all teams at the end of the heating phase. Higher temperatures are obtained for UPC in comparison with the other. The difference is slight.

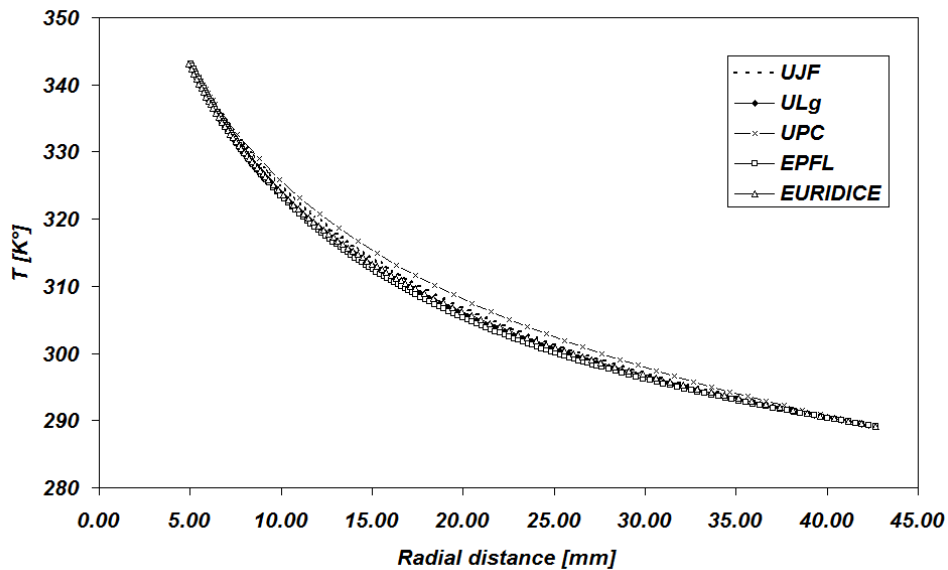


Figure 82: Comparison of the radial profile of temperature for the different teams at the end of the heating phase

TIMODAZ

Figure 83 presents the radial profile of the pore water pressure at the end of the heating phase. As observed previously, a difference appears between UPC and the other teams. Indeed, UPC obtained lower pore water pressure than other teams.

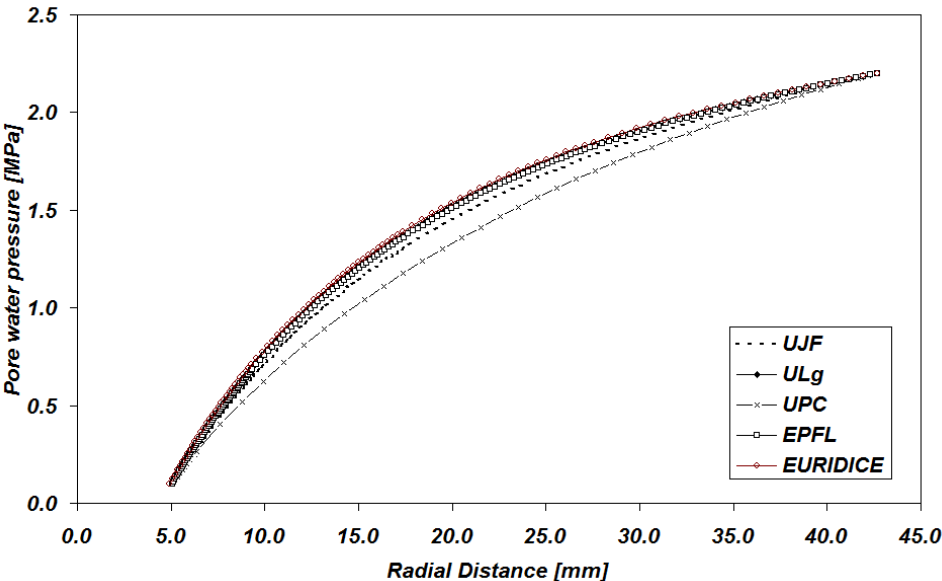


Figure 83: Comparison of the radial profile of pore water pressure for the different teams at the end of the heating phase

At the end of the stabilisation phase, at 194hrs, the results are the same for all teams. Figure 84 presents this comparison.

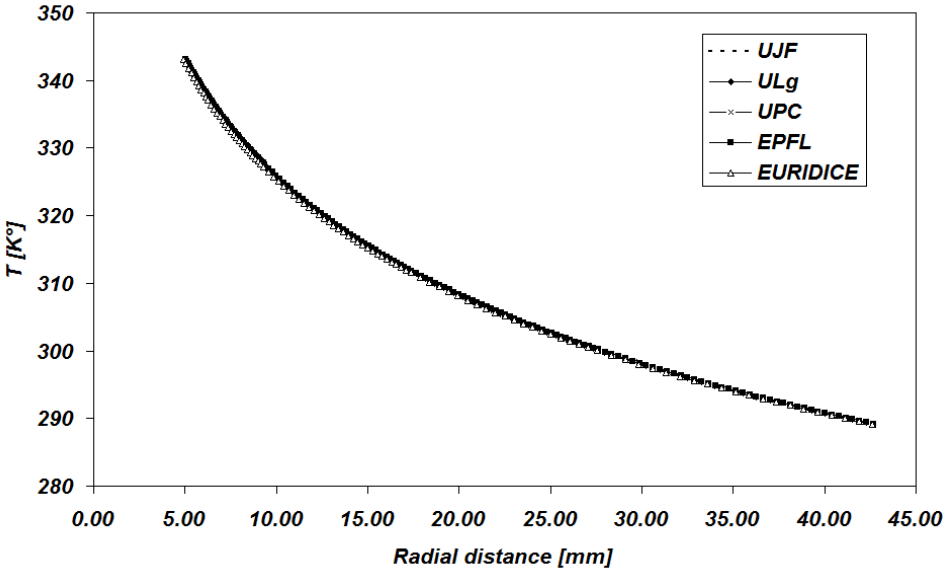


Figure 84: Comparison of the radial profile of temperature for the different teams at the end of the stabilisation phase

In term of pore water pressure, a difference is obtained between UPC and the other teams as seen in Figure 85 which illustrates a comparison of the radial profile of pore water pressure for all



teams at the end of the stabilisation phase. As in Figure 83, lower pore water pressures are obtained for UPC.

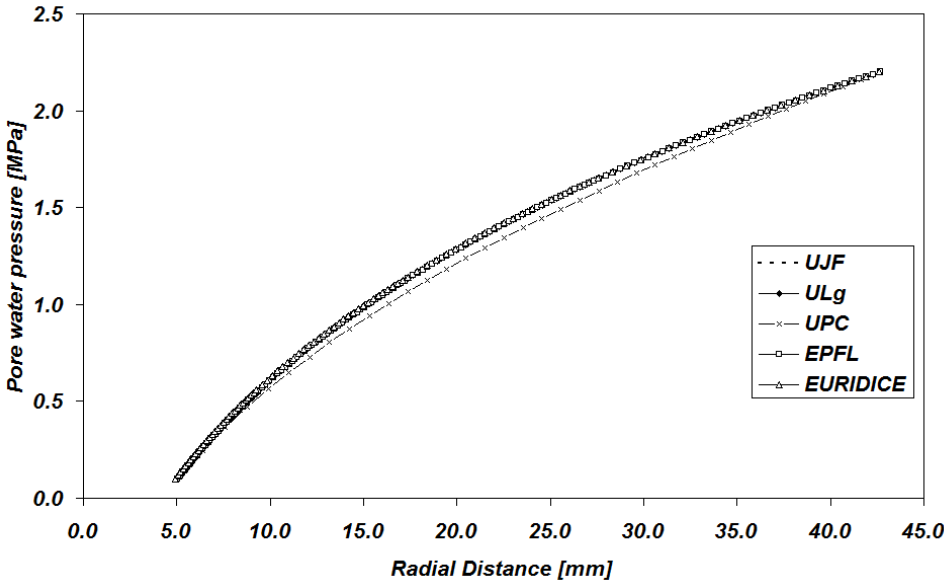


Figure 85: Comparison of the radial profile of pore water pressure for the different teams at the end of the stabilisation phase

On the other side, at the end of the modelling, all results are the same. Figure 86 illustrates this comparison of the radial profile of pore water pressure. We can show that all the teams have the same results.

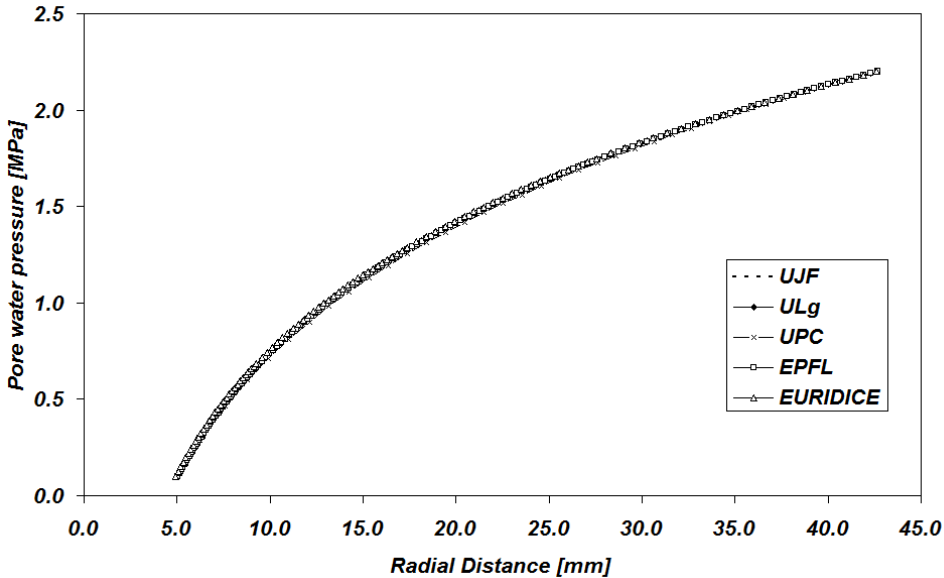


Figure 86: Comparison of the radial profile of pore water pressure for the different teams at the end of the modelling



In conclusion of this part, we have seen that the results obtained by the different teams are very similar for this calculation. The only difference comes from UPC which has a different evolution of the pore water pressure and temperature.

## 7 Additional computations (EPFL)

The Soil Mechanics Laboratory of EPFL performed the benchmark exercise as defined in Section 4, corresponding to the hollow cylinder test on Boom Clay. The problem is treated as a one dimensional process (radial-axisymmetric) that is an idealization of the hollow cylinder sample of a porous isotropic medium. The geometry, the initial conditions and the boundary conditions that have been considered are described in Section 4.

The evolution of the internal boundary conditions (in term of constant total radial stress  $\sigma_r$ , pore water pressure  $p_w$  and temperature  $T$ ) is described in Figure 87. The THM loading can be divided in three main phases. The first phase corresponds to a mechanical unloading along with a dissipation of the pore water pressure. In the second phase, it has been decided to go further with the unloading. So, the radial effective stress in the inner hole is decreased until zero. This phase does not correspond to the experimental procedure but can help in the understanding, in a constitutive point of view, of the induced mechanical damage of Boom Clay. The last phase consists in the thermal phase with a temperature cycle in the inner hole.

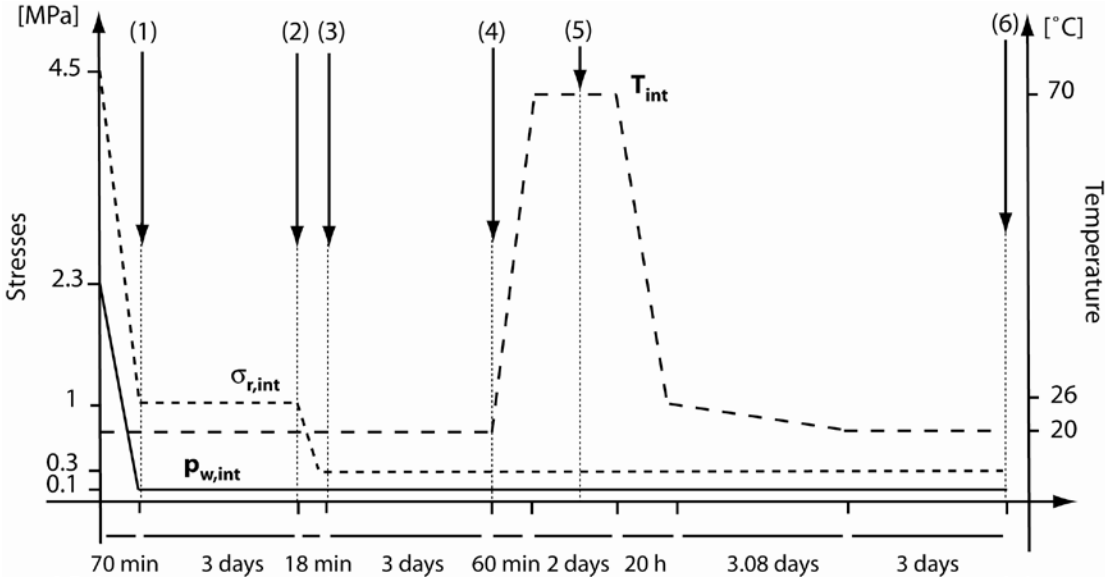


Figure 87: THM loading at the inner radius of the hollow cylinder. The x axis is not to scale. (1) to (6) represent the times when results are reported in Figure 92

### 7.1 Constitutive models and parameters

The main aims of the simulations performed by EPFL were twofold:



- (i) To validate the numerical tools by comparing simulation results with the results obtained by the other modelling teams on a relatively simple constitutive case without considering an advanced rheology of the material.
- (ii) To extend the study to the consideration of additional coupling effects thanks to a more advanced constitutive model.

Because of this double objective, the numerical simulations were performed in two steps. In the first step, each modelling teams used the same quite simple mechanical constitutive model (e.g. a perfectly plastic Drucker-Prager model) imposed in the exercise statement (see Section 4.4, Case A). In the second step, the ACMEG-T thermo-plastic constitutive model was used (see Deliverable 10 for a full description of the constitutive equations). The two steps of simulation were performed with the Lagamine finite element code, using successively the Drucker-Prager model and the ACMEG-T model. The thermo-hydro-mechanical field equations are described in Section 4.4.3.

The parameters governing the hydraulic and thermal diffusive processes as well as the parameters of the Drucker-Prager constitutive model were imposed in the benchmark statement and are reported in Section 4.5. On the contrary, the parameters required for the used of ACMEG-T model have been calibrated from experimental results of Baldi et al. (1991) and are reported in Table 11.

<b>Elastic parameters</b>		
$K_{ref}, G_{ref}, n^e, \beta'_s$	[MPa], [MPa], [-], [°C <sup>-1</sup> ]	130, 130, 0.4, 1.3 10 <sup>-5</sup>
<b>Isotropic plastic parameters</b>		
$\beta, \gamma_T, c, r_{iso}^e$	[-], [-], [-], [-]	18, 0.55, 0.012, 0.001
<b>Deviatoric plastic mechanical parameters</b>		
$b, d, \phi'_0, g, \alpha, a, r_{dev}^e$	[-], [-], [°], [-], [-], [-], [-]	0.6, 1.3, 16, 0.0085, 1, 0.007, 0.3

**Table 11: Set of the Boom Clay thermo-mechanical parameters used for the ACMEG-T model**

## 7.2 Simulation results

### 7.2.1 Calibration tests

In the first part of the benchmark, the calculations have been performed with the perfectly plastic Drucker-Prager model. In the second part of the benchmark exercise, the ACMEG-T model was used. This model considers additional features of the mechanical response of Boom Clay. In particular, the elastic part of the deformation is now governed by non-linear elasticity. Also, the hardening and/or softening irreversible processes are introduced through the evolution of the isotropic and deviatoric yield limit. Then, the progressive mobilization of plasticity inside the external yield limit is considered. Finally, the possible irreversible strain induced by thermal loading is taken into account through the thermo-plasticity. Figure 88 compares the mechanical response of Boom Clay submitted to triaxial compression at two different confining pressures, as experimentally observed by Baldi et al. (1991) and predicted by ACMEG-T and Drucker-Prager

TIMODAZ



models. After a linear elastic part, the Drucker-Prager prediction reaches a plateau in the deviatoric and volumetric plane. On the contrary, the ACMEG-T response shows a very small linear part followed by a progressive hardening process until reaching a plateau characterizing the critical state.

In addition, drained isotropic compression cycles (2; 4; 2; 8; 2; 5 MPa of mean effective stress) on Boom clay samples have been simulated with the set of material parameters of the ACMEG-T model. A comparison between model simulation and TBoom1 experimental results is shown in Figure 89. Also, the volumetric response of Boom Clay submitted to heating-cooling cycles at three different OCRs has been numerically simulated and compared with the results of Baldi et al. (1991) (Figure 90).

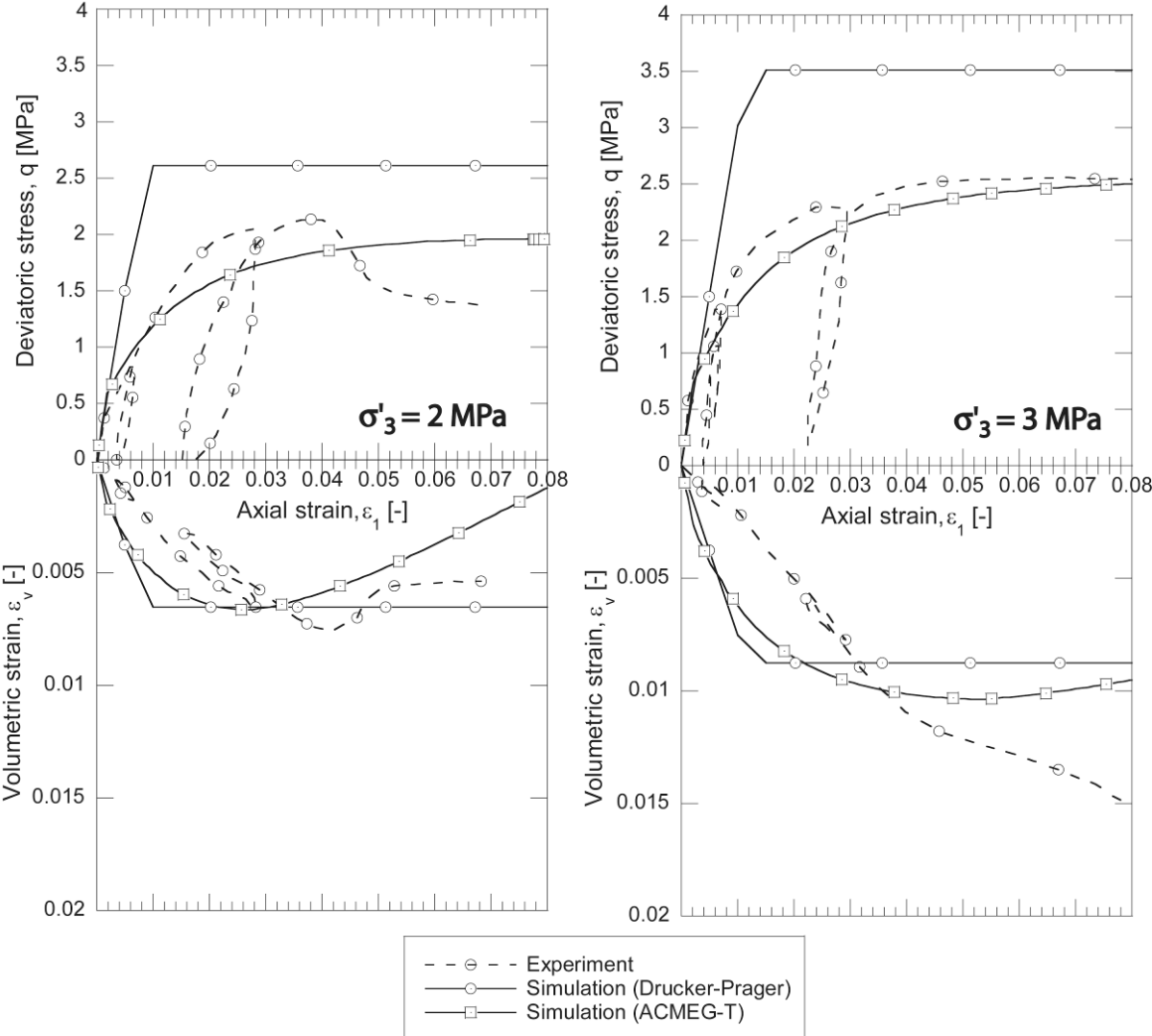


**Figure 88: Validation of the used geomechanical parameters by a simulation of conventional triaxial tests on Boom Clay at two different confining pressures ( $\sigma'_3$ ) and comparison with the experimental results of Baldi et al. (1991)**



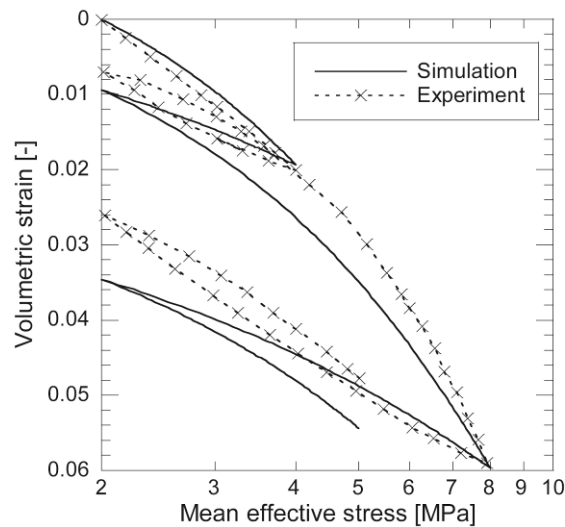


Figure 89: Isotropic compression test (TBoom1 from Baldi et al., 1991): Comparison between numerical simulation with the ACMEG-T model and experimental results

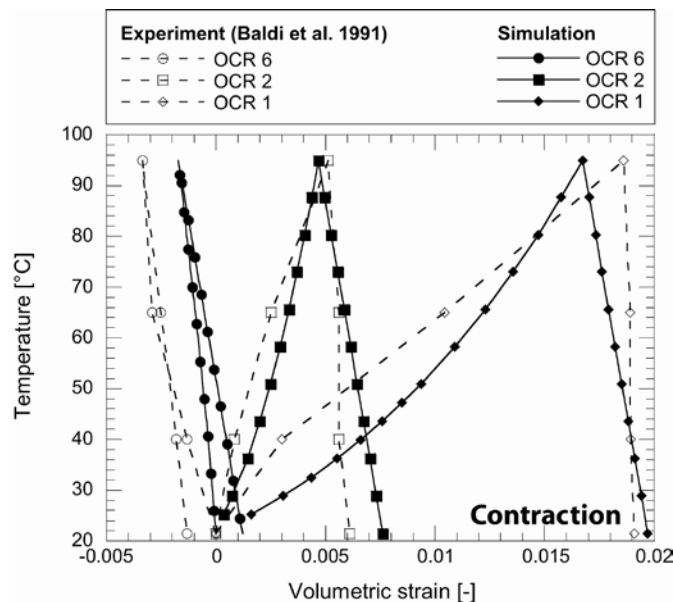


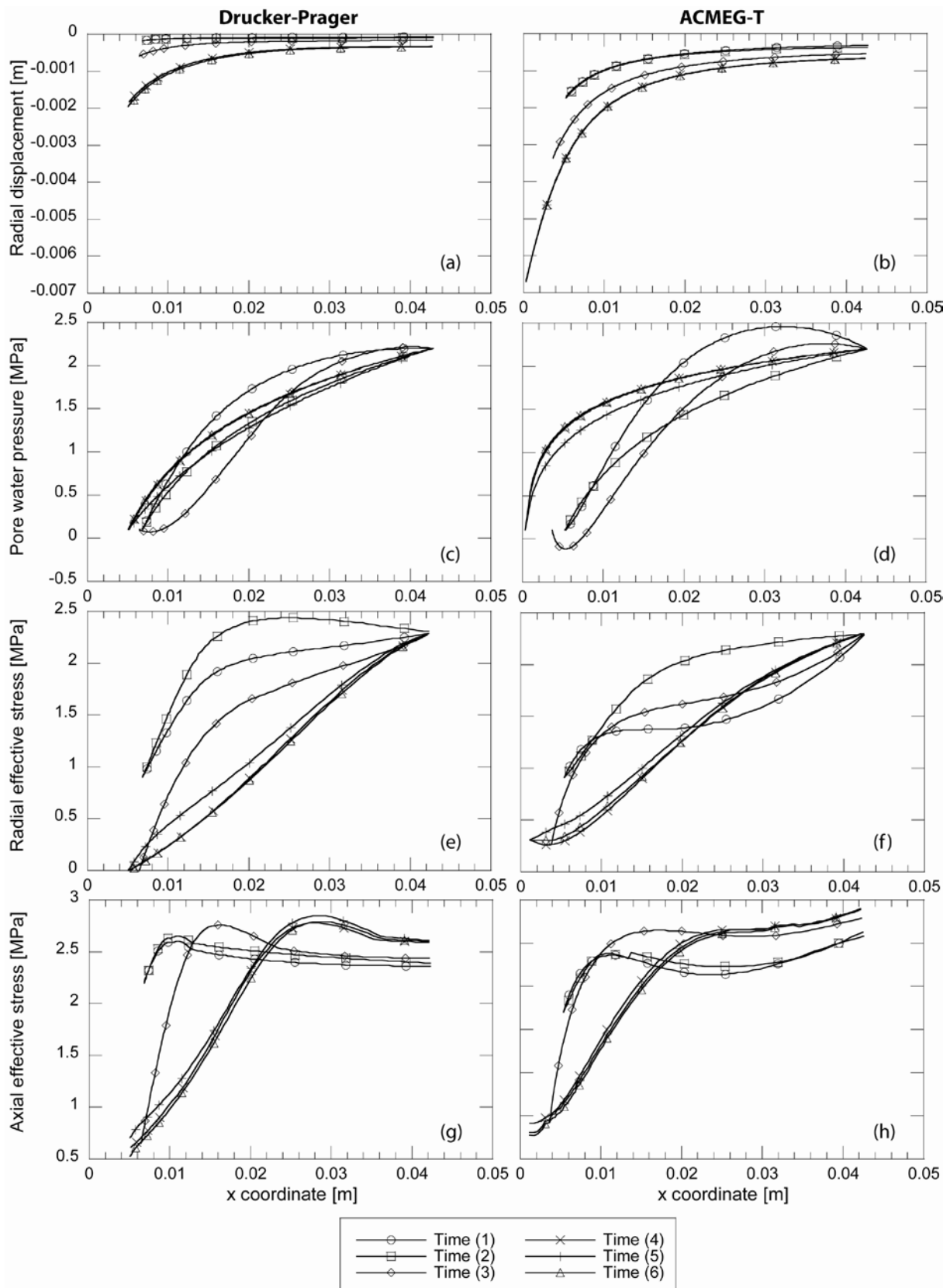
Figure 90: Temperature cycle on sample at three different overconsolidation ratios (TBoom9 from Baldi et al. (1991)): Comparison between numerical simulations with ACMEG-T model and experimental results

## 7.2.2 Benchmark exercise

The distribution in space for different times of the key variables is depicted in Figure 91. The times when the results are presented are reported in Figure 87. Those times have been chosen to be the most representative of the different loading steps. They correspond to the end of the first mechanical unloading (1), the end of the first equalization phase (2), the end of the second unloading phase (3), the end of the second equalization phase (4), the middle of the thermal phase (5) and the final state (6). Also, the variations in time of various variables at different

locations are depicted in Figure 92. The three chosen locations are the inner radius ( $x = 7$  mm), the middle of the hollow cylinder ( $x = 24.5$  mm) and the outer radius ( $x = 42$  mm).





TIMODAZ



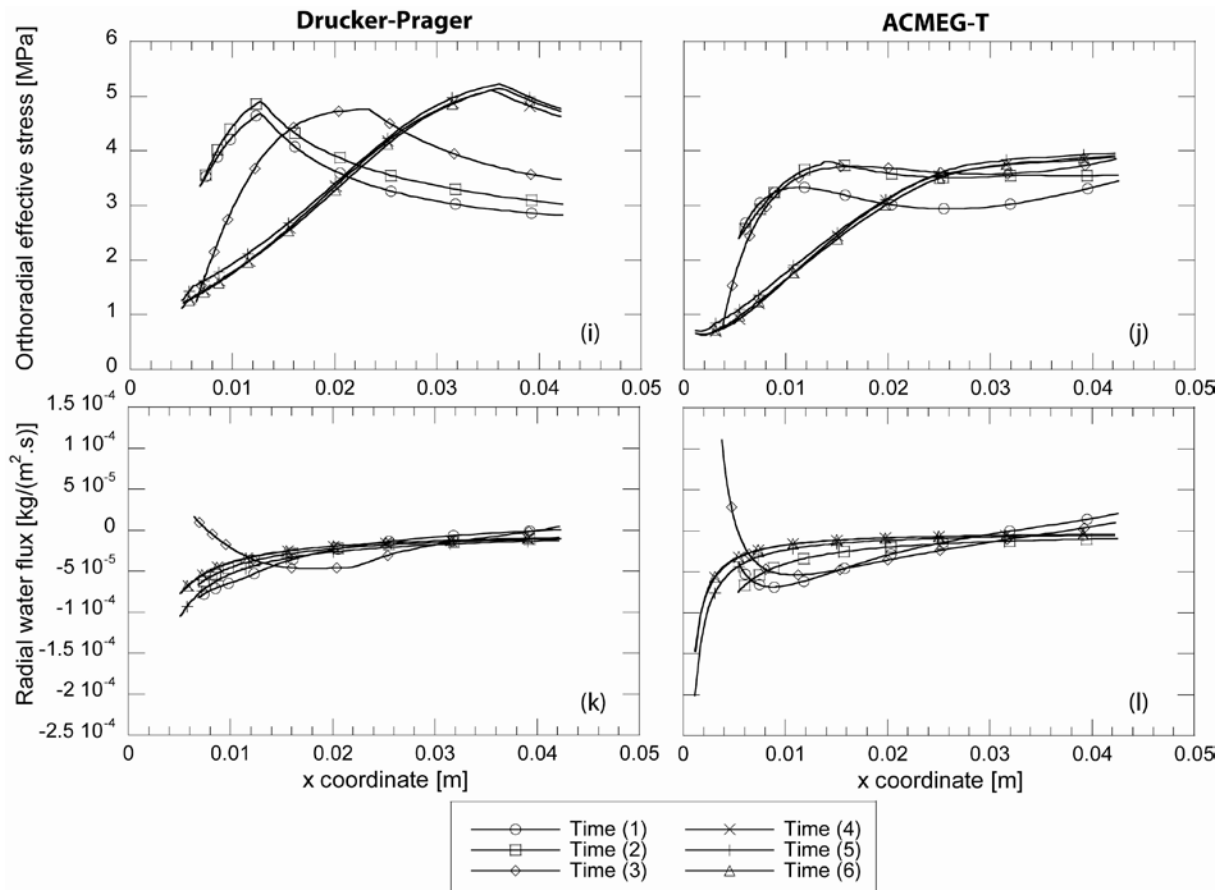


**Figure 91:** For different times, distribution in space of computed (a, b) radial displacement, (c, d) pore water pressure, (e, f) radial effective stress, (g, h) axial effective stress, (i, j) orthoradial effective stress and (k, l) radial water flux. Comparisons between predictions using the Drucker-Prager model (left) and ACMEG-T model (right). The selected times (1) to (6) are reported in Figure 106.

The Drucker-Prager model predicts a 2 mm radial displacement of the inner face of the hollow cylinder which is mainly produced during the second mechanical unloading. The first unloading up to 1 MPa of radial effective stress and the thermal phase produce only negligible displacement (Figure 91a). On the contrary, ACMEG-T foresees a quasi-closure of the inner hole (6.8 mm of convergence on the 7 mm of initial radius) which is split up into 1.6 mm of convergence during the first unloading and the rest during the second unloading. Thermal loading does not induce additional convergence (Figure 91b).

In the evolution of pore water pressure, several hydro-mechanical coupling effects can be observed. Due to the higher strains and displacements generated by the ACMEG-T model with respect to those produced by the Drucker-Prager model, the hydro-mechanical couplings are more visible in the results of ACMEG-T. The effects of the first mechanical unloading and the drainage of the hole are twofold. In the internal part of the cylinder, the pore water pressure dissipates following the drop of the pore water pressure imposed at the inner boundary. On the contrary, in the external part of the cylinder, the pore water pressure increases due to a hardening process which tends to diminish the pore space. During the first equalization phase, the pore water pressure reaches equilibrium. During the second unloading, similar trends are observed. In addition, a softening effect is observed in the vicinity of the hole, inducing a drop in pore water

**TIMODAZ**



pressure (Figure 91d). This hydro-mechanical effect produces a temporary inversion of the water flux from the inner hole to the soil (Figure 91i). The change of geometry predicted by ACMEG-T (e.g. a quasi-closure of the inner hole) considerably reduces the section for radial water seepage. Consequently, the water flux conservation requires that the water flux expressed per surface unit increases drastically in the vicinity of the quasi-closed hole (Figure 91k,l).

The evolution of the orthoradial effective stress predicted by the Drucker-Prager model clearly points out the propagation of the plastic zone through the hollow cylinder (Figure 91i). Indeed, the limit between the elastic and plastic zones is characterized by the peak of the orthoradial stress. The results of the simulation with the ACMEG-T model do not exhibit such a sharp transition between the elastic and plastic regions (Figure 91j). Indeed, due to the progressive mobilization of the plastic mechanisms, it is no longer possible to distinguish a clear elastic zone because the entire domain is plastic.

Figure 92a,b show that the temperature in the middle of the hollow cylinder evolves in parallel with the imposed temperature in the internal boundary. There is no transient process in the temperature diffusion. Consequently, the temperature propagation is governed by the thermal boundary conditions and not by thermal diffusion in the Boom clay. The difference in the temperature field predicted by the simulations with Drucker-Prager and ACMEG-T is due to the variation of geometry induced by the choice of the mechanical law. In terms of water flux evolution with time, Figure 92c,d show very limited transient periods followed by a long-time episode of steady-state. The decrease of radial water flux produced by the second unloading is due to the partial closure of the inner hole which increases the distance between internal and external pore water boundary conditions. In so doing, the hydraulic gradient decreases. During the temperature phase, the thermally-induced increase of the water permeability produces an increase of the radial water flux. The difference in radial water fluxes predicted by both simulations is due to the change of geometry.

Figure 93 depicts the followed stress paths in the  $(p' - q)$  plane at three locations in the hollow cylinder: at the inner face ( $x = 7$  mm), in the middle of the cylinder ( $x = 24.5$  mm) and at the outer face ( $x = 42$  mm). The prediction of the Drucker-Prager model clearly exhibits the elastic path until reaching the critical state line (Figure 93a). This plastic limit is reached at different steps in the loading procedure according to the location in the hollow cylinder. The first unloading produces plasticity in the near-field of the hole. This plastic zone progresses during the second unloading and reaches the middle of the cylinder during the second equalization phase. However, the external zone remains elastic during all the processes. On the contrary, the transition between elasticity and plasticity is not observable in the ACMEG-T prediction because progressive plasticity appears gradually in any location of the cylinder (Figure 93b). Due to the rapid decrease of the radial effective stress at the inner boundary, the unloading phases take place under quasi-undrained conditions in the middle of the cylinder. Then, the equalization phase enables the dissipation of excess pore water pressure, inducing an increase in the mean effective stress at constant deviatoric stress (a horizontal path in the  $(p' - q)$  plane). Finally, the predictions with ACMEG-T reach the critical state faster than the simulation with the Drucker-Prager model. Indeed, the Drucker-Prager critical state is shifted upward due to the relatively high cohesion.

TIMODAZ



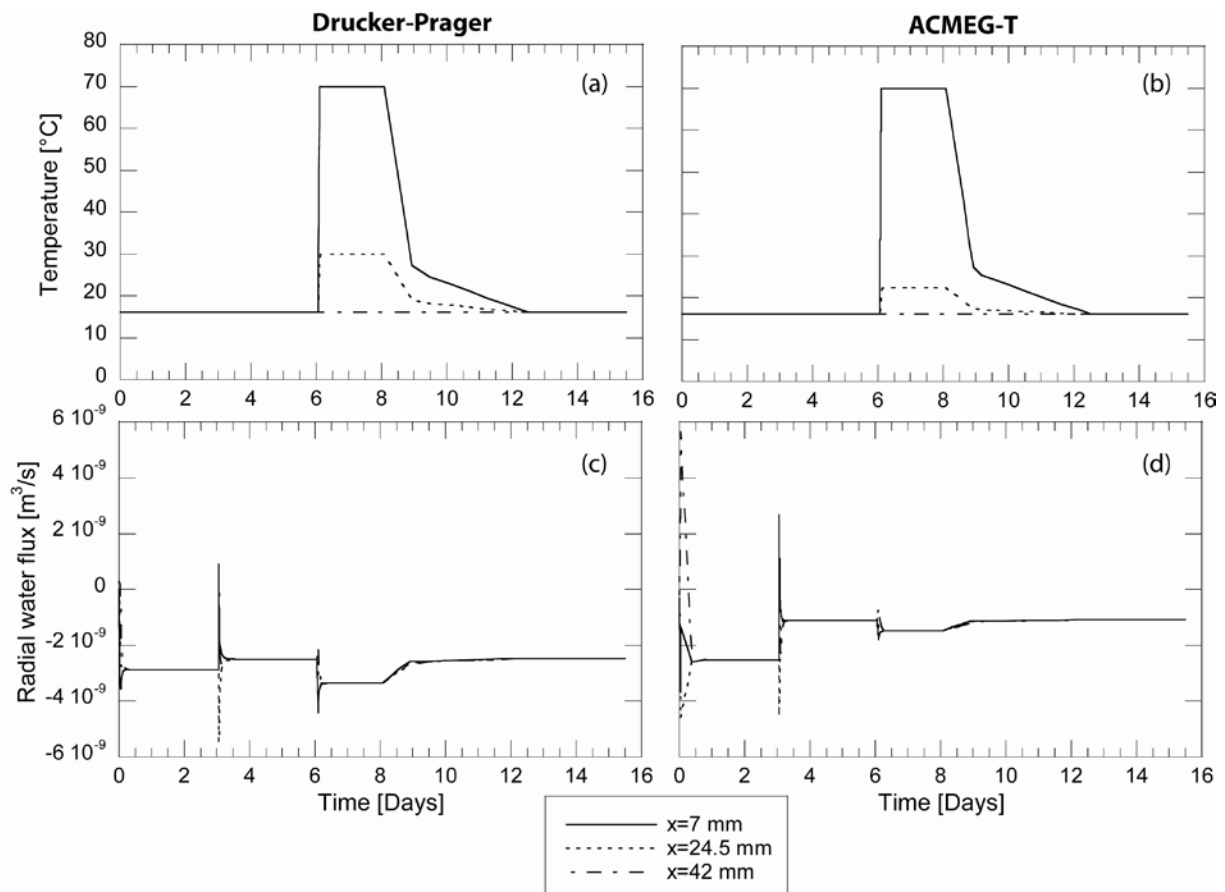


Figure 92: At different locations, variations in time of (a, b) temperature and (c, d) radial water flux. Comparisons between predictions using the Drucker-Prager model (left) and ACMEG-T model (right)

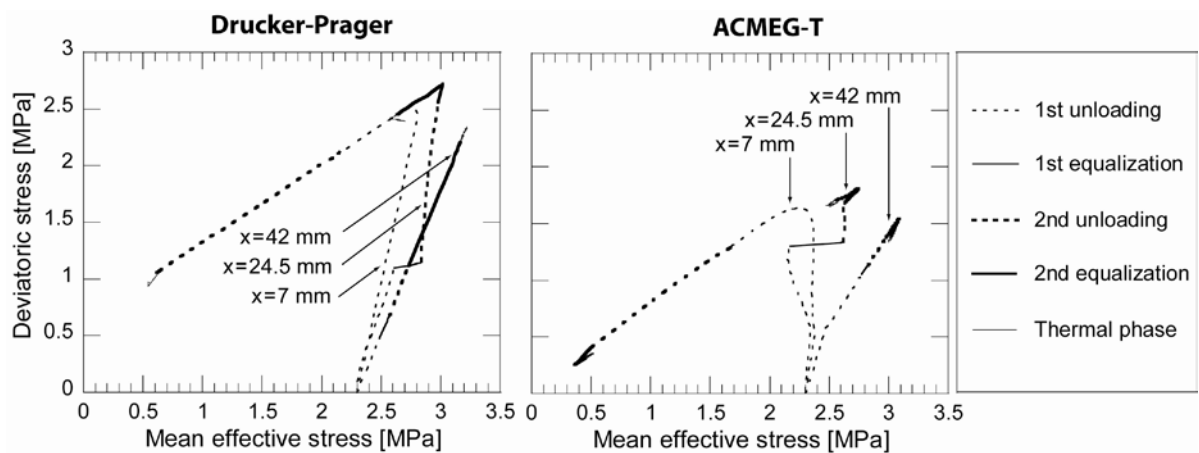
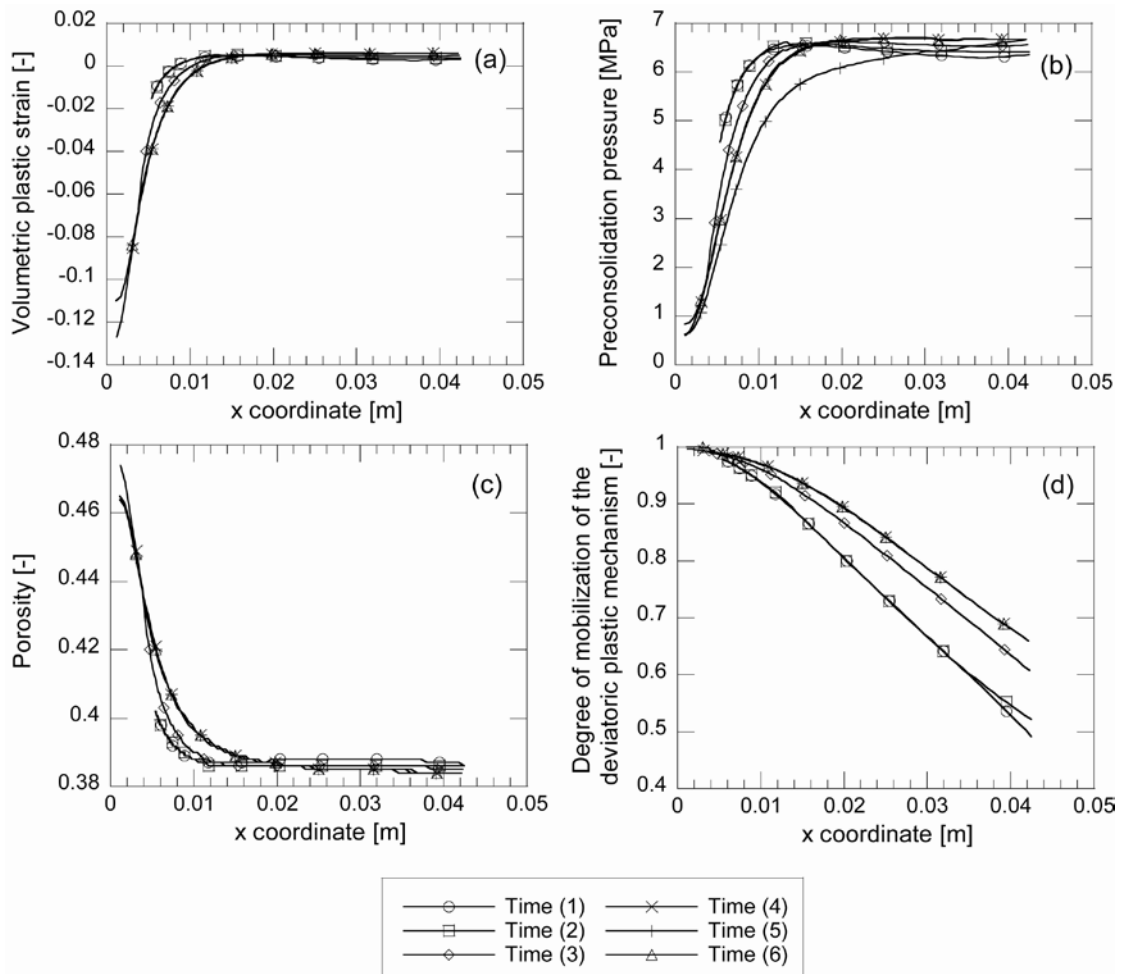


Figure 93: Stress paths in the (p'-q) plane at three different radial coordinates (7 mm, 24.5 mm and 42 mm). Comparisons between predictions using the Drucker-Prager model (left) and ACMEG-T model (right)



**Figure 94:** For different times, distribution in space of computed volumetric plastic strain (a), preconsolidation pressure (b), degree of mobilization of the plastic mechanism (c) and porosity (d), predicted by the ACMEG-T model. The selected times (1) to (6) are reported in Figure 87

Figure 94 presents the evolution of some plastic variables of the ACMEG-T model with respect to the radial coordinate. The two phases of mechanical unloading produces a drastic decrease in the mean effective stress in the vicinity of the hole along with an increase of the deviatoric stress. Consequently, the deviatoric plastic mechanism is mobilized in the softening part of the deviatoric yield limit, generating negative volumetric plastic strain. This plastic dilatancy strain reaches more than 12% at the inner hole face (Figure 94a).

On the contrary, the external part of the cylinder is subjected to plastic hardening characterized by positive volumetric plastic strain. However, this hardening effect is much lower (less than 1% of volumetric plastic strain) than the softening occurring in the inner part. This hardening part is mainly generated by the increase of the orthoradial stress around the softened zone, induced by stress redistribution. During the thermal phase, a small thermo-plastic hardening produces 2% of the volumetric plastic contraction strain in the first millimetres around the hole. The preconsolidation pressure evolution is directly related to the generated volumetric plastic strain and temperature. In that sense, the hardening process in the external part produces a slight increase of the preconsolidation pressure  $p'_c$  (from 6 to 6.5 MPa), while the internal part is

**TIMODAZ**



subjected to a huge decrease until it reaches less than 1 MPa (Figure 94b). Also, the thermal phase (time (5)) decreases  $p'_c$  in the whole cylinder domain. The porosity of Boom clay is strongly affected by the softening in the internal part which increases from 0.39 to 0.47 (Figure 94c). The degree of mobilization of the deviatoric plastic mechanism varies from 1 at the inner radius to 0.7 at the external radius at the end of the second equalization phase (Figure 94d).

### 7.3 Conclusions

The Soil Mechanics Laboratory of EPFL have performed the simulations of the hollow cylinder tests considering the parameters of Boom Clay with two distinct constitutive models: the Drucker-Prager model and the ACMEG-T model. The problem has been treated as a one-dimensional process. The parameters of the ACMEG-T model were determined from calibration on laboratory tests while the Drucker-Prager model parameters were given in the benchmark statement. The Drucker-Prager model, which is an elastic perfectly-plastic model, predicts a sharp transition between the elastic and plastic states. On the contrary, the results obtained with the ACMEG-T model exhibit a progressive mobilization of the plastic mechanisms, and it is no longer possible to distinguish a clear elastic zone because the entire domain is plastic.

The numerical modelling reveals the drastic increase of the deviatoric stress in the inner part of the cylinder induced by the inner radial stress decrease. Dilatancy plastic strain is produced at the inner hole face, while the external part of the cylinder is subjected to slight plastic hardening characterized by positive volumetric plastic strain. The predicted convergence of the inner hole clearly depends on the model used. The Drucker-Prager model forecasts 2 mm of radial displacement while the ACMEG-T model predicts a quasi-closure of the inner hole (6.8 mm of convergence on the 7 mm of initial radius). It is to note that the imposed mechanical unloading defined in the benchmark exercise was higher than the unloading that has been applied experimentally. It explains the higher convergence of the central hole obtained numerically.

## 8 Additional computations (CIMNE)

CIMNE did some additional computations to interpret the first experimental results obtained by LMR on sample Boom 13B\_bis (Labiouse, 2009).

### 8.1 Modelling domain, boundary conditions and parameters

The hollow cylinder test is modeled using the mesh presented in Figure 95 . A plane strain configuration is adopted, although the experimental conditions are rather plane stress. Two symmetry planes are used. 0-displacement and 0-flux are applied on these planes. Stresses and pore water pressure are prescribed on the circular inner- and outer boundaries according to the experimental schedule depicted in Figure 96 . In the experiment, a tomography was carried out before and after the mechanical unloading in the experiment allowing for evaluating the displacement profiles generated by the unloading in the sample.

TIMODAZ



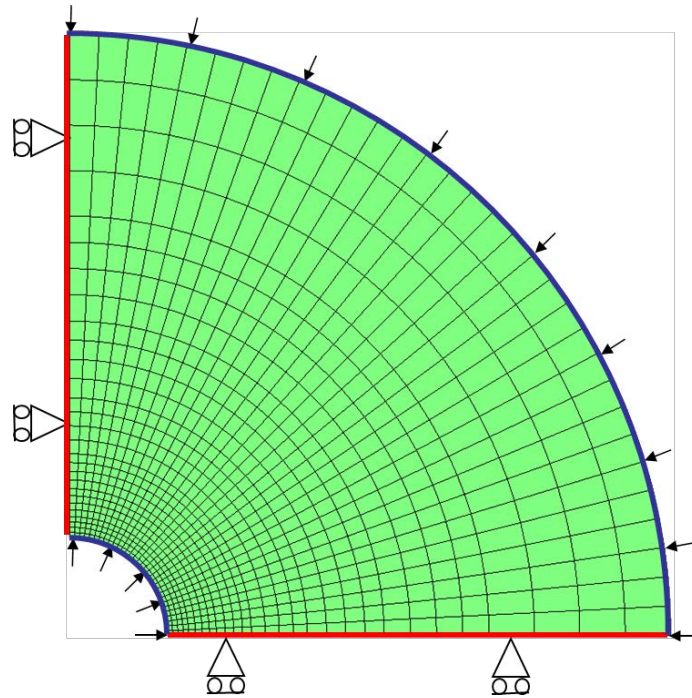


Figure 95: Mesh and boundary conditions used

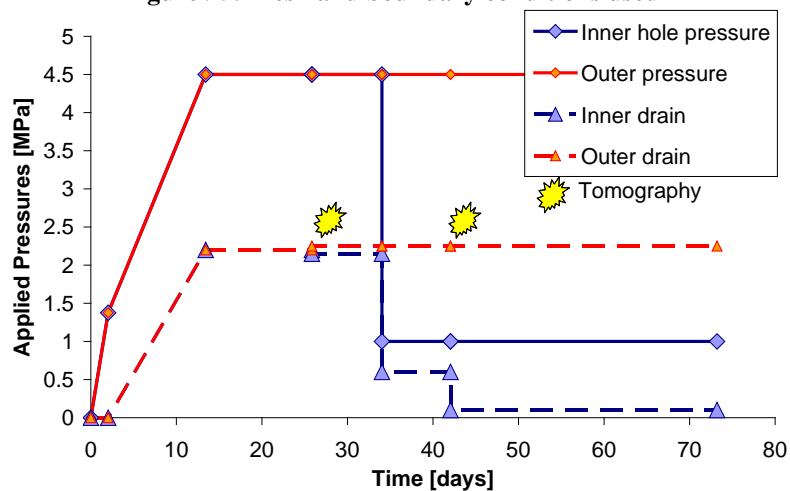


Figure 96: Pore water pressure and total stresses applied at the inner and outer boundaries

A list of relevant parameters is given in Table 12. As Boom clay presents a bedding plane structure due to its sedimentary origin, some anisotropic features may be considered. In the elastic domain, the stress-strain relationship is described by an anisotropic linear elastic constitutive law. The elastic domain is limited by a Mohr-Coulomb type yield surface. Plastic deformations are non-associated (null volumetric plastic strain) and perfect plasticity is considered.

$E_h$	500	[MPa]
$E_v$	250	[MPa]
$\nu_h$	0.125	
$\nu_{hv}$	0.125	
$G_v$	222	[MPa]
$c$	0.3	[MPa]
$\phi$	18	[°]
$k$	$2 \cdot 10^{-19}$	[m <sup>2</sup> ]

Table 12: Relevant parameters list for Boom clay

## 8.2 Simulation results (base case)

Simulation results are compared with measurements along the bedding plane, in the perpendicular direction and at 45° (see Figure 97).

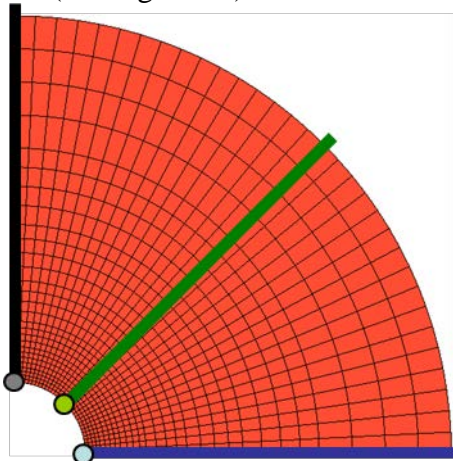


Figure 97: Location of the profiles for results output

The measured and simulated displacement profiles are shown in Figure 98. A qualitative agreement between measurements and simulation is observed: both shows a more important cavity wall displacement in the direction of the bedding plane, a displacement plateau (equivalent to 0 strain) in the farther field and a less displacement of the outer cylinder wall in the bedding plane direction.

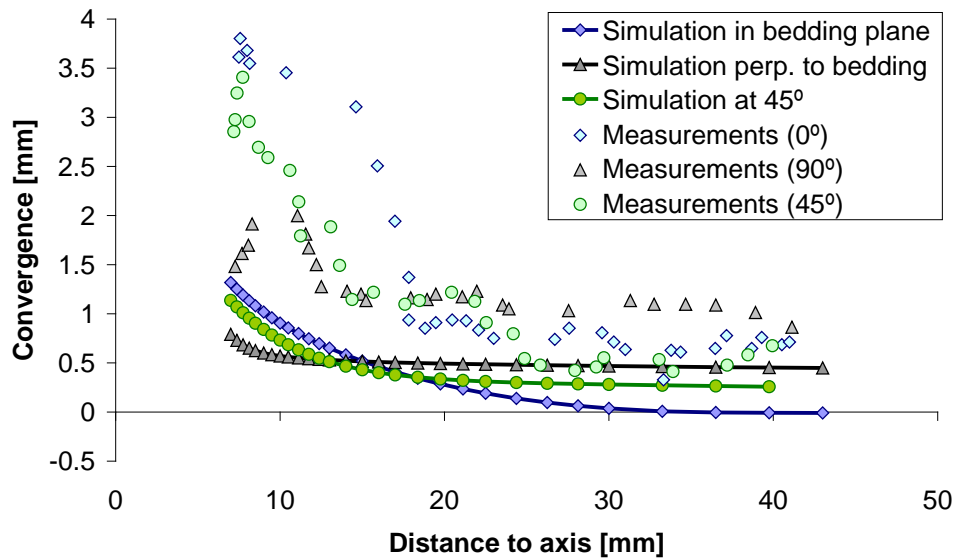


Figure 98: Comparison of measured and simulated displacement profiles in the three directions

The measured convergence of the central hole is compared to the simulation results in Figure 99.

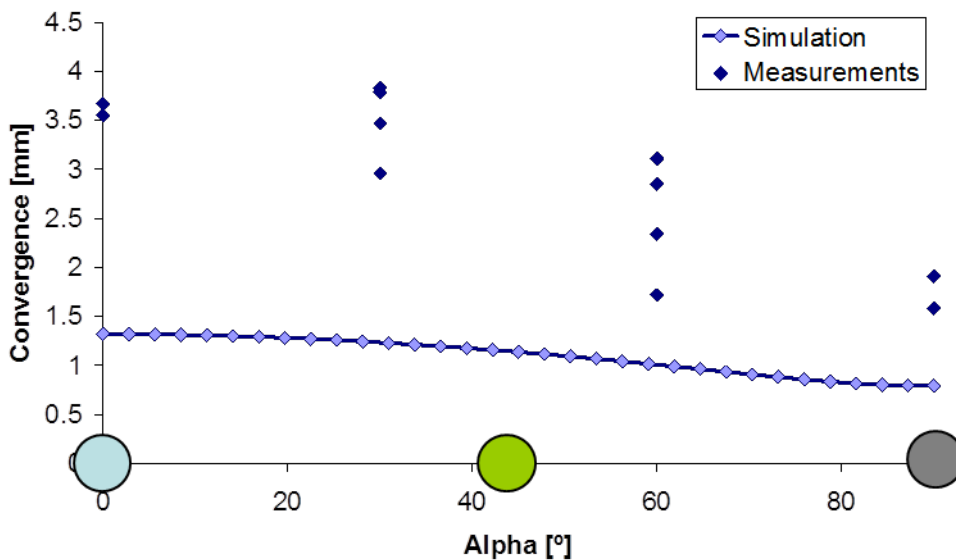


Figure 99: Comparison of measured and simulated central hole convergence in function of the angle between the bedding plane and the normal direction

### 8.3 Simulation results (variants)

Some changes were applied to the base case in order to increase our understanding of the system:

- Variant 1: only elastic case (no yield limit)
- Variant 2: associated flow rule (plastic volumetric strain is allowed)
- Variant 3: reduced friction angle, resulting in an increased intensity of the plastic mechanisms

The simulated displacement profiles for the elastic case (Variant 1, Figure 100 & Figure 101) are quite easy to understand in this stress controlled test: the stress relaxation causes more important strains in the low stiffness direction (perpendicular to bedding), resulting in more displacement. The simulation results for variant 1 (elastic case) differs one order of magnitude from the measurements. This is an indication that most of the strain observed in the experiment is due to plastic mechanisms. Moreover, the simulated convergence (radial displacement of the inner wall) shows an inverse tendency as the displacements.

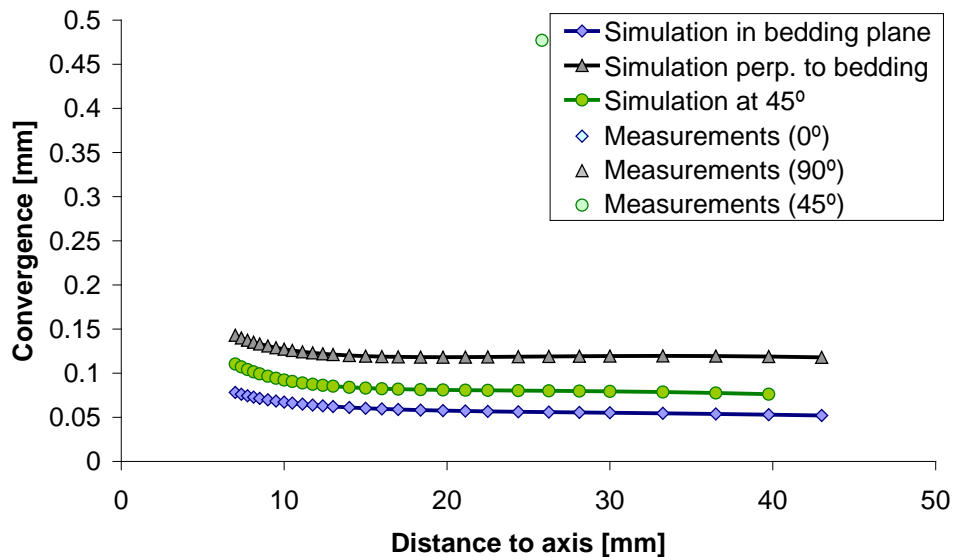
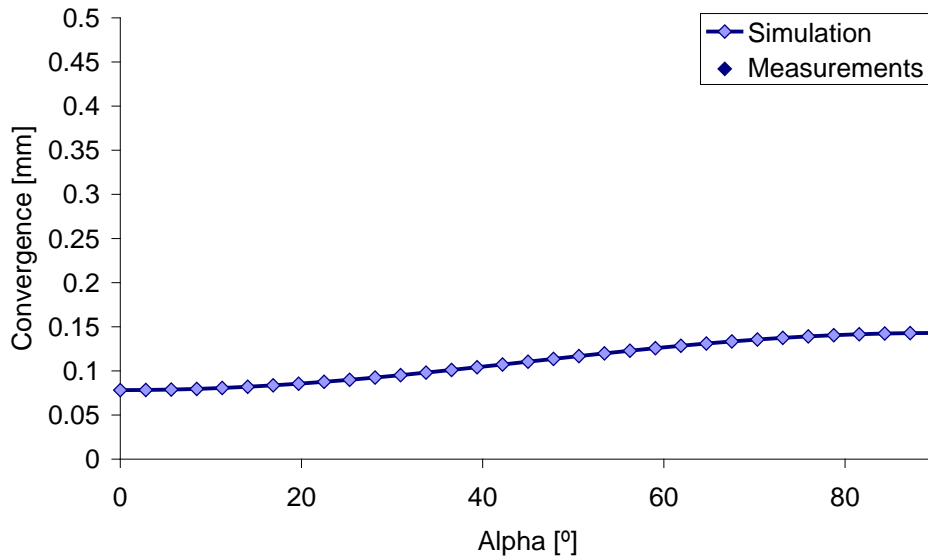
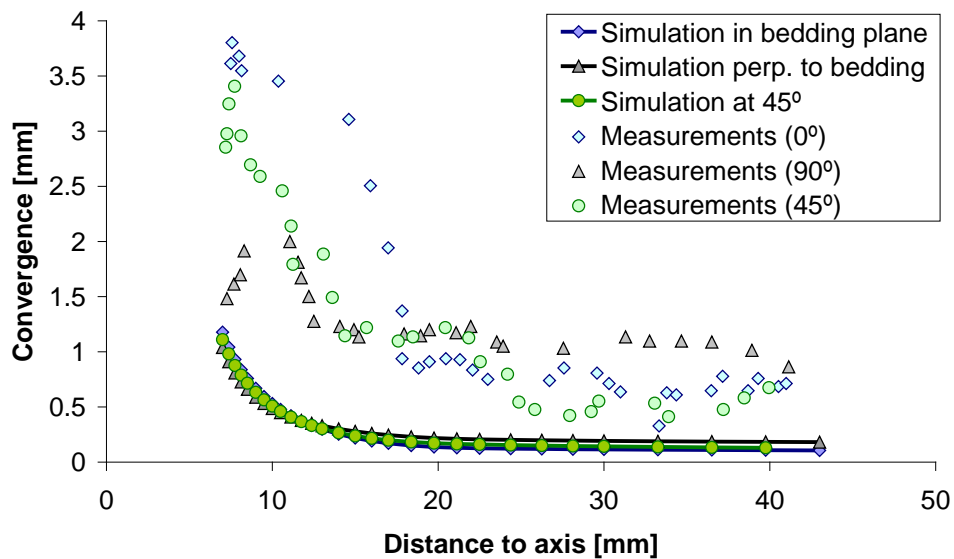


Figure 100: Comparison of measured and simulated displacement profiles in the three directions (elastic case)



**Figure 101: Comparison of measured and simulated central hole convergence in function of the angle between the bedding plane and the normal direction (elastic case)**

If volumetric plastic strains are allowed, the influence of the anisotropic part of the mechanical law (i.e. in the elastic region) is minimized and the sample behaviour seems to be most isotropic (Figure 102 & Figure 103).



**Figure 102: Comparison of measured and simulated displacement profiles in the three directions (Associated flow rule)**



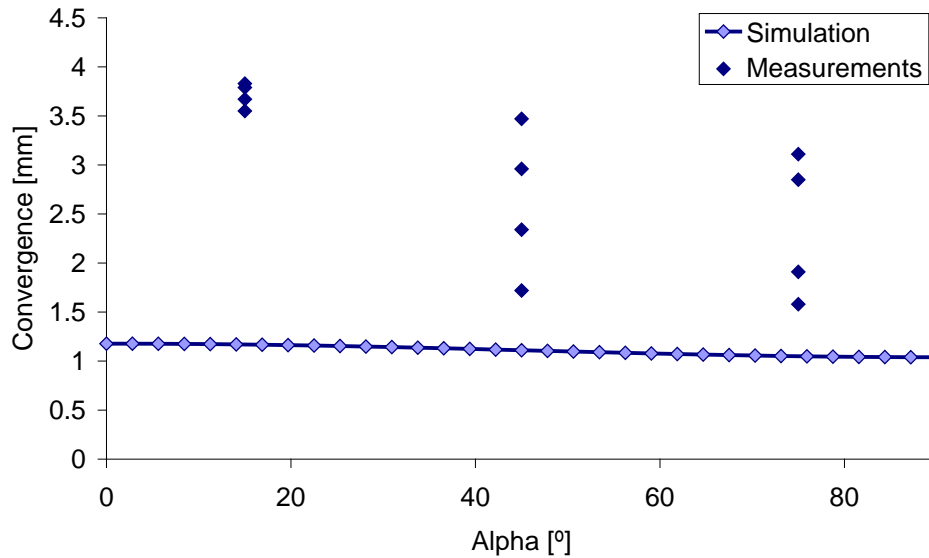


Figure 103: Comparison of measured and simulated central hole convergence in function of the angle between the bedding plane and the normal direction (Associated flow rule)

The difference between the developed plastic zone in the non-associated and associated case is depicted in Figure 104. In the non associated case, the plastic zone is clearly anisotropic.

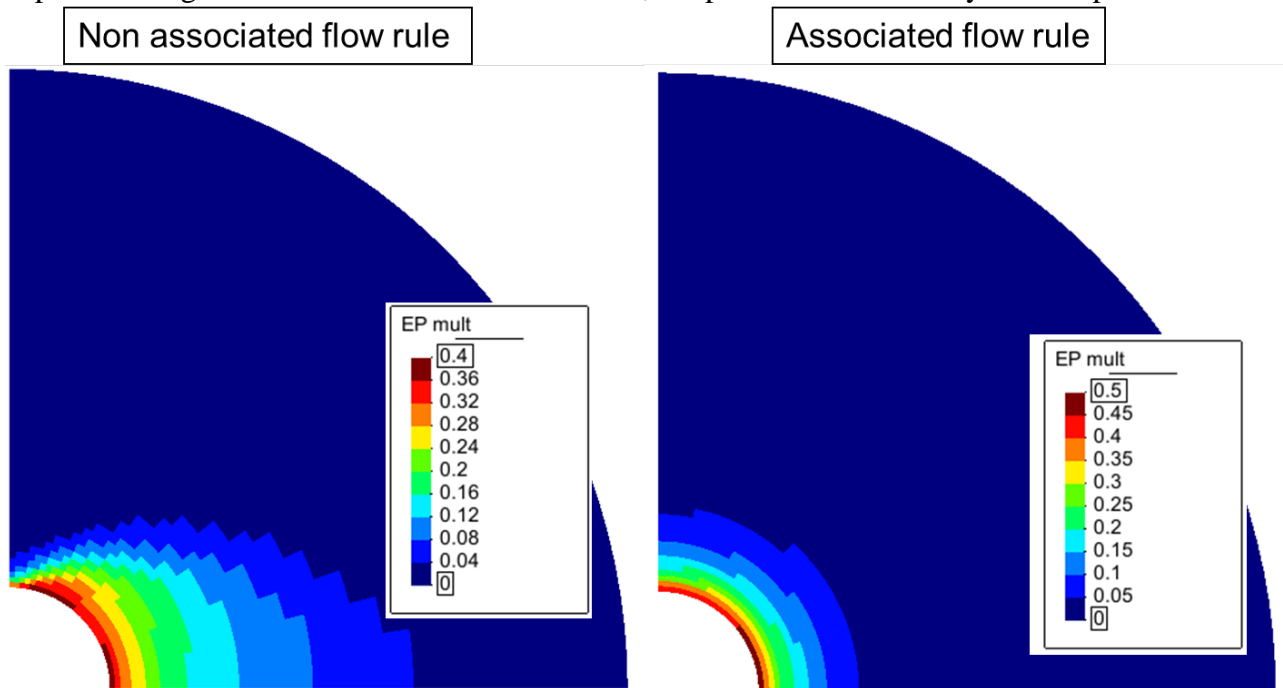


Figure 104: Comparison of the plastic zone for a non-dilatant material (non associated flow rule) and a dilatant material (associated flow rule)

A last variant was run: the friction angle was reduced to quite a low (and unrealistic) value in order to achieve a quantitative match of the measured displacement profiles (Figure 105 & Figure 106 )

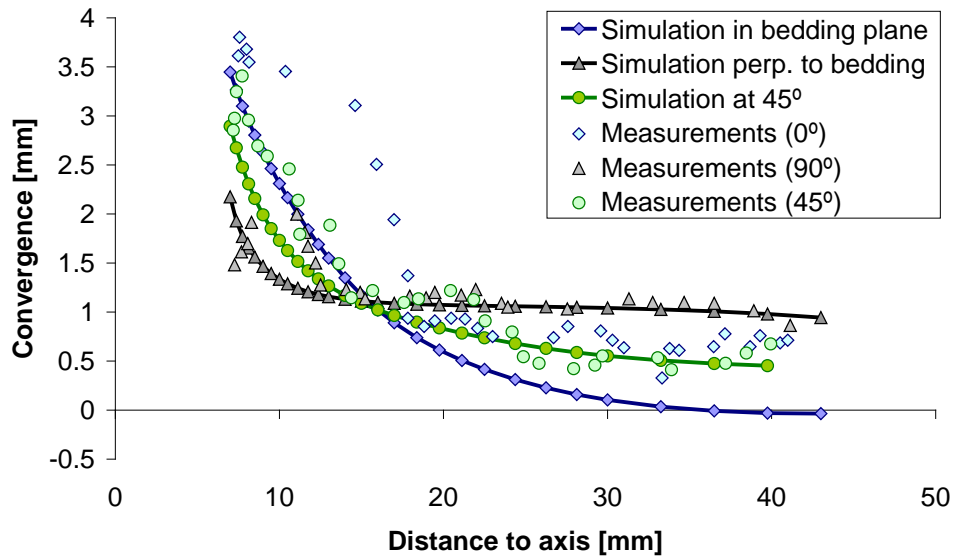


Figure 105: Comparison of measured and simulated displacement profiles in the three directions (reduced friction angle, 10°)

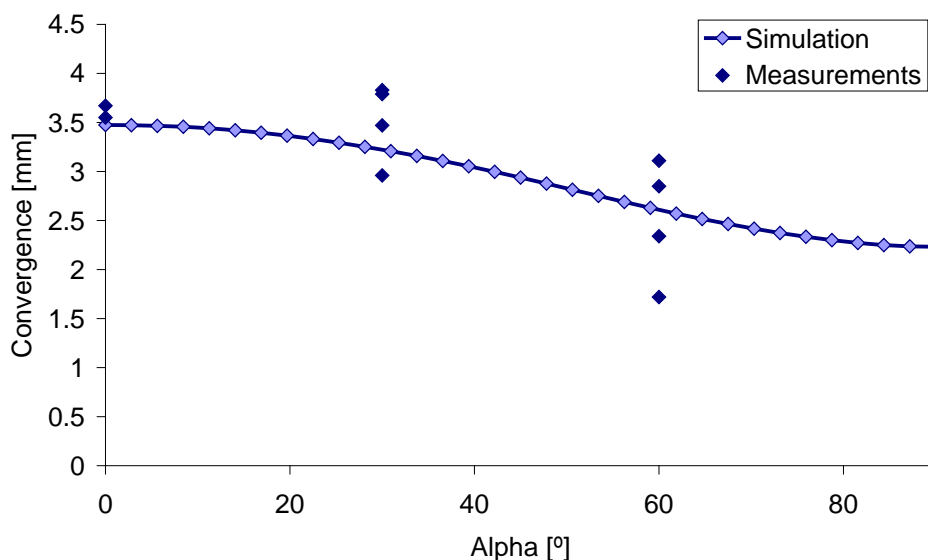


Figure 106: Comparison of measured and simulated central hole convergence in function of the angle between the bedding plane and the normal direction (reduced friction angle, 10°)

## 8.4 Discussion of the mechanisms

The joint execution of experiments and modeling exercises allows for an increased understanding of some processes:

- The stress relaxation occurring around a circular opening in Boom clay induces plastic strains localized around the opening and no strains (or less important strains) in the far field (a plateau is observed in the displacement profiles in the far field)

- The radial strains in the direction of the bedding plane are more important than in the perpendicular direction. This may be explained by the use of an isotropic plastic law and an anisotropic elastic law if the plastic law is non-associated.
- The observation of more important displacements of the outer boundary in the perpendicular direction to the bedding plane is purely due to the strain observed near the opening, corresponding to circumferential compression in the direction of the bedding plane.

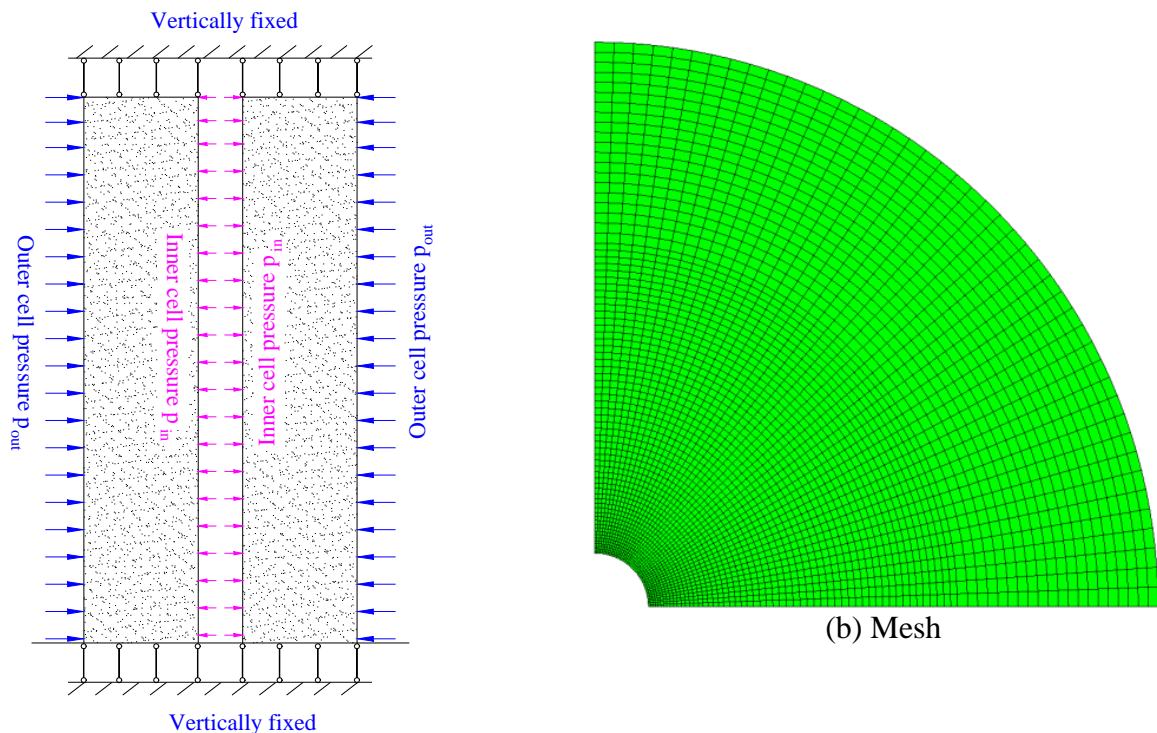
## 9 Additional computations (EURIDICE)

Hollow Cylinder Test on sample Boom 13B\_Bis performed by EPFL was simulated numerically, and two models (2D plane strain model and 2D axisymmetric model) have been employed.

### 9.1 2D plane strain model

For 2D plane strain model, actually we assume that the top and bottom of the sample are impermeable, and they are fixed in the normal direction (see Figure 107a). Due to the symmetric nature and plane strain condition of the problem, a quarter of the cross section is selected for numerical modelling (see Figure 107b).

The detailed hydro-mechanical boundary conditions have been introduced in section 3, based on which the hydro-mechanical boundary conditions used in the modelling are summarized in Table 13.



(a) Geometry and boundary conditions

Figure 107: The geometry, boundary conditions and mesh of the numerical modeling

TIMODAZ

Time interval (day)		0→2	2→14	14→34	34→34.0486	34.0486→42	42→67
Inner boundary	Pore pressure, MPa	0.1	0.1→2.3	2.3	2.3→0.7	0.7	0.2
	Radial pressure, MPa	0.1→1.5	1.5→4.6	4.6	4.6→1.1	1.1	
Outer boundary	Pore pressure, MPa	0.1	0.1→2.3	2.3			
	Radial pressure, MPa	0.1→1.5	1.5→4.6	4.6			

**Table 13: Hydro-mechanical boundary conditions along the inner and outer surfaces**

The initial porosity is 0.39, initial pore water pressure is 0.1MPa, and initial stresses are

$$\sigma_{r_0} = \sigma_{\theta_0} = \sigma_{z_0} = -0.1MPa .$$

Four cases are simulated to investigate the effects of hydro-mechanical anisotropy on the radial displacement in the sample.

Table 14 gives the main HM parameters, and the other parameters used in the modeling are the same as those presented in section 4.5.

Cases		$E_{par}$	$E_{per}$	$G_v$	$c$	$\phi$	$K_{par}$	$K_{per}$
		MPa	MPa	MPa	MPa	°	m <sup>2</sup>	m <sup>2</sup>
1	Mechanical anisotropy	600	300	133.3	0.3	10	$4.5 \times 10^{-19}$	$4.5 \times 10^{-19}$
2	Hydraulic anisotropy	300	300	133.3	0.3	10	$6.0 \times 10^{-19}$	$3.0 \times 10^{-19}$
3	Hydro-mechanical anisotropy	600	300	133.3	0.3	10	$6.0 \times 10^{-19}$	$3.0 \times 10^{-19}$
4	Hydro-mechanical isotropy	300	300	133.3	0.3	10	$4.5 \times 10^{-19}$	$4.5 \times 10^{-19}$

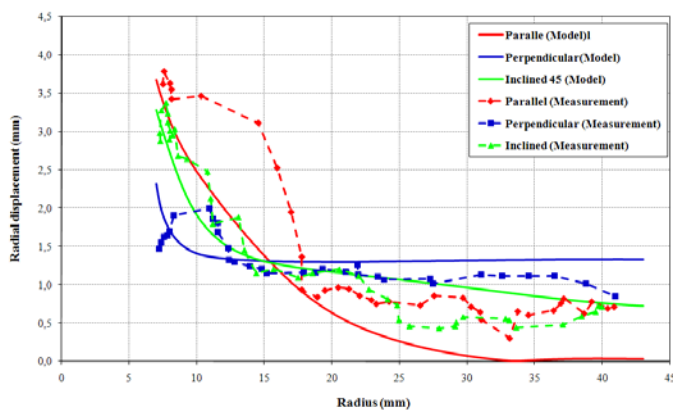
**Table 14: Hydro-mechanical parameters of four simulated cases**

The same constitutive laws as those presented in section 4.4 are employed, except that the intrinsic permeability is assumed to be constant in the present modelings.

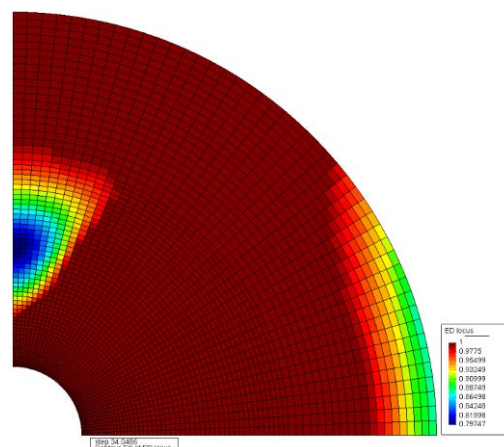
### 9.1.1 Modelling results

Case 1 only investigates the mechanical anisotropy with hydraulic behaviour being isotropic. Both the modelled and measured radial displacements in three radial directions along the sample are shown in Figure 108. The modelling gives the consistent trend of the anisotropic radial displacements to that of measured displacements, and the magnitude of the displacements could be considered good (Figure 108a). The contour of the plastic indicator just after unloading (i.e. Day 34.0486 in Table 13) shows that the sample in the perpendicular direction to the bedding plane has less plastic zone (see Figure 108b), which could explain the higher convergence of the sample in the parallel direction to the bedding plane.





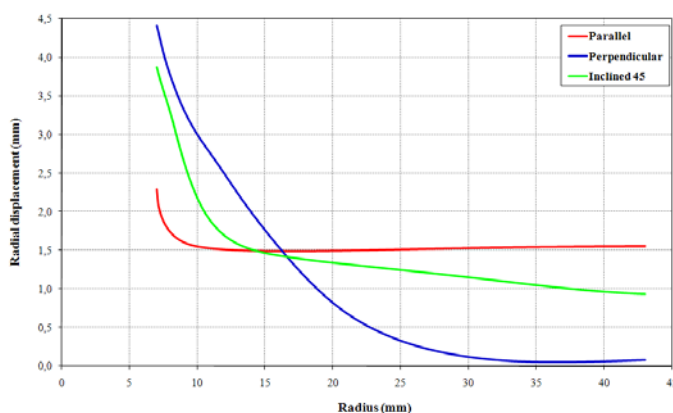
(a) Profile of radial displacement in the sample



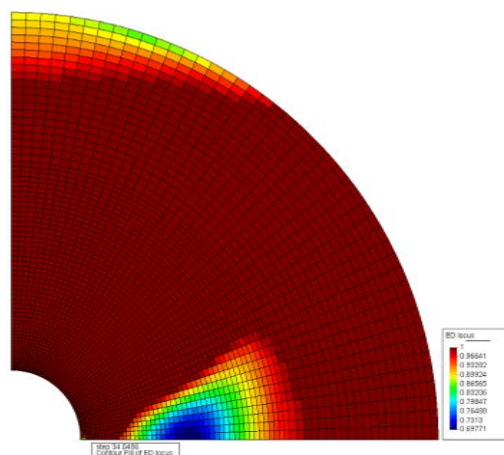
(b) Plastic indicator just after unloading

**Figure 108: Modeling results of Case 1**

Case 2 only investigates the hydraulic anisotropy with mechanical behaviour being isotropic. The modelled radial displacements in three radial directions along the sample are shown in Figure 109a. The modelling gives the reverse trend of the anisotropic radial displacements to that of Case 1 (Figure 109a). The contour of the plastic indicator just after unloading (i.e. Day 34.0486 in Table 13) shows that the sample in the parallel direction to the bedding plane has less plastic zone (see Figure 109b), which could explain the higher convergence of the sample in the perpendicular direction to the bedding plane.



(a) Profile of radial displacement in the sample



(b) Plastic indicator just after unloading

**Figure 109: Modeling results of Case 2**

Case 3 investigates both hydraulic anisotropy and mechanical anisotropy, and the average of the intrinsic permeability in the two directions is the same as the intrinsic permeability in Case 1. The modelled radial displacements in three radial directions along the sample are shown in Figure 110a. The modelling also gives the reverse trend of the anisotropic radial displacements

to that of Case 1 (Figure 110a). The contour of the plastic indicator just after unloading (i.e. Day 34.0486 in Table 13) shows that the sample in the parallel direction to the bedding plane has less plastic zone (see Figure 110b), which could explain the higher convergence of the sample in the perpendicular direction to the bedding plane.

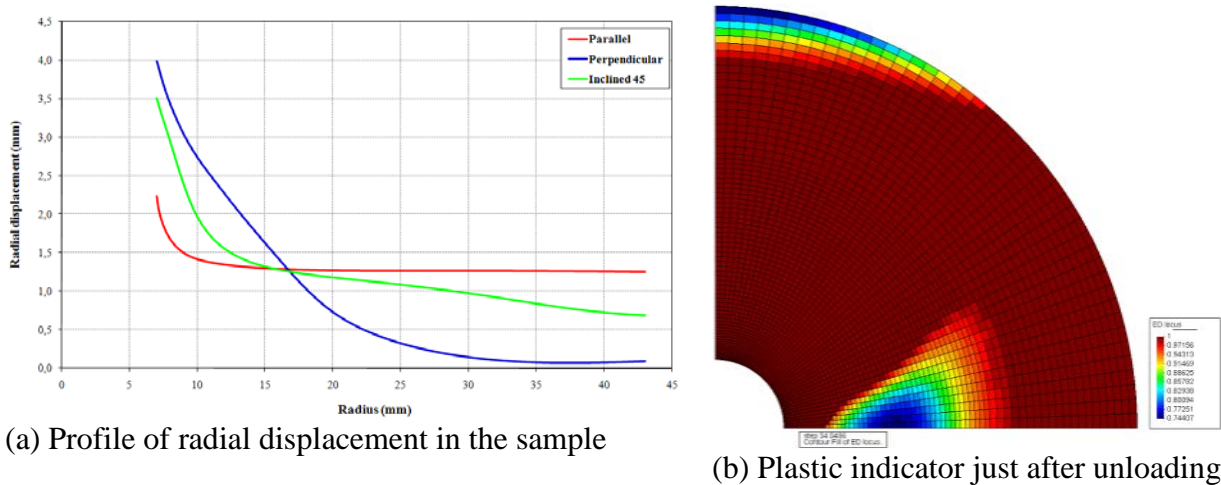


**Figure 110: Modeling results of Case 3**

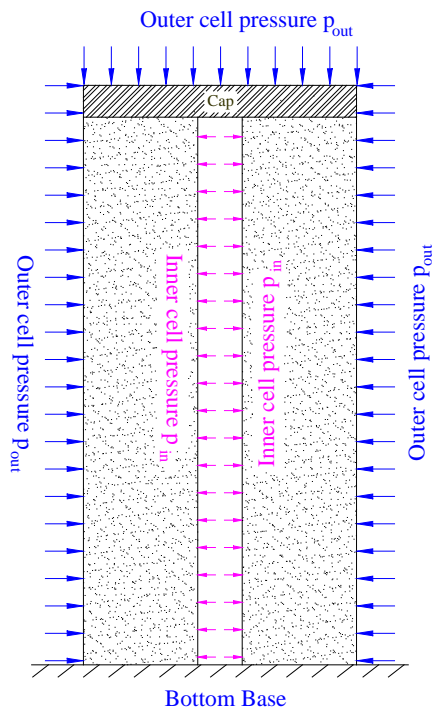
The results of the above three cases indicate that mechanical anisotropy might contribute to the measured anisotropic convergence, while hydraulic anisotropy presents anisotropic convergence on the contrary, and it seems that hydraulic anisotropy plays much more important role than mechanical anisotropy.

## 9.2 2D axisymmetric model

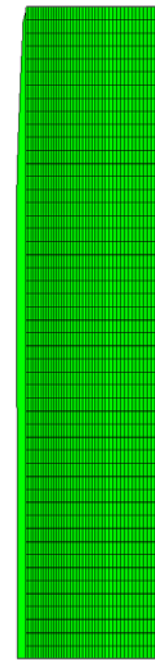
Based on our discussion with EPFL about the detailed test conditions, it is confirmed that the rigid top cap is not fixed but subjected to vertical stress boundary condition, the actual geometry and boundary conditions are illustrated in Figure 111a, and the test condition is actually not plane strain condition.

2D axisymmetric model without considering the anisotropic hydro-mechanical behaviour of the sample has been simulated. The hydro-mechanical boundary conditions at inner and outer surfaces of the sample are the same as those shown in Table 13. The bottom of the sample is assumed to be impermeable and vertically fixed. The top of the cap is subjected to the same history and magnitude of pressure as the radial pressure at the outer surface (see Table 13).

To compare with the 2D axisymmetric model, Case 4 of 2D plane strain model in Table 14 is modelled, and the same HM parameters are used in these two models.



(a) Geometry and boundary conditions



(b) Mesh (deformed)

Figure 111: The geometry, boundary conditions and mesh of the numerical modeling

## 9.2.1 Modelling results

Both the modelled and measured axial displacements at the top cap are shown in Figure 112, and by using the set of HM parameters of Case 4 in Table 14, the 2D axisymmetric model underestimates the measured axial displacement, but gives the similar trend of the displacement. Figure 113 gives the modelled radial convergence at the inner surface of the sample just after unloading (i.e. Day 34.0486 in Table 13). Figure 114 presents the modelled profile of the radial displacement in the sample just after unloading (i.e. Day 34.0486 in Table 13) for both 2D plane strain model and 2D axisymmetric model (at the cross-section without effect of top cap restriction).

Based on the present modelling, it is indicated that hollow cylinder test on Boom clay by EPFL is not exactly plane strain problem, plane strain model gives higher convergence than 2D axisymmetric model under the same conditions, and it seems that smaller Young's modulus should be used to obtain good comparison of the vertical displacement between modelling and measurement.

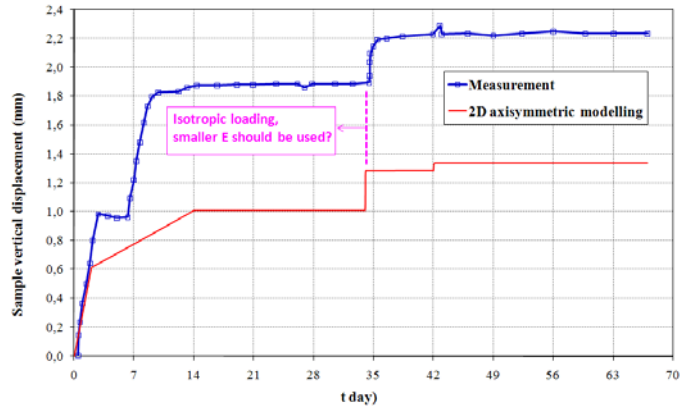


Figure 112: The axial displacement at the top of the sample

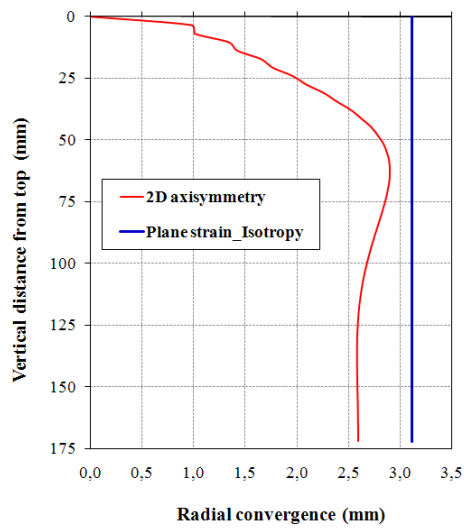


Figure 113: Vertical profile of the convergence along the inner surface of the sample

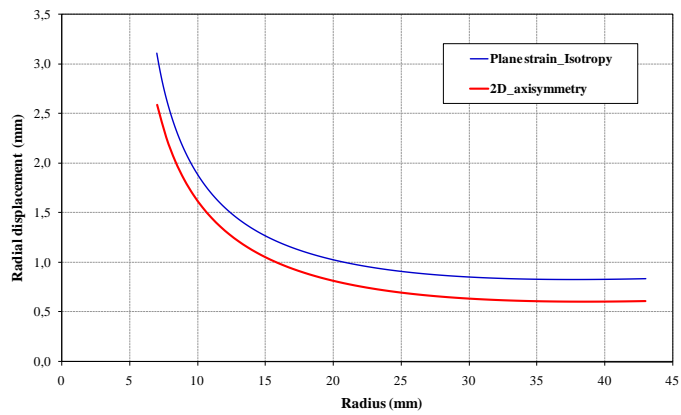


Figure 114: Radial displacement profile of the sample

## 10 Additional computations (UJF)

In order to model the experimental test on Boom Clay hollow cylinder an elasto-plastic model has been used. The elastic part of the model is characterized by cross anisotropy, which is described by five independent parameters and the yield field is a strain cohesion softening Drucker-Prager model. To describe the post-peak behaviour, where the localized zones appear, a second gradient model to the mechanical part is added. Doing so the computation is not affected by mesh-dependency and the objectivity of the solution is reached.

The main problem of this model is that its elastic part is linear while the elastic behaviour of Boom Clay is strongly non linear. The parameters taken into account are shown in Table 15 .

$E_{//}$	$E_{\perp}$	$\nu_{///}$	$\nu_{//\perp}$	$G_{//}$
800 MPa	300 Mpa	0,1125	0,1125	3,5955 MPa
$G_{//\perp}$	$C_0$	$C_f$	$\phi_0 = \phi_f$	$\psi$
3,5955 MPa	300	100	18°	0°

Table 15: Mechanical parameters

The loading path for the experimental test is the same used at Lausanne for the 13B\_B test (Figure 115). Specifically, the first unloading path seventy minutes-long is taken into account for the computation.

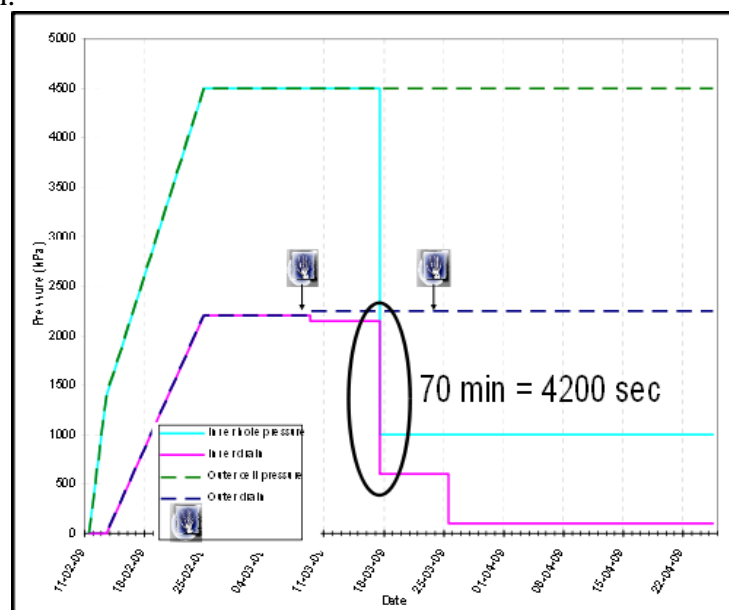


Figure 115: Loading path using in the experimental test in Lausanne.

From Figure 116, where loading plastic point and unloading elastic point are plotted, it is possible to observe how the localization phenomenon clearly appears around the inner part of the sample. At the beginning of the unloading, the plastic deformation appears around the element at 45 degrees because the coupling behaviour effect between spherical and deviatoric stress is maximum in this zone.

TIMODAZ

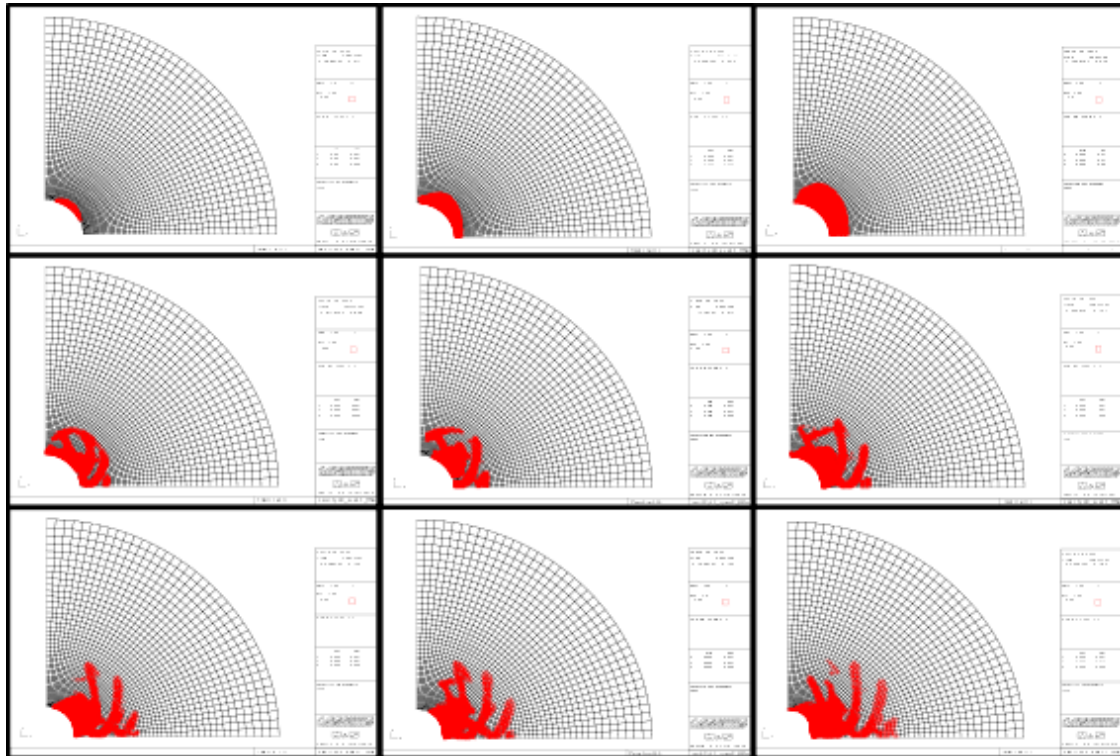


Figure 116: Localization phenomena at different times: 2268 s - 2940 s - 3360 s - 3617 s - 3711 s - 3900 s - 4026 s - 4100 s - 4200 s. Red points represent the plastic loading

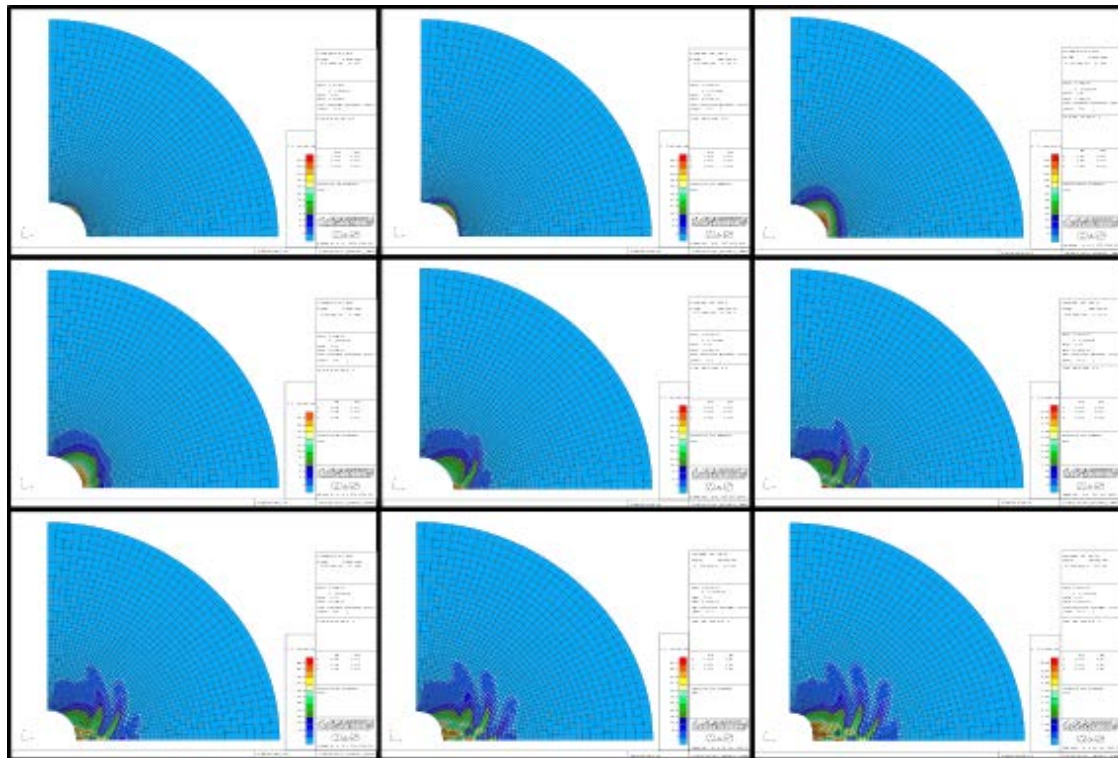


Figure 117: Equivalent plastic strains at different times: 2268 s - 2940 s - 3360 s - 3617 s - 3711 s - 3900 s - 4026 s - 4100 s - 4200 s

TIMODAZ

This is the first important difference with an isotropic elasto-plastic model where, at the beginning of the unloading, the solution is axially symmetric.

Another result perfectly consistent with the experimental test is that the direction of the maximum ovalization is not vertical (as it is expected for an elastic problem with cross-anisotropy) but horizontal. We can explain this aspect seeing the Figure 116 and Figure 117 where the plastic strain clearly tends to move in the direction of the most rigid plane (the bedding plane). The localization begins around the element at 0 degrees accumulating plastic strains as a consequence the displacements are bigger in the horizontal direction.

This aspect is confirmed observing Figure 118 and Figure 119 where the deviator and the mean stress for three elements at the internal radius are plotted.

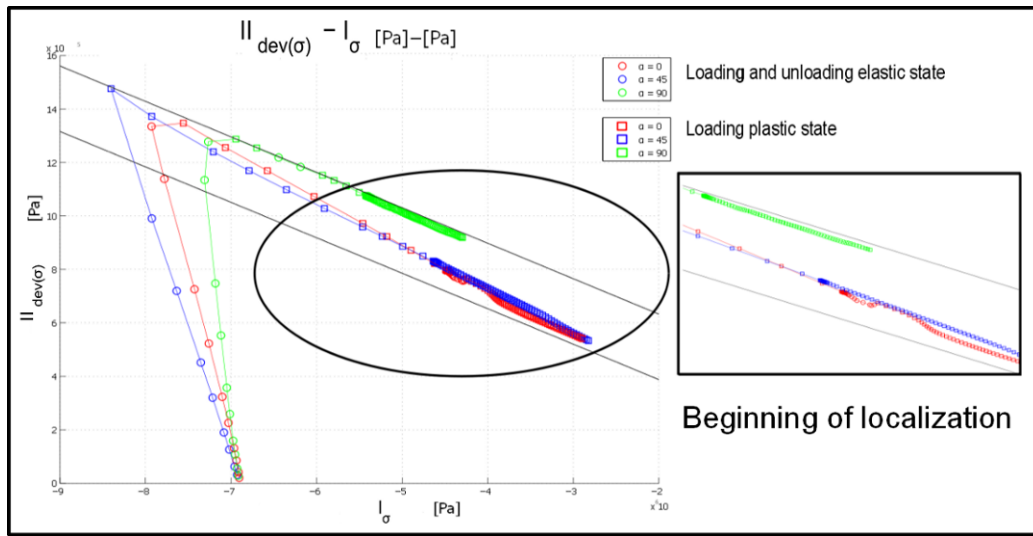


Figure 118: Stress state at the inner radius of cylinder for elements at 0, 45 and 90 degrees

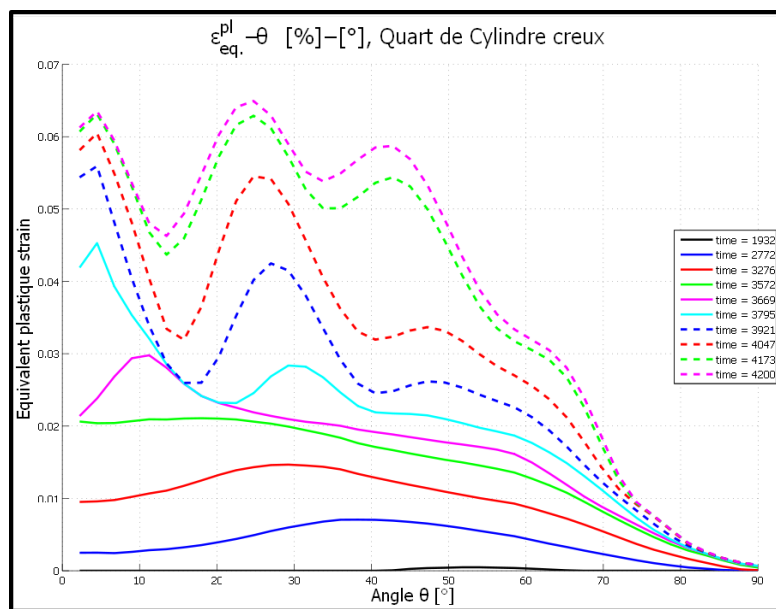
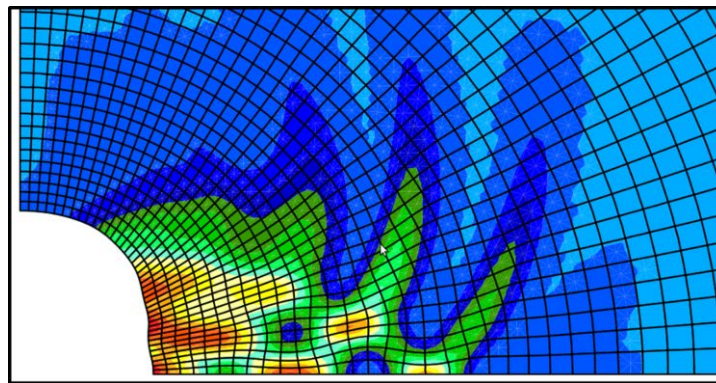


Figure 119: Equivalent plastic strains at inner radius for different times

In Figure 118 it is possible to see that the blue line satisfies the yield criterion before than the red one, but after the first plastic state the latest decreases faster than the former, which means that the plasticity rate is bigger for the element at 0 degrees. The green line rests almost parallel to the yield criterion, meaning that the Kuhn-Tucker condition is satisfied but not the persistence one, therefore the point is not loading plastically and the plastic strains are not so important as they are for the element at 0 and 45 degrees.

It is worthwhile to point out that the constitutive law is characterized by softening on the cohesion so the uniqueness Hill theorem is not respected and the uniqueness of the solution cannot be proofed. The solution obtained with this symmetry is one of the possible solutions that can be found with this constitutive law.

Considering the enlargement in Figure 118, it is possible to observe that at the beginning of localization the time step is very little because the variation of plastic strain field is very strong and some shear bands start to be created. In order to find another possible solution, i.e. different kinds of shear bands, it would be necessary to impose a perturbation to the initial strain rate of the numerical problem.



**Figure 120: Enlargement of equivalent plastic strain at the end of unloading (4200 s)**

In Figure 119 the evolution of the equivalent plastic strains at the inner quart of circle is presented. At the end of unloading path the peaks of the curve correspond to the angles where the localization begins (5, 25 and 43 degrees). This feature can be also appreciated in Figure 120, where three shear bands spread toward the external part of the cylinder. Two of these bands begin at 25 and 43 degrees and reflex themselves at the bottom of the cylinder where the vertical displacements are blocked. As it is observed from Figure 120, the internal part of the cylinder is irregular because of the presence of shear bands.

This aspect is in good agreement with the X-ray Tomography image result where it is possible to see that the internal configuration of the cylinder is not regular, even if the order of magnitude of the displacement between numerical and experimental results is not comparable.

For a better understanding of the displacement evolution (see Figure 121) two considerations have to be done:

- At the beginning of the unloading the maximum displacement is toward 90 degrees because along the vertical direction the Young modulus is smaller than in the horizontal one. Due to the localization of plastic deformation, the horizontal becomes the direction where the displacements are more important.

**TIMODAZ**

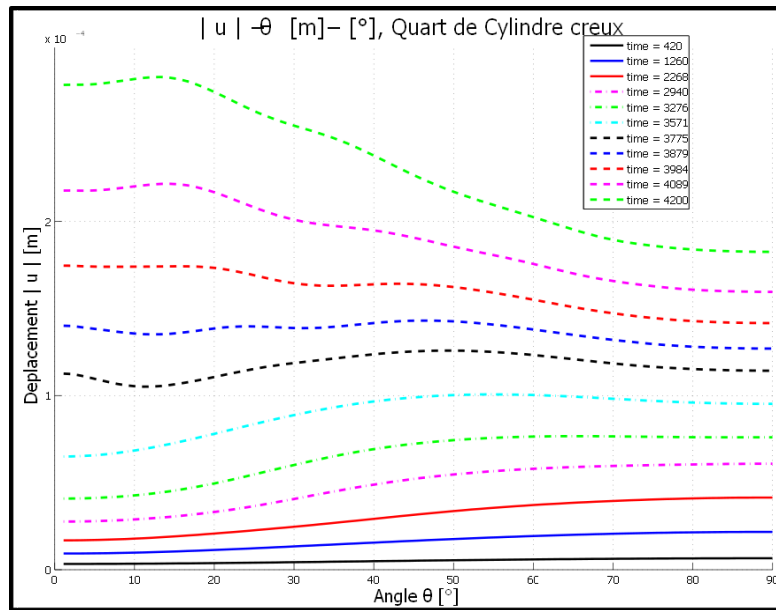


Figure 121: Displacement evolution along the inner quart of the cylinder

- Using the elasto-plastic parameters shown in Table 15, the order of magnitude of the displacement is not comparable to the ones obtained by the experimental tests for which the displacements are few millimetres.

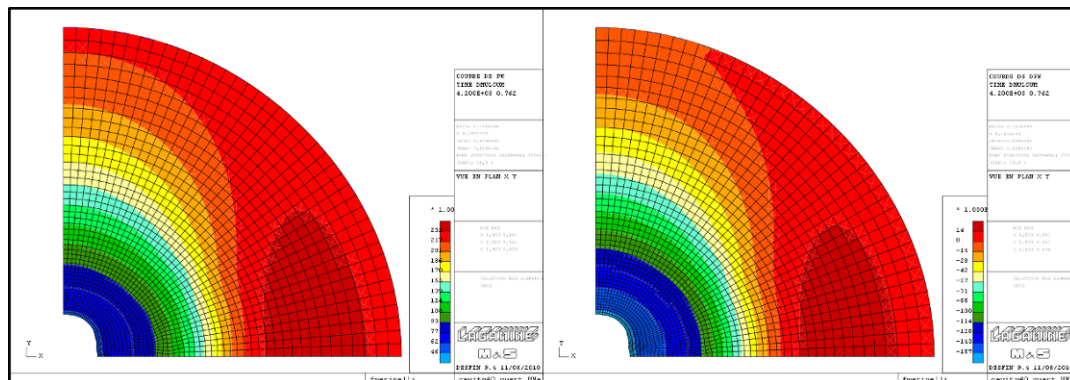


Figure 122: Trend of water pore-pressure field (left) and increment of water pore-pressure field (right)

Moreover, the unloading rate is not so slow to consider the problem completely drained. The water pore-pressure during the unloading is generated as shown on Figure 122. The presence of cross-anisotropy influences the water pressure fields, as well. Indeed, the solution is not axisymmetric as it would be for an isotropic elastic law.

The gradient of water pressure is bigger along the horizontal direction respect to the vertical one, where near the external radius the water pressure presents negative increment.

From Figure 126 and Figure 127 it is possible to see that in presence of the shear bands (at 0 degrees) the displacement does not evolve continuously, in contrast to the vertical direction where this variable shows a continuous behaviour.

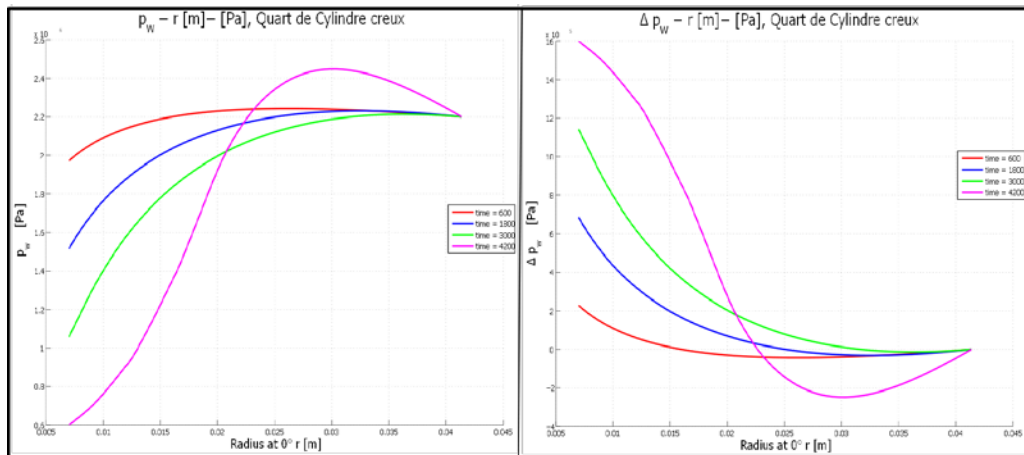


Figure 123: Trend of the water pore-pressure in the section at 0 degrees

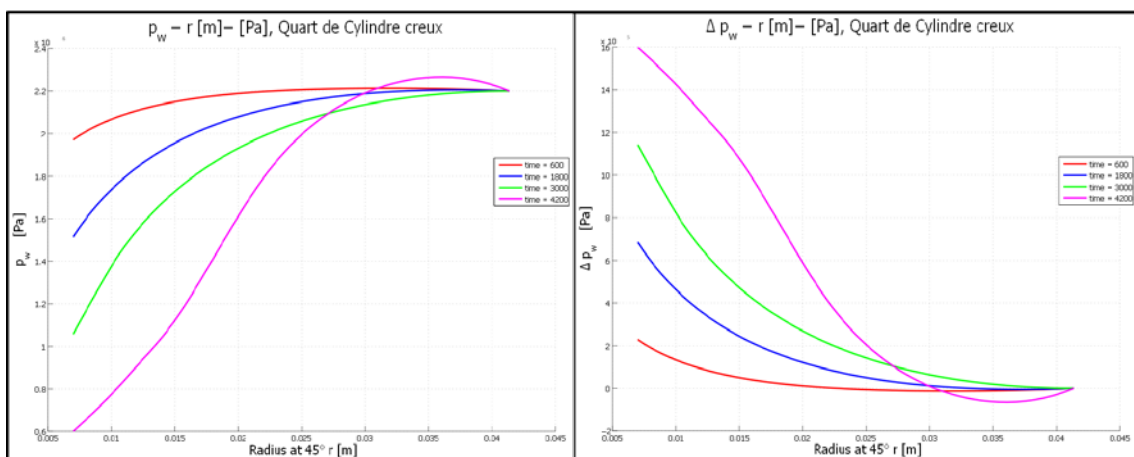


Figure 124: : Trend of the water pore-pressure in the section at 45 degrees

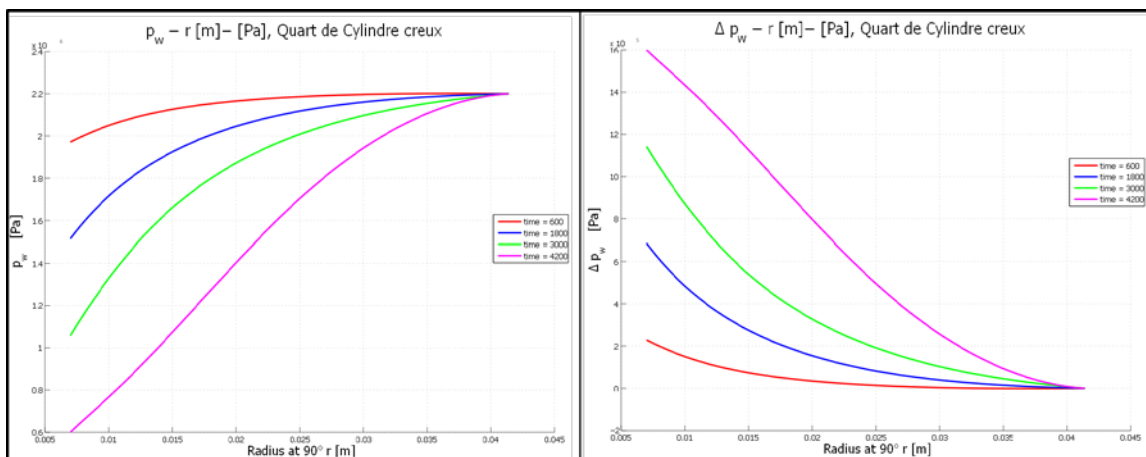


Figure 125: Trend of the water pore-pressure in the section at 90 degrees

TIMODAZ

IMR -N°: **D13 – Annex 1**

Dissemination level: **PU**

Date of issue of this report: **30/08/10**

111/142



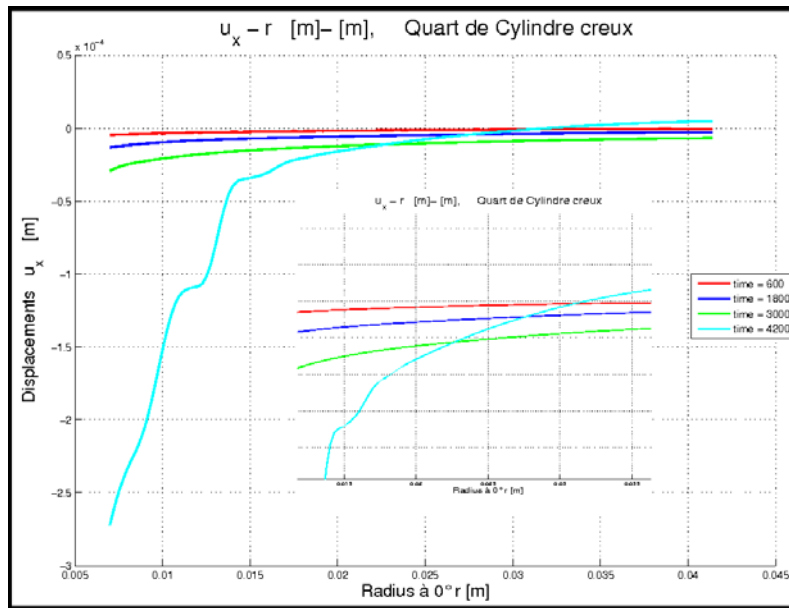


Figure 126: Trend of displacements along 0 degrees

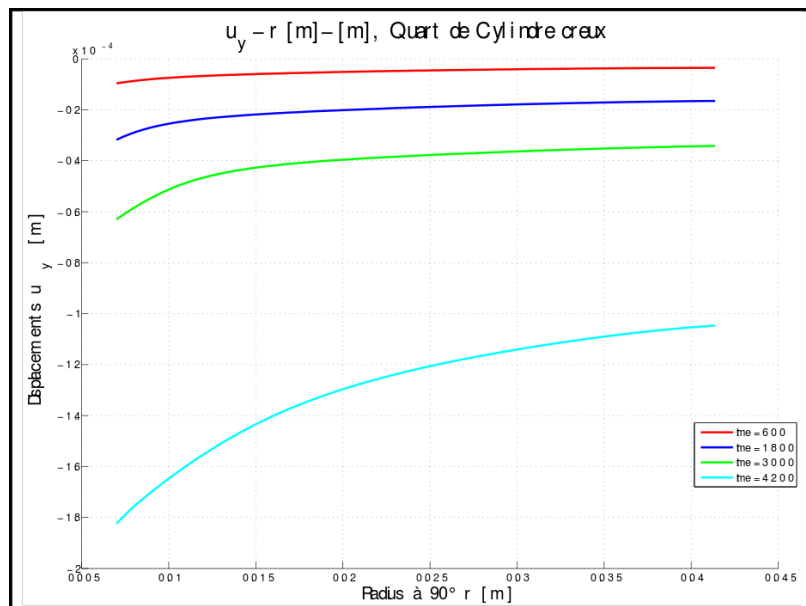


Figure 127: Trend of displacements along 90 degrees

## 11 Additional computations (ULg)

This section presents the results of numerical simulations performed by ULg in addition to the calculations that have been done in the context of the benchmark exercises (Section 4 to 6). Those additional computations address three distinct aspects. (i) Applying the same geometry

TIMODAZ

IMR -N°: **D13 – Annex 1**

Dissemination level: **PU**

Date of issue of this report: **30/08/10**

112/142



and boundary conditions that the ones defined in the benchmark exercise, a Mohr-Coulomb criterion, in stead of the Drucker-Prager yield limit, has been considered. (ii) Then, in order to study a possible anisotropic response of the Boom-Clay, numerical simulations considering 2D plane strain problem have been performed. (ii) Finally, 2D axisymmetric conditions have been assumed in order to study the effects of axial boundary conditions on the behaviour of the mid-plane section.

## 11.1 Mohr Coulomb criterion

This section summarises a comparison between two elastoplastic perfectly plastic constitutive laws. The two models are respectively the Drucker-Prager and the Mohr-Coulomb yield limit. In a first part, results obtained by using the Mohr-Coulomb criterion will be briefly described. As realised in the preceding section for the Drucker-Prager modelling, the results will be represented in two parts, on the first hand the hydro-mechanical modelling and on the second hand, the thermo-hydro-mechanical modelling.

In a third section, the comparisons between the two models will be established.

### 11.1.1 Mohr-Coulomb criterion- mechanical model

A Mohr-Coulomb criterion has been used in this calculation. This mechanical model is a non-associated elastoplastic constitutive law. The geometric representation in the stress space of this criterion is characterized by an irregular hexagonal pyramid. The trace of this yield limit in the deviatoric space represents an irregular hexagon. This criterion incorporate a dependence on the third stress invariant and thus on the Lode angle  $\beta$ .

The Mohr-Coulomb criterion is given by the following expression:

$$f \equiv \frac{I_\sigma}{3} \sin(\phi) + II_{\hat{\sigma}} \cos(\beta) - \frac{III_{\hat{\sigma}}}{\sqrt{3}} \sin(\beta) \sin(\phi) - c \cos(\phi) = 0 \quad (11.1)$$

where  $\beta$  is the Lode angle defined by:

$$\beta = -\frac{1}{3} \sin^{-1} \left[ \frac{3\sqrt{3}}{2} \frac{III_{\hat{\sigma}}}{II_{\hat{\sigma}}^3} \right] \quad (11.2)$$

with  $I_\sigma$  : the first stress invariant,  
 $II_{\hat{\sigma}}$  : the second deviatoric stress invariant,  
 $III_{\hat{\sigma}}$  : the third stress invariant;

and  $\phi$  represents the friction angle. This criterion predicts identical friction angles under triaxial compression paths and triaxial extension paths.



## 11.1.2 Results of the modelling: hydro-mechanical aspect

For the whole calculation, results obtained with a Mohr-Coulomb criterion are similar to those established with a Drucker-Prager criterion.

### *Pore water pressure*

The evolution of the radial profiles of pore water pressure is plotted in Figure 128. The pore pressure decrease at the lining of the cavity is due to the diminution of the pressure at the inner cavity. When the stabilisation occurs, a drawdown of the pore pressure appears.

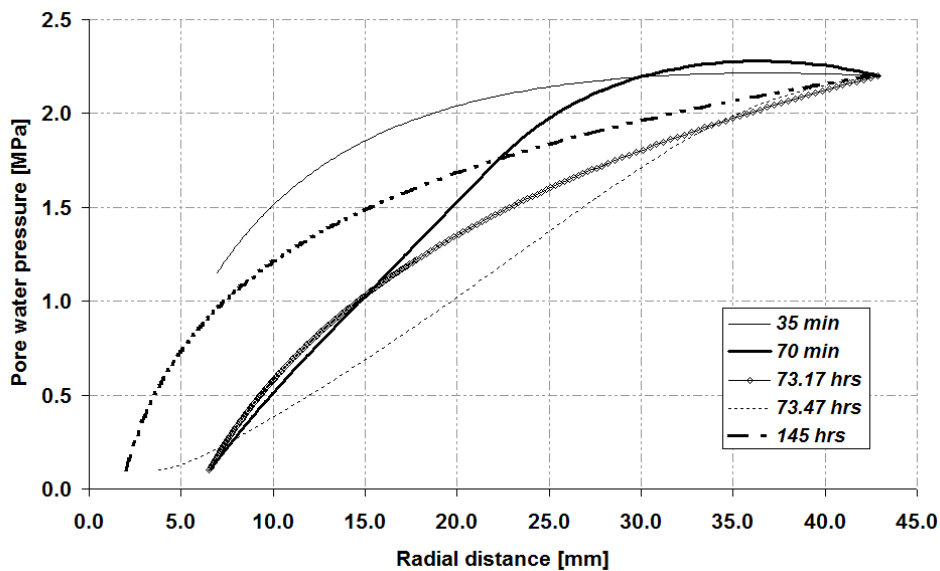


Figure 128: Pore water pressure vs radial distance for several times

### *Stress path*

Figure 129 exhibits the stress path at the inner radius for the Mohr-Coulomb criterion. During the excavation phase, the first stress invariant and the second deviatoric stress invariant increases until they reach the Mohr-Coulomb criterion. At that moment, the stress state follows the yield limit. Due to the fact that the criterion is influenced by the Lode angle, the evolution of the stress state on the yield surface is not linear in the  $(I_{\sigma}, II_{\sigma})$  plane. At the end of the deconfining phase, the stress state is plastic.

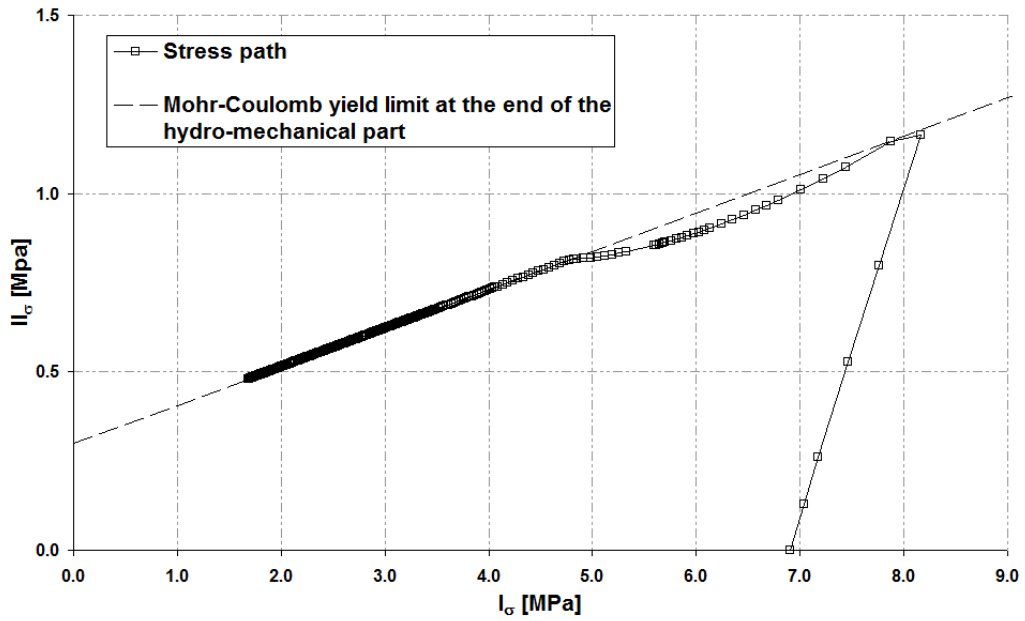


Figure 129: Evolution of the stress path during the excavation phase. The Mohr-Coulomb criterion is plotted at the end of hydro-mechanical part

Figure 130 represents the stress path followed by the stress state during the excavation phase in the deviatoric space. The evolution of Lode angle is observed once the yield limit is reached.

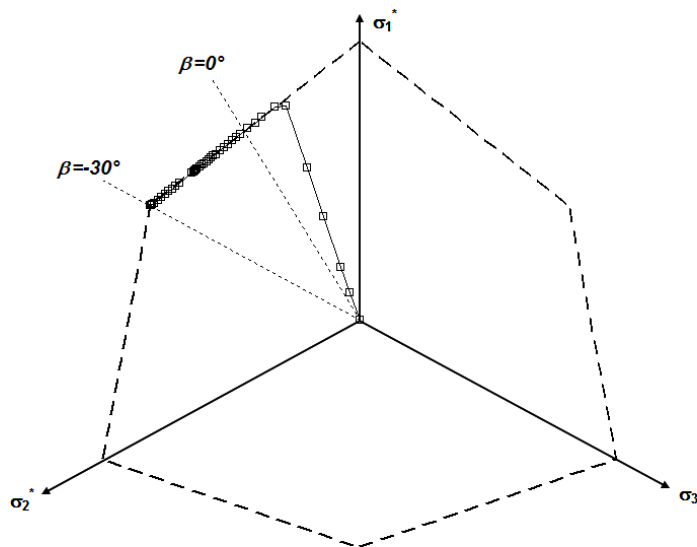


Figure 130: Representation of the stress path in the deviatoric plane at the inner radius. The black dot line corresponds to a pure shear line ( $\beta = 0^\circ$ )

### *Radial displacements*

The profile of the radial displacements is plotted at different times in Figure 131. The convergence increases with the reduction of the total radial stress and the final value of the radial displacements at the end of the hydro-mechanical part is equal to 5.03 mm.

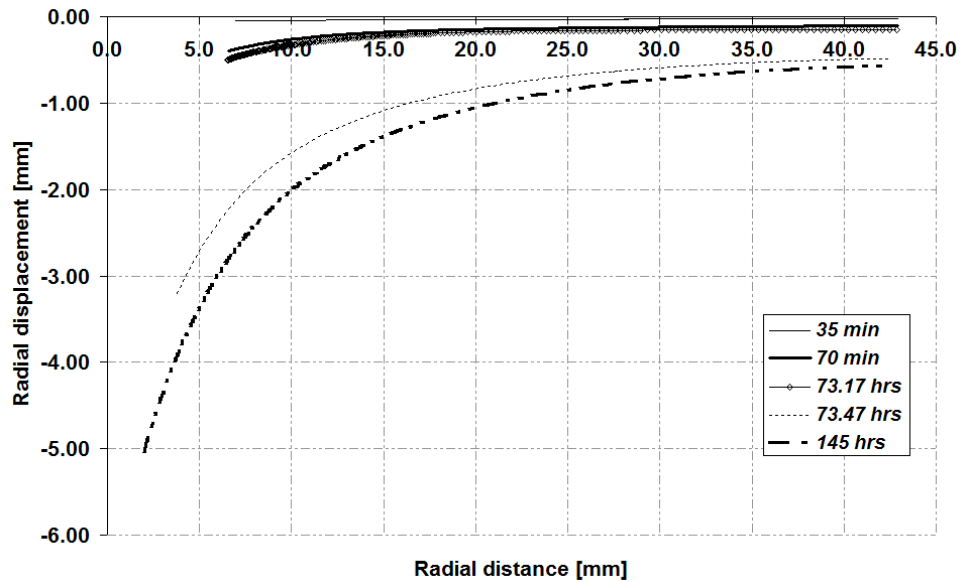


Figure 131: Evolution of the radial displacements with the radial distance for different times

### *Plastic indicator*

The evolution of the stress state through the plastic indicator is represented in Figure 132. During the excavation, the plastic radius increases thanks to the excavation. At the end of the excavation phase, stress state is plastic in the whole sample.

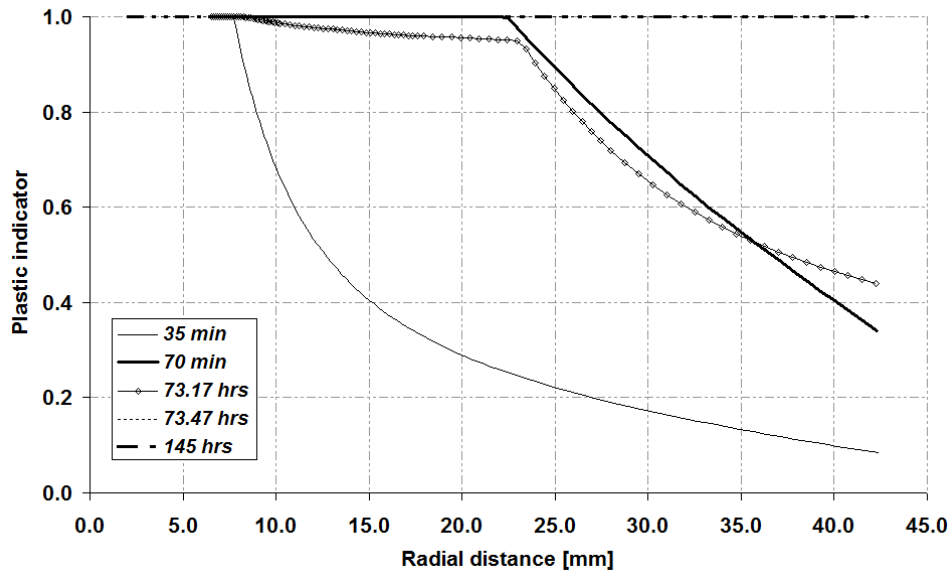


Figure 132: Plastic indicator as a function of the radial distance at several times

### 11.1.3 Results of the modelling: thermo-hydro-mechanical aspect

The thermo-hydro-mechanical behaviour of the clay sample modelled with a Mohr-Coulomb yield limit is the same as the behaviour obtained with the Drucker-Prager criterion.

#### *Pore water pressure*

Figure 133 presents the radial evolution of the pore water pressure. During the temperature increase, the pore water pressure increases due to the dilation of water. A pore pressure decrease is induced by thermal consolidation during the stabilisation phase. At last, the pore pressure increases when the temperature increases.

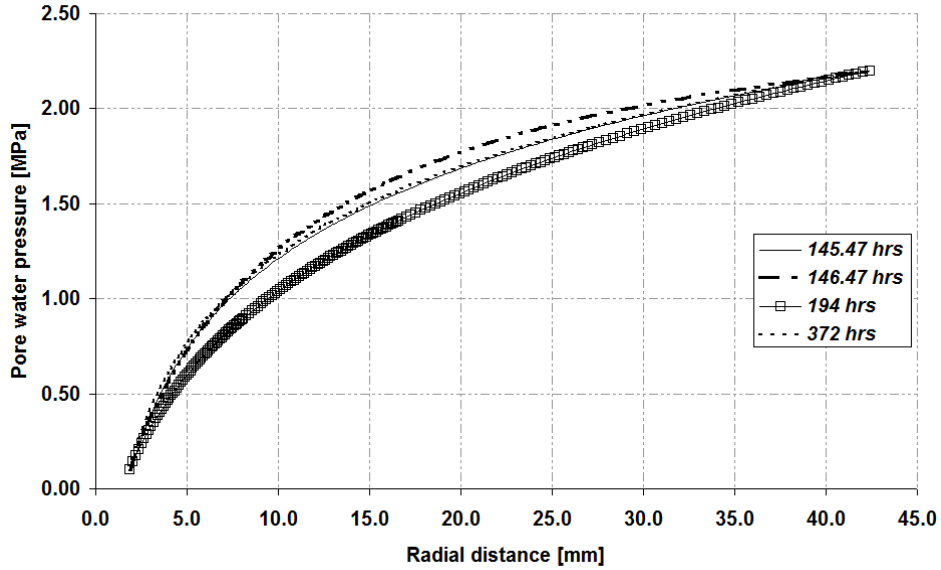


Figure 133: Pore water pressure as a function of the radial distance at different times

### Stress path

The evolution of the stress state during the heating/cooling phase is plotted in Figure 134. Once again, a slight variation of the stress state is observed during the heating/cooling cycle. Moreover, a variation of the Lode angle is noticed during this cycle. At the end, an elastic unloading appears.

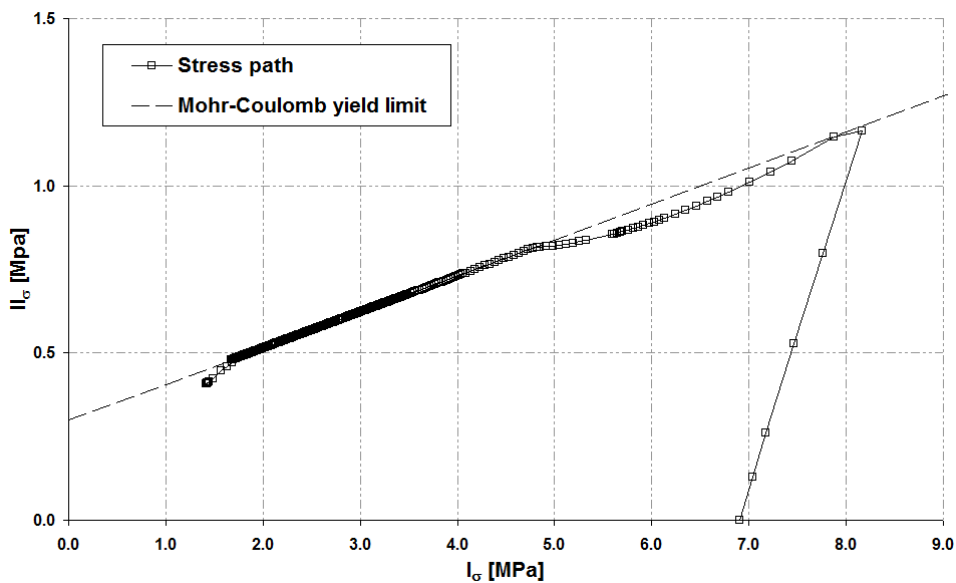


Figure 134: Stress path evolution at the surface of the cavity during the whole modelling

Figure 135 represents the evolution of the stress path during the whole modelling in the deviatoric space. As compare to the hydro-mechanical part, the stress path goes away from the yield limit during the heating/cooling cycle.

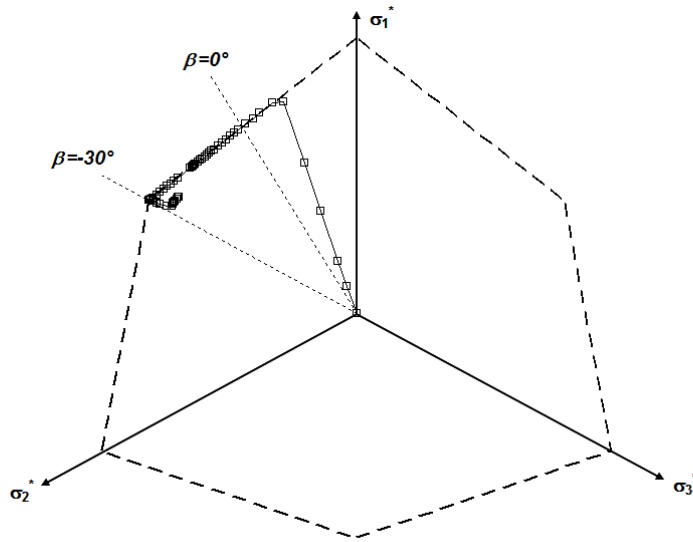


Figure 135: Representation of the stress path in the deviatoric plane

**Radial displacements**

Figure 136 exhibits radial profiles of the radial displacements during the heating/cooling cycle. The effect of the thermal phase does not affect the convergence of the cavity.

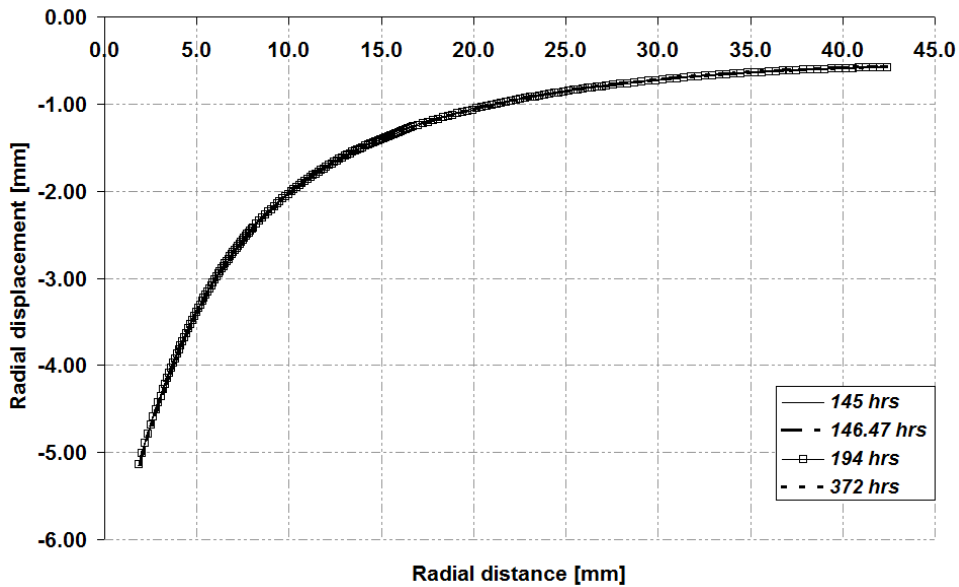


Figure 136: Radial displacements vs radial distance during the heating/cooling cycle

**Plastic indicator**

Figure 137 represents the plastic indicator versus the radial distance for several times. When the pore pressure decreases, the mean effective stress decreases and, stress state becomes elastic



(194 hrs). After this time, the pore pressure increases and the stress state comes closer to plastic state.

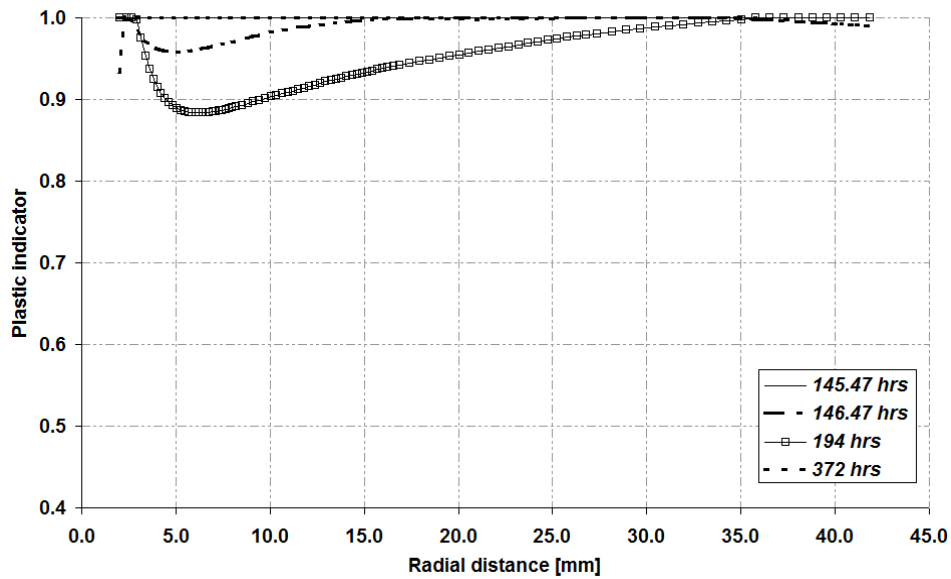


Figure 137: Plastic indicator as a function of the radial distance for several times

#### 11.1.4 Comparison Mohr-Coulomb Drucker-Prager

In this part, a comparison between the two mechanical models will be established at the end of the calculation (at 372 hrs). For the simplicity of this report, only a few results will be presented.

##### *Pore water pressure*

In Figure 138, the difference obtained in the profile of the pore pressure for the two models is shown. The profile associated to the Mohr-Coulomb criterion show higher pressure than the profile with the Drucker-Prager. This difference is caused by the higher convergence of the cavity for the Mohr-Coulomb criterion.

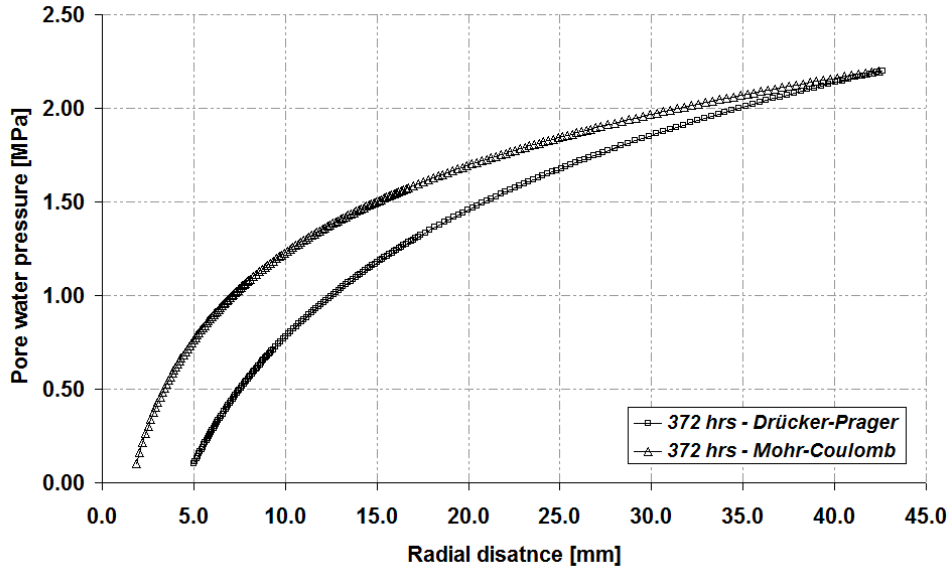


Figure 138: Comparison between the two models at the end of the calculation

*Radial displacement*

Figure 139 represents the convergence of the cavity for the two models. The Mohr-Coulomb criterion allows a plastic behaviour at a lower stress as the Drucker-Prager criterion. Consequently, the convergence in the Mohr-Coulomb criterion is higher.

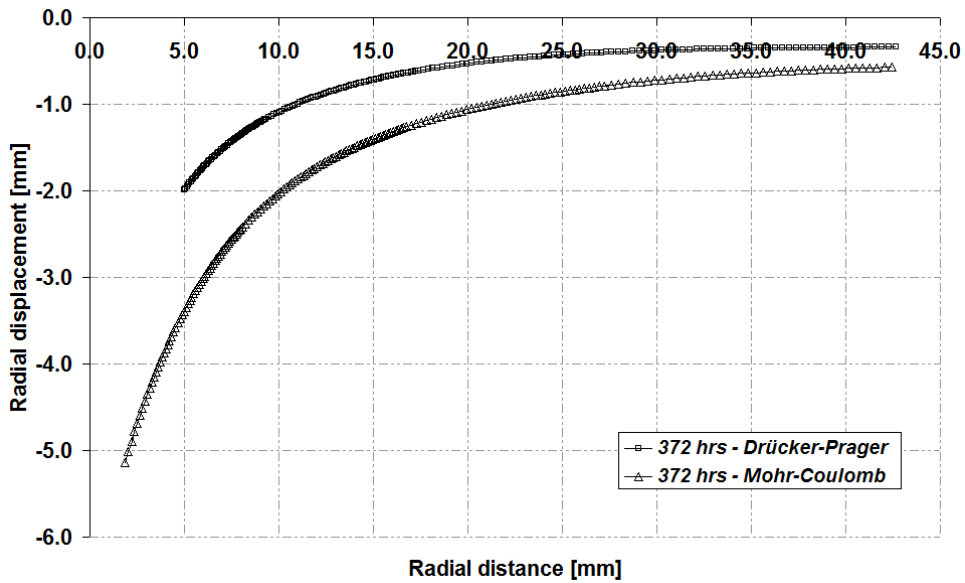


Figure 139: Comparison of the radial displacements at the end of the modelling

*Stress path*



Figure 140 represents the stress path for the two mechanical models. The Mohr-Coulomb criterion allows a plastic behaviour at a lower stress state as compare to the Drucker-Prager criterion.

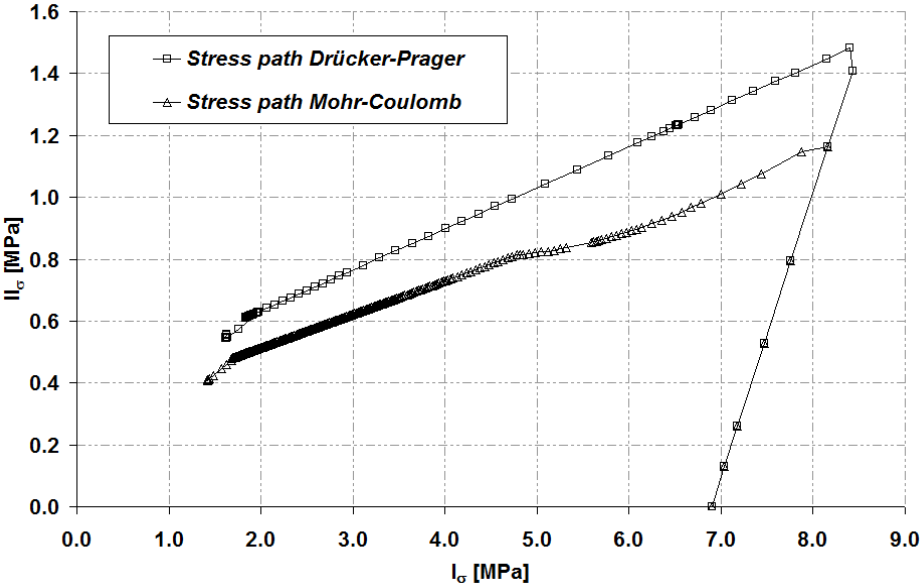


Figure 140: Stress path for the two mechanical models.

Figure 141 illustrates stress path in the deviatoric plane for the two criteria. This figure permits to compare the different plastic behaviour defined by the two yield limits.

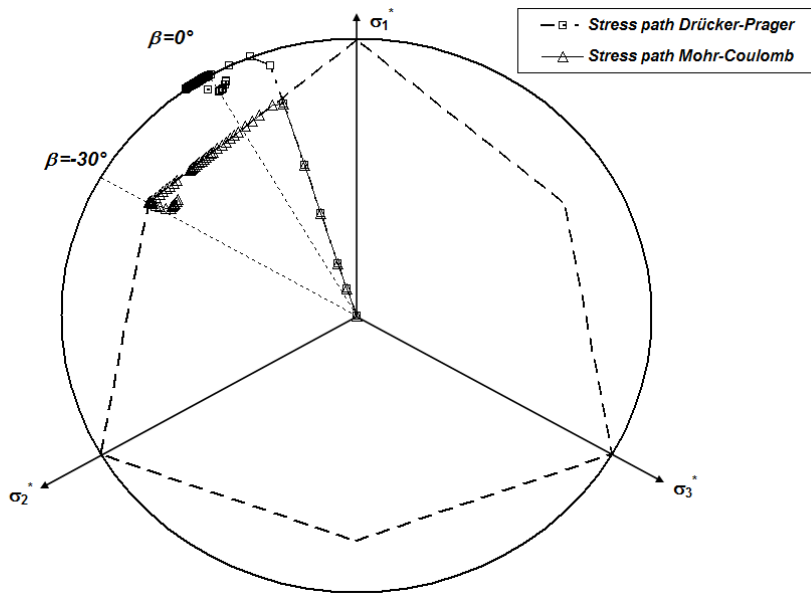


Figure 141: Representation of the stress path in the deviatoric plane for the two mechanical models.



## 11.2 2D plane strain case

### 11.2.1 Introduction

The one-dimensional axisymmetric problem, as treated in the first part of the report, allowed us to obtain interesting results, at least qualitatively, and provided us a simple case to compare results obtained by the different teams. However, this case is subject to some limitations. In particular, the directional dependency of the radial displacements induced by mechanical anisotropy of the rock can not be reproduced by 1D simulations. Also, the modelling of possible strain localisations requires a 2D plane strain modelling. Finally, in order to study the effect of axial boundary conditions (at the top and the bottom of the hollow cylinder), 2D axisymmetric simulations must be performed.

So, in this section, two specific geometries of the problem are treated. They will be successively addressed in the two next sub-sections. The objective of the 2D plane strain modelling is to catch the anisotropic response of the materials and the possible strain localisations. For that case, the numerical results will be compared with experimental measurements. 2D axisymmetric case aims at studying the effect of axial boundary conditions.

### 11.2.2 Geometry and boundary conditions

The objective of this simulation is to reproduce the behaviour of the material in the mid-plane section of the hollow cylinder, assuming plane strain conditions. Because of the symmetry of the problem, a quarter of the entire section is considered (Figure 142). In term of mechanical conditions, the inner and outer boundaries are stress controlled. The total stress at the external boundary is kept constant at 4.5 MPa all along the simulation, while the internal stress is decreased in agreement with the experimental conditions. Let's note that those conditions are a bit different from the case considered in the benchmark exercise above. The decrease of the internal stress is limited down to 1.0 MPa, as applied in the experiment, instead of 0.1 MPa for the benchmark case. Because of the problem symmetry, the displacements of the radial boundaries are perpendicularly constrained. In term of hydraulic conditions, the pore water pressure is controlled in the inner and outer boundaries. Constant water pressure of 2.2 MPa is maintained at the external radius while the internal pore water pressure is decreased from 2.2 MPa to 0.6 MPa. Those values differ also from the pore pressure imposed for the benchmark exercise. The radial boundaries are assumed impervious (because of the symmetry of the problem). The boundary conditions are summarized in Figure 143. The simulations are limited to the isothermal conditions.

TIMODAZ



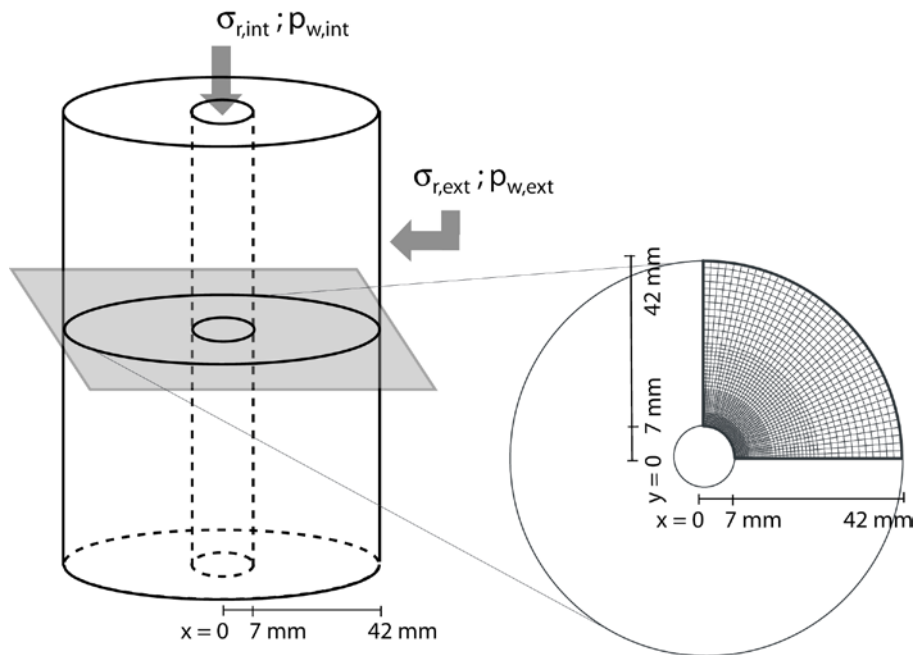


Figure 142: Modelling of the hollow cylinder in two dimensional axisymmetric conditions by a quarter of the entire section.

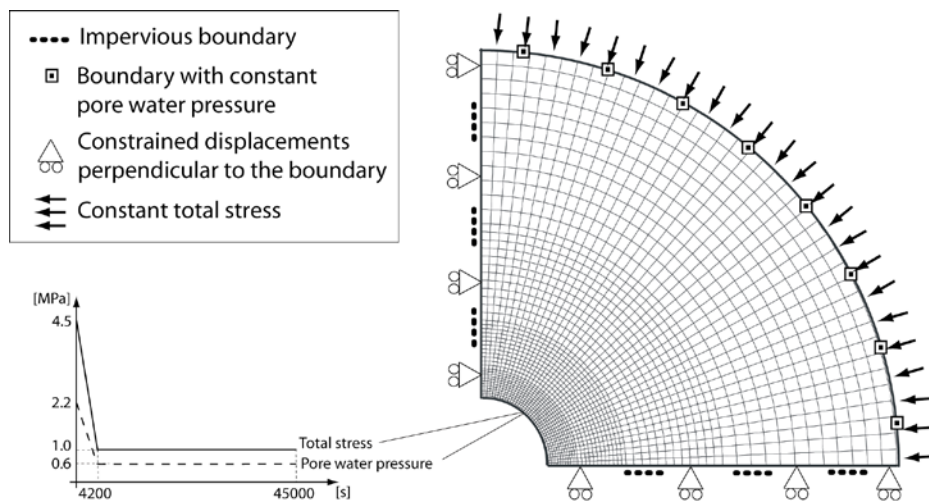


Figure 143: Hydro-mechanical boundary conditions of the two dimensional axisymmetric case.

### Constitutive model and material parameters

In order to reproduce the anisotropic response of the materials, a Drucker-Prager hardening model (similarly to the benchmark exercise) has been coupled with cross-anisotropic elasticity and also a dependency of the cohesion with the major principal stress direction with respect to bedding orientation.

The elasto-plastic stress-strain relations are expressed in the anisotropic axis. In the present case, the anisotropic axes correspond to the global axes with bedding oriented in the x direction (Figure 144).

TIMODAZ



$$C_{ijkl}^e = \begin{bmatrix} \frac{1 - \nu_{//\perp} \nu_{\perp//}}{E_{//} E_{\perp} \det} & \frac{\nu_{////} + \nu_{\perp//} \nu_{//\perp}}{E_{//} E_{\perp} \det} & \frac{\nu_{////} \nu_{\perp//} + \nu_{\perp//}}{E_{//} E_{\perp} \det} \\ \frac{\nu_{////} + \nu_{\perp//} \nu_{\perp//}}{E_{//} E_{\perp} \det} & \frac{1 - \nu_{//\perp} \nu_{\perp//}}{E_{//} E_{\perp} \det} & \frac{\nu_{\perp//} + \nu_{\perp//} \nu_{////}}{E_{//} E_{\perp} \det} \\ \frac{\nu_{//\perp} + \nu_{//\perp} \nu_{////}}{E_{//} E_{//} \det} & \frac{\nu_{//\perp} + \nu_{////} \nu_{//\perp}}{E_{//} E_{//} \det} & \frac{1 - (\nu_{////})^2}{E_{//} E_{//} \det} \end{bmatrix} \begin{matrix} 2G_{////} \\ 2G_{//\perp} \\ 2G_{//\perp} \end{matrix} \quad (11.7)$$

with

$$\det = \frac{1 - 2\nu_{\perp//} \nu_{//\perp} - \nu_{////} \nu_{////} - 2\nu_{\perp//} \nu_{////} \nu_{//\perp}}{(E_{//})^2 E_{\perp}} \quad (11.8)$$

The plastic part of the model, using a hardening Drucker-Prager law, is similar to the plastic model used in the benchmark exercise as described in section 4.4.1.

The model parameters of the Boom Clay (BC) used in the benchmark exercise has been retrieved and the elastic constant has been modified to consider elastic anisotropy (Table 16 and Table 17). However, the complexity of the material behaviour has been addressed progressively. Five cases have been considered as summarized in Table 18.

Geomechanical characteristics		Boom Clay				
		Case 1	Case 2	Case 3	Case 4	Case 5
Young elastic modulus [MPa]	$E_{//}$	500	500	500	500	500
Young elastic modulus [MPa]	$E_{\perp}$	250	250	250	250	250
Poisson ratio [-]	$\nu_{////}$	0.125	0.125	0.125	0.125	0.125
Poisson ratio [-]	$\nu_{//\perp}$	0.125	0.125	0.125	0.125	0.125
Initial cohesion [kPa]	$c_0$	-	300	300	300	270 (0°) 255 (45°) 525 (90°)
Final cohesion [kPa]	$c_f$	-	300	100	300	90 (0°) 85 (45°) 175 (90°)
Softening parameter [-]	$\beta_c$	-	-	0.01	-	0.01
Initial friction angle [°]	$\phi_{c0}$	-	18	5	10	5
Final friction angle [°]	$\phi_{cf}$	-	18	18	10	18
Hardening parameter [-]	$\beta_{\phi}$	-	-	0.01	-	0.01
Dilatation angle [°]	$\psi$	-	0	0	0	0
Biot's coefficient [-]	$b$	1	1	1	1	1

Table 16: Geomechanical characteristics

TIMODAZ



Hydraulic characteristics		Boom Clay
Initial porosity	$n_0$	0.39
Initial intrinsic permeability [m <sup>2</sup> ]	$k_{int}^{sat}$	$4.10^{-19}$
Water specific mass [kg/m <sup>3</sup> ]	$\rho_w$	1000
Fluid dynamic viscosity [Pa.s]	$\mu_w$	$10^{-3}$
Liquid compressibility coefficient [MPa <sup>-1</sup> ]	$1/\chi_w$	$5.10^{-4}$

Table 17: Hydraulic characteristics

Case	Clay	HM coupling	Cross-anisotropic elasticity	Perfect plasticity	Friction angle hardening	Cohesion softening	Reduced friction angle ( $\phi = 10^\circ$ )	Anisotropic cohesion
1	BC							
2	BC							
3	BC							
4	BC							
5	BC							

Table 18: Summary of the different cases modelled in 2D plane strain conditions

### Experimental results

The objective of this parametric study is to determine the most suitable set of parameters able to reproduce the intensity of radial displacement as a function of the radial direction with respect to the bedding orientation. The experimental measurements of the central hole displacement show a clear directional dependency (Figure 145a). The initial circular hole is transformed into an oval hole after the mechanical unloading. The displacements in the direction parallel to bedding is much than twice larger than the displacement perpendicularly to bedding (Figure 145b).

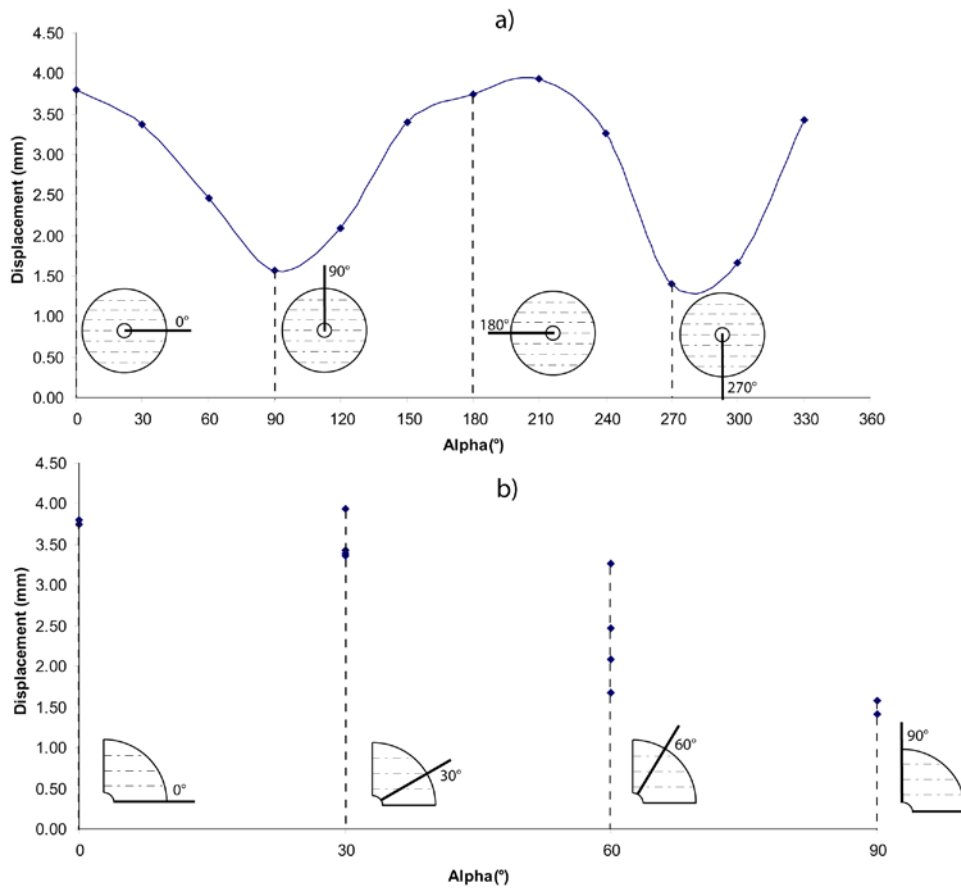


**Figure 145: Experimental measurements of the central hole displacement at the end of the mechanical unloading and pore water pressure dissipation. The measurements in the entire section (a) are reported in the quarter of the section (b) by considering the symmetry of the problem**

### *Results of numerical simulations*

The purely elastic case (Case 1) emphasises the anisotropic behaviour of the material (Figure 146). The larger displacements are obtained in the more compressible direction (perpendicular to bedding). However, this case largely underestimates the obtained displacement (around 0.1 mm) with respect to experimental results (2 to 4 mm). It shows that a plastic model is required to reproduce the large displacements observed in experiment.

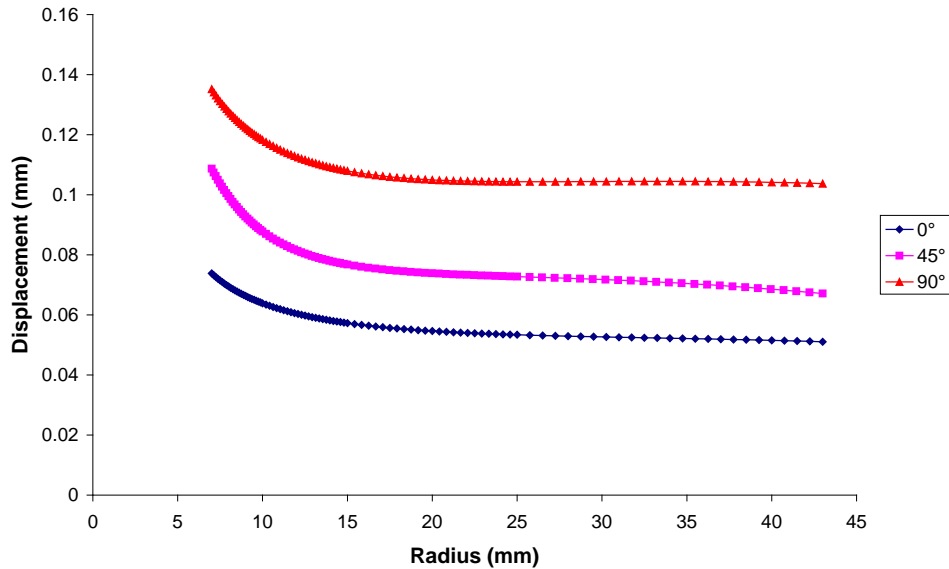


**Figure 146: Radial displacement versus radial distance in case 1 after mechanical unloading and water pressure dissipation in the direction parallel ( $\alpha=0^\circ$ ), perpendicular ( $\alpha=90^\circ$ ) and at  $45^\circ$  to the bedding plane**

The first extension of the elastic case consists in a perfectly plastic Drucker-Prager model for which a constant friction angle of  $18^\circ$  and a cohesion of 300 kPa is considered. Once again, directional dependency of the radial displacement is obtained but the displacements remains much lower than the experimental results (Figure 147). The plastic component tends to counterbalance the effect of elastic anisotropy. The intensity of plastic shear strain is larger in the direction perpendicular to bedding (Figure 148). Consequently, the direction which is the more rigid in purely elastic case becomes the less rigid in elasto-plasticity. This is probably due to non-linear hydro-mechanical transient effect. During consolidation process, the dissipation of pore water pressure is slower in the more rigid direction. As a consequence, mean effective stress is lower in that direction which reduces the shear strength inducing higher plastic shear strain.

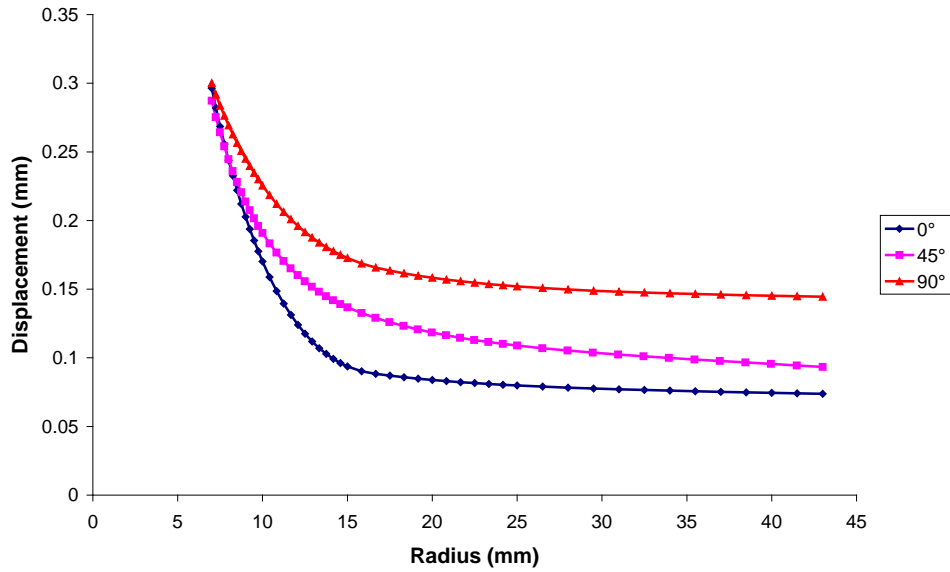


**Figure 147: Radial displacement versus radial distance in case 2 after mechanical unloading and water pressure dissipation in the direction parallel ( $\alpha=0^\circ$ ), perpendicular ( $\alpha=90^\circ$ ) and at  $45^\circ$  to the bedding plane**

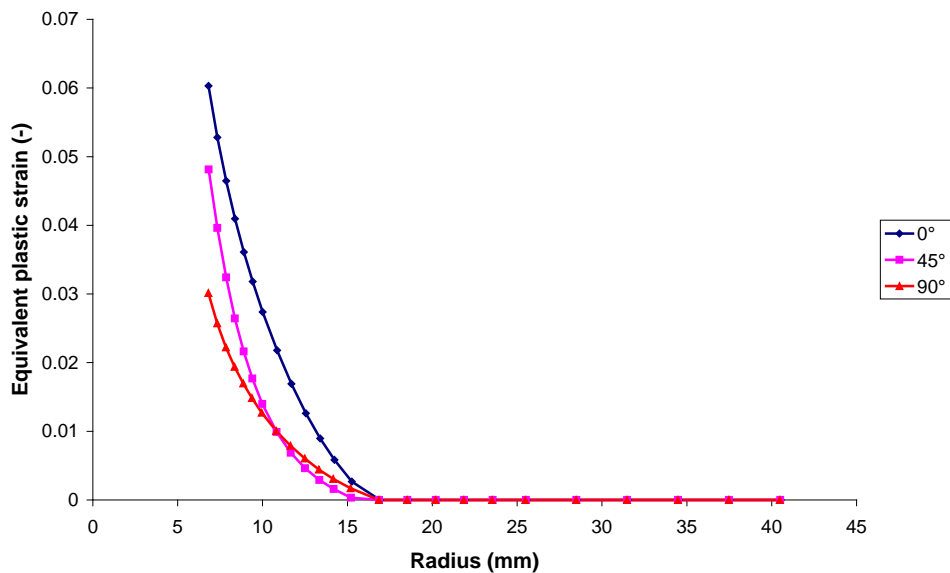


**Figure 148: Equivalent plastic strain versus radial distance in case 2 after mechanical unloading and water pressure dissipation in the direction parallel ( $\alpha=0^\circ$ ), perpendicular ( $\alpha=90^\circ$ ) and at  $45^\circ$  to the bedding plane**

In order to enhance the radial displacement, as observed experimentally, it is clear that the plastic strength must be drastically reduced. To this end, two alternatives are considered. Case 3 which uses a combined friction angle hardening and cohesion softening corresponds to case C of the benchmark exercise. The cohesion softening allows us to model the post peak response of the Boom Clay. After passing through a maximum of strength, the residual strength is less than the peak strength. The magnitude of displacements obtained in the simulations is now more in agreement with the experimental displacements (Figure 149). However, the effect of the



direction on the central hole displacements is not large enough with respect to the experimental observations (Figure 150).

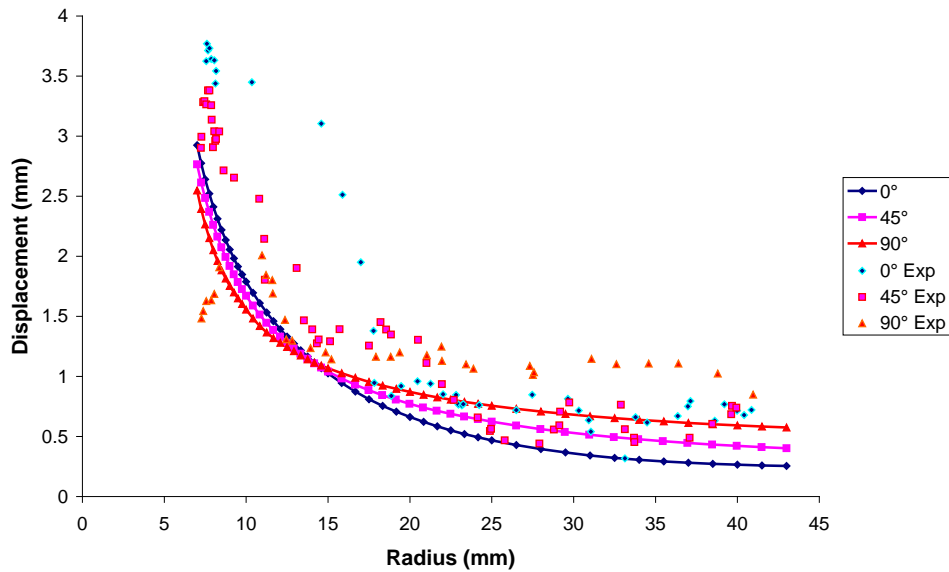


**Figure 149: Radial displacement versus radial distance in case 3 after mechanical unloading and water pressure dissipation in the direction parallel ( $\alpha=0^\circ$ ), perpendicular ( $\alpha=90^\circ$ ) and at  $45^\circ$  to the bedding plane. Comparison with experimental measurements**

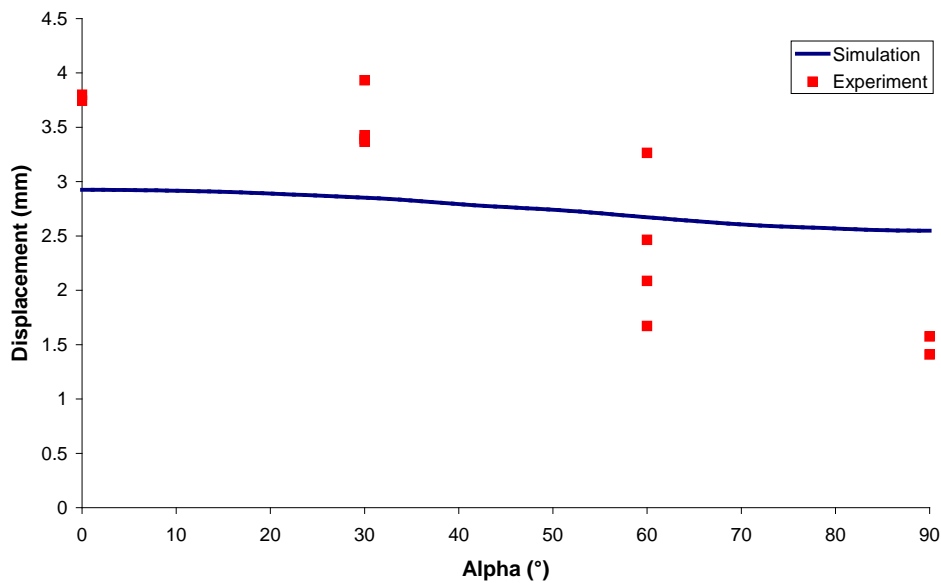


**Figure 150: Central hole displacement as a function of the orientation with respect to bedding plane in case 3. Comparison with experimental measurements**

The second alternative is to keep a perfectly plastic Drucker-Prager model and reduce the friction angle from  $18^\circ$  to  $10^\circ$ . In that case, the anisotropic radial displacements of the central hole are much better reproduced (Figure 152). However, the displacements of the outer region



perpendicularly to bedding are negative which correspond to extension of that external zone (Figure 151). This aspect is not in agreement with experiment.

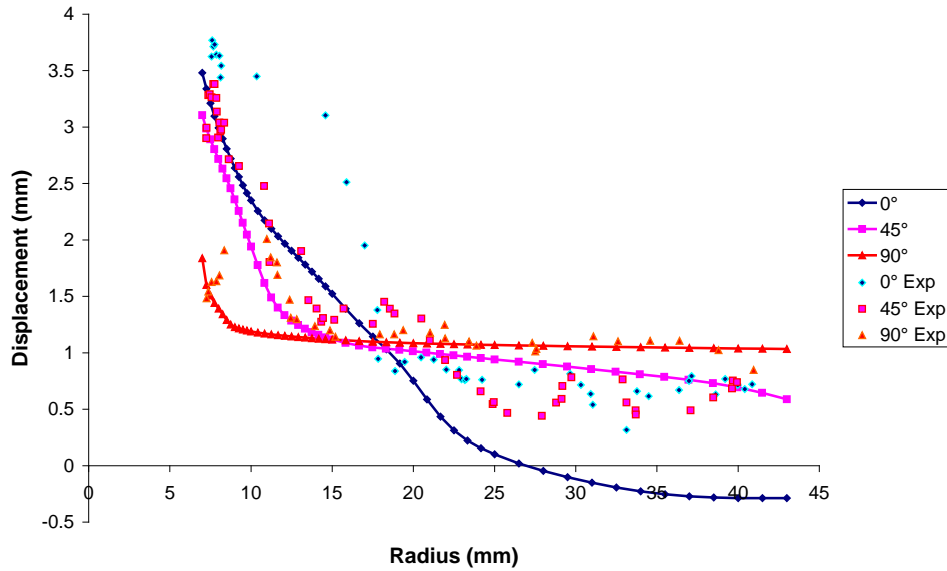


**Figure 151: Radial displacement versus radial distance in case 4 after mechanical unloading and water pressure dissipation in the direction parallel ( $\alpha=0^\circ$ ), perpendicular ( $\alpha=90^\circ$ ) and at  $45^\circ$  to the bedding plane. Comparison with experimental measurements**

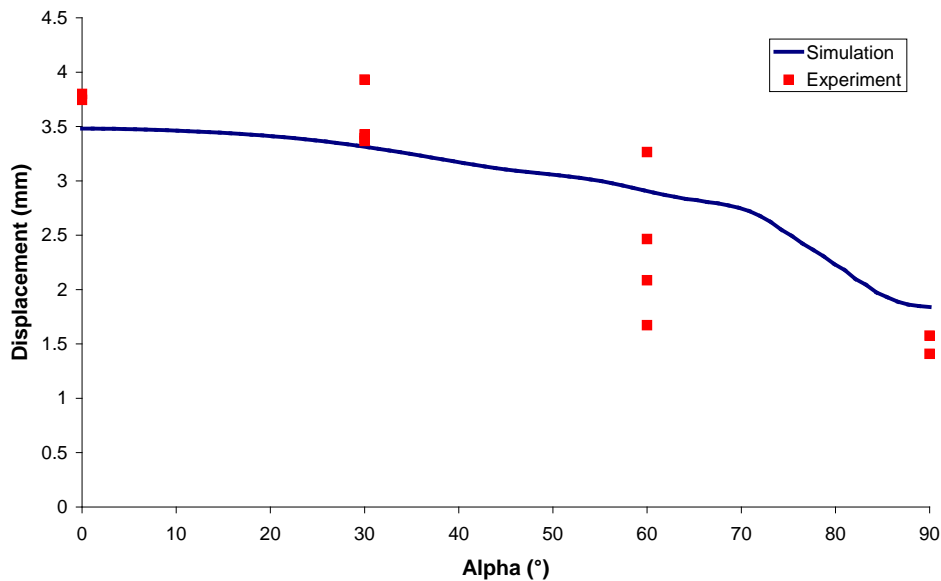


**Figure 152: Central hole displacement as a function of the orientation with respect to bedding plane in case 4. Comparisons with experimental measurements**

Finally, in addition to elastic anisotropy, shear strength may also be affected by the direction of loading with respect to the direction of bedding. To reproduce that effect, an extended Drucker-Prager yield limit has been developed considering that the material cohesion depends on the angle between major principal stress and the normal to the bedding plane (Figure 153). Three cohesion values are defined, for principal stress parallel ( $\theta = 0^\circ$ ), perpendicular ( $\theta = 90^\circ$ ) and

TIMODAZ



with an angle of  $45^\circ$  ( $\theta = 45^\circ$ ) with respect to normal to the bedding plane. Between those values, cohesion varies linearly with  $\theta$ . The considered value of  $c(\theta)$  is reported in (Case 5).

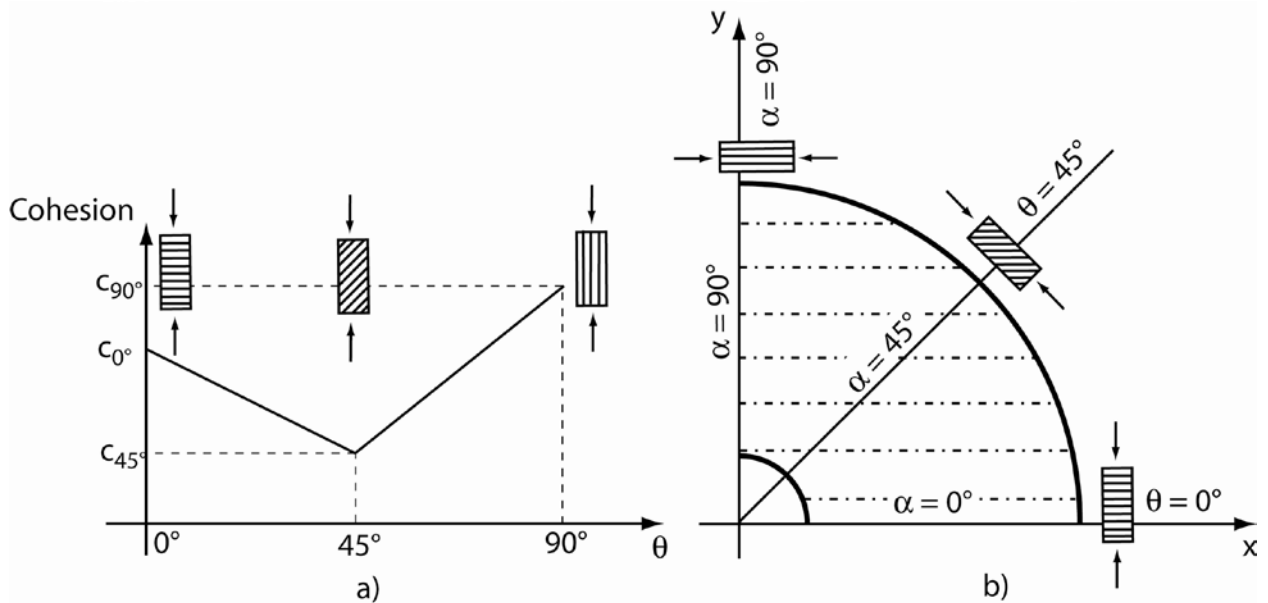


**Figure 153: (a) Variation of cohesion according to the angle between major principal stress and bedding plane. (b) Representation in the hollow cylinder geometry, the major principal stress being circumferential.  $\alpha$  is the angle between bedding plane and the considered direction and  $\theta$  is the angle between the normal to the bedding plane and the major principal stress**

This anisotropic plastic criterion allows us to get the best agreement with respect to the experimental measurements. However, it remains a small discrepancy in the obtained displacements in the outer zone for  $\alpha = 0^\circ$  (Figure 154). As experimentally observed, the central hole displacement is almost constant between  $\alpha = 0^\circ$  and  $\alpha = 30^\circ$  (at a value of 4 mm) and then decreases to 2 mm for  $\alpha = 90^\circ$  (Figure 155).

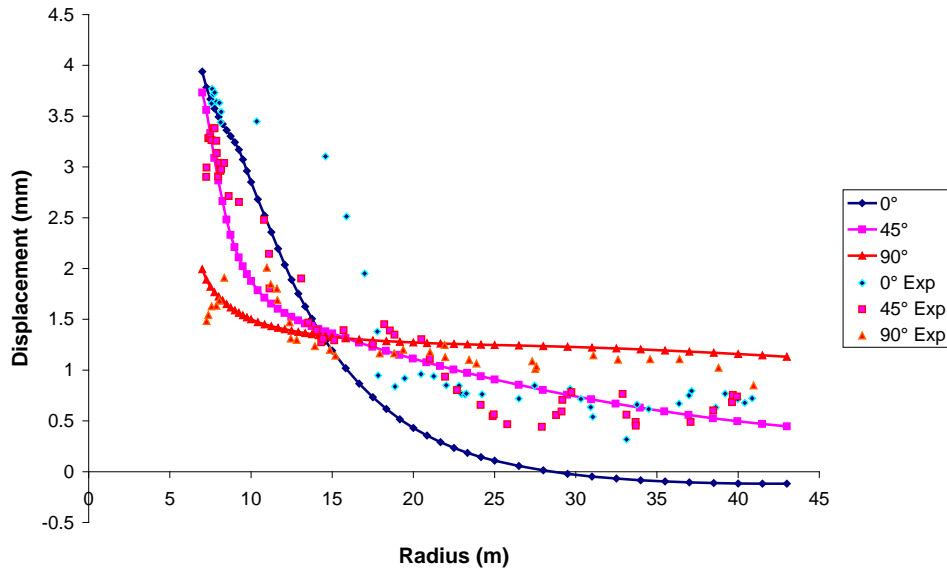


**Figure 154: Radial displacement versus radial distance in case 5 after mechanical unloading and water pressure dissipation in the direction parallel ( $\alpha=0^\circ$ ), perpendicular ( $\alpha=90^\circ$ ) and at  $45^\circ$  to the bedding plane. Comparison with experimental measurements**

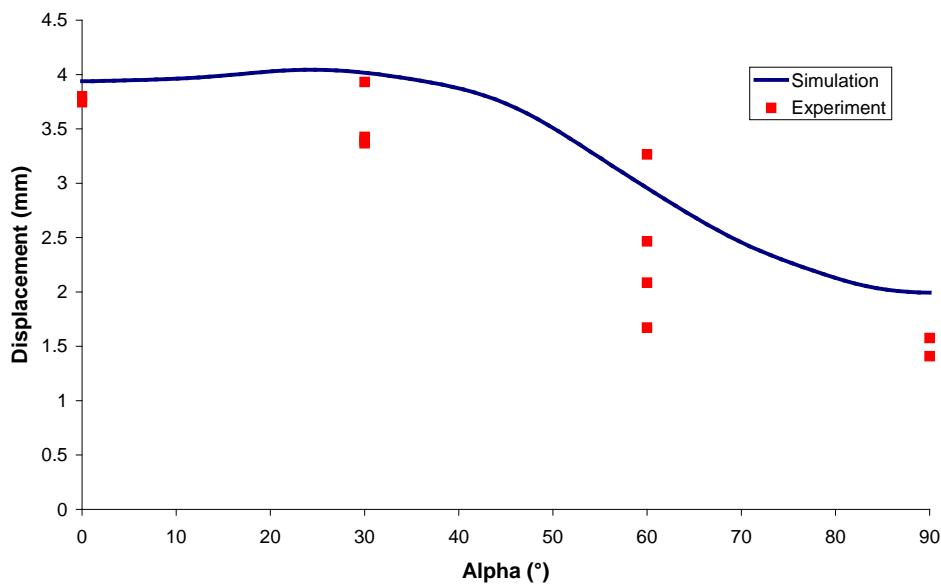


**Figure 155: Central hole displacement as a function of the orientation with respect to bedding plane in case 5. Comparison with experimental measurements**

### Strain localisation

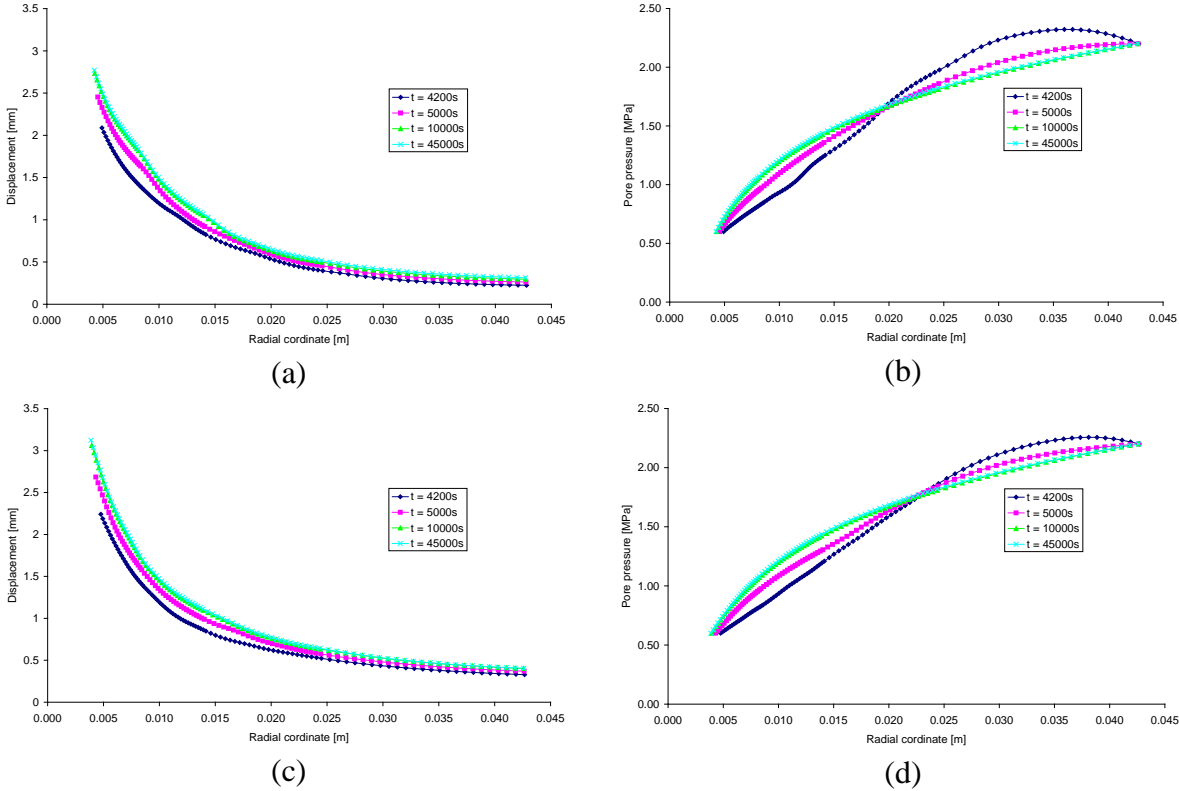
In the previous modelling, the aspects of strain localization are not highlighted in the results even if the phenomenon is numerically observed in some of them. This is especially the case when the constitutive model with a strain softening cohesion is considered. It is well known that the classical finite elements suffer of a pathological mesh dependency for the modelling of strain localization. That is the reason why it is proposed to revisit the previous 2D plane strain

TIMODAZ



modelling using the local second gradient model (See deliverable D10) in order to properly model the post peak behaviour by introducing an internal length scale. Once strain localization is modelled, the conditions of symmetry have to be considered with care; indeed due to localization, the response of an axi-symmetric problem can be no more symmetric. In theory, it would be thus necessary to model the whole transverse section of the hollow cylinder but for computational cost reasons, it has been decided to consider only a quarter of the section.

The following results have been obtained for the Case 3 (friction hardening and cohesion softening) with a parameter D of the second gradient law equal to 3 N. presents the radial displacement profiles and the pore pressure distribution in three directions. In each direction, we observe that the displacement still evolves after the excavation (4200 s) up to 10000 s. After this time, there are very few displacement modifications. This latter observation has to be correlated to the pore pressure distribution, where we see that after the excavation, the overpressures are drained and the consolidation takes place. After 10000 s, the pore pressure profile does not evolve much and we are more or less in a steady state.



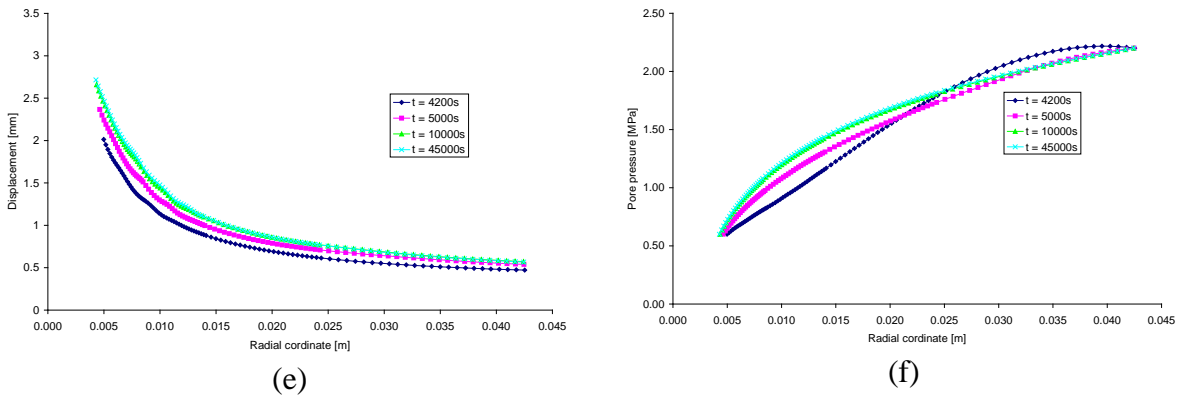


Figure 156: Radial displacement and pore pressure distribution for  $\alpha = 0^\circ$  (a-b),  $\alpha = 45^\circ$  (c-d) and  $\alpha = 90^\circ$  (e-f)

Figure 157(a) presents a comparison between the displacements in three different directions, at the end of the modelling (45000 s). At the inner hole, we observe that the maximum convergence occurs for  $\alpha = 45^\circ$ . For  $\alpha = 0^\circ$  and  $\alpha = 90^\circ$ , the convergence are more or less the same. At the outer face, the displacements are less important (around 0.5 mm) with a maximum value at  $\alpha = 90^\circ$  and a minimum value at  $\alpha = 0^\circ$ . Figure 157(b) presents the evolution of the convergence with  $\alpha$ . The latter figure highlights the fact that the maximum displacement actually occurs at  $\alpha = 45^\circ$ . The curve ‘Previous results’ shows the results obtained without considering localization.

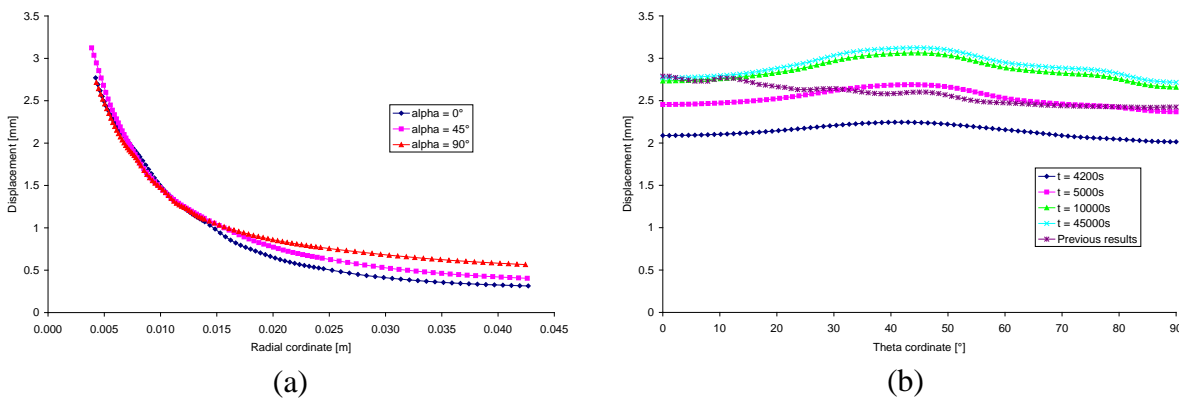
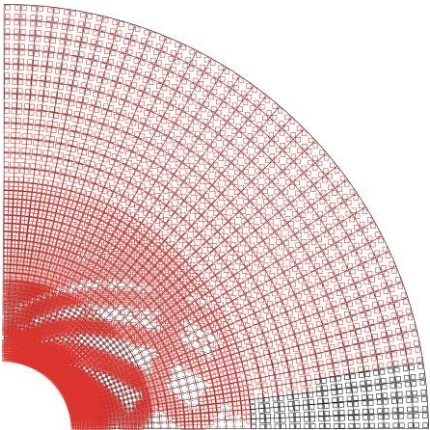


Figure 157: Comparisons of the displacement profile (a) and the inner hole convergence (b) for different directions

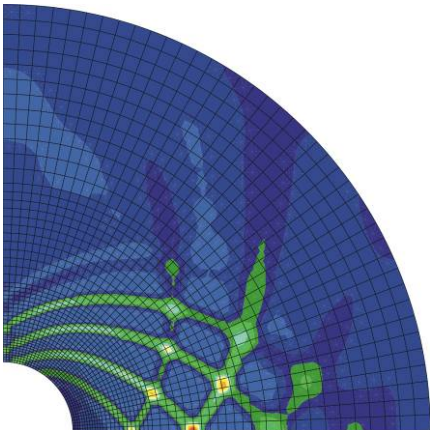
Figure 158 presents the map of the plastic point and the contour of the normalized increment of the deviatoric strain for different time steps. After the excavation, almost all the section is plastic but it is clear that some shear bands pattern appears. Between these bands, the behaviour is elastic and the contour of the increment deviatoric strain highlights the activity of the bands in terms of shear strains. At  $t = 5000$  s and  $t = 6000$  s, the process of shear banding shows that some bands occur and then become less active. The competition between these different bands is clearly observed. At  $t = 10000$  s, the localization pattern becomes more stable and the final structure of the most active shear bands is only composed of three bands. It is to be emphasised that the most active shear bands occur at the beginning of the modelling (at the end and right



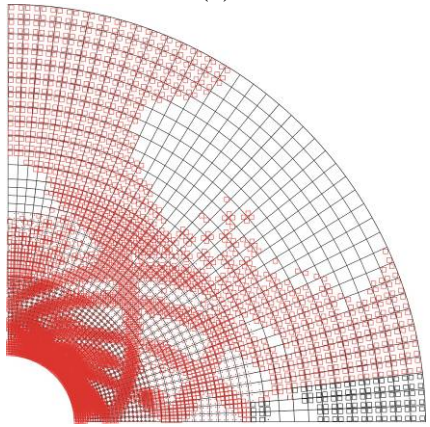
after the excavation). Concerning the plastic points, it has to be pointed out that the outer area at  $\alpha = 90^\circ$  is elastic after 10000 s.



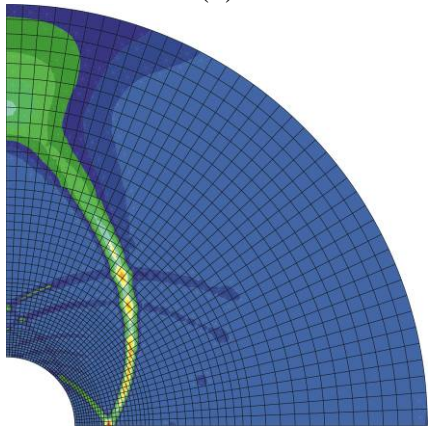
(a)



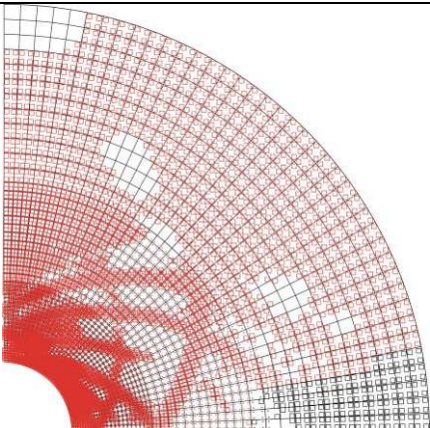
(b)



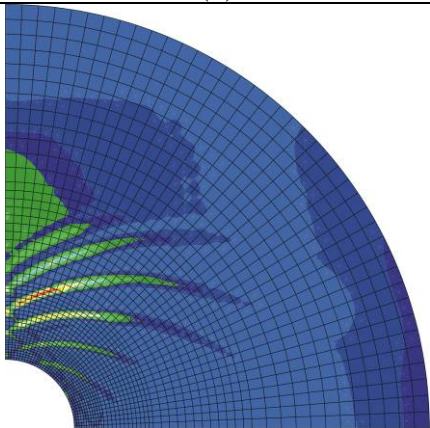
(c)



(d)



(e)



(f)



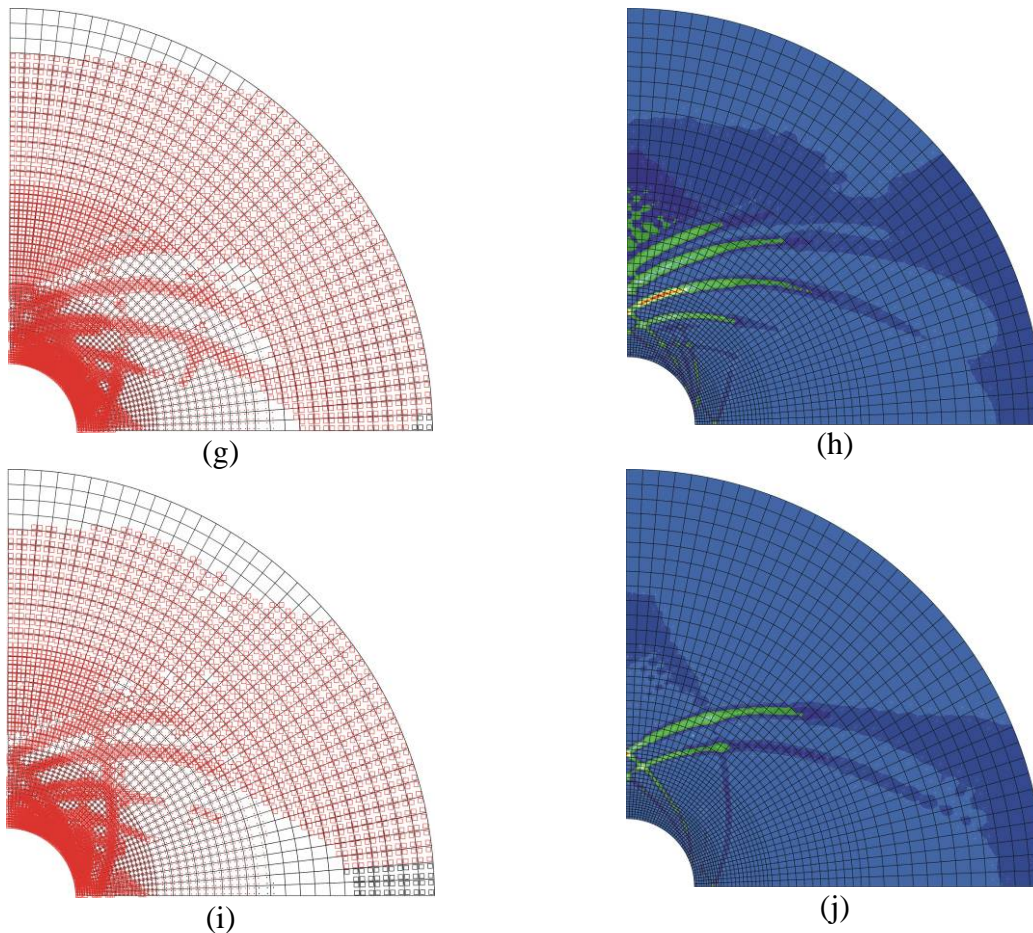


**Figure 158: Plastic point map and contour of normalized increment of deviatoric strain at  $t = 4200$  s (a-b),  $t = 5000$  s (c-d),  $t = 6000$  s (e-f),  $t = 10000$  s (g-h) and  $t = 45000$  s (i-j)**

Figure 159 shows the total equivalent deviatoric strain after the excavation and at the end of the modelling ( $t = 45000$  s). After the excavation, it is clear that the response of the model is not isotropic and that the shear bands affect the deviatoric strain distribution. At the end of the modelling, we see the maximum of the strain at  $\alpha = 45^\circ$  as the results of the localization processes occurring during the modelling. Be careful that the minimum and the maximum are not the same on both pictures.

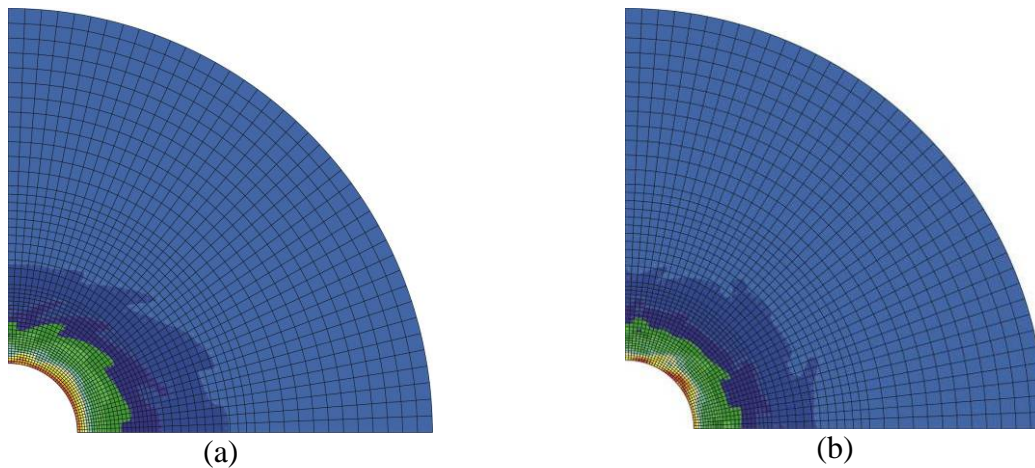


Figure 159: Contour of the equivalent deviatoric strain at  $t = 4200$  s (a) and  $t = 45000$  s (b)

### 11.32D axisymmetric case

The simulations of the 1D axisymmetric and 2D plane strain cases assumed plane strain conditions in the axial direction. However, in the experiment, conditions are different. The sample is stuck on a steel cap, at the top, and on the base, at the bottom. The sample and the top cap are subjected to a confining pressure of 4.5 MPa. So, the axial conditions are stress-controlled and the radial displacements are constrained at the top and at the bottom. To study the effect of the axial boundary conditions, a 2D axisymmetric case has been simulated. Case A and C of Table 8 have been considered. The boundary conditions are reported in Figure 160. The obtained results in term of the evolution of radial displacement in the mid-section of the sample are compared with the results of 1D axisymmetric simulation in Figure 161 and Figure 162 for cases A and C, respectively. It shows almost identical results. It proves that the effect of axial boundary conditions on the behaviour of the mid-section may be considered as negligible.

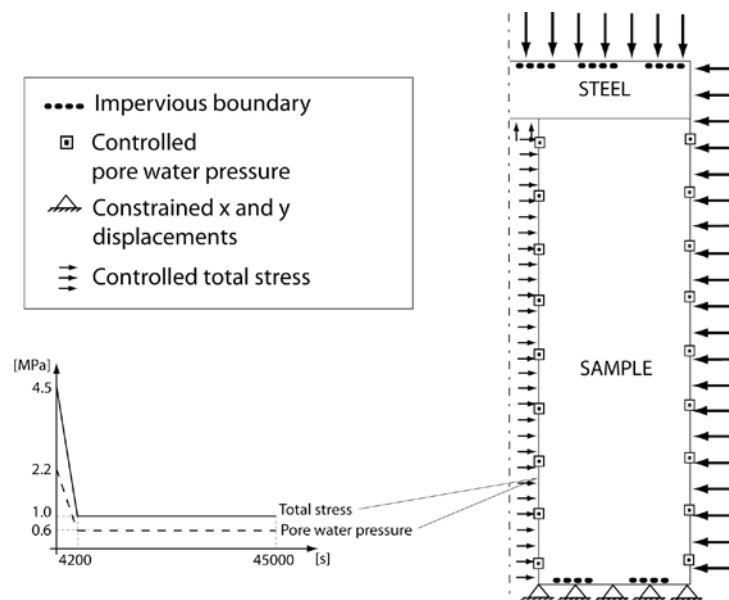
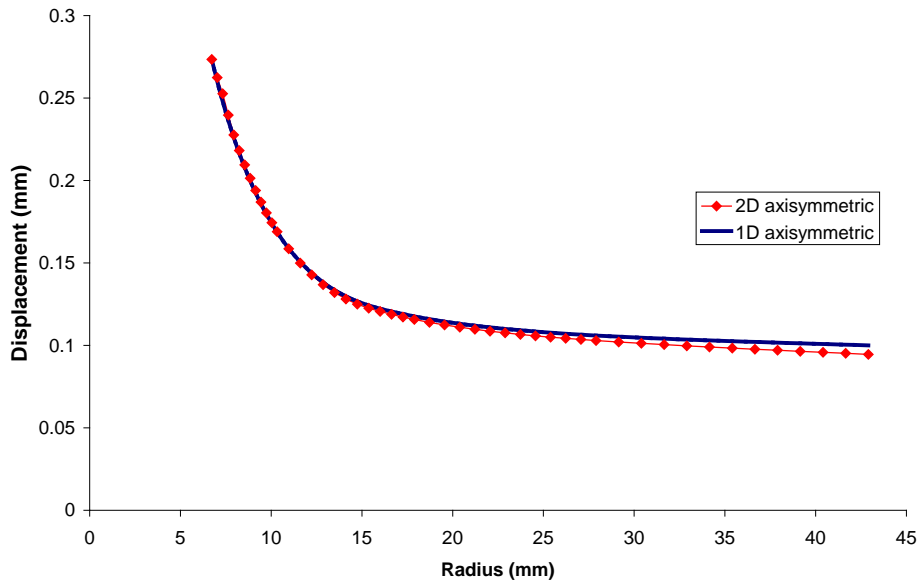
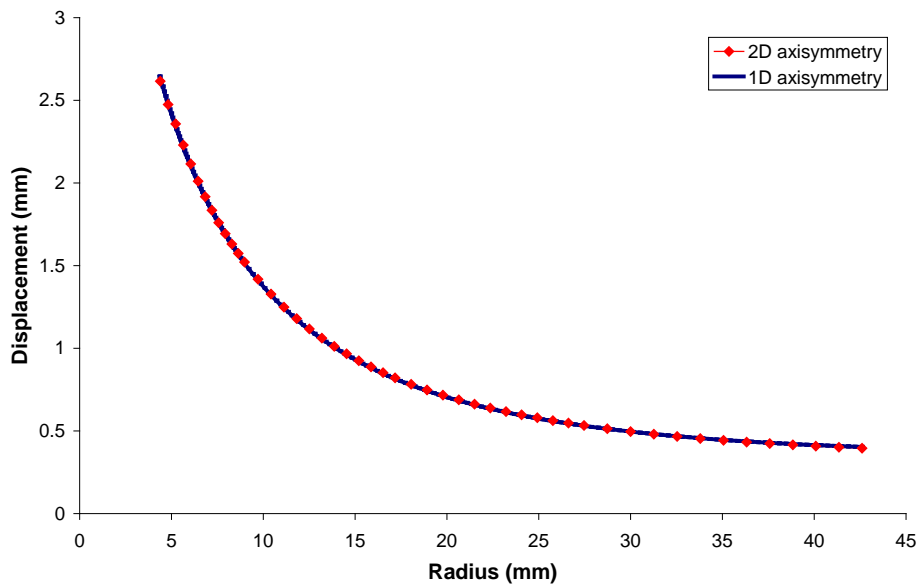


Figure 160: Boundary conditions for the 2D axisymmetric simulations  
TIMODAZ



**Figure 161: Radial displacement versus radial distance in case A in the mid-section of the sample after mechanical unloading and water pressure dissipation. Comparisons with the results obtained by 1D axisymmetric simulations**



**Figure 162: Radial displacement versus radial distance in case C in the mid-section of the sample after mechanical unloading and water pressure dissipation. Comparisons with the results obtained by 1D axisymmetric simulations**

In addition, the deformed mesh is shown in Figure 163. For case A, the axial displacement of the top cap is 0.23 mm while it is 0.41 mm for case C. The deformed geometry is barrel-shaped with



no radial displacement at the top and at the bottom while the maximum radial displacement is observed in the mid-section.

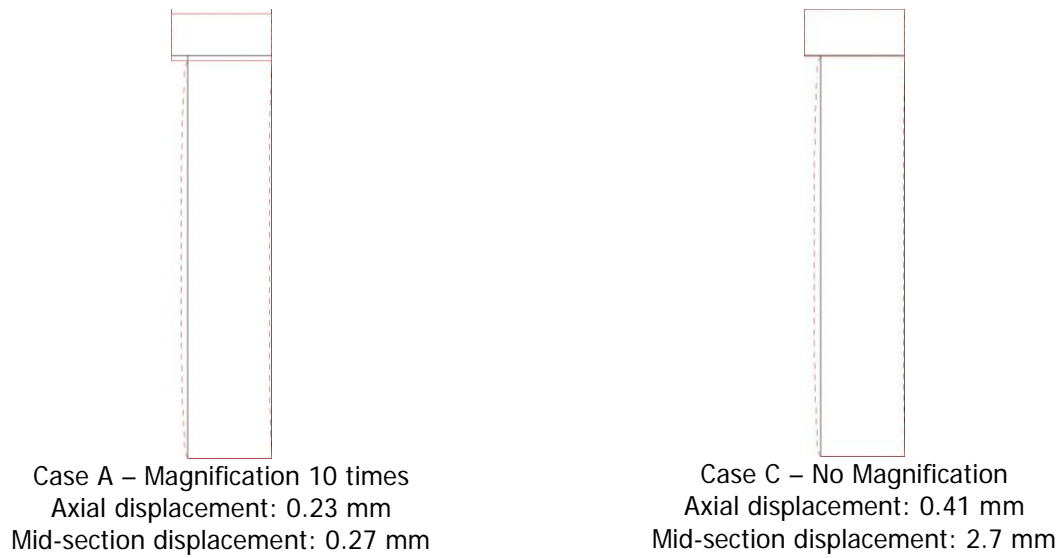


**Figure 163: Deformed mesh obtained in 2D axisymmetric simulations. (a) Case A, (b) Case C**

